97N24654

NASA Conference Publication 10193

Physics & Process Modeling (PPM) and Other Propulsion R&T

Volume I: Materials Processing, Characterization, and Modeling; Lifing Models

Proceedings of the PPM and Other Propulsion R&T Conference
held at the Cleveland Airport Marriott
sponsored by NASA Lewis Research Center
Cleveland, Ohio
May 1, 1997

NASA Conference Publication 10193

Physics & Process Modeling (PPM) and Other Propulsion R&T

Volume I: Materials Processing, Characterization, and Modeling; Lifing Models

Proceedings of the PPM and Other Propulsion R&T Conference
held at the Cleveland Airport Marriott
sponsored by NASA Lewis Research Center
Cleveland, Ohio
May 1, 1997

National Aeronautics and
Space Administration

Office of Management

Scientific and Technical
Information Program

1997

FOREWORD

The Propulsion Systems Program is one of six Propulsion Systems Research and Technology Base Programs within the NASA Aeronautics Enterprise. This program, which consists of a number of projects that are structured to address the critical technology needs of a range of vehicle classes, focuses on the goals of safety, environment, capacity, efficiency, affordability, performance, and survivability.

The Propulsion Systems Program relies on a number of critical technical competencies to perform research and develop technologies. Among these competencies are propulsion materials and structures. On May 1, 1997, individuals involved in materials and structures research under several of the Propulsion Systems Program projects met at the Cleveland Airport Marriott, in Cleveland, Ohio, to discuss their progress at the PPM and Other Propulsion R&T Conference. Representatives of government, industry, and universities heard presentations on material processing, material characterization, modeling, lifing, applied life models, design, vibration control, mechanical components, and tribology. This publication contains figures and supporting text from those presentations.

The majority of the research discussed was performed under the Physics & Process Modeling (PPM) project, which is focused on using physics-based models and process modeling techniques to reduce time, cost, and risk barriers to revolutionizing turbine engines and power systems. Other Propulsion Systems Program projects represented in the conference were Smart, Green Engine (SGE); Fast, Quiet Engine (FQE); High Temperature Engine Materials Program (HITEMP); and Hybrid Hyperspeed Propulsion (HHP). Also represented were the Rotorcraft Systems Program and the NASA Lewis Director's Discretionary Fund.

This conference was held in conjunction with three other conferences at the NASA Lewis Materials and Structures Technology Symposium. The other conferences addressed Advanced Subsonic Technology, Enabling Propulsion Materials, and the High Temperature Engine Materials and Structures Project.

Conference Chairs:

Douglas A. Rohn
L. James Kiraly

PROGRAMS AND PROJECTS

Papers contained herein support the goals of the following projects:

Program or Project	**Paper Numbers**
Propulsion Systems Program	
Physics and Process Modeling (PPM) project	3, 4, 8, 10, 11, 12, 15, 16, 17, 19, 20, 24, 25, 26, 27, 30, 31, 32, 33, 34, 35, 36
Smart Green Engine (SGE) project	28, 29
Fast, Quiet Engine (FQE) project	1, 6
High Temperature Engine Materials Program (HITEMP)	14, 18
Hybrid Hyperspeed Propulsion (HHP) project	2, 7, 9, 13
Rotorcraft Systems Program	22, 23, 37
Lewis Director's Discretionary Fund	5

CONTENTS OF VOLUME I

MATERIALS PROCESSING

MATERIALS CHARACTERISTICS

MATERIALS MODELING

LIFING MODELS (1)

LIFING MODELS (2)

THE EFFECT OF HYDROGEN ANNEALING AND SULFUR CONTENT ON THE OXIDATION RESISTANCE OF PWA 1480

JAMES L. SMIALEK
NASA Lewis Research Center

INTRODUCTION

For many decades the dramatic effect of trace amounts of reactive elements on alumina and chromia scale adhesion has been recognized and widely studied. Although various theories have been used to account for such behavior, the connection between scale adhesion and sulfur segregation was initially reported by Smeggil et al., 1986 (ref. 1). This study found strong surface segregation of sulfur from very low levels in the bulk, which could then be curtailed by the addition of reactive elements. It was assumed that the reactive elements, which are strong sulfide formers, acted by gettering sulfur in the bulk, thus precluding sulfur segregation and weakening of the oxide-metal bond. Subsequent studies confirmed that adhesion could be produced by reducing the sulfur impurity level, without reactive elements (ref. 2,3).

The understanding of this phenomenon has been applied to modern single crystal superalloys (figures 1, 2; ref. 4), where the addition of Y, although very effective, is problematic. Also problematic is definition of the level of sulfur that is acceptable and below which no further adhesion benefit is reached. Published works have indicated a broad transition defined by various materials and oxidation tests.

The present study describes the oxidation behavior of one superalloy (PWA 1480) as a function of various sulfur contents produced by hydrogen annealing for various temperatures, times, and sample thicknesses. The purpose is to define more precisely a criterion for adhesion based on total sulfur reservoir and segregation potential (figure 3).

EXPERIMENTAL PROCEDURE

Oxidation coupons were electrodischarge machined from polycrystalline bar stock of PWA 1480, to 13 x 25 mm coupons with thicknesses of 0.25, 0.5, 1.3, 2.5, or 5.1 mm and polished through 600 grit emery. The starting sulfur content was determined to be about 6.2 ppmw by GDMS (glow discharge mass spectroscopy, Shiva Technologies). Hydrogen annealing was performed in a flowing H_2/Ar mixture for 8-100 hr at 1000°C to 1300°C, as indicated in figure 5. All samples were clean and metallic, with less than ±0.03 mg/cm^2 weight change after annealing. Cyclic oxidation was performed in air at 1100°C (2012°F) with a cycle frequency of 1-hr, for up to 500 or 1000 hr. Scales were characterized by x-ray diffraction and SEM.

RESULTS AND DISCUSSION

Gravimetric Data

The effect of annealing temperature on the 1100°C cyclic oxidation weight change curves is shown in figure 6 for a specimen thickness of 0.5 mm (20 mils) and annealing time of 20 hr. The 1000° and 1100° C anneals did little to improve the cyclic oxidation resistance over that of the as-received control sample, resulting in more than 20 mg/cm^2 weight loss after 500 1-hr cycles. The 1200° and 1300°C annealing treatments, however, resulted in 1000 hr weight changes of only +0.10 and -3.4 mg/cm^2, respectively. This represents a very significant improvement.

The effect of annealing time on oxidation behavior is shown in figure 7 for 0.5 mm (20 mil) samples annealed at 1200°C. Here a significant improvement was noted by only an 8 hr anneal, producing a weight loss of only 6.7 mg/cm^2 after 1000 hr. The 1000 hr weight changes of the 20, 50, and 100 hr samples were all excellent (+0.10, +0.36, and +0.16 mg/cm^2, respectively). Finally the effect of specimen thickness is shown in figure 8. Here a 20 hr anneal at 1200°C produced very adherent scales for 0.25 and 0.5 mm (10 and 20 mil) samples, but substantial weight losses for 1.3 and 2.5 mm (50 and 100 mil) thicknesses.

The dependence of adherence (as exhibited by the 500 hr cyclic oxidation weight change) can be seen as a function of annealing temperature, time, and sample thickness in figures 9-11. Weight losses are reduced dramatically for temperatures over 1200°C, times over 20 hr, and samples under 0.5 mm (20 mil) thickness. Each figure also shows the improved performance of longer anneal times, higher anneal temperatures, or thinner samples between the individual curves of each family.

Scale phases were identified from X-ray diffractometer scans as primarily Al_2O_3, $Ni(Al,Cr)_2O_4$, and $CrTaO_4$. A greater relative amount of Al_2O_3 is noted for the more oxidation resistant samples, and more $NiCr_2O_4$ and $CrTaO_4$ for the samples with poor oxidation resistance. SEM/EDS analysis revealed a complex multiphase segmented scale on the control sample with clusters of high Cr or Ta oxides as compared to a relatively uniform Al_2O_3 scale on the 0.5 mm sample annealed at 1200°C for 20 hr.

Effect of Sulfur Content

The effect of hydrogen annealing on sulfur content is summarized in figure 12. The sulfur content was progressively reduced as the annealing time and temperature increased and the thickness decreased. Many values in the 0.1-0.3 ppmw range were obtained. These levels had been associated with the most oxidation resistant samples in previous studies (ref. 4). The 500 hr weight change of all the samples tested is shown in figure 13 as function of the sulfur content for the 5 sets of sample thicknesses. For each curve, the final weight change diminishes from a relatively large loss at the starting sulfur content, becoming much less severe at about 1 ppmw, and extremely small at 0.1 ppmw. Despite scatter in the sulfur data, an overall detrimental trend with sample thickness can also be discerned (figure 14).

Adhesion Criteria

A fundamental approach has been suggested to define a critical sulfur content (ref. 5). This concept claims that a limit to an adhesion benefit is reached when the sample contains a total amount of sulfur less than that required to produce ~1 monolayer of segregation. The implication is that about one monolayer will produce significant spallation events, but, with no replenishment, it is unable to sustain repetitive degradation. The equivalence between bulk sulfur content and segregated monolayers has been approximated:

$$C_s\,(\text{ppmw}) = (8.27\times10^{-2}\ \text{gm/cm}^2)*N_m A/W \qquad \text{(ref. 5)}$$

where: C_s = bulk sulfur content in ppmw; N_m = number of segregated monolayers; A = sample surface area in cm^2; and W = sample weight in gm. The 1 monolayer criterion is shown on the "adhesion map" of figure 16 for PWA 1480 samples of density = 8.42 gm/cm^3. The weight change data are represented by symbols, where the degree of shading corresponds to a weight change interval. The 0 and -10 mg/cm^2 contour lines obtained from figures 13 and 14 mark the transition from excellent adherence (solid symbols) to poorly performing (lightly shaded symbols). Excellent behavior is thus indicated for samples having a total sulfur content less than about one monolayer equivalent. This appears to be as good a criterion that can be made at this time, given the scatter in the sulfur data. It should also be noted that the thermodyanmic equilibrium surface concentration of sulfur at 0.1 ppmw bulk is predicted to be vastly reduced from the 30 % saturation value (ref. 4). Thus low bulk levels also produce low equilibrium segregation levels, which can then benefit scale adhesion regardless of specimen thickness.

CONCLUDING REMARKS

This study has shown the strong dependence of superalloy oxidation resistance on low levels of sulfur impurity contents. Extraordinary improvements are possible from desulfurization by hydrogen annealing. Typical sample thickness ~1 mm may be easily desulfurized to <1ppmw by annealing at 1200°C. Sulfur segregation is reduced which in turn produces excellent cyclic oxidation behavior at 1100°C (very small weight changes of only 0.5 to 1 mg/cm^2 after 1000 hours). A basic criteria of scale adhesion was developed which suggests that a critical sulfur content of 0.1-1 ppmw is required to obtain the maximum adhesion for alloys without Y. The benefit of low sulfur superalloys may be taken by reducing the amount of Y required, by operating without a coating, or by extending oxidative lives with coatings.

ACKNOWLEDGEMENTS

The author is grateful to D. Humphrey for performing the hydrogen annealing treatments.

REFERENCES

1) Smeggil, J.G., Funkenbusch, A.W., and Bornstein,N.S., "A Relationship between Indigenous Impurity Elements and Protective Oxide Scale Adherence Characteristics," Metall. Trans., Vol 17A, 1986, pp. 923-932.

2) Smeggil, J.G., "Some Comments on the Role of Yttrium in Protective Oxide Scale Adherence," Mater. Sci. and Engineer., Vol. 87, 1987, pp. 261-265.

3) Smialek, J.L., "Adherent Al_2O_3 Scales Produced on Undoped NiCrAl Alloys," Metall. Trans., Vol 18 A, 1987, pp. 164-167.

4) Smialek, J.L., "Oxidation Resistance and Critical Sulfur Content of Single Crystal Superalloys," Presented at IGTI, Birmingham, U.K., June 10-13, 1996; Paper 96-GT-519, ASME, 1996, pp. 1-7.

5) Smialek, J.L., "Effect of Sulfur Removal on Al_2O_3 Scale Adhesion," Metall. Trans., Vol. 22A, 1991, pp. 739-752.

Previous Studies Have Shown:

- Conventional SX superalloys contain ~3-10 ppmw sulfur impurity
- Unacceptable cyclic oxidation resistance (w/o Y)
- Sulfur segregation saturates at about 30 at.%
- Desulfurization improves scale adhesion (in melt or hydrogen annealing)
- 0.1 ppmw appears to be lower limit needed
- Acceptable upper limit still needs to be defined

Fig. 1

Correlation of Weight Change With Sulfur Content for the Oxidation of Superalloys

1100-1200 °C, 200-1500 hr

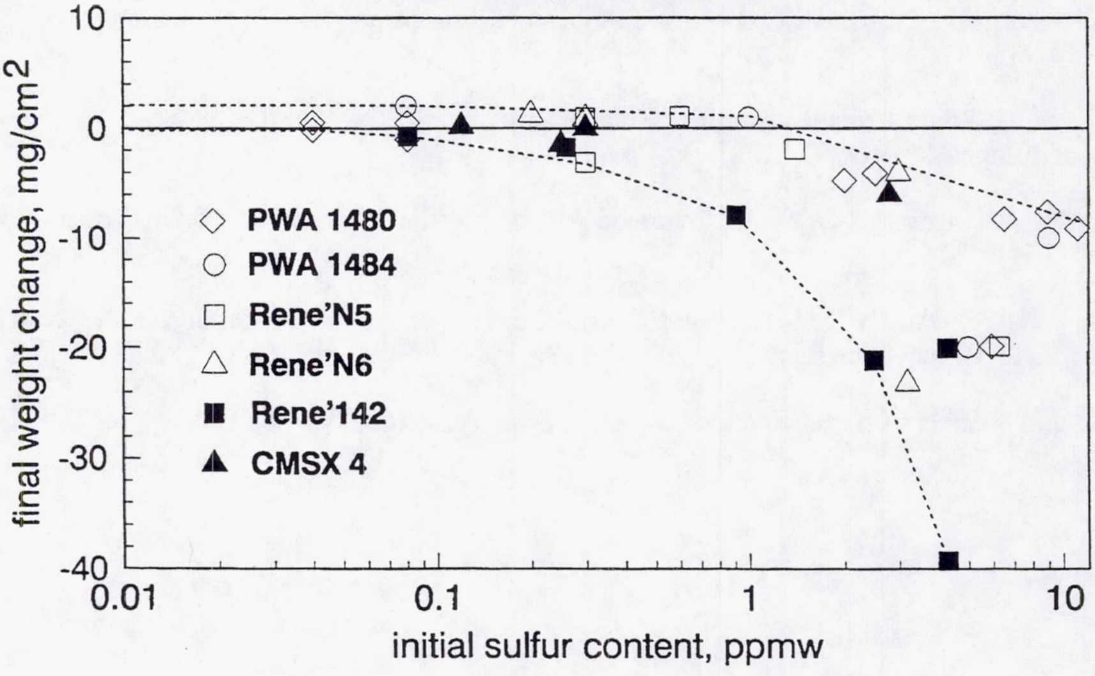

Fig. 2

Motivations

(Tubbs and Smialek, 1989; 1995)

- Hydrogen annealing effects on sulfur content (T, t, L)
- Sulfur diffusivity vs temperature
- Optimum annealing conditions
- Quantified sulfur effect on cyclic oxidation
- Critical sulfur content vs thickness:
  (adhesion map)
- Internally consistent data base:
  (one ingot, one anneal process, one oxidation test)

Fig. 3

Experimental Strategy

- Partial hydrogen annealing matrix: Dt/L^2
  - L: 10, 20, 50, 100, 200 mils (0.25 - 5 mm)
  - t: 8, 20, 50, 100 hr
  - $D=A^*\exp(-Q/RT)$
  - T: 1000°, 1100°, 1200°, 1300°C (1830-2370°F)
- GDMS measurement of ppm levels of sulfur
- Cyclic oxidation: 1100°C, 1-hr cycles, 500-1000 hr
- Weight change, XRD, SEM/EDS

Fig. 4

Selection of Hydrogen Annealing Parameters

(sample thickness, temperature, time)

	control	1000 °C	1100 °C	1200 °C	1300 °C
control	b,c				
8 hr		a		b,c	
20 hr		a,b	b	a,b,c,d	b,c, e
50 hr				b	
100 hr		a	d	a,b,c,d,e	d

a	b	c	d	e	
10	20	50	100	200	mils
0.25	0.5	1.3	2.5	5.1	mm

Fig. 5

Effect of Annealing Temperature

20 hr hydrogen anneal; 1100 °C cyclic oxidation

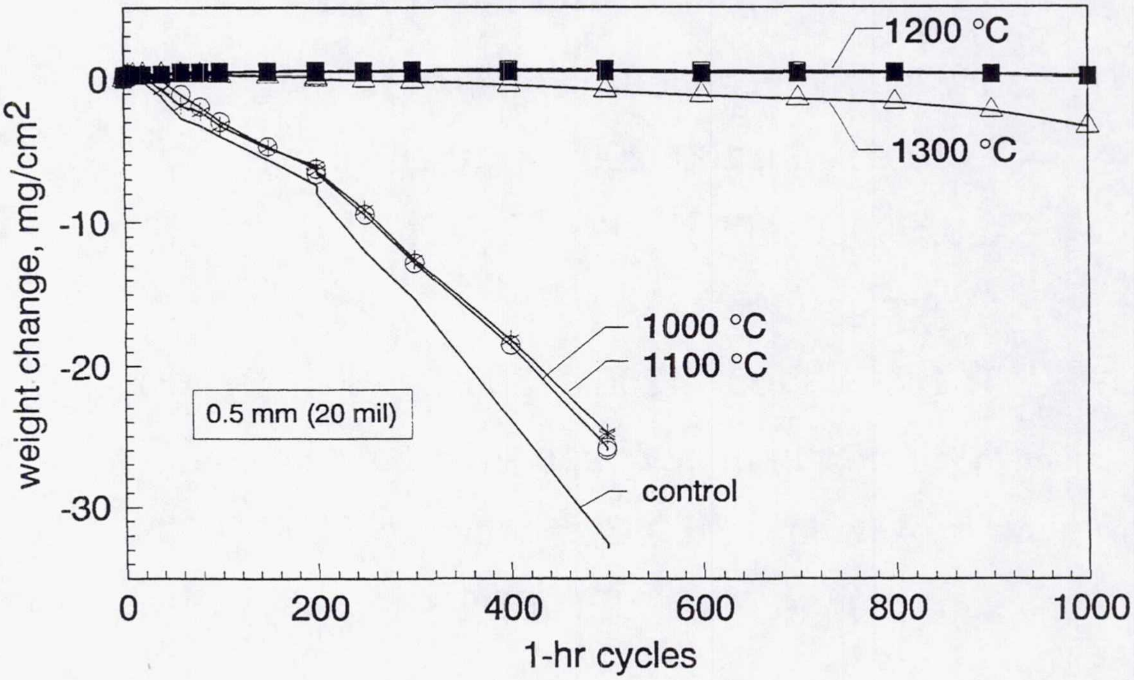

Fig. 6

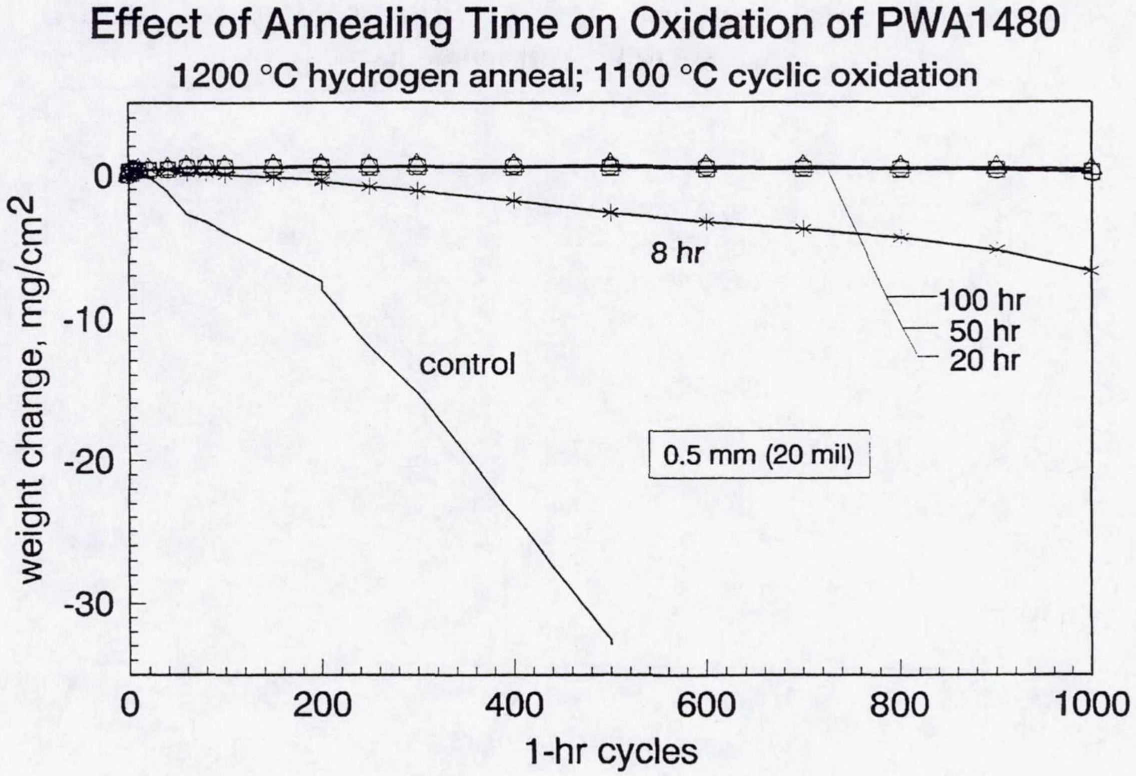
Effect of Annealing Time on Oxidation of PWA1480
1200 °C hydrogen anneal; 1100 °C cyclic oxidation
weight change, mg/cm2
0
-10
-20
-30
0
200
400
600
800
1000
1-hr cycles
8 hr
100 hr
50 hr
20 hr
control
0.5 mm (20 mil)

Fig. 7

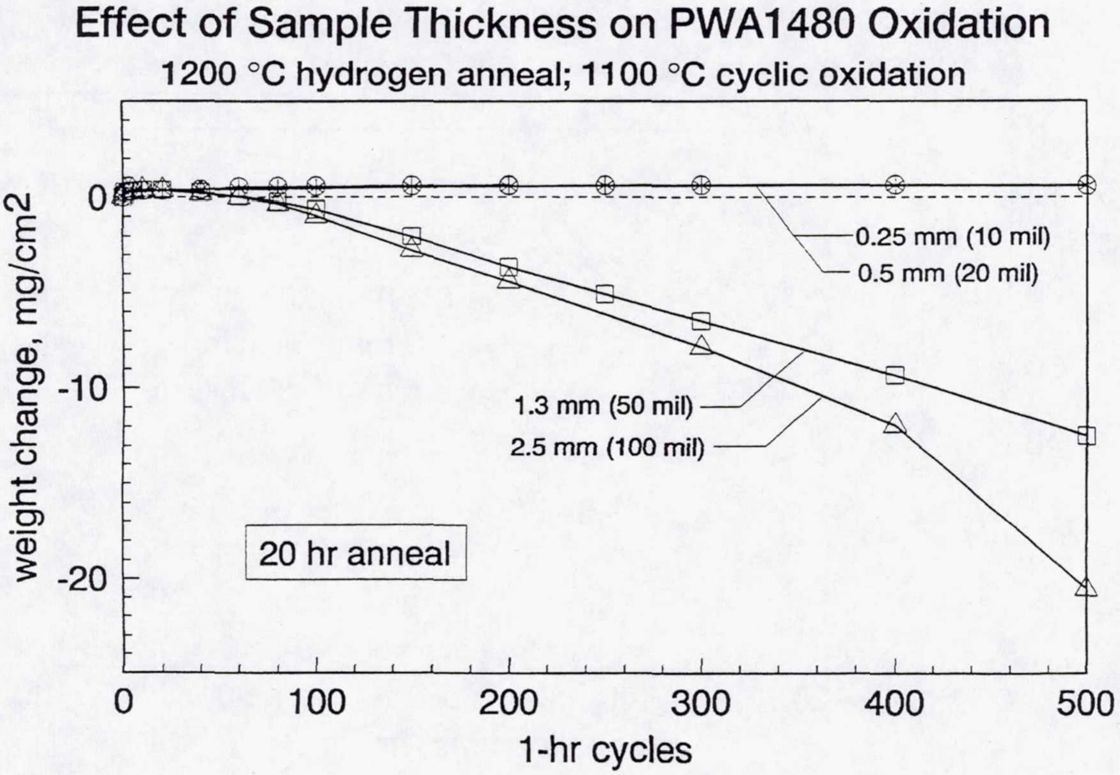
Effect of Sample Thickness on PWA1480 Oxidation
1200 °C hydrogen anneal; 1100 °C cyclic oxidation
weight change, mg/cm2
0
-10
-20
0
100
200
300
400
500
1-hr cycles
0.25 mm (10 mil)
0.5 mm (20 mil)
1.3 mm (50 mil)
2.5 mm (100 mil)
20 hr anneal

Fig. 8

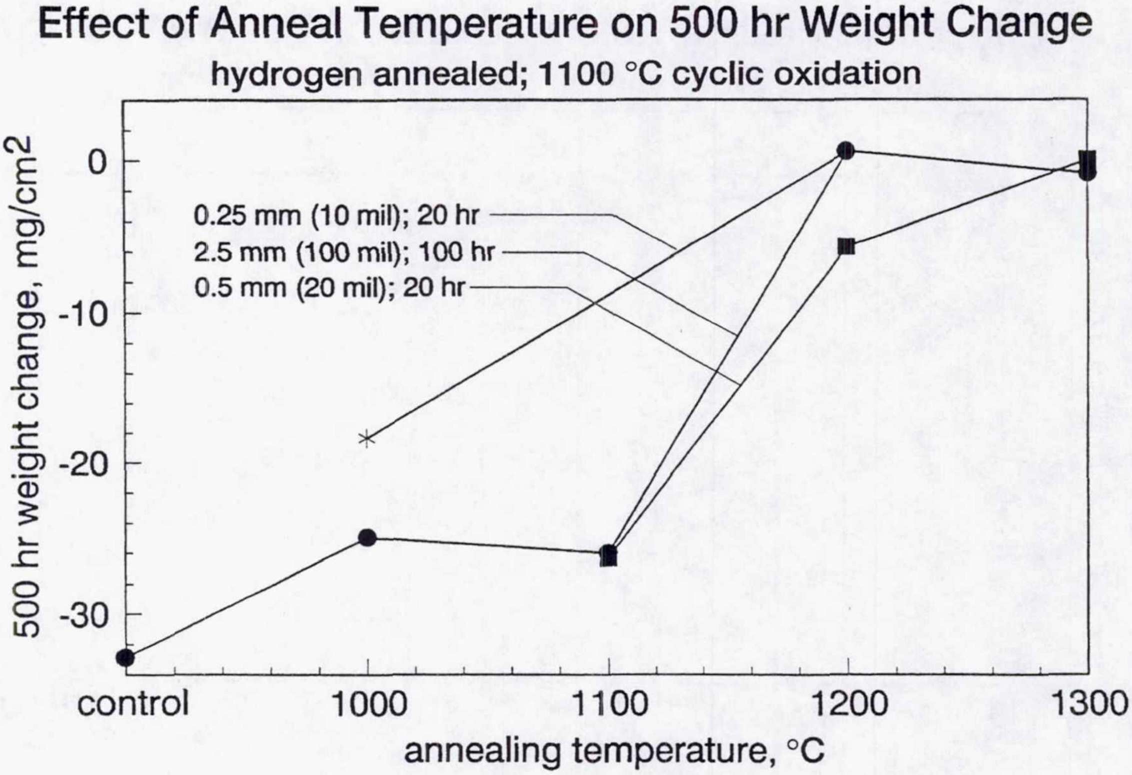
Effect of Anneal Temperature on 500 hr Weight Change
hydrogen annealed; 1100 °C cyclic oxidation
500 hr weight change, mg/cm2
0
-10
-20
-30
0.25 mm (10 mil); 20 hr
2.5 mm (100 mil); 100 hr
0.5 mm (20 mil); 20 hr
control
1000
1100
1200
1300
annealing temperature, °C

Fig. 9

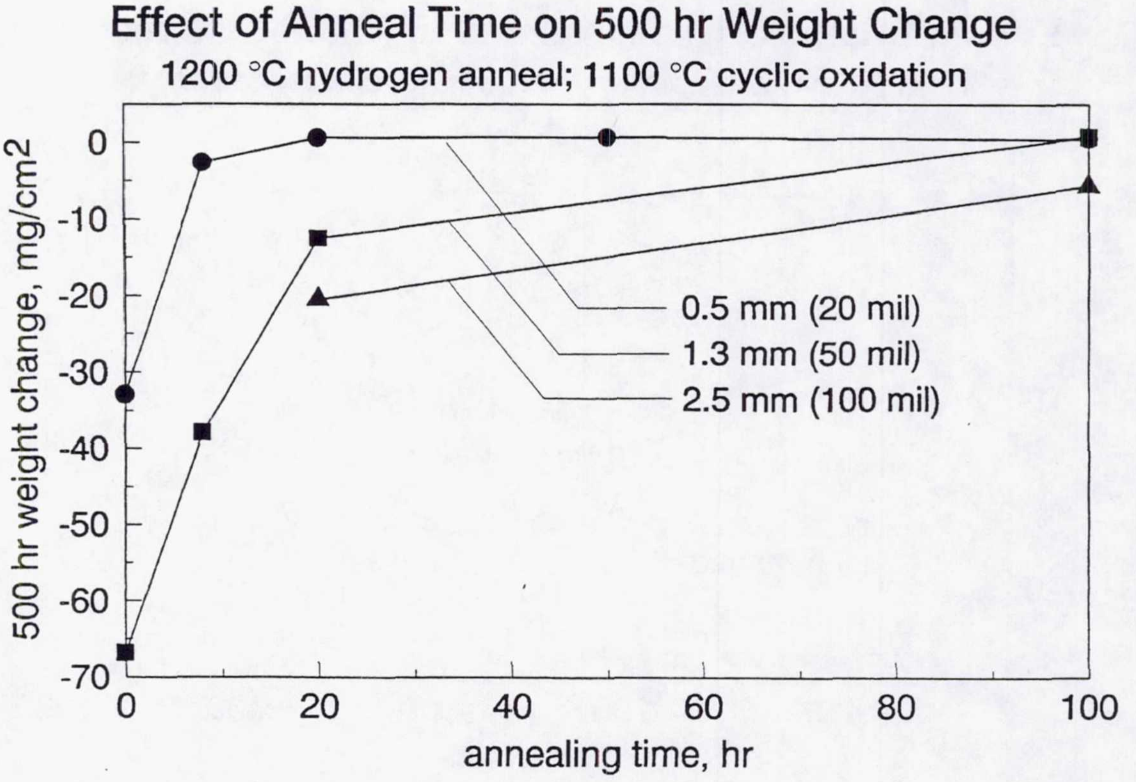
Effect of Anneal Time on 500 hr Weight Change
1200 °C hydrogen anneal; 1100 °C cyclic oxidation
500 hr weight change, mg/cm2
0
-10
-20
-30
-40
-50
-60
-70
0.5 mm (20 mil)
1.3 mm (50 mil)
2.5 mm (100 mil)
0
20
40
60
80
100
annealing time, hr

Fig. 10

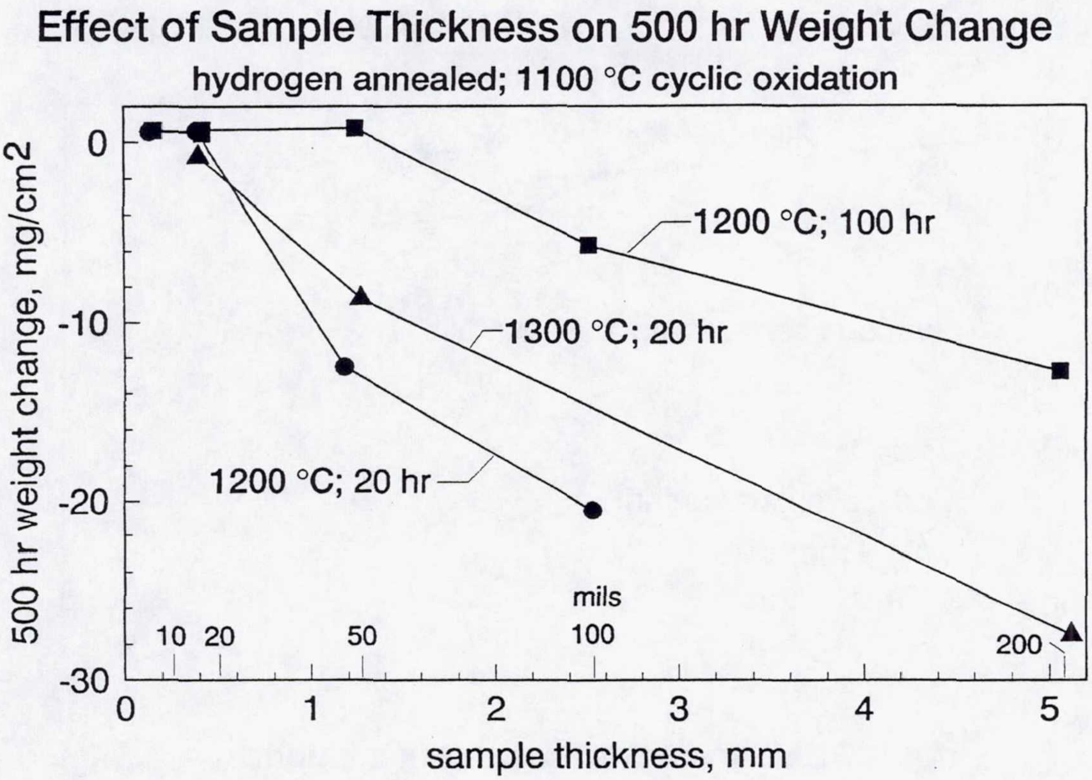

Fig. 11

Sulfur Content after Hydrogen Annealing

(vs sample thickness, temperature, time)

	control	1000°C	1100°C	1200°C	1300°C
control	6.2, 6.2 b, c				
8 hr		4.9 a		.8, 2.0 ⓑ, c	
20 hr		4.6, 3.9 a, b	2.1, 2.6 b, c	.15 .28 1.5 1.5 ⓐ ⓑ c, d	.06 .34 3.3 ⓑ ⓒ e
50 hr				0.05 ⓑ	
100 hr		4.3 a	2.1 d	.12 .14 .12 .4 1.4 ⓐ ⓑ ⓒ ⓓ e	.01 ⓓ

key: ⓧ <1 ppmw S

a	b	c	d	e	
10	20	50	100	200	mils
0.25	0.5	1.3	2.5	5.1	mm

Fig. 12

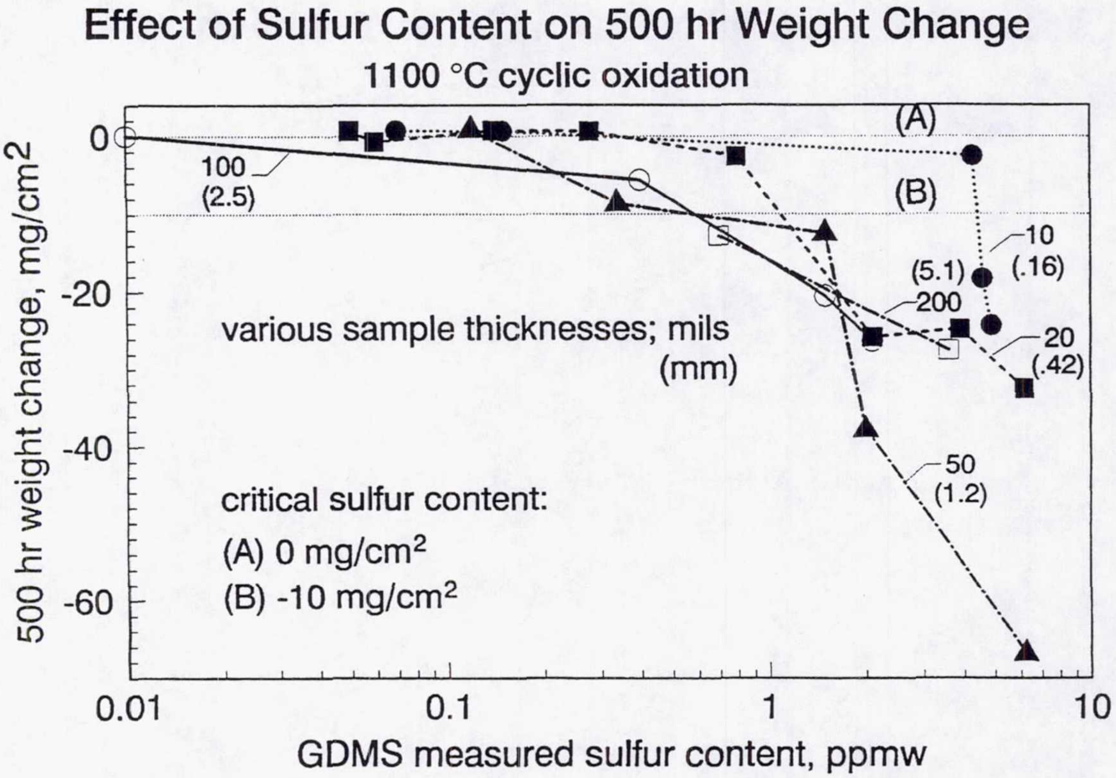

Effect of Sulfur Content on 500 hr Weight Change

1100 °C cyclic oxidation

Fig. 13

Critical Sulfur Contents (ppmw) for PWA 1480

(1100 °C cyclic oxidation)

mg/cm^2	10 (0.16)	20 (0.42)	50 (1.21)	100 (2.54)	200 mils (nom.) (5.09) mm (avg.)
0.0	1.6	0.4	0.20	0.20	0.15
-10.0	3.8	1.2	0.65	0.65	0.49

Fig. 14

Equivalence Between Bulk and Surface Sulfur Content

($N_m = 1$; one sulfur atom per one (001) Ni atom)

- C_s (ppmw) = 8.27×10^{-2} gm/cm^2 $\times N_m A / \rho V$
- $C_s \times L \sim 8.27 \times 10^{-2}$ cm $\times N_m$

Fig. 15

Oxide Adherence Map for Desulfurized PWA1480

1100 °C, 1-hr cycles, 500 hours

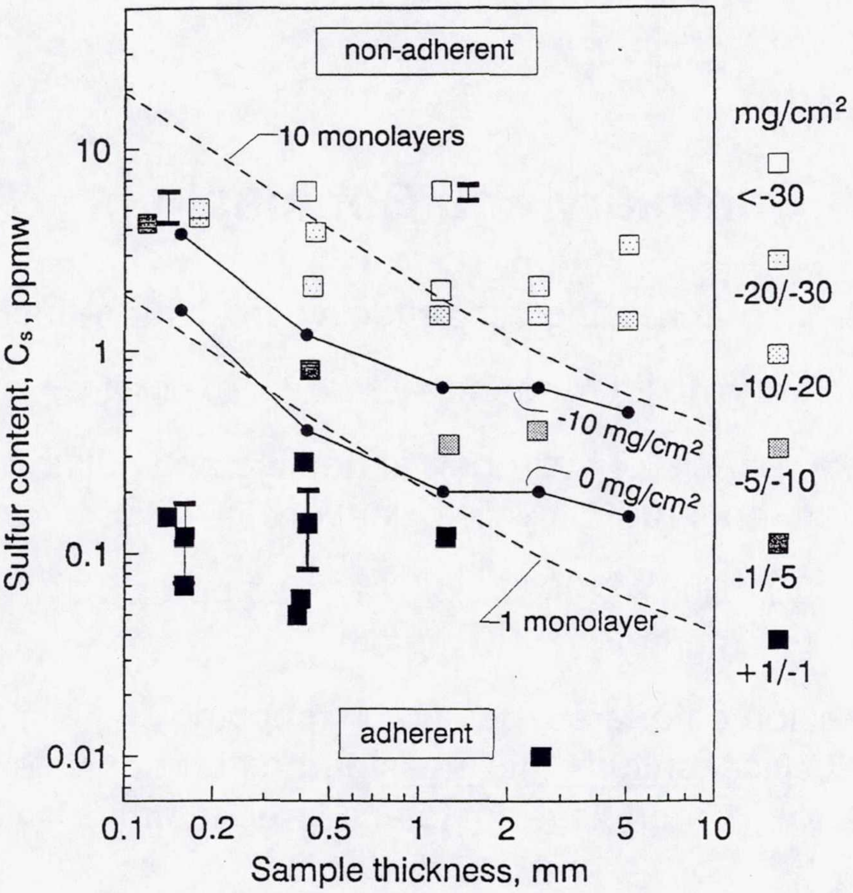

Fig. 16

Why Is ~1 Monolayer Equivalent Critical ?

- Saturation at 0.3 monolayers; sufficient for massive Al_2O_3 spallation
  - Repeated spallation events cause depletion zones, trigger Ni,Cr,Ta-rich oxides; conversely,
  - Limited sulfur reservoir limits spallation events
- Low bulk sulfur reduces equilibrium saturation level (~0.01 monolayer @ 0.2 ppmw sulfur)

Fig. 17

Summary and Conclusions

- Hydrogen annealing very effective in sulfur reduction

  Strong T, t, L dependence, e.g., $\exp(-Dt/L^2)$
- Strong effects of hydrogen annealing and sulfur content on 1100°C cyclic oxidation:

  <20 mils, >1200°C, >20 hr, <0.3 ppmw S:
  ($+1$ mg/cm^2 vs -30 mg/cm^2)
- Adhesion criteria suggested by mapping:
  Critical <u>sulfur • thickness</u> parameter equivalent
  to ~ 1 monolayer of total segregation

Fig. 18

Future Considerations

- Complete D_s, critical anneal evaluations
- Evaluate critical S/Y ratios
- Evaluate melt desulfurized PWA1484
- Coatings and TBC's
- HT-XPS segregation vs C_s

Fig. 19

FACTORS INFLUENCING RESIDUAL STRESSES IN YTTRIA STABILIZED ZIRCONIA THERMAL BARRIER COATINGS*

ROY T.R. McGRANN, Edmund F. Rybicki, and John R. Shadley
The University of Tulsa
Tulsa, Oklahoma

and

William J. Brindley
NASA Lewis Research Center
Cleveland, Ohio

Introduction

To improve gas turbine and diesel engine performance using thermal barrier coatings (TBC's) requires an understanding of the factors that influence the in-service behavior of thermal barrier coatings. One of the many factors related to coating performance is the state of stress in the coating. The total stress state is composed of the stresses due to the in-service loading history and the residual stresses.

Residual stresses have been shown to affect TBC life [1], the bond strength of thermal spray coatings [2], and the fatigue life of tungsten carbide coatings [3]. Residual stresses are first introduced in TBC's by the spraying process due to elevated temperatures during processing and the difference in coefficients of thermal expansion of the top coat, bond coat, and substrate. Later, the residual stresses can be changed by the in-service temperature history due to a number of time and temperature dependent mechanisms, such as oxidation, creep, and sintering. Silica content has also been shown to affect sintering and the cyclic life of thermal barrier coatings [4, 5]. Thus, it is important to understand how the spraying process, the in-service thermal cycles, and the silica content can create and alter residual stresses in thermal barrier coatings.

Objectives and Approach

There are three primary objectives of this work. The first objective is to determine how residual stresses are affected by the substrate temperature as the top coat is applied. Two temperatures were selected to represent a range of possible substrate temperature conditions. The second objective is to determine the effect of post-processing thermal cycles on the build up of coating residual stresses. The third objective is to determine the effect of silica (SiO_2) content in the powder on the coating residual stresses.

The approach involves four replicates of each of the twelve test conditions to determine the reproducibility of the residual stresses. The through-thickness residual stresses in the coating were evaluated using the Modified Layer Removal Method [6]. Figure 3 is the test matrix used to reach these objectives.

Specimen Composition, Dimensions and Preparation Procedures. The specimens consisted of three materials (1) a B1900 substrate (a high strength, high temperature nickel base alloy with a chemical composition of 64%Ni, 8%Cr, 10%Co, 6%Al, 1%Ti), (2) a Ni-36Cr-6Al-1.0Y bond coat, and (3) a yttria stabilized zirconia (YSZ), ZrO_2-8%Y_2O_3 top coat. The B1900 substrate material was prepared as castings of 50.8 mm (two inch) long bars, 25.4 mm (one inch) wide and 4.8 mm (0.190 in) thick. The bars were surface ground and then stress relieved. The stress relief heat treatment was a standard superalloy solution treatment at 1090°C (1994°F) for four hours followed by an aging treatment at 870°C (1598°F) for sixteen hours. The surface oxide was lightly ground off. One side of each specimen was grit blasted and thickness measurements were made. The bond coat and top coat were applied to the specimens by air plasma spraying (APS). The thickness of each specimen was measured on a preset grid before and after the application of the bond coat. Next, the top coat was applied to the specimens. The temperature of the coating face of the specimens was monitored by a pyrometer during top coat spraying. For the specimens referred to as the "higher processing temperature specimens," the substrate was preheated to 500°C (932°F). After the first pass of the top coat application, the coated surface temperature was controlled to 500°C.

---

* Work funded under NASA Contract NCC3-338.

For the "lower processing temperature specimens," the substrate was initially at room temperature. Over the course of two or three top coat application passes, the coating surface temperature rose to 260°C (500°F.

Thermal Cycling. The combined effects of processing substrate temperature and post-processing thermal cycling were investigated. One thermal cycle is defined as heating the specimen in air in a resistance heated furnace to 1100°C (2012°F) for one hour, removing the specimen from the furnace while still at 1100°C, and static air cooling to room temperature. Specimens were subjected to zero, one, ten, twenty or thirty thermal cycles.

Procedure For Evaluating Residual Stresses. The "Modified Layer Removal Method" was used to determine the through-thickness residual stress distributions in the top coat [9]. The procedure involves attaching strain gauges to the uncoated side of the specimen and removing layers of the coating. Figure 4 shows the free-body diagram used to develop the method. Layers of about 0.13 mm (5 mils) were removed from the coating by polishing using a metallurgical polishing wheel. Thickness measurements of the specimen are made after each layer is removed. Changes in strain gauge readings are recorded as layers are removed. The strain and thickness changes are inputs for the residual stress analysis back-computation procedure. The analysis is applied to each layer removed and calculates the residual stress in the layer removed and the change in stress distribution for the remaining piece. The stresses are summed in the back-computation procedure, for each layer removed, to evaluate the residual stress distribution in the material removed. The material properties used in this calculation are the modulus of elasticity for the substrate and the coating, 206 GPa (3 x 10^7 psi) and 34.5 GPa (5 x 10^6 psi), respectively, and Poisson's ratios of 0.3 and 0.18 for the substrate and coating, respectively.

Results And Discussion

Through-Thickness Residual Stress Distributions. Two through-thickness residual stress distributions, that are representative of the behavior of the residual stresses, were selected for illustration. Figure 5 shows the through-thickness residual stress data for three specimens with the higher processing temperature and no thermal cycling. The second example, shown in Figure 6, illustrates the residual stress data for the specimens with a higher temperature after ten thermal cycles. Both figures are for specimens with a "standard" (STD) coating powder, i.e., a coating powder in which the silica content was not controlled.

Average Coating Residual Stress. The average residual stress through the thickness of the YSZ coating was calculated for each set of specimens listed in the test matrix. First, the average residual stress through the coating thickness for the individual specimens was calculated. Then, the average stress for each set of specimens was calculated. Figure 7 shows the average compressive stress for each combination of thermal cycling, processing substrate temperature, and silica content.

Effects Of Substrate Temperature. A comparison of the average through-thickness residual stresses for specimens with the higher processing temperature and the specimens with the lower processing temperature reveals a consistent difference. The mean residual stress through the coating thickness is shown versus substrate temperature in Figure 8. This figure shows that, for the three cases of thermal cycling involving different substrate processing temperatures (zero, one, and ten cycles), the coatings applied with the higher processing temperature have a higher average compressive residual stress than the coatings applied with the lower processing temperature. For the case of zero thermal cycles, coatings applied with the higher processing temperature had 3.8 MPa (0.6 ksi) more compressive residual stress. The residual stresses in specimens with the higher processing temperature and no thermal cycles agree with previously published findings [7, 8]. For one cycle, the difference between the higher and lower processing temperature specimens is 7.1 MPa (1.0 ksi); and, for ten thermal cycles, the difference is 8.7 MPa (1.3 ksi) difference. For zero, one, and ten thermal cycles, the higher substrate processing temperature specimens had higher average compressive residual stresses.

Effect Of Number Of Thermal Cycles. An important finding of this study is that processing can generate residual stresses to which thermal cycling "adds" further residual stresses. The residual stresses due to processing are most likely due to thermal expansion mismatch strains on cooling from the process temperature. The changes in residual stresses due to cycling may indicate a change in the TBC system by some means, such as ceramic sintering, ceramic creep, bond coat creep or bond coat oxidation. The effect of the number of thermal cycles on coating residual stress shows a pattern of increasing compressive residual stress with increasing number of thermal cycles, for cycles one through ten.. The effect of the number of thermal cycles on the average through-thickness residual stress is shown in Figure 9. This figure and Figure 7 show a marked increase of compressive residual stress during the first cycle. The trend is then for the residual stress to reach an fairly constant level as the number of thermal cycles increases. The greatest increase in coating compressive residual stresses occurs during the first thermal cycle. As shown in Figure 7, after the first cycle, there is a 17.1 MPa (2.48 ksi) increase in compressive residual stress for the specimens with the lower processing temperature and a 20.4 MPa (2.95 ksi) increase for the specimens with the higher processing temperature [9]. In contrast, the increase in compressive residual stress in the coating due to cycles two through thirty is only 7.1 MPa (1.0 ksi) for the lower processing temperature and there is a 6.6 MPa (0.96 ksi) increase in compressive residual stress in the coating from cycles two through ten for the higher processing temperature.

Effect of Silica Content during Thermal Cycling. The effect of the difference of the silica content in the spray powder is shown in Figure 10. In the as-sprayed condition (0 cycles), the compressive residual stress of the 1.0% silica coating is 27 MPa (3.9 ksi) while the residual stress for the 0.1% silica content is practically zero. Interestingly, after ten cycles the residual stresses begin to approach each other: the compressive residual stress in the coating applied using the lower silica content powder increases to 11.4 MPa (1.65 ksi) while the compressive residual stress in the coating applied using the higher silica content powder decreases to 15.1 MPa (2.19 ksi).

Trends of Residual Stresses. The results demonstrate six features of residual stresses in these TBC's:

1. Compressive residual stresses in the YSZ coating can be controlled by controlling the processing temperature of the specimen.
2. Top coat residual stresses were more compressive for the higher processing temperature of 500°C than for the lower processing temperature of 260°C.
3. The effect of the post-processing thermal cycle history considered here was to increase the compressive residual stresses in the STD top coats for both the higher and lower processing temperatures.
4. For the STD coating powder, the first thermal cycle produced a larger change in top coat residual stress than cycles two through ten combined for both processing temperatures, but with a greater change in the residual stresses (6.6 MPa) occurring during cycles two through ten for the higher processing temperature than the change in residual stress (5.0 MPa) for the lower processing temperature.
5. The effect of silica in the as-sprayed condition was to dramatically increase the coating compressive residual stress.
6. The residual stress in the coating applied using the higher silica content powder became less compressive with thermal cycling while the compressive residual stress for the lower silica case became more compressive.

References

[1]. Sumner, I. and D. Ruckle, "Development of Improved-Durability Plasma Sprayed Ceramic Coatings for Gas Turbine Engines," NASA Technical Memorandum 81512, 1980.

[2] Greving, D.J., J.R. Shadley, and E.F. Rybicki, "Effects of Coating Thickness and Residual Stresses on the Bond Strength of ASTM C633-79 Thermal Spray Coating Test Specimens," *Journal of Thermal Spray Technology*, December, 1994, Vol. 3, No. 4, pp. 371-378.

[3]. Pejryd, L., J. Wigren, D. J. Greving, J.R. Shadley, and E.F. Rybicki, "Residual Stresses as a Factor in the Selection of Tungsten Carbide Coatings for a Jet Engine Application," *Journal of Thermal Spray Technology*, September, 1995, Vol. 4, No. 3, pp. 268-274.

[4]. Miller, R.A., W.J. Brindley, J.G. Goedjen, R. Tiwari, and D. Mess, "The Effect of Silica on the Cyclic Life of a Zirconia-Yttria Thermal Barrier Coating," Proceedings of NTSC '94, pp. 49-54.

[5]. Goedjen, J.G., W.J. Brindley, and R.A. Miller, "Sintering of Plasma-Sprayed Sol Gel Zirconia-Yttria as a Function of Silica Content," Proceedings of NTSC '95, pp. 73-77.

[6]. Greving, D.J., E.F. Rybicki, and J.R. Shadley, "Through-Thickness Residual Stress Evaluations for Several Industrial Thermal Spray Coatings Using a Modified Layer-Removal Method," *Journal of Thermal Spray Technology*, December, 1994, Vol. 3, No. 4, pp. 379-388.

[7]. Cassenti, B.N., A.M. Brickley, and G.C. Sinko, "Thermal and Stress Analysis of Thermal Barrier Coatings," AIAA/SAE/ASME 17th Joint Propulsion Conference, Colorado Springs, CO, July 27-29, 1981, AIAA-81-1482.

[8]. Wigren, J., L. Pejryd, B. Gudmundsson, R.T.R. McGrann, D.J. Greving, E.F. Rybicki, and J.R. Shadley, "Process and In-Service Residual Stresses in Thermal Barrier Systems," Proceedings of NTSC '96, pp. 847-854.

[9]. McGrann, R.T.R., J.A. Graves, E.F. Rybicki, J.R. Shadley, and W.J. Brindley, "Effects of Substrate Temperature and Thermal Cycles on Residual Stresses in Yttria Stabilized Zirconia Thermal Barrier Coatings," Proceedings of NTSC '96, pp. 885-890.

OUTLINE

- Background
- Objectives and Approach
- Experimental Procedure
- Residual Stress Results
- Summary and Conclusions

Fig. 1

OBJECTIVES

Evaluate Residual Stress Changes Due to

- Controlling Substrate Temperature During Spraying (260°C and 500°C)
- Thermal Cycles (Zero, One, Ten, Twenty, Thirty)
- Silica Content (0.1% and 1.0%)

Fig. 2

TEST MATRIX

Thermal Cycles	Number of Samples Tested			
	Lower Temp. (260°C)			Higher Temp. (500°C)
	STD	0.1% SiO_2	1.0% SiO_2	STD
Zero (As-sprayed)	4	4	4	4
One	4			4
Ten	4	4	4	4
Twenty	4			
Thirty	4			

Fig. 3

Modified Layer Removal Method

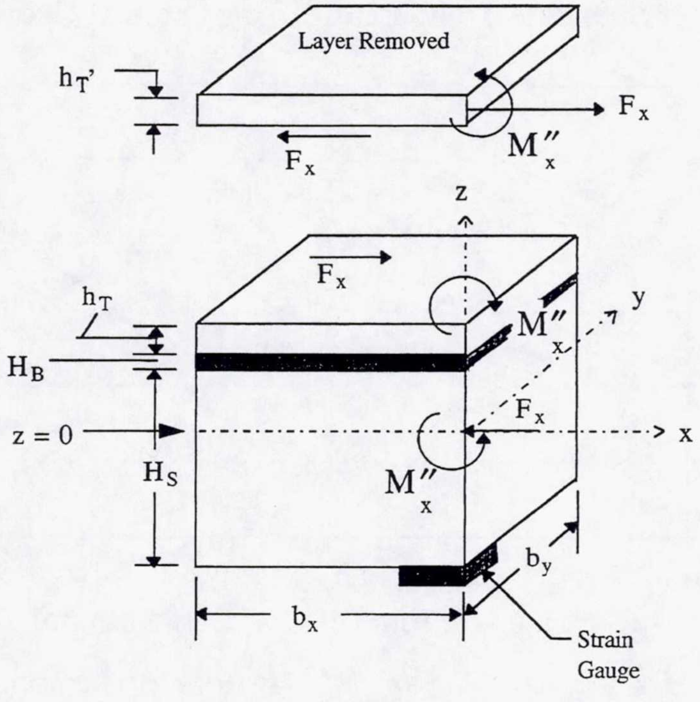

Fig. 4

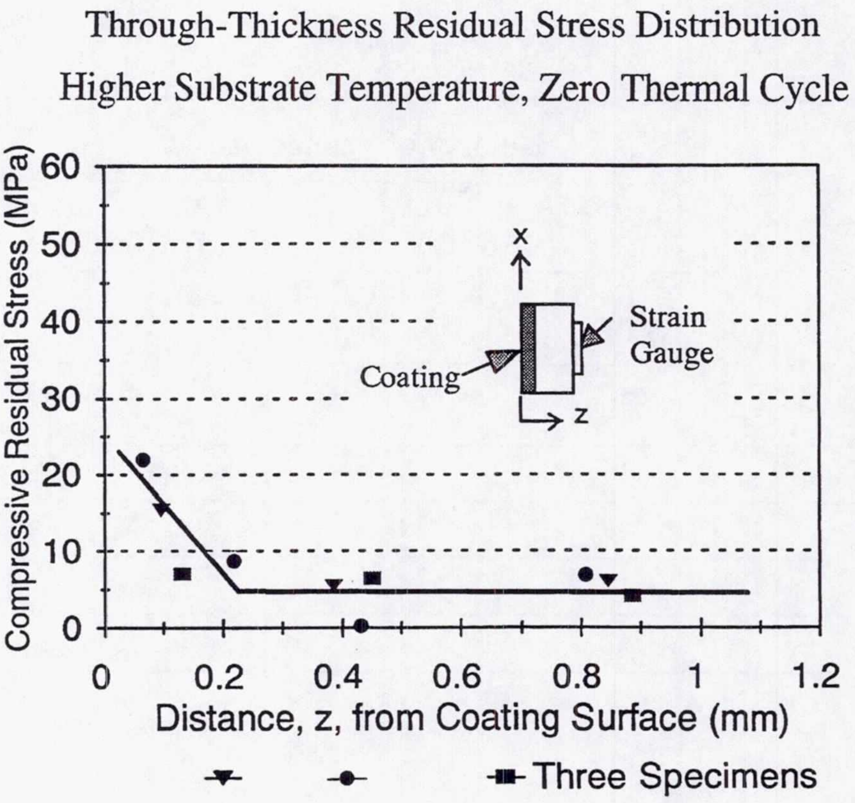
Through-Thickness Residual Stress Distribution
Higher Substrate Temperature, Zero Thermal Cycle

Fig. 5

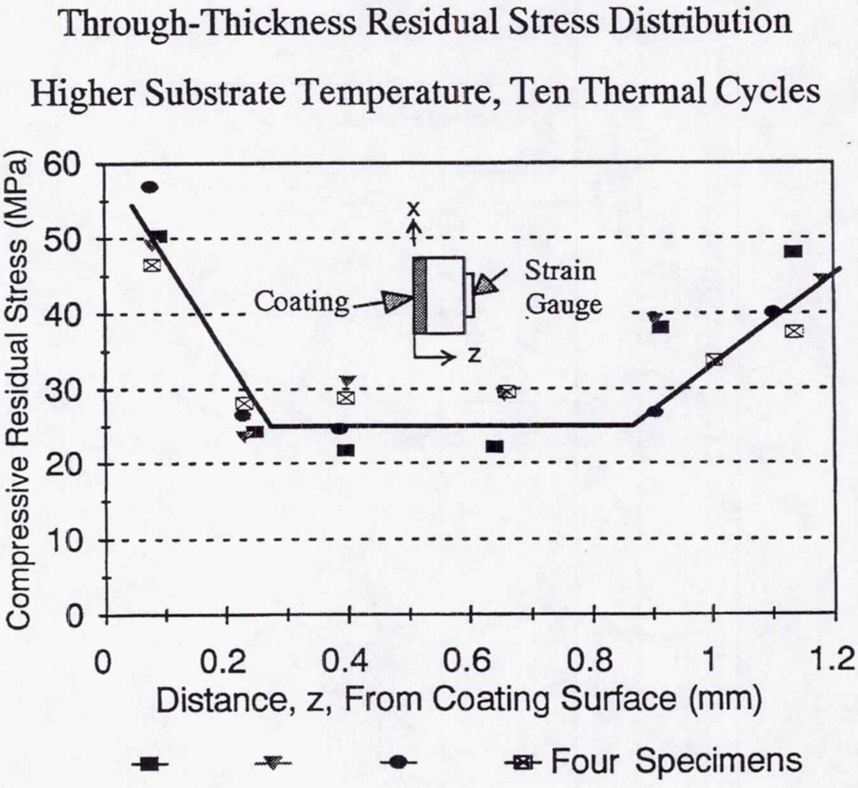
Through-Thickness Residual Stress Distribution
Higher Substrate Temperature, Ten Thermal Cycles

Fig. 6

Average Compressive Residual Stress (MPa)				
Cycles	Lower Temp. (260°C)			Higher Temp. (500°C)
	STD	0.1% SiO_2	1.0% SiO_2	STD
Zero	**3.0**	**0**	**27.6**	**6.8**
One	**20.1**			**27.2**
Ten	**25.1**	**11.4**	**15.1**	**33.8**
Twenty	**19.8**			
Thirty	**27.0**			

Fig. 7

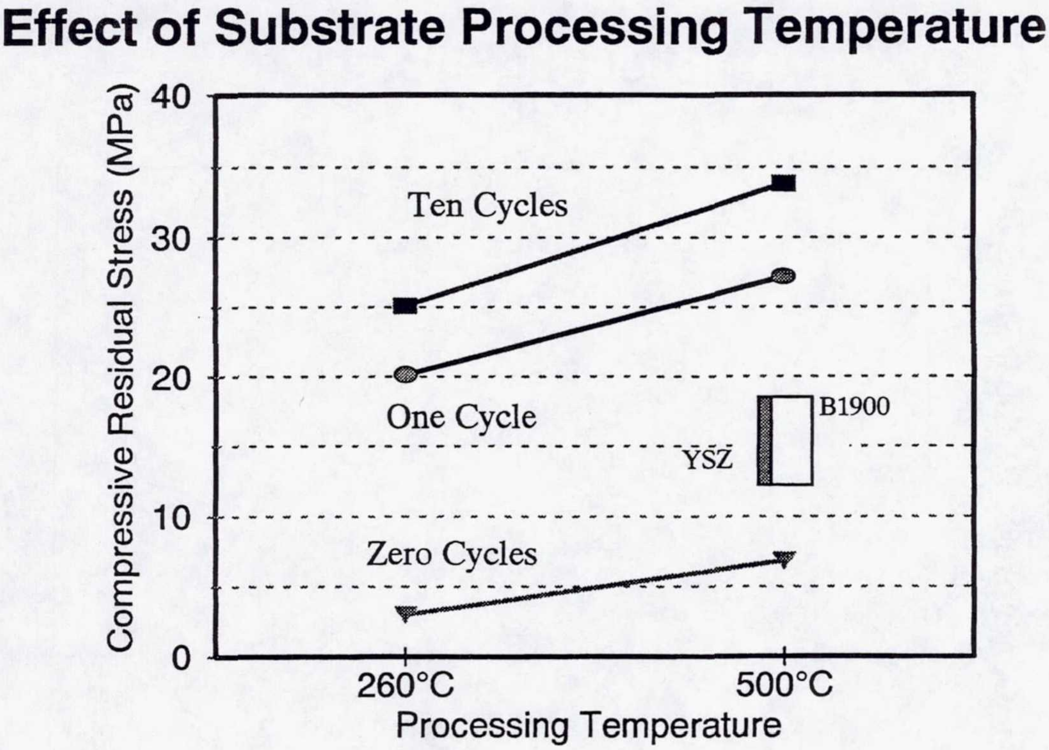

Fig. 8

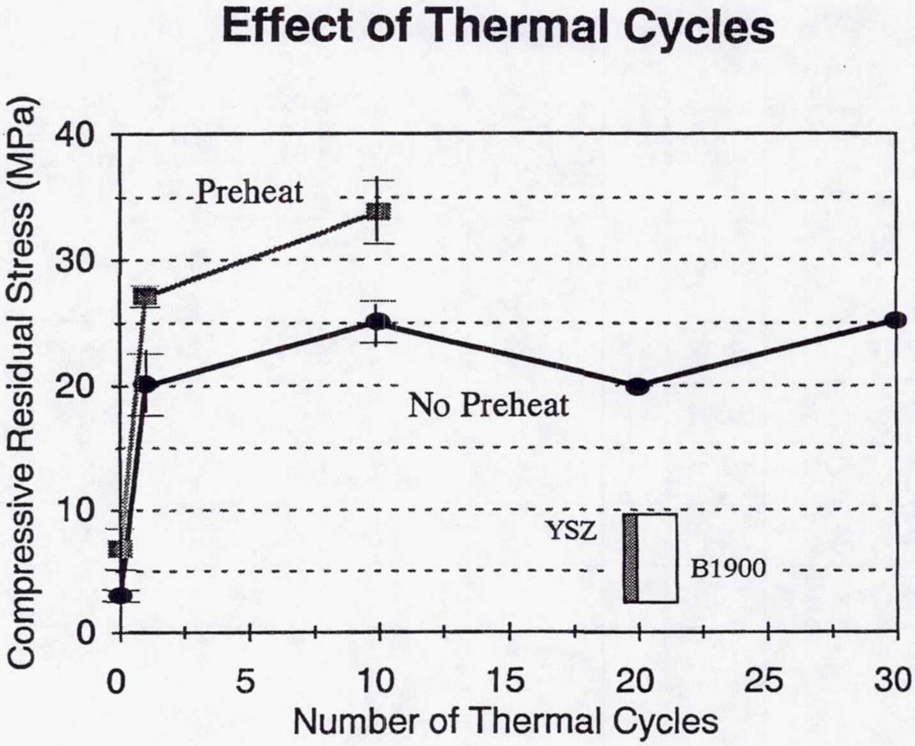
Effect of Thermal Cycles
Compressive Residual Stress (MPa)
40
30
20
10
0
Preheat
No Preheat
YSZ
B1900
0
5
10
15
20
25
30
Number of Thermal Cycles

Fig. 9

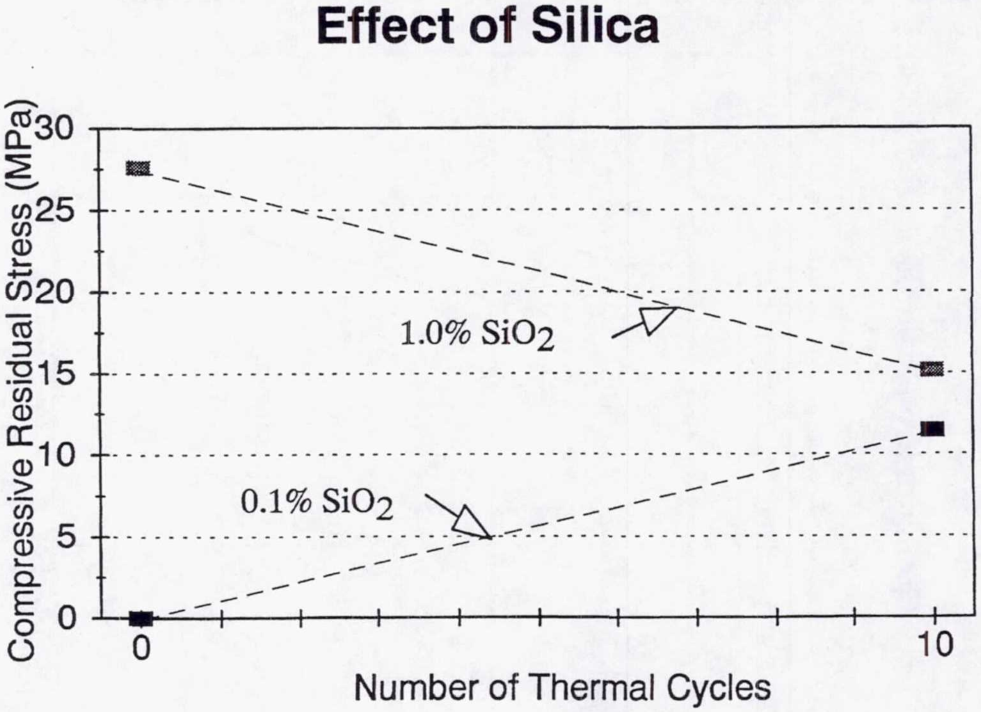
Effect of Silica
Compressive Residual Stress (MPa)
30
25
20
15
10
5
0
1.0% SiO2
0.1% SiO2
0
10
Number of Thermal Cycles

Fig. 10

CONCLUSIONS: Substrate Temperature

- The higher substrate processing temperature (500°C) produced higher compressive residual stresses in the YSZ top coat.
- Compressive residual stresses in the YSZ top coat increased for both processing temperatures as a result of one and ten thermal cycles.

Fig. 11

CONCLUSIONS: Thermal Cycles

- The residual stress change in the YSZ top coat due to the first cycle was greater than the change due to cycles two through ten by a factor of three.
- The residual stress level in the YSZ top coat after thirty cycles was equal to the residual stress level after ten cycles.

Fig. 12

CONCLUSIONS: Silica Content

- The residual stress for the lower (0.1%) SiO_2 content coating is close to zero in the as-sprayed condition and became more compressive after ten thermal cycles.
- The residual stress for the higher (1.0%) SiO_2 content coating is very compressive in the as-sprayed condition and became less compressive after ten thermal cycles.

Fig. 13

Suggestions for Further Work

- Residual Stresses and Oxidation and Sintering
- Material Property Determination Methods
- Residual Stresses and Other Application Processes

Fig. 14

IN-SITU CURE MONITORING OF THE IMMIDIZATION REACTION OF PMR-15*

SHERYL COSSINS
South Dakota School of Mines and Technology
Rapid City, South Dakota

and

Dr. Jon J. Kellar
Department of Metallurgical Engineering

Dr. Robb M. Winter
Department of Chemical Engineering

South Dakota School of Mines and Technology
Rapid City, South Dakota

Glass fiber reinforced polymer composites are becoming widely used in industry. With this increase in production, an in-situ method of quality control for the curing of the polymer is desirable. This would allow for the production of high-quality parts having more uniform properties.[1] Recently, in-situ fiber optic monitoring of polymer curing has primarily focused on epoxy resins and has been performed by Raman or fluorescence methods.[2-6] In addition, some infrared (IR) investigations have been performed using transmission or ATR cells.[7-9] An alternate IR approach involves using optical fibers as a sensor by utilizing evanescent wave spectroscopy.

Initial work at South Dakota School of Mines and Technology (SDSM&T) concerning the curing of epoxy adjacent an embedded silica optical fiber has been monitored in-situ by evanescent wave spectroscopy.[10] The epoxy studied was partially fluorinated and therefore had a refractive index lower than that of the silica optical fiber. The lower refractive index of the partially fluorinated epoxy allowed the fiber to be used as a waveguide for the internal reflection of IR light. This evanescent wave samples the polymer at the fiber/polymer interface. This combination of epoxy/silica served as a model composite system.

The bands used to monitor the cure of the epoxy were as follows: the C-N overtone absorbance band at 4725 cm^{-1} and the NH_2 combination band of the hardener at approximately 4925 cm^{-1}. It was found that the C-N band increased and the NH_2 band decreased over time. This result was expected, as epoxies react with the NH_2 in the curing agent to form C-N bonds while curing.

This method of cure monitoring has been applied to a PMR-15 composite system. Optical grade sapphire fiber has been chosen as the sensor due to its

* Work funded under NASA Grant NGT3-52312

wide transmission range, high refractive index, and strength. The system will be used to determine the end of the immidization reaction or "gel point". It is important to know when the gel point has been reached because it is at this point that the Lewis Research Center Group increases the temperature and pressure applied in order to crosslink the polymer. Before the final product is made, PMR-15 can go through undesired temperature cycling simply through shipping and storing. This causes the polymerization reaction to be at different stages for different batches or lots of PMR-15. Because of this batch to batch variation, the time to reach the gel point can vary. By monitoring the reaction in-situ, the gel point can be found for each batch and variation in the quality of the final product may be reduced.

In order to monitor the PMR-15 reaction, we must first identify the bands present and determine which will be changing during the reaction. Spectra of the raw products of PMR-15 were collected using diffuse reflectance infrared Fourier transform (DRIFT) Spectroscopy. Spectra were also collected for the cured and uncured PMR-15 polymer. During the immidization reaction primary amines are converted to tertiary amines. Therefore, the reaction is complete when the primary and secondary amine bands have disappeared or stopped decreasing. Some examples of near-IR bands for the raw materials are as follows: 4,4'-methylene dianiline (MDA): amine stretching and bending combination 5000-5050 cm^{-1}, aromatic primary amines 6550-6850 cm^{-1}; 3,3',4,4'-benzophenone tetracarboxylic dianhydride (BTDA): aromatic CH stretch 5900-6100 cm^{-1}, carboxylic acid stretch 5300-5400 cm^{-1}; 5-norbornene-2,3-dicarboxylic anhydride (Nadic): carboxylic acid stretch 5300-5400 cm^{-1}. Complete identification of the bands is ongoing.[11-12]

Design of a curing cell to duplicate conditions at Lewis Research Center has been completed. The requirements of this cell were to maintain a temperature of 600 °F ± 1 °F for 60 to 90 minutes, to accommodate up to three 150 μm diameter sapphire fibers, and be easily cleaned without damage to the fibers. It was also designed to have a nitrogen blanket to prevent occurrence of oxidation reactions. Experiments to monitor the immidization reaction are currently being performed.

<u>References</u>

1. V. Kierman, Laser Focus World, August, 49 (1995).

2. C. Sung and H. Nak, Materials Science and Engineering, A162, 241 (1993).

3. K.E. Chike, M.L. Myrick, R.E. Lyon and S.M. Angel, Applied Spectroscopy **47**,1631 (1993).

4. J.F. Maguire and P.L.Talley, Journal of Advanced Materials, **26**, 1 (1995).

5. J.F. Aust, M.K. Higgins, P. Groner, S.L. Morgan, and M.L. Myrick, Analytica Chimica Acta, **293**, 119 (1994).

6. J.F. Aust, K.S. Booksh, and M.L. Myrick, Applied Spectroscopy, **50**, 382 (1996).

7. L. Xu, J.H. Fu, and J.R. Schlup, J. Am. Chem. Soc, **116**, 2821 (1994).

8. Jovan Mijovic and Sasa Andjelic, Macromolecules, **29**, 2787 (1995).

9. Lisheng Xu and John R. Schlup, Applied Spectroscopy, **50**, 109 (1996).

10. S. Cossins, M. Connell, W. Cross, R. Winter and J. Kellar, Applied Spectroscopy, **50**, 900 (1996).

11. B.G. Osborne and T. Fearn, *Near Infrared Spectroscopy in Food Analysis* (Longman Scientific and Technical, New York, 1986), p. 28.

12. A. Garton, *Infrared Spectroscopy of Polymer Blends, Composites and Surfaces* (Oxford University Press, New York, 1992), p. 136.

In-situ Cure Monitoring of the Immidization Reaction of PMR-15

Presented by
Sheryl Cossins
South Dakota School of Mines and Technology

Under the direction of
Dr. Jon Kellar and Dr. Robb Winter
SDSM&T
and
Dr. Chris Johnston
Lewis Research Center

May1, 1997

Fig. 1

OUTLINE

- Objectives
- Evanescent Wave Spectroscopy
- Silica Fiber Sensor
- PMR-15 Reaction
- IR Bands
- Summary of Results
- Conclusions
- Future Research

Fig. 2

OBJECTIVES

- Fiber selection
- Identification of PMR-15 IR bands
- Curing cell design
- Monitor immidization reaction of PMR-15

Fig. 3

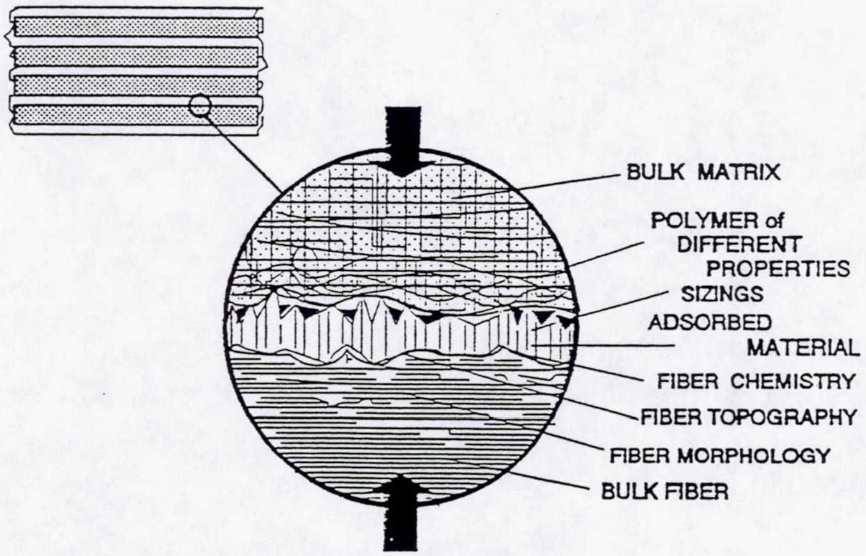

FIBER-MATRIX INTERPHASE

P.J. Herrera-Franco and L.T. Drzal, Composites, 23, 1 (1992).

Fig. 4

FIBER OPTIC WAVEGUIDES

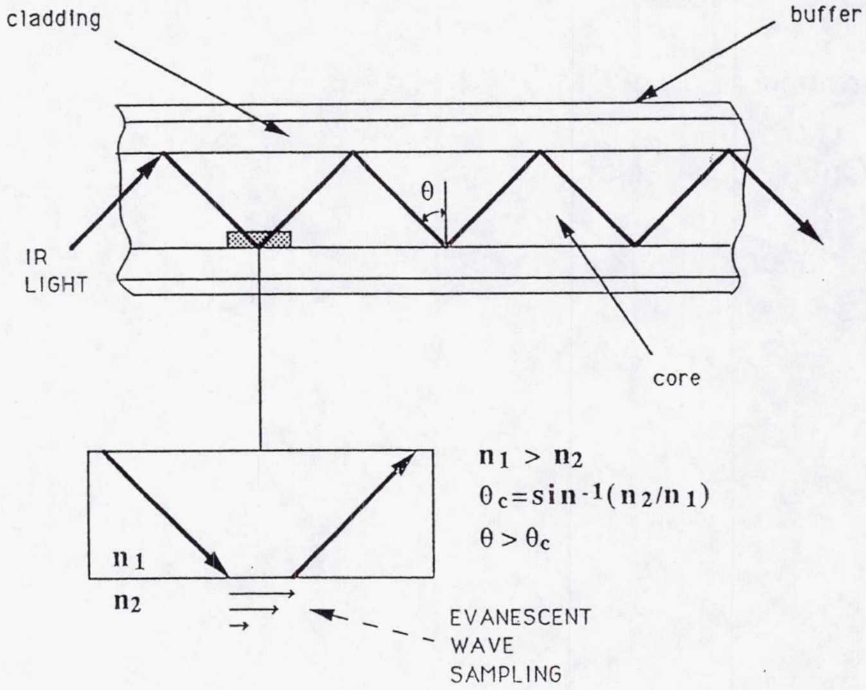

Fig. 5

SILICA FIBER SENSOR

- Create 1 cm sensing region in 140 µm diameter silica fiber
- Embed in Epo-Tek 328
- Heat to 150 °C for 1 hour
- Collect spectra during cure

Fig. 6

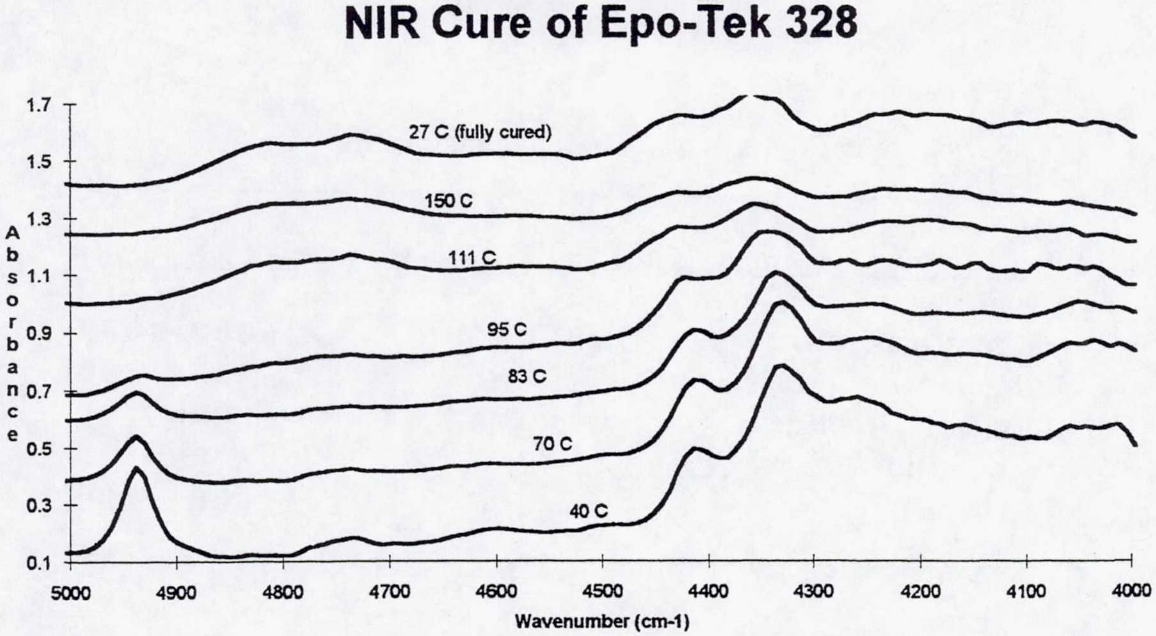

Cossins, Connell, Cross, Winter, Kellar, Applied Spectroscopy, **50**, 900 (1996).

Fig. 7

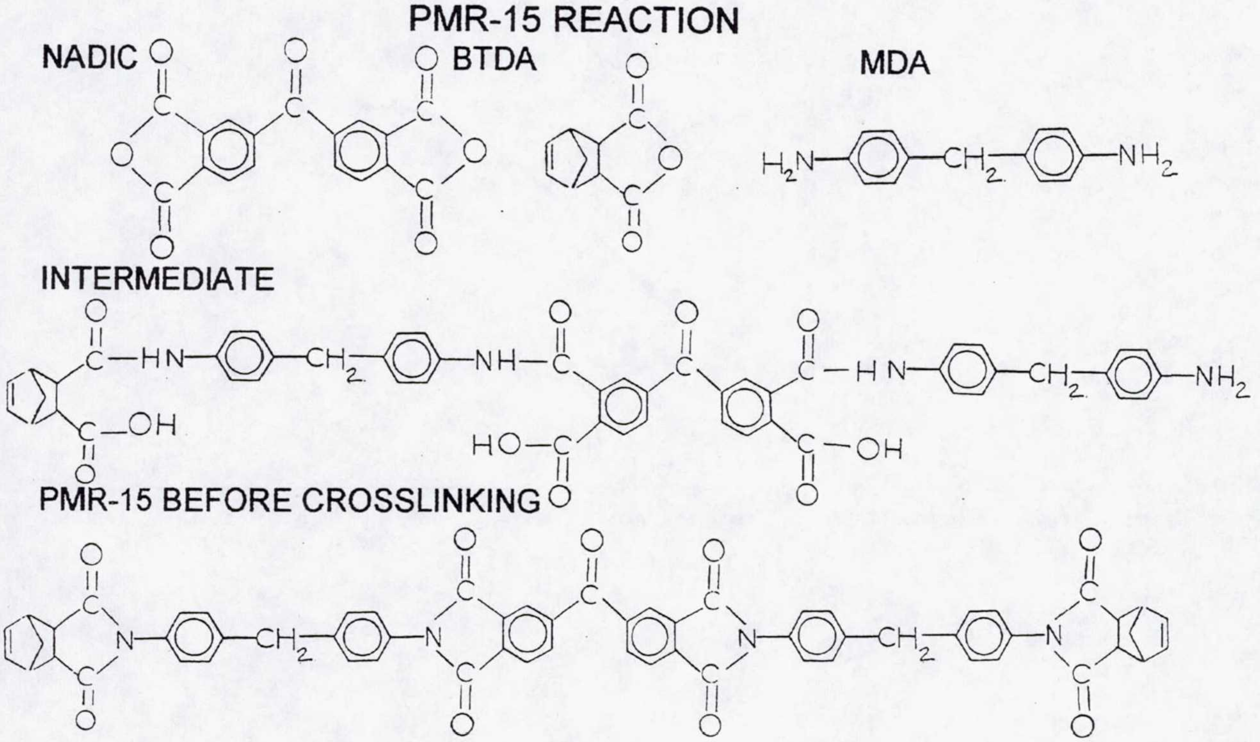

Fig. 8

Infrared Fibers and Their Transmission Ranges.

Fiber Type (core material)	Range (cm^{-1})
fused silica (ultra low -OH)	**26000-4000**
chalcogenide glass	**3333-1000**
zirconium fluoride	20000-2325
silver halide	3000-625
sapphire	**12000-2200**

Fig. 9

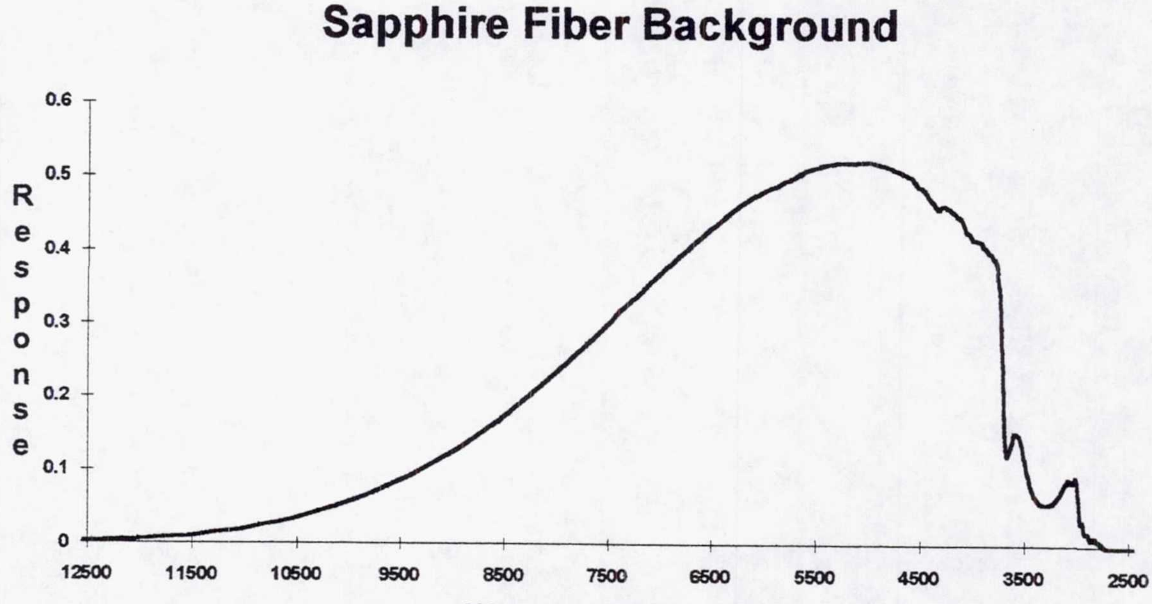

Fig. 10

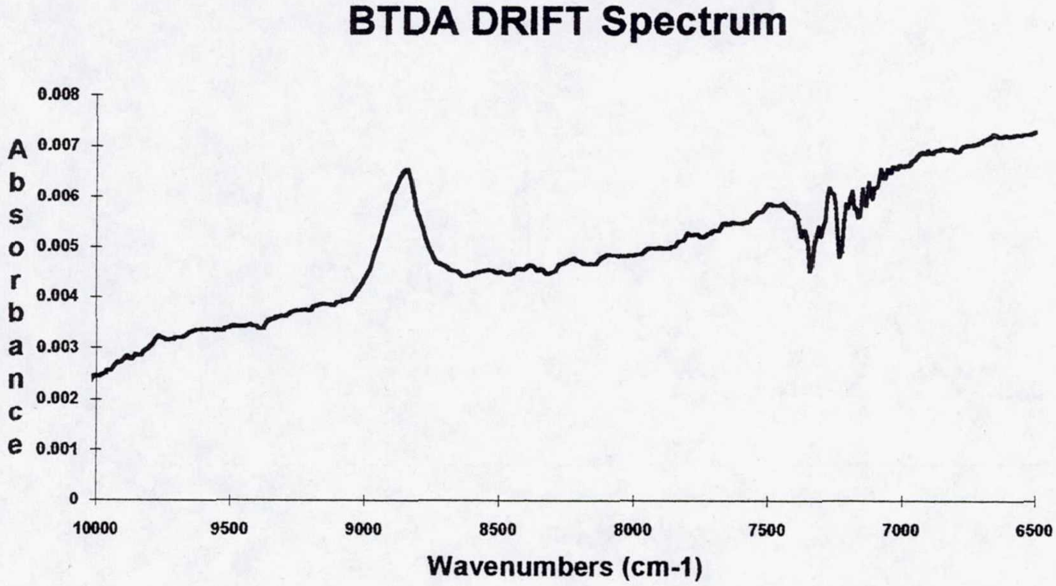
BTDA DRIFT Spectrum
Absorbance
0.008
0.007
0.006
0.005
0.004
0.003
0.002
0.001
0
10000
9500
9000
8500
8000
7500
7000
6500
Wavenumbers (cm-1)

Fig. 11

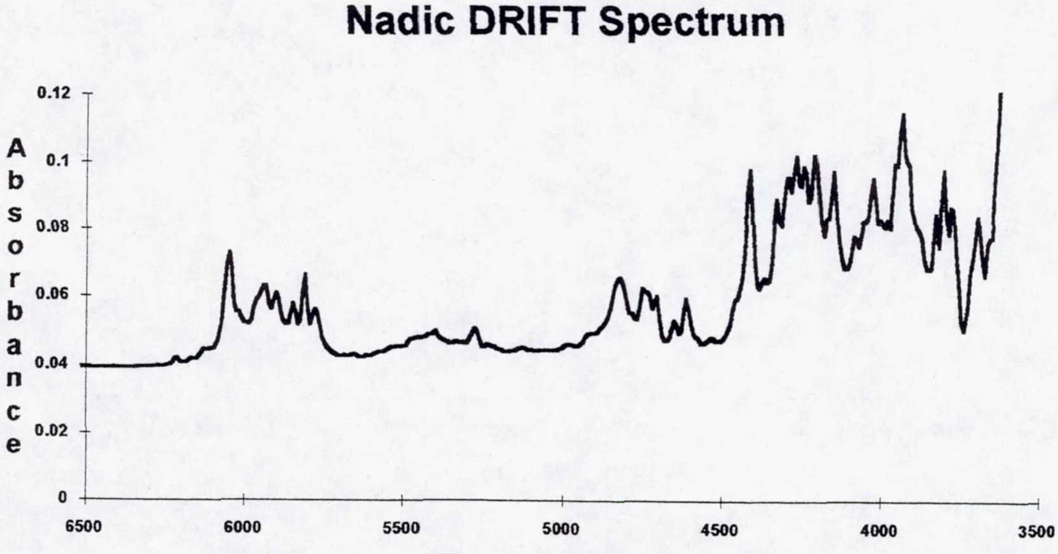
Nadic DRIFT Spectrum
Absorbance
0.12
0.1
0.08
0.06
0.04
0.02
0
6500
6000
5500
5000
4500
4000
3500
Wavenumber (cm-1)

Fig. 12

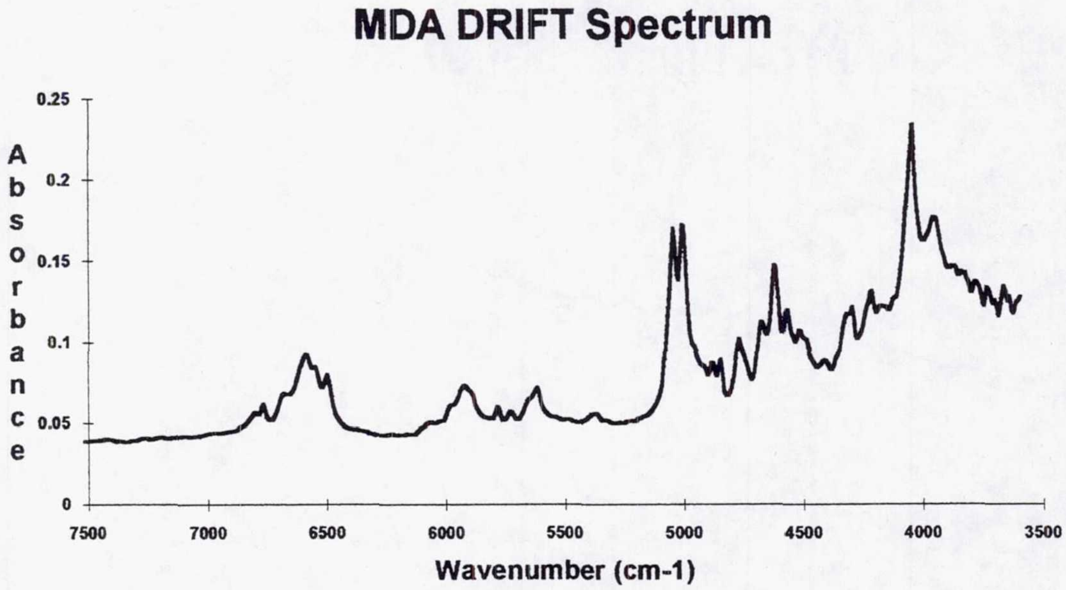
MDA DRIFT Spectrum
Absorbance
0.25
0.2
0.15
0.1
0.05
0
7500
7000
6500
6000
5500
5000
4500
4000
3500
Wavenumber (cm-1)

Fig. 13

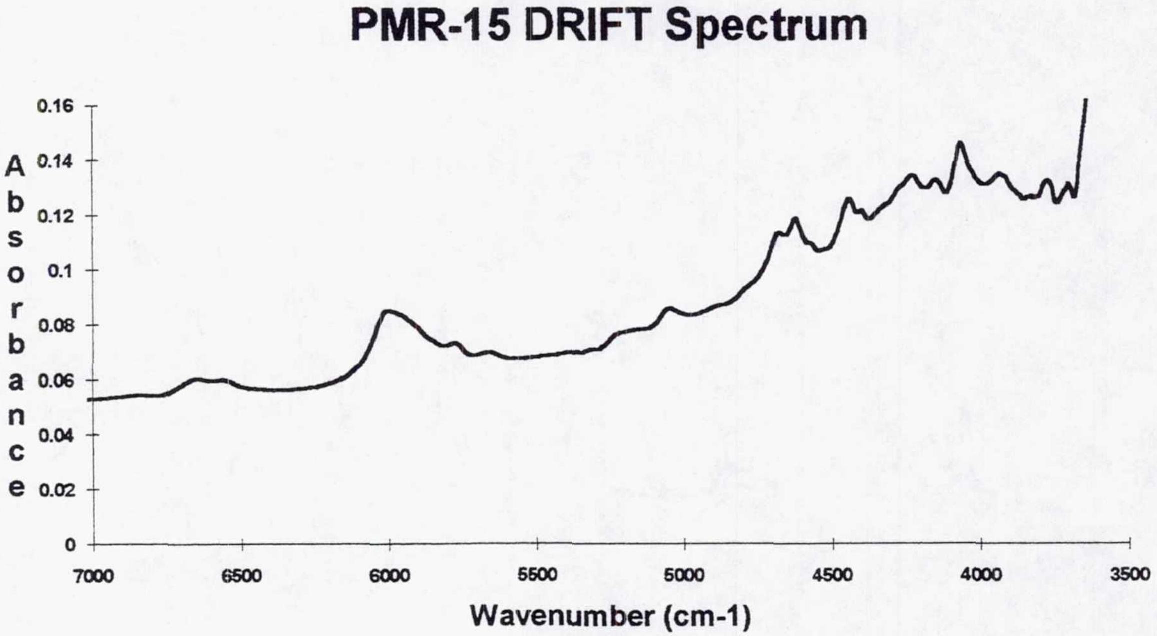
PMR-15 DRIFT Spectrum
Absorbance
0.16
0.14
0.12
0.1
0.08
0.06
0.04
0.02
0
7000
6500
6000
5500
5000
4500
4000
3500
Wavenumber (cm-1)

Fig. 14

SUMMARY OF RESULTS

- Sapphire fiber chosen
- Heating cell designed
- Possible IR bands for cure monitoring identified

Fig. 15

CONCLUSIONS

- Monitoring of the immidization reaction of PMR-15 is possible

Fig. 16

FUTURE WORK

- Obtain fiber spectrum and compare to DRIFT
- Identify and monitor IR bands changing with cure
- Develop correlation of band change to gel point

Fig. 17

ELECTRON BEAM CURED EPOXY RESIN COMPOSITES FOR HIGH TEMPERATURE APPLICATIONS*

CHRISTOPHER J. JANKE
Oak Ridge Centers for Manufacturing Technology
Oak Ridge National Laboratory**
Oak Ridge, TN 37831-8048

George F. Dorsey
Lockheed Martin Energy Systems, Inc.***
Oak Ridge, TN 37831-8097

Stephen J. Havens
Oak Ridge Institute for Science and Education,
Oak Ridge, TN 37831-0117

Vincent J. Lopata
Atomic Energy of Canada Ltd. - Whiteshell Laboratories,
Pinawa, Manitoba, Canada ROE 1LO

Michael A. Meador
NASA Lewis Research Center
Cleveland, OH 44135

Introduction

Electron beam curing of Polymer Matrix Composites (PMCs) is a nonthermal, nonautoclave curing process that has been demonstrated to be a cost effective and advantageous alternative to conventional thermal curing. Advantages of electron beam curing include: reduced manufacturing costs; significantly reduced curing times; improvements in part quality and performance; reduced environmental and health concerns; and improvement in material handling. In 1994 a Cooperative Research and Development Agreement (CRADA), sponsored by the Department of Energy Defense Programs and 10 industrial partners, was established to advance the electron beam curing of PMC technology. Over the last several years a significant amount of effort within the CRADA has been devoted to the development and optimization of resin systems and PMCs that match the performance of thermal cured composites. This highly successful materials development effort has resulted in a board family of high performance, electron beam curable cationic epoxy resin systems possessing a wide range of excellent processing and property profiles. Hundreds of resin systems, both toughened and untoughened, offering unlimited formulation and processing flexibility have been developed and evaluated in the CRADA program.

---

*Cooperative Research and Development Agreement (CRADA) No. Y1293-0233.

**Managed by Lockheed Martin Energy Research Corporation for the U.S. Department of Energy under contract DE-AC05-96OR22464.

***Managed by Lockheed Martin Energy Systems for the U.S. Department of Energy under contract DE-AC05-84OR21400.

Our research has determined that conventional epoxy resins can be cured by exposure to electron beam radiation as provided by a high energy/power electron beam accelerator to provide materials with high glass transition temperatures and mechanical properties comparable to thermally cured epoxies (1-3). A cationic photoinitiator at a concentration of 1-3 parts per hundred of the epoxy resin is required for this process. These cationic photoinitiators are triaryl sulfonium and diaryliodonium salts of weakly nucleophilic anions. Diaryliodonium salts of the hexafluoroantimonate anion have been found to be the most effective commercially available photoinitiators. The cationic photoinitiator decomposes when subjected to irradiation from ultraviolet light or high energy electrons to produce a Bronsted acid (proton) which catalyzes the ring opening polymerization of the epoxy group. The weakly nucleophilic anion from the initiator is not strongly attracted to the cation that is generated, nor does it interfere with the growing polymer chain (4). Properties of the electron beam cured cationic epoxies include: glass transition temperatures (T_g's) ranging from 100-400°C (212-752°F), high flexural moduli [up to 4.0 GPa, (580 ksi)], low moisture absorption (<2%), good toughness obtained by the addition of toughening agents [0.41-0.92 $MPam^{½}$] (373-837 psi in ^{½}); and low-moderate cost of the epoxy resin-photoinitiator compositions.

Several toughened and untoughened compositions were selected for evaluation as composite matrices. PMCs made from these easily processed resins have exhibited: low shrinkage after electron beam cure, low void content (0.6-1.8%) and good mechanical properties with IM7 carbon fiber [0° flexural strengths, 1.71-2.01 GPa (248-292 ksi); 0° flexural moduli, 150-196 GPa (21.8-28.4 msi; and 0° interlaminar shear strengths 77-89 MPa (11.2-12.9 ksi)]. Many composite parts manufactured via hand lay-up, tow/tape placement, filament winding, resin transfer molding (RTM), and vacuum assisted resin transfer molding (VARTM) have been produced using these materials, demonstrating their fabrication versatility.

Electron beam processing is potentially more economical than conventional thermal cure processing. Complex part shapes can be made with inexpensive tooling and part throughput is extremely high. Since electron beam curing is at near ambient temperatures, inexpensive, lightweight, and disposable fabrication tools or mold materials such as thermoplastics, foam plastics, plasters, waxes, and wood can be used instead of metals. Electron beam processing also allows the simultaneous curing of several different cationic epoxy resin compositions. Thus, a single composite structure fabricated from electron curable cationic epoxies with different thermal and mechanical properties can be cured in a single cycle. As electron beam curing can be conducted at room temperature or lower, stresses are reduced. This factor can be critical in the design of structures such as cryogenic tanks that must perform at low temperatures. Electron beam curable epoxy resins are friendly to the environment and greatly reduce the amount of waste generated in composite fabrication processes. No hardener such as an amine is required - only a few parts per hundred of a relatively nontoxic photoinitiator. Formulated and prepregged resin have essentially unlimited pot life and shelf life at room temperature provided that the resins are not exposed to ultraviolet or sunlight.

One particular epoxy resin-photoinitiator composition (designated Electron Beam Resin 8H) exhibited a very high glass transition temperature after electron beam curing; T_g, 396°C (745°F) from the peak of the DMA tan delta curve. This resin was extensively evaluated as a matrix resin for PMCs using Hercules IM7-GP-12K carbon fiber. Unidirectional prepreg of 8H with this fiber was manufactured by YLA, Inc. of Benicia, California. All test panels (16 plies unidirectional x 30.5

cm x 30.5 cm) were prepared using conventional lay-up techniques. Intermediate debulks were conducted under vacuum bag pressure every four plies at room temperature for 15 minutes. The final debulk and bleed cycle was performed under vacuum bag pressure at 70°C (158°F) for one hour. The panels were electron beam cured at the Whiteshell Laboratories of Atomic Energy of Canada Limited (AECL) using the AECL I10/1 Electron Linear Accelerator. Curing was performed under vacuum bag pressure while the panels were at room temperature at a dose per pass of 50 kGy for a total dose of 250 kGy.

In a thermal cure cycle there is a considerable decrease in resin viscosity as temperature increases, followed by an abrupt increase in viscosity with the onset of gelation. This factor combined with autoclave pressures may allow poorly laid-up laminates to be well consolidated. Since electron beam curing occurs at near ambient temperature, there is no viscosity decrease before gelation and curing. Thus, lay-up technique is critical in obtaining, good laminate properties. To date the best series of panels had a void volume of 1.77% by acid digestion, with the following room temperature mechanical properties: 0° flexural strength, 1.99 GPa (288 ksi); 0° flexural modulus, 196 GPa (28.4 msi); 0° compressive strength, 1.57 GPa (228 ksi); 0° compressive modulus, 149 GPa (21.6 msi); and 0° interlaminar shear strength, 77 MPa (11.2 ksi). Long term aging studies were conducted on early specimens of these laminates at NASA Lewis Research Center (LeRC). Weight loss in air after 1000 hours at 232°C (450°F) was only 4.25% but 18.4% after 1000 hours at 288°C (550°F). Mechanical properties were not significantly changed after 1000 hours at 232°C, but noticeably deteriorated on aging at 288°C.

Future efforts in the area of electron beam cured PMC's for high temperature applications will focus on improving the quality of electron beam resin 8H laminates and more extensive testing. Research efforts will also be directed toward the development of electron beam curable polyimides as part of a project sponsored by NASA LeRC.

References

1. Janke, C. J.; Dorsey, G. F.; Havens, S. J.; and Lopata, V. J.: Electron Beam Curing of Epoxy Resins by Cationic Polymerization. SAMPE International Symposium, vol. 41, 1996, pp. 196-206.

2. Janke, C. J.; Dorsey, G. F.; Havens, S. J.; and Lopata, V. J.: Toughened Epoxy Resins Cured by Electron Radiation. SAMPE International Technical Conference, vol. 28, 1996, pp. 877-889.

3. Lopata, V. J.; Chung, M.; Janke, C. J.; and Havens, S. J.: Electron Curing of Epoxy Resins: Initiator and Concentration Effects on Curing Dose and Rheological Properties. SAMPE International Technical Conference, vol. 28, 1996, pp. 901-910.

4. Crivello, J. V.; Lam, J. H. W.; and Volante, C. N.: Photoinitiated Cationic Polymerization Using Diaryliodonium Salts. Journal of Radiation Curing, vol. 4, July 1977, pp. 1-16.

Acknowledgements

THE EBEAM CRADA TEAM

- **AECL Technologies, Inc.**
- **Applied Poleramic, Inc.**
- **The Boeing Company**
- **Ciba-Geigy Corporation**
- **E-BEAM Services, Inc.**
- **Lockheed Martin Aero and Naval Systems**
- **Lockheed Martin Energy Systems, Inc.**
- **Lockheed Martin Tactical Aircraft Systems**
- **Nicolet Imaging Systems**
- **Northrop Grumman Corporation**
- **Sandia Corporation**
- **UCB Chemicals Corporation**

- **Department of Energy Defense Programs**
- **YLA, Inc. - Sean Johnson, Susan Robataille and Steve Smith**

Presentation Outline

- **Introduction**
- **Electron Beam Curable Cationic Epoxy Resins & Composites - Advantages and Highlights**
- **High Temperature Composite Properties**
  - **Weight Loss**
  - **Flexural Properties**
  - **Interlaminar Shear Properties**
- **Conclusions**
- **Future Research Areas**

Introduction

- **Electron Beam Curing is a Very Fast, Nonthermal, Nonautoclave curing method that uses High-Energy, High-Power Radiation to cure polymer matrix composites.**

ADVANTAGES OF PMC ELECTRON BEAM CURING OVER THERMAL CURING

- Shorter cure times
- Amenable to high production rates
- Lower overall energy requirements
- Reduced thermal stresses in cured part
- Effective with thick PMC parts
- Lower tooling costs
- Reduced environmental, safety, and health concerns
- Improved material handling
- Reduced overall manufacturing costs (25% - 65% Cost Savings vs. Thermal Curing)

The CRADA Has Developed Hundreds Of EB Curable Cationic Epoxy Resin Systems (Toughened and Untoughened)

Epoxies

- Bisphenol A Liquid Epoxy Resins
- Bisphenol F Epoxy Liquids
- Epoxy Novolac Resins
- Multifunctional Epoxy Resins
- Cycloaliphatic Epoxy Liquids
- Hydrocarbon Epoxies
- Toughened Epoxies
- Flexible Epoxies
- Fusion Solid Epoxies
- Multi-Epoxy Resins (Blends)
- Diluted Liquid Epoxy Resins
- Multifunctional Epoxy Diluents

Cationic Initiators (w/ Various Anions)

- Diaryliodonium Salts
- Triarylsulfonium Salts
- Iron Complexes
- Diaryldisulfones
- Triazine Compounds

Tougheners

- Engineering Thermoplastics
- Hydroxy-Containing Thermoplastics
- Reactive Flexibilizers
- Elastomers
- Rubbers
- Undissolved Thermoset Particles
- Undissolved Thermoplastic Particles
- Polyarylates

Advantages of Electron Beam Curable Cationic Epoxies

- Most Commercially Available (Non-Amine Containing) Epoxies EB Cure
- Unlimited Variety Of Epoxy Resin Systems Can Be Formulated
- No Hardeners Required (less environmental/health concerns)
- Indefinite Shelf Life (must be kept away from UV)
- No Oxygen Inhibition Problems During Cure
- Resin System Costs Are Comparable To Thermally Curable Epoxy Variants

Advantages of Electron Beam Curable Cationic Epoxies (Resin Properties Only)

- **Minimal Volatile Emissions During Cure; (< 0.1%)**
- **Wide Range Of T_gs (tan delta); 130 to >395°C; (T_g - T_{cure}) ranged from 100 to > 370°C**
- **Very Low Water Absorption After 48 hr. H_2O boil; some < 1% most < 2%: vs. thermal cured epoxies 3-6%**
- **Low Shrinkage; 2 - 3% vs. thermal cured epoxies 4-6% vs. EB cured acrylates 8-20%**
- **Resins Are Toughenable; RT K_{1c}s ranged from 0.41-0.97 MPa $m^{0.5}$ vs. 0.90 for Fiberite 977-3; -100°C K_{1c}s surpass RT values**
- **Low Total Mass Loss; 0.05-1.00% for resins after vacuum oven aging @125°C/5days vs. goal of <1% for composites**

Highlights of EB Curable Cationic Epoxy Containing Composites

- **Many Cat. Epoxies Have Been Successfully Prepregged**
  - Numerous prepregs have been made via solution dip, direct hot melt coating, and film calendering methods
- **Many Cat. Epoxies Have Been Processed Using Several Fabrication Methods**
  - Many PMC parts have been manufactured via hand lay-up, tow placement, filament winding, RTM, and VARTM processes
- **Void Contents Are Comparable To Autoclave Cured PMCs**
  - Many PMCs fabricated using hand lay-up and filament winding processes have less than 1% void contents
- **Improved Mechanical Properties Compared To Autoclave Cured PMCs**
  - PMCs exhibit some mechanical properties exceeding those of Fiberite's, autoclave cured, 977-2 and 977-3 toughened epoxy PMCs
- **Cryogenic & Thermal Cycling Of PMCs Showed Excellent Retention Of Properties**
  - Mechanical properties of PMCs after cryogenic & thermal cycling were unaffected and in some cases increased in value

Property Comparison Of Electron Beam Cured Versus Thermal Cured IM7/Resin (X) Unidirectional Laminates (Data Normalized to 62% fiber volume)

Resin Systems	Fiberite 977-2 (Fiberite Marketing Literature Data)	Fiberite 977-3 (Fiberite Marketing Literature Data)	EB Resin 8H	EB Resin 2	EB Resin 3	EB Resin 4	EB Resin 5
Cure Conditions	Autoclave Cured (6 hrs. @ 350°F @ 85 psi)	Autoclave Cured (3 hrs. @ 355°F @ 85 psi)	**250 kGy**	**150 kGy**	**150 kGy**	**150 kGy**	**150 kGy**
Void Volume, %	Not Reported	Not Reported	**1.77**	**0.72**	**1.24**	**0.64**	**1.18**
Tg, °C (Tan Delta)	200	190/240	**396**	**392**	**232**	**212**	**212**
0° Flex. Str., MPa (ksi)	1641 (238)	1765 (256)	**1986 (288)**	**2006 (291)**	**1793 (260)**	**1765 (256)**	**1710 (248)**
0° Flex. Mod., GPa (msi)	147 (21.3)	150 (21.7)	**196 (28.5)**	**163 (23.6)**	**163 (23.7)**	**154 (22.3)**	**150 (21.8)**
0° Comp. Str., MPa (ksi)	1580 (230)	1680 (244)	**1565 (227)**				
0° Comp. Mod., GPa (msi)	152 (22)	154 (22.3)	**149 (21.6)**				
0° ILSS, MPa (ksi)	110 (16)	127 (18.5)	**77 (11.2)**	**79 (11.5)**	**79 (11.5)**	**89 (12.9)**	**77 (11.2)**
Hot/Wet 0° ILSS*, MPa (ksi)		89 (12.9)	**61 (8.8)**				

* 1 wk. in H_2O @ 160°F, tested @ 220°F

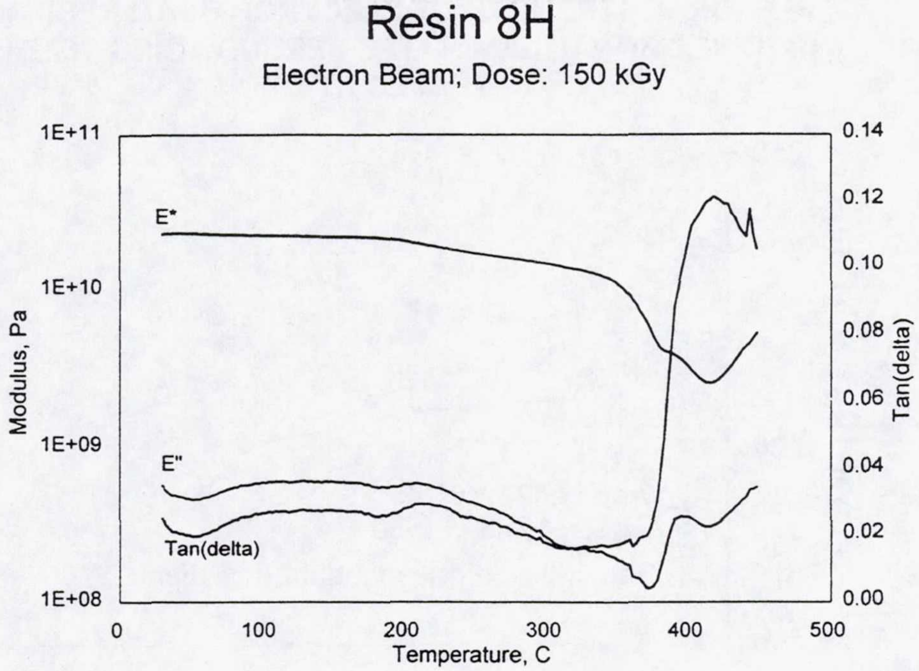
Resin 8H
Electron Beam; Dose: 150 kGy
1E+11
1E+10
1E+09
1E+08
Modulus, Pa
0.14
0.12
0.10
0.08
0.06
0.04
0.02
0.00
Tan(delta)
E*
E"
Tan(delta)
0
100
200
300
400
500
Temperature, C

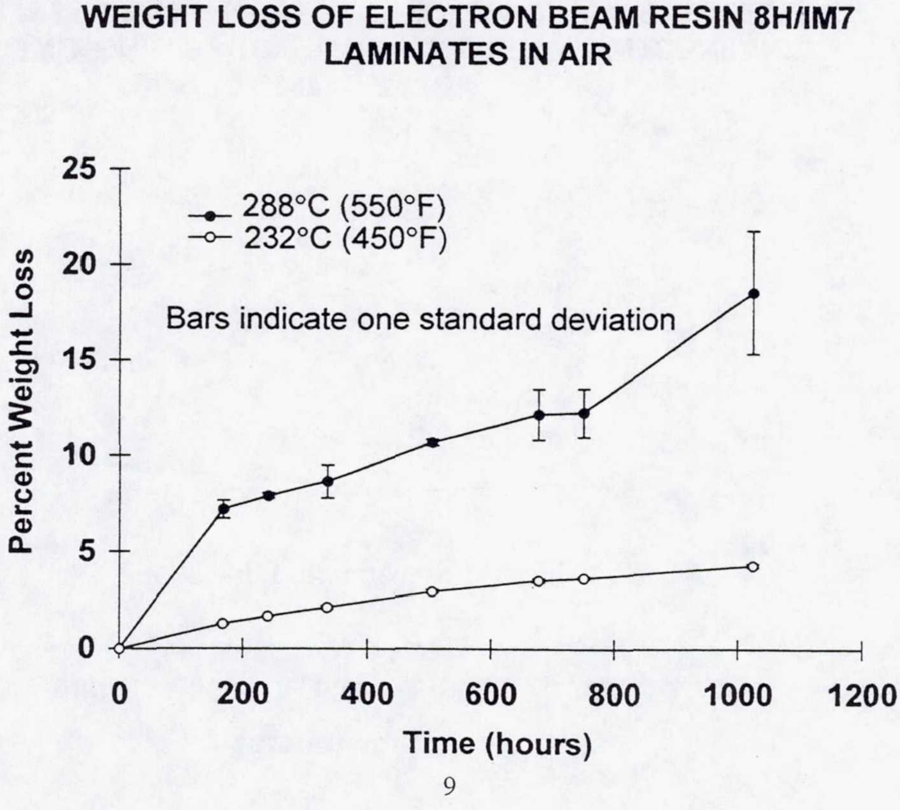
WEIGHT LOSS OF ELECTRON BEAM RESIN 8H/IM7
LAMINATES IN AIR
288°C (550°F)
232°C (450°F)
Bars indicate one standard deviation
25
20
15
10
5
0
Percent Weight Loss
0
200
400
600
800
1000
1200
Time (hours)

FLEXURAL STRENGTH OF ELECTRON BEAM RESIN 8H/IM7 UNIDIRECTIONAL LAMINATES VERSUS AGING TIME IN AIR-TESTED AT 25°C

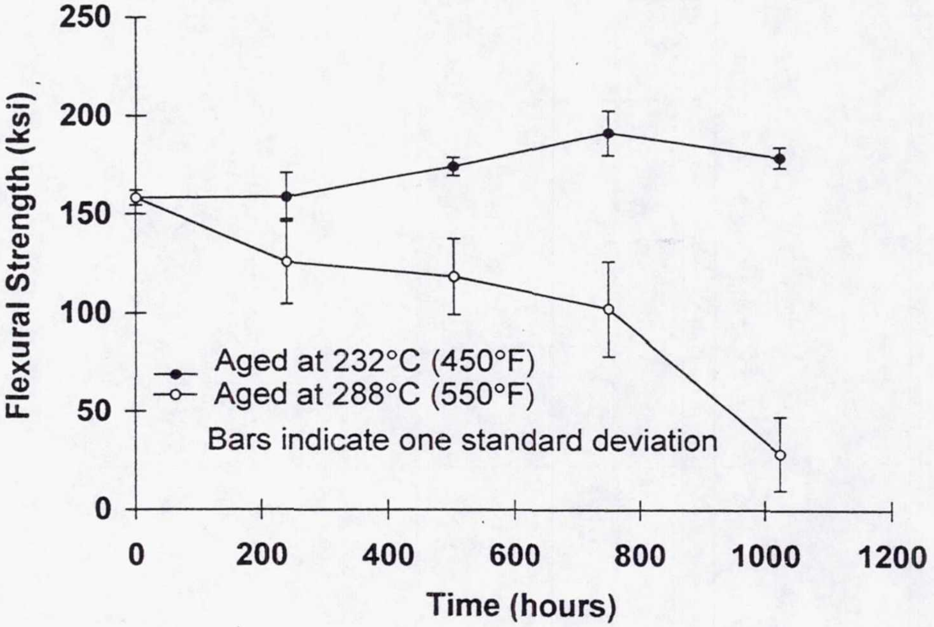

FLEXURAL STRENGTH OF ELECTRON BEAM RESIN 8H/IM7 UNIDIRECTIONAL LAMINATES VERSUS AGING TIME IN AIR AT 232°C (450°F)

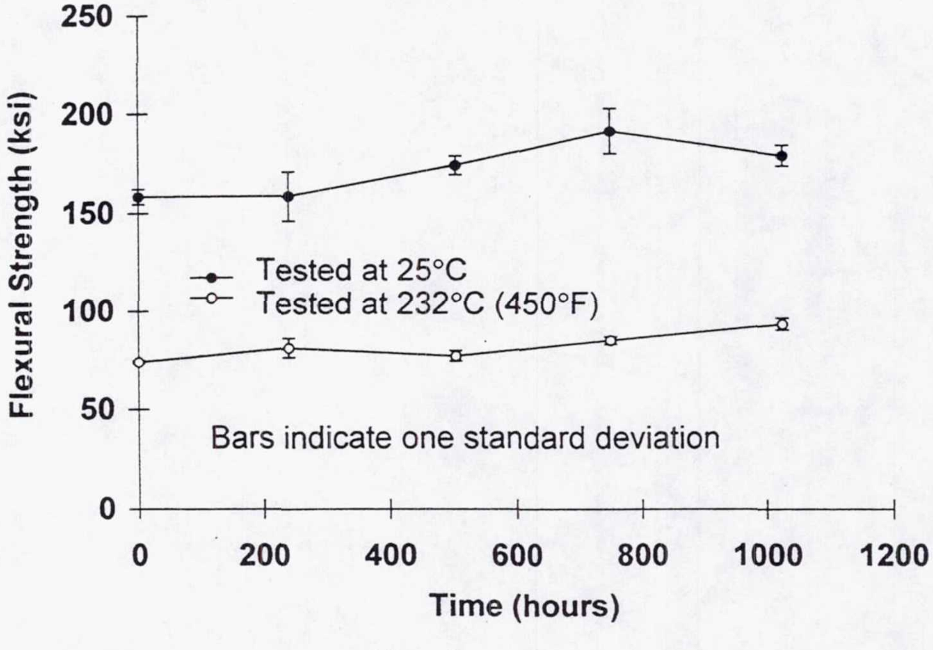

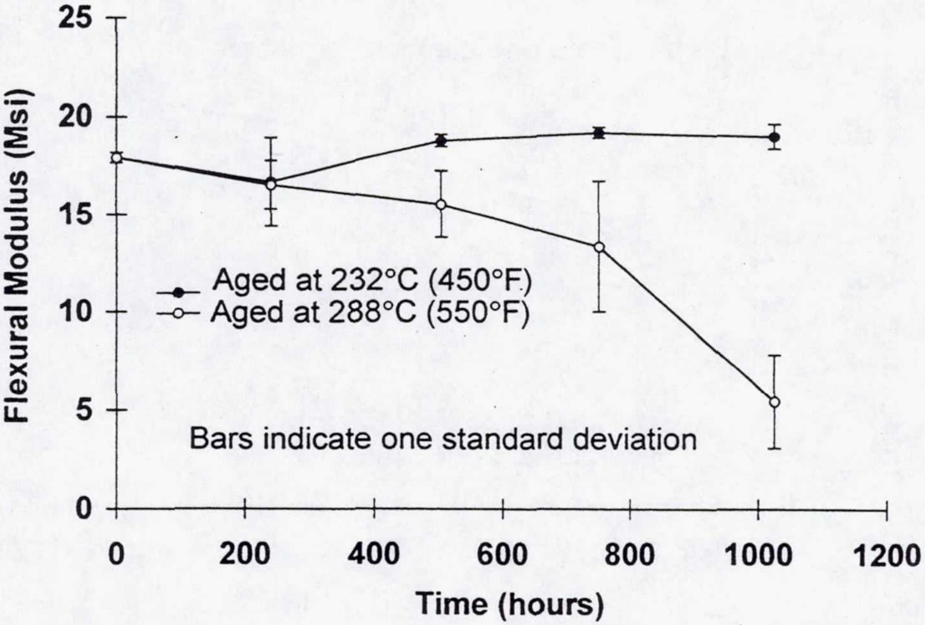

FLEXURAL MODULUS OF ELECTRON BEAM RESIN 8H/IM7 UNIDIRECTIONAL LAMINATES VERSUS AGING TIME IN AIR - TESTED AT 25°C

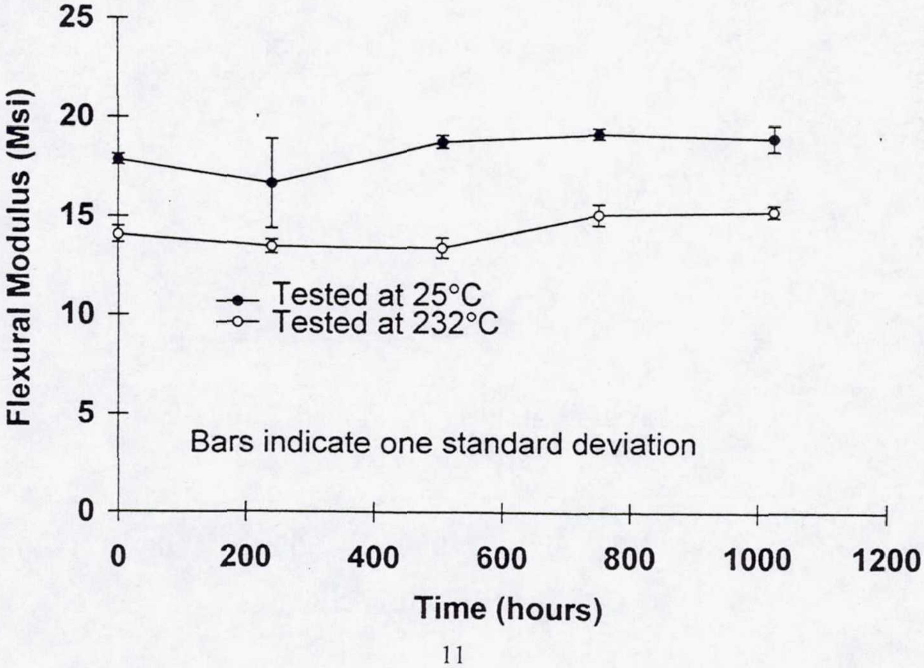

FLEXURAL MODULUS OF ELECTRON BEAM RESIN 8H/IM7 UNIDIRECTIONAL LAMINATES VERSUS AGING TIME IN AIR AT 232°C (450°F)

INTERLAMINAR SHEAR STRENGTH OF ELECTRON BEAM RESIN 8H/IM7 UNIDIRECTIONAL LAMINATES VERSUS AGING TIME IN AIR - TESTED AT 25°C

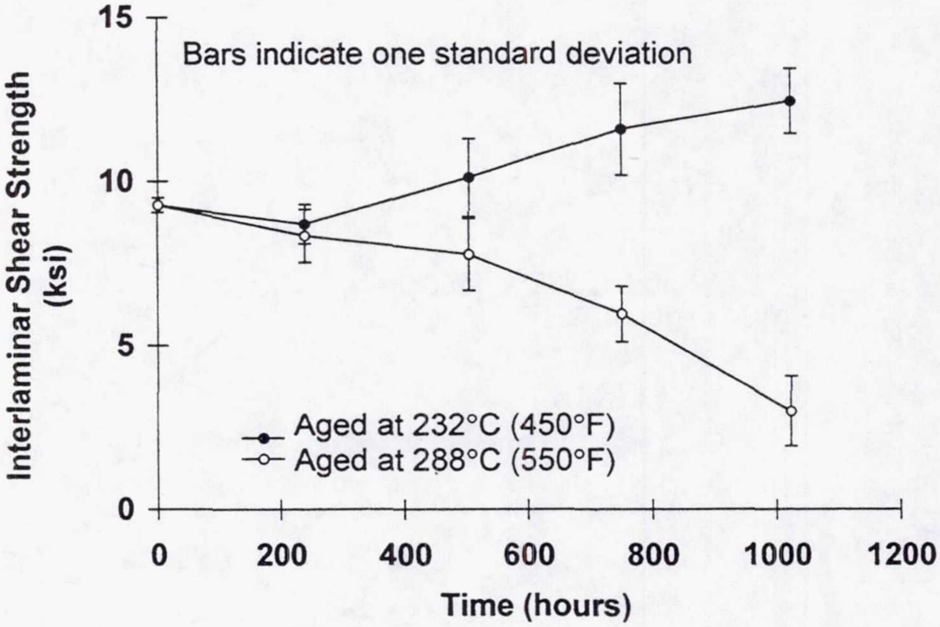

INTERLAMINAR SHEAR STRENGTH OF ELECTRON BEAM RESIN 8H/IM7 UNIDIRECTIONAL LAMINATES VERSUS AGING TIME IN AIR AT 232°C (450°F)

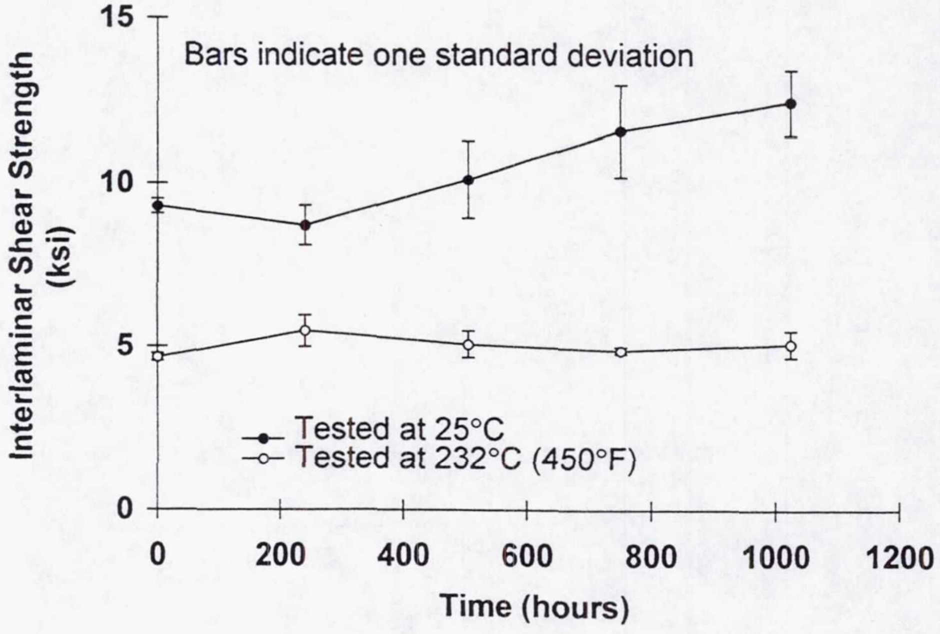

SUMMARY AND CONCLUSIONS

- Electron Beam Resin 8H exhibited a glass transition temperature of 396°C (745°F) after electron beam cure at room temperature
- Electron Beam Resin 8H/IM7 laminates exhibit good mechanical properties at 25°C
- Weight loss for the laminates is 4.25 and 18.4% after 1000 hours in air at 232°C (450°F) and 288°C (550°F), respectively
- Mechanical properties of Electron Beam Resin 8H are not affected by aging at 232°C, but are degraded by aging at 288°C

FOCUS OF FUTURE HIGH TEMPERATURE ELECTRON BEAM RESIN RESEARCH

- Optimize Electron Beam Resin 8H/IM7 fabrication to maximize mechanical properties
- Rerun aging tests on optimized laminates
- Explore feasibility of electron beam curable polyimides by screening of model compounds

JOINING OF SILICON CARBIDE-BASED CERAMICS BY REACTION FORMING METHOD*

M. SINGH
NYMA, Inc.
Engineering Services Division
Brook Park, Ohio

and

J.D. Kiser
NASA Lewis Research Center
Cleveland, Ohio

Introduction

Recently, there has been a surge of interest in the development and testing of silicon-based ceramics and composite components for a number of aerospace and ground based systems. The designs often require fabrication of complex shaped parts which can be quite expensive. One attractive way of achieving this goal is to build up complex shapes by joining together geometrically simple shapes. However, the joints should have good mechanical strength and environmental stability comparable to the bulk materials. These joints should also be able to maintain their structural integrity at high temperatures. In addition, the joining technique should be practical, reliable, and affordable. Thus, joining has been recognized as one of the enabling technologies for the successful utilization of silicon carbide based ceramic components in high temperature applications.

Overviews of various joining techniques, i.e., mechanical fastening, adhesive bonding, welding, brazing, and soldering have been provided in recent publications [1-3]. The majority of the techniques used today are based on the joining of monolithic ceramics with metals either by diffusion bonding, metal brazing, brazing with oxides and oxynitrides, or diffusion welding [4-6]. These techniques need either very high temperatures for processing or hot pressing (high pressures). The joints produced by these techniques have different thermal expansion coefficients than the ceramic materials, which creates a stress concentration in the joint area. The use temperatures for these joints are around 700 °C.

Ceramic joint interlayers have been developed as a means of obtaining high temperature joints [7-11]. These joint interlayers have been produced via pre-ceramic polymers [8-9], in-situ displacement reactions [10], and reaction bonding [11] techniques. Joints produced by the pre-ceramic polymer approach exhibit a large amounts of porosity and poor mechanical properties. On the other hand, hot pressing or high pressures are needed for in-situ displacement reactions and reaction bonding techniques. Due to the equipment required, these techniques are impractical for joining large or complex shaped components.

The reaction processing technique [12] reported here is unique in terms of producing joints with tailorable microstructures. The formation of joints by this approach is attractive since the

---

* Work funded under NASA Contract NAS3-27186.

thermomechanical properties of the joint interlayer can be tailored to be very close to those of the silicon carbide base materials. In this paper, the microstructure and mechanical properties of reaction formed joints in Cerastar RB-SiC material are presented. The high temperature flexural strength of joints has been measured up to 1350 °C in air. Scanning electron microscopy has been used to characterize the fracture surfaces. The flexural strength of joints has been compared to those of bulk Cerastar RB-SiC material.

Experimental Procedures

The Cerastar reaction-bonded silicon carbide (RB-SiC) materials used in this study were provided by Carborundum Co., Gardner, MA. These materials were fabricated by the reaction bonding of coarse and fine silicon carbide grains with silicon using a liquid silicon infiltration process. As processed samples were sectioned, mounted, and polished for metallographic studies. For joining studies, 6 cm x 3 cm size silicon carbide pieces were machined from SiC plates. These pieces were cleaned in acetone and dried. Joining is carried out by initially applying a carbonaceous mixture to the joint areas between the silicon carbide pieces. The specimen is then heated to 100 °C for 15-20 minutes. Next, the joint area is infiltrated with molten silicon at 1425 °C for 15 minutes. Molten silicon reacts with carbon to form silicon carbide, with a controllable amount of residual silicon phase in the joints.

Flexure bars were machined from the joined pieces, with joints in the middle of the flexure bars. Four-point flexural strength testing was carried out with MIL-STD-1942 (MR) configuration B specimens with 20 mm inner and 40 mm outer spans. Flexure tests were carried out at room temperature, 800, 1200, and 1350 °C in air. A number of Cerastar RB-SiC bars were heat treated at 1200 °C for 4 hrs. in air. For the as-machined and heat treated Cerastar RB-SiC materials, at least six to nine specimens were tested at room temperature, and three specimens were tested at each high temperature. Three joint thicknesses were investigated. For each joint thickness, at least three joined specimens were tested at room temperature while two were tested at high temperatures. After testing, fracture surfaces were examined by optical and scanning electron microscopy to identify the failure origins.

Results and Discussion

Microstructure

An optical micrograph of as received Cerastar RB-SiC material is shown in Fig. 6. This micrograph shows the distribution of coarse and fine silicon carbide grains (gray) in a silicon phase (white). There are pools of silicon and some porosity in this material. Microstructures of reaction formed joints are shown in Fig. 7 (a-c). In Fig. 7(a), the joint was very thick (~ 350 μm) and silicon rich. This joint will be referred to as Joint A. Two thinner joints, referred to as Joints B and C are shown in Fig. 7 (b) and (c). These joints contain silicon carbide and silicon phase. The joint thickness and composition have a strong influence on the room and high temperature properties of the joined materials.

Flexural Strength and Fractography

The room and high temperature flexural strengths of the as-machined and heat treated Cerastar

RB-SiC along with the joined materials are shown in Fig. 10. The average room temperature strengths of as-machined and heat treated Cerastar RB-SiC specimens were 157±11 MPa and 202±14 MPa, respectively. Thus, the flexural strength of heat treated bars is higher at room temperature. Healing of machining flaws by silica formation is one possible explanation. The flexural strength of the specimen containing thick joint A is about 44±2 MPa. In flexure bars with thick joints, fracture always occurred at the joints. In addition to being thick, this joint was also rich in silicon. The microscopic examination of fracture surfaces of specimens with thick joints tested at room temperature revealed the failure mode to be typically brittle. Specimens containing thinner joints, B and C, have flexural strengths comparable to those of bulk materials. In the flexure specimens with thinner joints, fracture always occurred in the bulk materials away from the joint. In this case, the fracture origins appear to be inhomogeneities inside the specimen. This observation indicates that the material strength is not limited by the joint strength but by the strength of the bulk materials. In addition, there is no significant loss in strength of materials with thin joints up to 1350 °C.

Conclusions

It has been demonstrated that the reaction forming approach can be used to produce strong joints in reaction bonded silicon carbide materials. Thin (SiC-rich) joints show no significant strength loss at high temperatures and have properties at least similar to the bulk parent material used in this study.

References

[1] R.W. Messler, Jr., "Joining of Advanced Materials", Butterworth-Heinemann, Boston, MA (1993).
[2] Mel M. Schwartz, "Ceramic Joining", ASM International, Materials Park, OH (1990).
[3] C.H. Bates, M.R. Foley, G.A. Rossi, G.J. Sandberg, and F.J. Wu, "Joining of non-oxide ceramics for high temperature applications", Ceramic Bulletin, 69, 3 (1990) 350-356.
[4] O.M. Akselsen, "Diffusion bonding of ceramics", J. Mater. Sci., 27 (1992) 569-579.
[5] O.M. Akselsen, "Advances in brazing of ceramics", J. Mater. Sci., 27 (1992) 1989-2000.
[6] T.J. Moore, "Feasibility study of the welding of SiC", J. Am. Ceram. Soc., 68, 6 (1985) C 151-153.
[7] T. Iseki, K. Arakaw, and H. Suzuki, "Joining of dense silicon carbide by hot pressing", J. Mater. Sci. Letters, 15 (1980) 1049-1050.
[8] S. Yazima, K. Okamura, T. Shishido, Y. Hasegawa and T. Matsuzawa, "Joining SiC to SiC using Polyborosiloxane", Ceramic Bulletin, 60, 2 (1981) 253.
[9] I.E. Anderson, S. Ijadi-Maghsoodi, O. Unal, M. Nosrati, and W.E. Bustamante, "Development of a compound for low temperature joining of SiC ceramics and CFCC composites", Ceramic Trans., The American Ceramic Society, Westerville, OH (1996).
[10] C.H. Henager, Jr. and R.H. Jones, "Joining SiC ceramics using displacement reactions", Ceramics Trans., Vol. 77, I. Reimanis, C.H. Henager, Jr., and A.P. Tomsia, eds., The American Ceramic Society, Westerville, OH (1997).
[11] B.H. Rabin and G.A. Moore, "Joining of SiC-based ceramics by reaction bonding methods", J. Mater. Synth. Process., 1, 3 (1993) 195-201.
[12] M. Singh, S.C. Farmer, and J.D. Kiser, "Joining of silicon carbide-based ceramics by reaction forming approach", Ceram. Engg. and Sci. Proc., The American Ceramic Society, Westerville, OH (1997).

OBJECTIVES

- To develop an affordable approach for the joining of silicon carbide-based materials.
- To characterize the microstructure and mechanical properties of reaction-formed joints.

Fig. 1

JOINING REQUIREMENTS

- Joint properties comparable to base materials.
    - Use temperature > 1200 °C
    - Good mechanical strength
    - Oxidation and corrosion resistance
    - Low CTE mismatch to minimize the residual stresses
    - Thermal shock resistance
- Leak tight joints.
- Practical, reliable, and affordable technique adaptable to in-field installation, service, and repair.

Fig. 2

Flow Chart for the Joining of Silicon Carbide-Based Ceramics by Reaction Forming Method (Schematic)

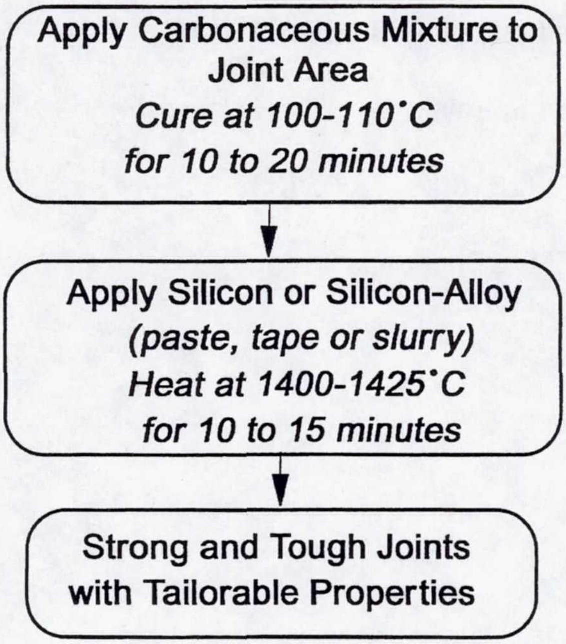

Apply Carbonaceous Mixture to Joint Area

Cure at 100-110°C for 10 to 20 minutes

Apply Silicon or Silicon-Alloy

(paste, tape or slurry)

Heat at 1400-1425°C for 10 to 15 minutes

Strong and Tough Joints with Tailorable Properties

Fig. 3

EXPERIMENTAL PROCEDURES

- Material: Cerastar RB-SiC (Carborundum Co., Gardener, MA).
- Joining: As machined pcs. (6 cm x 3 cm x 0.8 cm) cleaned with acetone and dried.
- Butt joints formed between the pieces and three joint thicknesses evaluated.
- Flexure bars (50 mm x 4 mm x 3mm) were machined with joints in the middle of the bars.
- Monolithic specimens heat treated at 1200 °C for four hours to minimize surface machining flaws.

Fig. 4

CHARACTERIZATION

- Microstructure (Optical microscopy)
- Four-point flexure tests (40/20 span)
- Loading rate : 0.5 mm/min
- Test temperatures (25, 800, 1200, 1350 ºC), Air
- Fractography (SEM, Optical microscopy)

Fig. 5

Microstructure of As-Received Cerastar RB-SiC

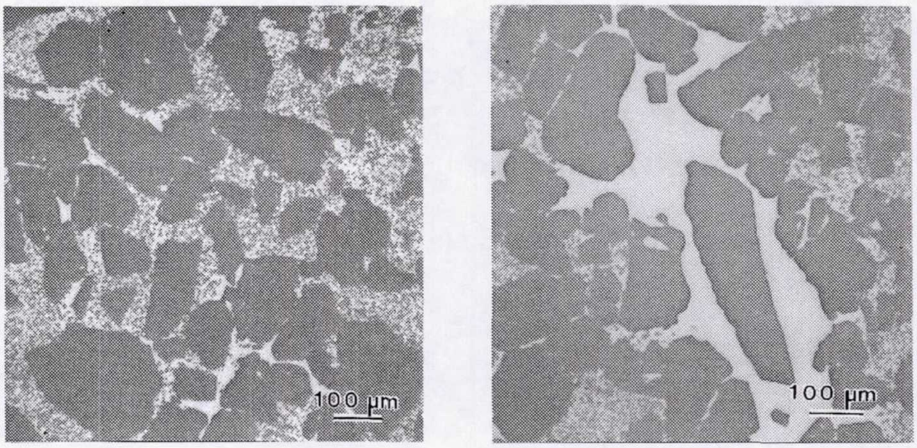

- Fabricated by the reaction bonding of coarse α-SiC grains with silicon phase.
- Uneven distribution of both phases.

Fig. 6

Microstructures of Reaction Formed Joints in Cerastar RB-SiC

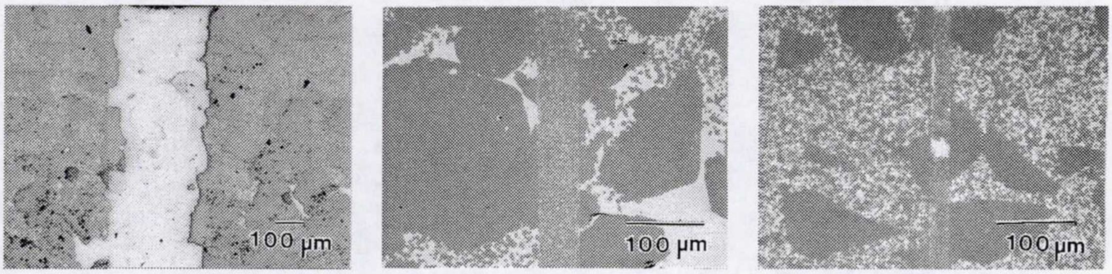

Joint A (~350 µm) Joint B (~50-55 µm) Joint C (~20-25 µm)

Fig. 7

Flexural Strength of Cerastar RB-SiC Ceramics as a Function of Temperature

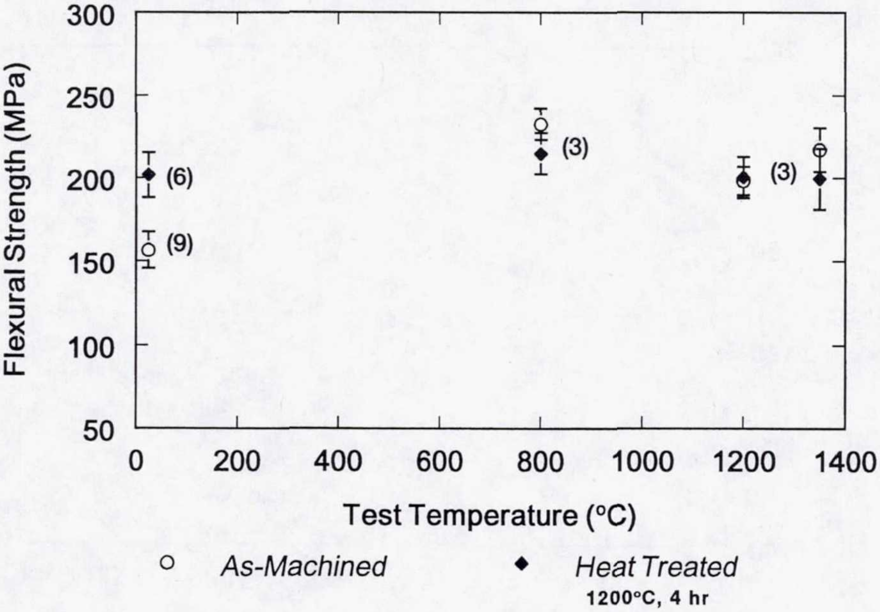

Fig. 8

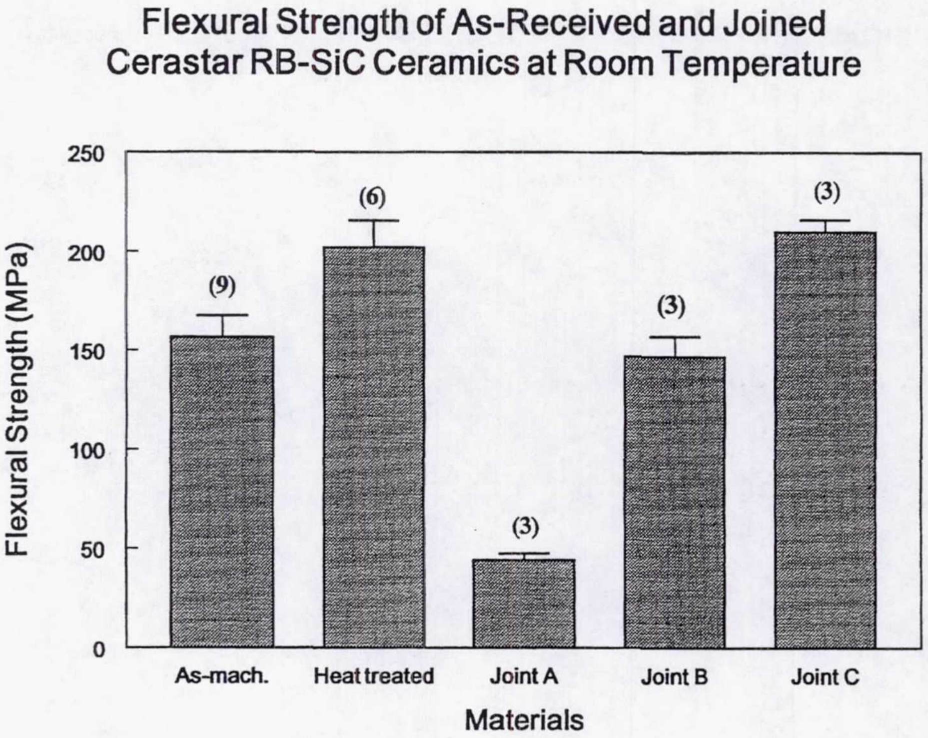
Flexural Strength of As-Received and Joined
Cerastar RB-SiC Ceramics at Room Temperature
Flexural Strength (MPa)
250
200
150
100
50
0
(9)
(6)
(3)
(3)
(3)
As-mach.
Heat treated
Joint A
Joint B
Joint C
Materials

Fig. 9

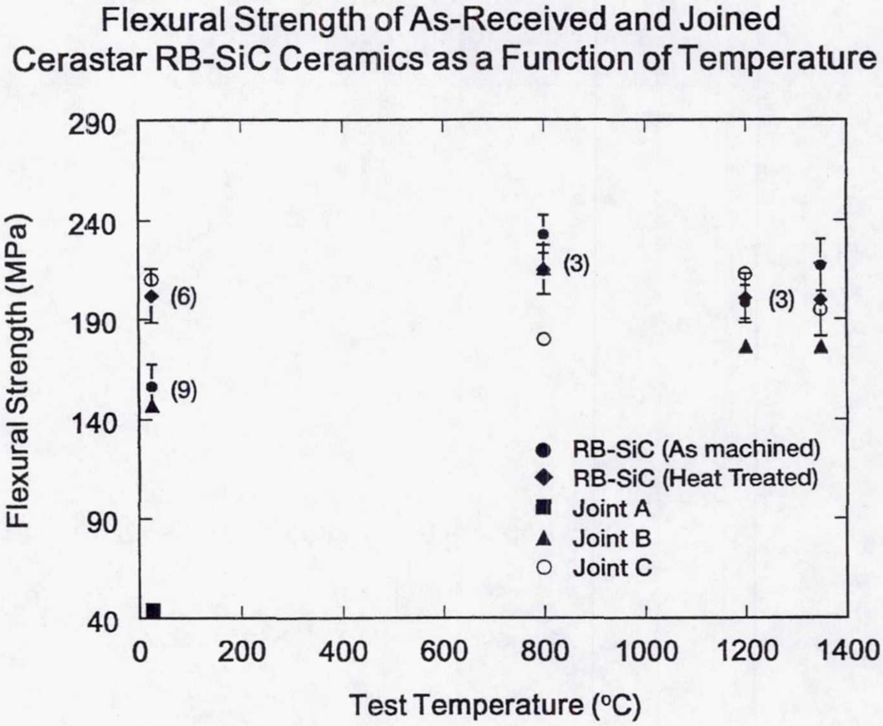
Flexural Strength of As-Received and Joined
Cerastar RB-SiC Ceramics as a Function of Temperature
Flexural Strength (MPa)
290
240
190
140
90
40
(6)
(9)
(3)
(3)
RB-SiC (As machined)
RB-SiC (Heat Treated)
Joint A
Joint B
Joint C
0
200
400
600
800
1000
1200
1400
Test Temperature (°C)

Fig. 10

Fractographs Showing the Failure Behavior in Thick (~350 μm) Joints

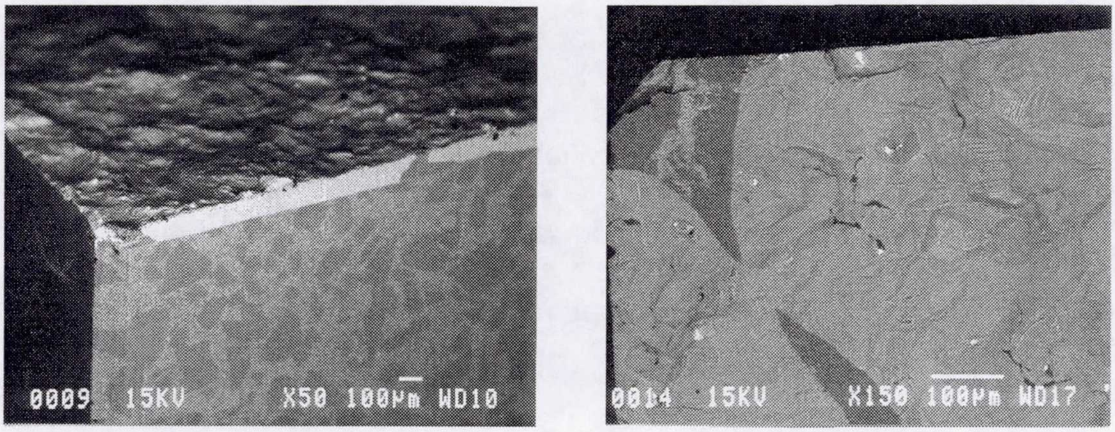

- Flexure bars always fracture at thick joints because of their poor mechanical strength.

Fig. 11

Fractographs Showing the Failure Behavior in Thin (~ 50 μm) Joints

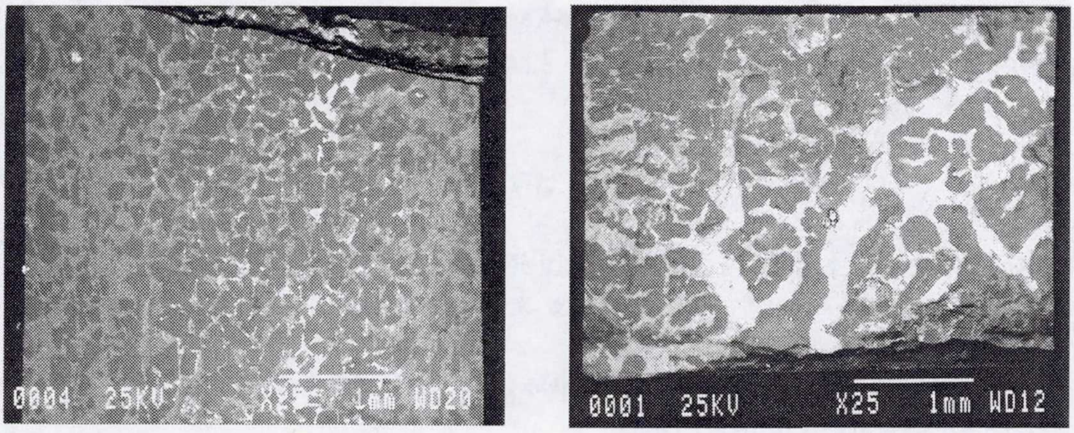

- Joined flexure bars fail away from the joint regions.

Fig. 12

SUMMARY OF RESULTS

- A reaction based joining approach for silicon carbide materials has been developed.
- The thickness of the reaction formed joints can be tailored.
- Thin joints (< 60 μm) have good room and high temperature properties.
- Failure of flexure bars with thin joints occurs away from the joint regions.

Fig. 13

CONCLUSIONS

- A reaction based joining approach for silicon carbide materials has been developed. Using this approach, joints with tailorable thickness and good room and high temperature properties can be produced.

FOCUS OF FUTURE RESEARCH

- Joining of other types of silicon carbide (Hexoloy-SA, RFSC) and characterization of high temperature thermomechanical properties.
- Joining of fiber reinforced composites (C/SiC and SiC/SiC) and characterization of joint properties.

Fig. 14

THERMODYNAMIC STUDIES OF HIGH TEMPERATURE MATERIALS VIA KNUDSEN CELL MASS SPECTROMETRY

NATHAN S. JACOBSON and Michael P. Brady[*]
NASA Lewis Research Center
Cleveland, OH 44135

The Knudsen Cell technique is a classic technique from high temperature chemistry for studying condensed phase/vapor equilibria. It is based on a small enclosure, usually about 1 cm in diameter by 1 cm high, with an orifice of well-defined geometry. This forms a molecular beam which is analyzed with mass spectrometry. There are many applications to both fundamental and applied problems with high temperature materials. Specific measurements include vapor pressures and vapor compositions above solids, activities of alloy components, and fundamental gas/solid reactions (ref. 1).

The basic system is shown in Fig. 2. Our system can accommodate a wide range of samples, temperatures, and attachments, such as gas inlets. It is one of only about ten such systems world-wide.

In order to obtain precise data, there are a number of critical experimental issues. These include selection of an inert Knudsen cell material, uniform temperature throughout the cell and accurate temperature measurement. A common problem in all types of mass spectrometry is to identify the gases ('parent molecules') which form a particular peak in the mass spectrometer. This is done via the mass-to-charge ratio, isotopic abundances, and various other techniques (ref. 1). It is also critical to separate the background composition from a given peak. This is accomplished with the shutter shown in Fig. 2. Finally the measured ion current must be converted to a vapor pressure and/or thermodynamic activity. A standard of known vapor pressure, such as gold or silver, is used to calibrate the system. In our twin cell configuration, this calibration is done *in-situ* as an integral part of each experiment.

Two examples will be discussed. First consider the vaporization of a cylindrical alumina combustor in a stream of high temperature combustion gases. This problem is illustrated in Figs. 6-8. The problem is to determine how hot the combustor can be before volatility becomes a limiting issue. In general, vapor pressures greater than ~10^{-6} bar lead to recession rates greater than 10 mils/10,000 hrs, which are not acceptable for long term operation (ref. 2). To do this calculation, Knudsen cell measurements on Al-O(g) species together with estimates on Al-O-H(g) species are needed (refs. 3 and 4). These are put into a free energy minimization program together with the combustion gas composition (ref. 5). The results are shown in Fig. 8. At temperatures greater than 2170 K, volatility becomes a limiting issue.

---

[*] Formerly NRC Associate at NASA LeRC, Currently at Oak Ridge National Laboratory

The second example is thermodynamic activity measurements in the Ti-Al and Ti-Al-X systems. These are important for many application including: prediction of oxidation properties (i.e. will TiO or Al_2O_3 be the stable oxide?) (ref. 6), prediction of alloy/fiber reactions (ref. 7), and phase diagram assessments. For these measurements, we use a unique twin cell flange for comparing the alloy to the standard *in-situ*. This is illustrated in Figs. 10 and 11. Measurements were made of aluminum activity and where possible titanium activity. The Ti-Al phase diagram is shown in Fig. 12 and sample measurements about the γ–TiAl phase field are shown in Fig. 13. These have been shown consistent with measurements of other investigators. A critical issue in oxidation is understanding the effect of alloying elements. For example it is known chromium promotes oxide formation. Is this by increasing Al activity and decreasing Ti activity? Measurements are currently underway to determine this. Al activity measurements are shown in Fig. 15.

A brief description of high temperature Knudsen cell mass spectrometry has been given. It has been used many years on many systems. However it continues to provide useful applied and fundamental data on high temperature materials. NASA LeRC has a unique facility for this technique. Two specific examples are discussed: vaporization of Al_2O_3 and thermodynamic activity measurements for Ti-Al-X alloys.

References:

1. Hilpert, K.: "Chemistry of Inorganic Vapors" in Structure and Bonding 73, Springer-Verlag, Berlin, 1990.

2. Jacobson, N. S.: High Temperature Durability Considerations for the HSCT Combustor", NASA TP 3162, January 1992.

3. Paule, R. C.: Mass Spectrometric Studies of Al_2O_3 Vaporization Processes. High Temp. Sci., vol. 8, no. 3, 1976, pp. 257-266.

4. Chase, M. W., Jr., et. al., eds.: JANAF Thermochemical Tables, 3rd Edition, American Chemical and American Physical Society, New York, NY, 1985.

5. Eriksson, G. A. and Hack, K.: ChemSage—A Computer Program for the Calculation of Complex Chemical Equilibria, Met. Trans. vol. 21B, 1991, pp. 1013-1023.

6. Brady, M. P., et. al.: The Oxidation and Protection of Gamma Titanium Aluminides, JOM, vol. 48, no. 11, 1996, pp. 46-50.

7. Misra, A. K.: Reaction of Ti and Ti-Al Alloys with Alumina, Met. Trans. vol. 22A, 1991, pp. 715-721.

Knudsen Cell Technique

- Classic techique from High Temperature Chemistry to study solid/vapor equilibria.
- Small cell, well defined orifice—form molecular beam to analyze vapor, generally with mass spectrometry.
- Many applications to high temperature materials.

Fig. 1

High Temperature Knudsen Cell Mass Spectrometer

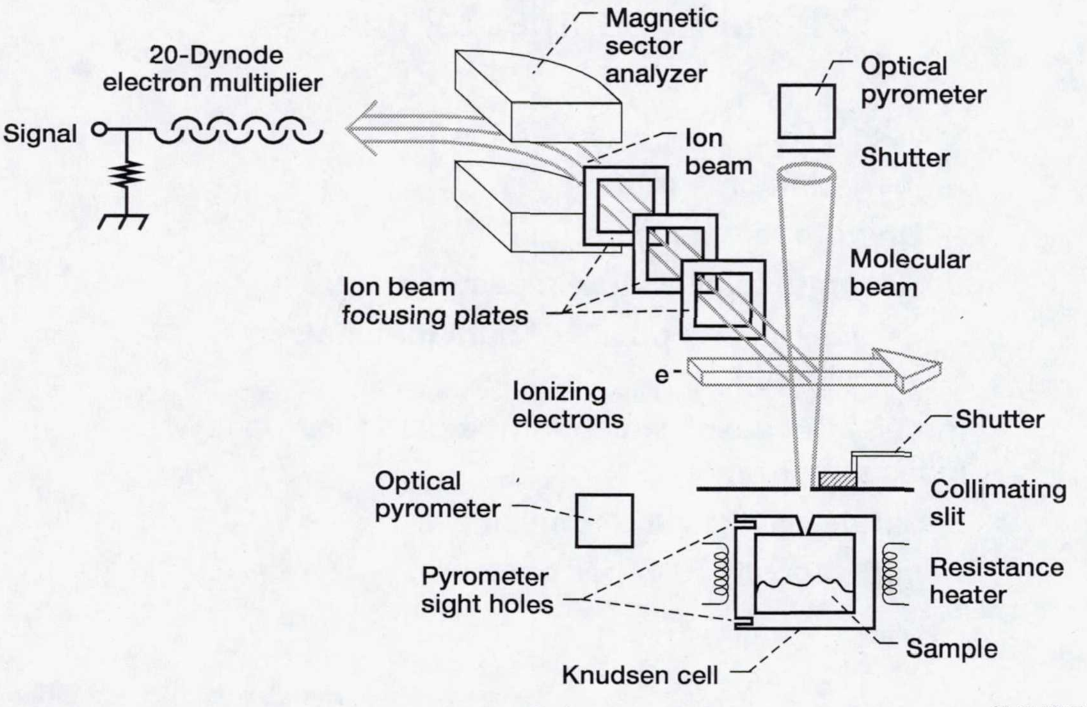

Fig. 2

CD-91-52433

Knudsen Cell Measurements

- Basic and applied problems:
  - Vapor pressures above solids
  - Activities of alloy components
  - Gas/solid reactions

- Much of the tabulated thermodynamic data is from this technique.

- Only about 10 laboratories worldwide have this capability.

Fig. 3

Critical Experimental Issues

- Knudsen Cell:
  - Inert container material.
  - Uniform temperature.
  - Accurate temperature measurement.
    - Use melting points of pure materials to calibrate.
- Identify the gases which form a particular peak in mass spectrometer.
- Separate background from signal.
- Relate intensity to vapor pressure.

Fig. 4

Types of Measurements

- Identify vapor species—e.g., $Al_2O(g)$ over $Al_2O_3(s)$.
- Determine absolute vapor pressures.
- Heats of vaporization
  - Second law: Slope of ln P vs. 1/T = $\Delta H/R$
- Compare vapor pressure of an alloy component to that of a pure metal.
  - $a(A) = P(A)/P^o(A)$
- Leak in external gas—look at gas/solid reaction.

Fig. 5

Example 1: Vaporization of Alumina

- Actual problem: cylindrical alumina combustor with a stream of hot combustor gases (N_2, O_2, CO_2, H_2O)
- How hot can we make the alumina before volatility becomes an issue?
- Long term operation < 10 mils/10,000 hr — < 10^{-6} bar

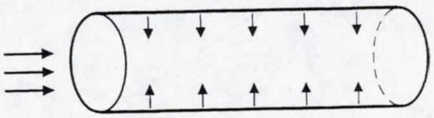

Fig. 6

Equilibrium Vaporization of Al_2O_3 into a Vacuum

- R. C. Paule, H. Temp. Sci. 8, 257 (1976) + many other Knudsen Cell Studies.
- Main reactions:
  - $Al_2O_3 = 2\,Al(g) + 3\,O\,(g)$
  - $Al_2O_3 = 2\,AlO(g) + O(g)$
  - $2\,O(g) = O_2(g)$
- Suppressed by oxygen.

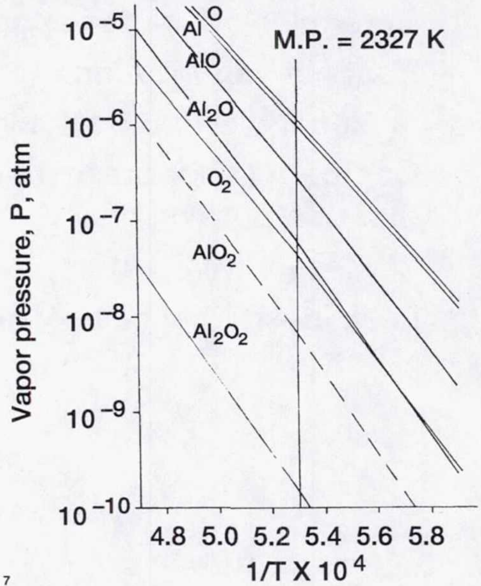

Fig. 7

Equilibrium Vaporization of Al_2O_3 into a Combustion Atmosphere

- Use thermodynamic data from Knudsen Cell investigations and estimates for Al-O and Al-O-H
- Computer code which considers all vaporization reactions:

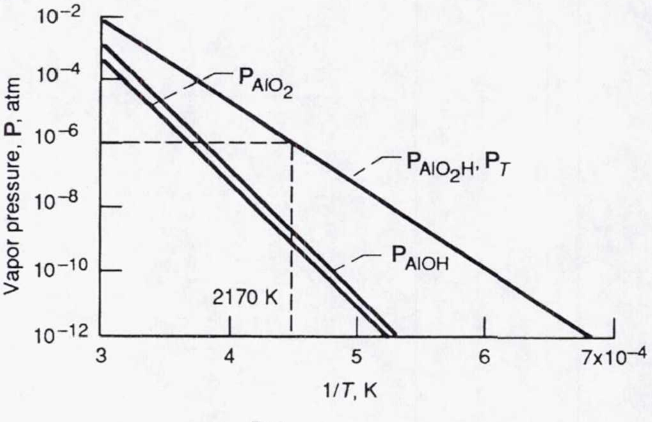

Fig. 8

Example 2: Thermodynamic Activity Measurements in Ti-Al and Ti-Al-X

- Activity: “Escaping tendency”—ratio of vapor pressure of metal in alloy to pure metal—tells how tightly bound metal is in alloy.
- Uses:
  - Predict oxidation characteristics.
  - Predict alloy/fiber reactions (Misra, Met. Trans. 22A, 715 (1991)).
    - $3\underline{Ti} + Al_2O_3 = 3\,TiO + 2\underline{Al}$
  - Phase diagram assessments.

Fig. 9

Double Cell Technique

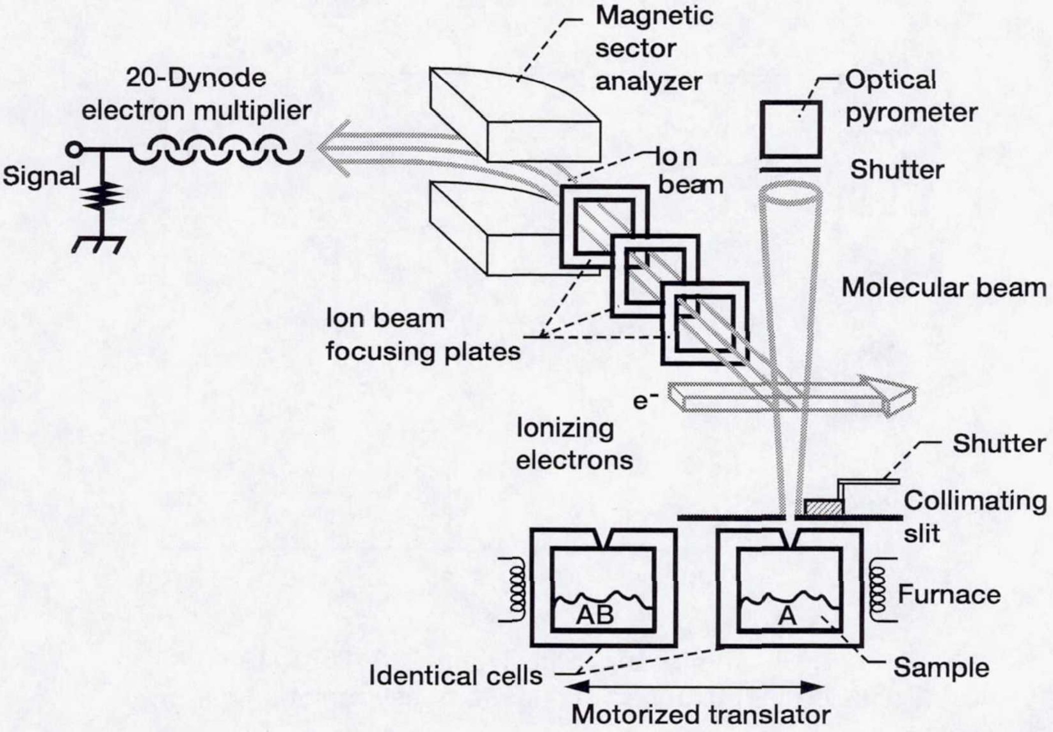

Fig. 10

CD-93-65925

Knudsen Cell Flange

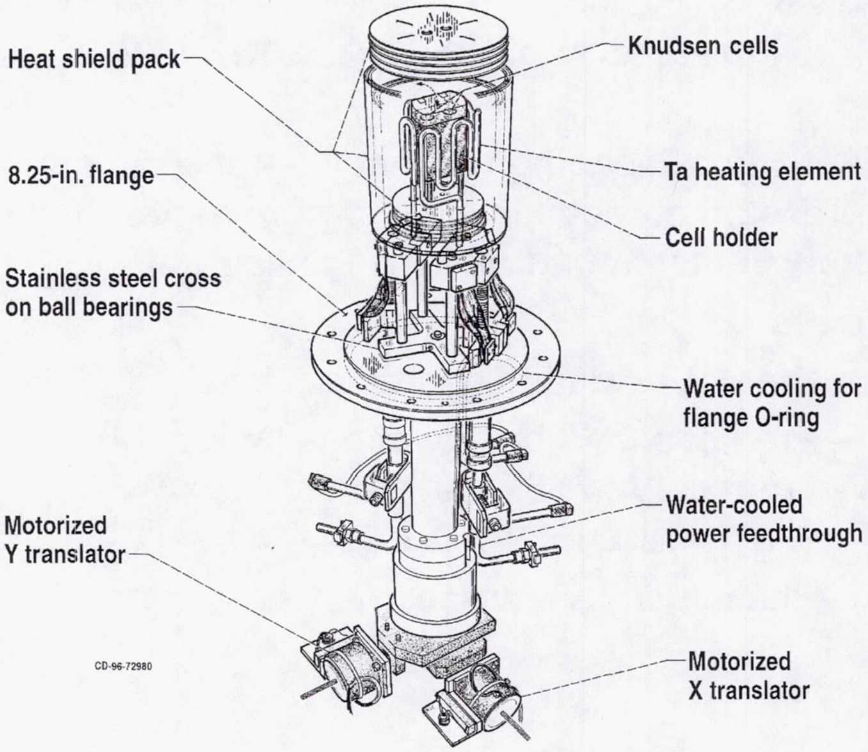

Fig. 11

Ti-Al Phase Diagram

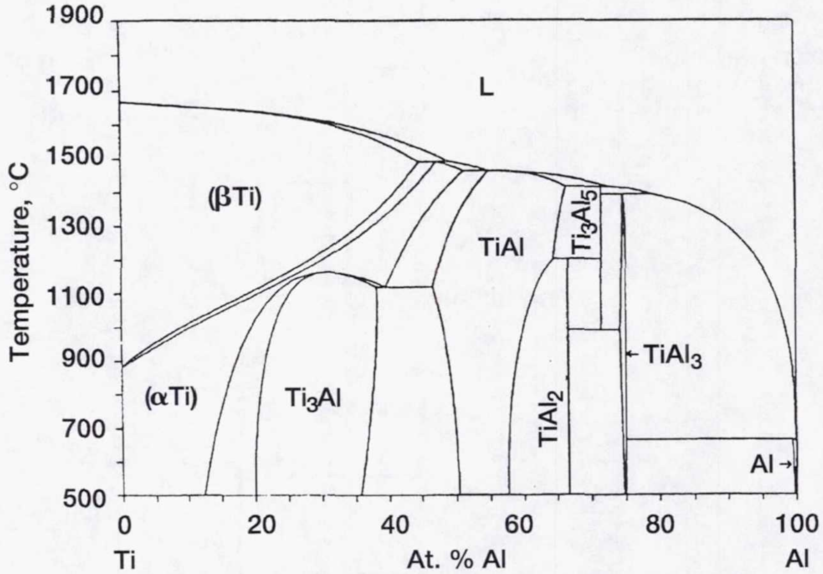

Kattner, Lin, and Chang, Met. Trans. 23A, 2081 (1992).
Focus on γ-TiAl and adjacent two phase regions.

Fig. 12

Al Activity Data Near γ-Ti-Al

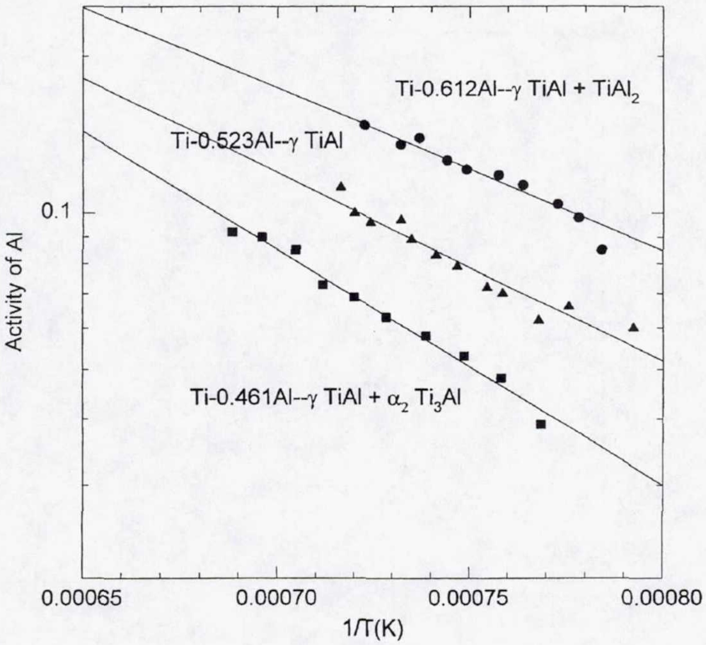

Fig. 13

Ti-Al-X Studies

- Alloying additions (esp. Cr) promote Al_2O_3 formation and limit TiO formation.
- Is this by increasing a(Al) and decreasing a(Ti)?
- Examine
  - Ti-48Al-2Cr Ti-48Al-13Cr
  - Ti-48Al-2Nb Ti-48Al-13Nb
  - Ti-48Al-2Nb-2Cr
- Work in progress—currently looking at a(Ti)

Fig. 14

Activity of Al in Ti-Al-X Alloys

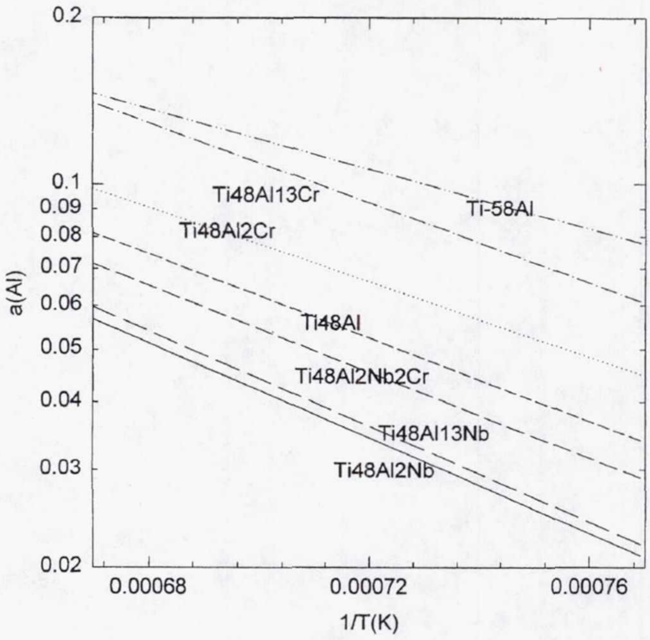

Fig. 15

Summary

- Classic experimental technique for studying solid/ vapor equilibria.
  - Unique facility at NASA LeRC.
- Experimental Technique
  - Inert cell.
  - Precise temperature measurement.
  - Convert ion intensities to partial pressures.
- Many, many applications. Two examples:
  - Vaporization of Al_2O_3.
  - Thermodynamics of Ti-Al-X alloys.

Fig. 16

MECHANICAL PROPERTIES OF Cu-Cr-Nb ALLOYS*

DAVID L. ELLIS

Case Western Reserve University / NASA Lewis Research Center
Cleveland, OH

Introduction

The Cu-Cr-Nb alloys were originally developed under the Earth-To-Orbit program for the Orbital Transfer Vehicle (OTV). The planned use was the combustion chamber of the regeneratively cooled rocket engine. The primary materials properties of interest were the elevated temperature tensile and creep strengths, low cycle fatigue (LCF) lives, and thermal conductivities. The currently used alloy NARloy-Z (Cu-3 wt.% Ag-0.5 wt.% Zr) was used as the standard for comparison for the new alloys.

The Cu-Cr-Nb alloys are strengthened by the high melting point intermetallic compound Cr_2Nb. The density of this phase is lower than Cu, so as the alloying levels are increased the density of the alloy decreases (Figure 7). At the higher alloying level tested, Cu-8 at.% Cr-4 at.% Nb (Cu-8 Cr-4 Nb) has a 4.1% lower density than NARloy-Z.

The objective of the current work is to expand the developmental work conducted previously to develop a database suitable for the initial design of a hypersonic vehicle heat exchanger. Experimental work was concentrated on the tensile strength, creep lives, LCF lives and thermal conductivities. The mechanical properties will be presented in this paper. Thermal conductivities have been previously reported (1).

Experimental Procedure

All Cu-Cr-Nb samples were made from conventionally Ar gas atomized powder produced by the Special Metals Corporation. The powder was canned in 5.08 cm (2") O.D. mild steel extrusion cans. The cans were extruded at 857°C (1575°F) using a round die with a 16:1 reduction in area.

Samples were machined from the extruded bars. For tensile and creep samples, a subsize design conforming to ASTM Standard E 8 (2) were used. The elevated temperature tensile tests were conducted in vacuum using a nominal strain rate of 1.1×10^{-4}/sec. Creep tests were conducted in vacuum using a constant load creep frame. Creep testing also was conducted on NARloy-Z samples for direct comparison to the Cu-Cr-Nb alloys.

Fully reversed, strain controlled LCF tests were conducted at room temperature, 538°C (1000°F) and 650°C (1200°F). A triangular waveform with a constant strain rate of 0.002/s was used. For the elevated temperature LCF tests, an inductively heated graphite susceptor was placed around the sample to provide heating. Oxidation was minimized by flowing Ar over the sample.

Results And Discussion

The chemical compositions of the alloys are listed in Figure 5. The alloying levels were near the values for stochiometric Cr_2Nb. A slight excess of Cr was chosen for increased hydrogen embrittlement resistance (3). The microstructures of all Cu-Cr-Nb alloys were very similar. Two typical transmission electron microscope (TEM) micrographs are presented in Figure 6. The images show the presence of large amounts of Cr_2Nb precipitates in a nearly pure Cu matrix. The interactions between dislocations and precipitates are currently under investigations, but as the images demonstrates, the extremely fine (<15 nm) Cr_2Nb are the primary strengtheners for the alloys.

---

* Work funded under NASA Grant NCC 3-463

The tensile strength of the alloys are presented in Figure 8. The values for NARloy-Z are the minimum design values reported by Rocketdyne (4). The average values are between 5% and 10% higher. Work is currently underway to tensile test NARloy-Z samples for direct comparisons. The results show clearly that the Cu-Cr-Nb alloys have a significant advantage in yield strength at all temperatures tested. In particular, the Cu-Cr-Nb alloys have approximately twice the elevated temperature strength of NARloy-Z above 400°C. An alternative way of looking at the results is the Cu-Cr-Nb alloys maintain their yield strengths to a much higher temperature than NARloy-Z. To a lesser extent, Cu-Cr-Nb alloys have a higher ultimate tensile strength (UTS) than NARloy-Z.

Three typical creep curves are presented in Figure 9. The stress for NARloy-Z had to be decreased to achieve comparable creep lives at the test temperatures. Figure 10 compares the creep lives for Cu-8 Cr-4 Nb and NARloy-Z. For simplicity, the lives of Cu-4 Cr-2 Nb are not shown, but they were approximately half that of Cu-8 Cr-4 Nb samples. In all cases, the Cu-Cr-Nb alloys have a much greater life and stress capability. It is particularly interesting to note that the creep life of Cu-8 Cr-4 Nb tested at 800°C is nearly identical to NARloy-Z at 650°C. This again indicates the possibility for increased operating temperatures and/or stresses with the Cu-Cr-Nb alloys.

A typical set of Cu-8 Cr-4 Nb LCF loops are presented in Figure 11. Cu-8 Cr-4 Nb exhibits some strain hardening, but not as much as many other alloys. The LCF lives of Cu-8 Cr-4 Nb and NARloy-Z are presented in Figure 12. At room temperature, Cu-8 Cr-4 Nb is equal to NARloy-Z at 2% total strain, the worst case, even though it has a lower ductility. At lower total strains, Cu-8 Cr-4 Nb lives were approximately 50% greater than NARloy-Z. The results for elevated temperature LCF testing showed that the Cu-8 Cr-4 Nb samples had lives 50% to 200% greater than NARloy-Z at 538°C. The results from testing at 650°C showed little difference from the 538°C tests. This again indicates the possibility of increased temperature capability over NARloy-Z.

Summary And Conclusions

The Cu-Cr-Nb alloys have significantly higher strengths than NARloy-Z at all temperatures tested. Usable strengths were retained up to approximately 700°C (1300°F). The creep properties of the Cu-Cr-Nb alloys were also greatly improved over NARloy-Z. The lives at a given stress were increased by up to 2-3 orders of magnitude with the largest increases occurring at the higher temperatures. Alternatively, the Cu-Cr-Nb alloys were capable of supporting a stress 10% to 50% greater than NARloy-Z for a given life. LCF testing showed Cu-8 Cr-4 Nb was equal to or better than NARloy-Z at room temperature. At elevated temperatures, the Cu-8 Cr-4 Nb was clearly superior to NARloy-Z and did not have any significant change in LCF between 538°C and 650°C.

Taken in total, the results indicate the possibility of trade-offs of temperature and stresses that could greatly increase the operating parameters of hypersonic vehicle heat exchangers.

Future Work

Future work will focus on completing the tensile testing of NARloy-Z to provide a direct comparison to the Cu-Cr-Nb data. In addition, research will examine the oxidation behavior of the Cu-Cr-Nb alloys in air and two potential engine environments. Since the fabrication of heat exchangers may require a sheet product, several tests will be conducted to determine a suitable rolling schedule and heat treatments.

Acknowledgment

The author would like to thank Michael Verrilli of the Structures and Acoustics Division of NASA Lewis Research Center for performing the LCF testing on the Cu-8 Cr-4 Nb alloy. The author would also like to acknowledge the help of Ron Phillips and Sharon Thomas of Gilcrest in conducting the tensile testing and Don Ulmer of Rocketdyne for providing the NARloy-Z.

References

(1) D.L. Ellis and G.M. Michal, "Mechanical and Thermal Properties of Two Cu-Cr-Nb Alloys and NARloy-Z," NASA CR-198529, NASA Lewis Research Center, Cleveland, OH (Oct. 1996)

(2) *1992 Annual Book of ASTM Standards, Vol. 03.01*, ASTM, Philadelphia, PA, (1992), pp. 130-149

(3) D.L. Ellis, A.K. Misra and R.L. Dreshfield, "Effect of Hydrogen on Cr2Nb and Cu-Cr-Nb Alloys," Hydrogen Effects On Materials Behavior, Proc. Of Fifth Intl. Conf., Moran, WY (Sept. 1994)

(4) Materials Properties Manual, 4th Ed., Rockwell International, Rocketdyne Div., (Oct. 30, 1987)

Background

- Originally developed for Orbital Transfer Vehicle (OTV) under Earth-To-Orbit (ETO) program
- Alloys designed to meet needs of combustion chamber liner
  - High elevated temperature strength and creep resistance
  - Long low cycle fatigue (LCF) life
  - High thermal conductivity
  - Properties that meet or exceed those of currently used NARloy-Z (Cu-3 Ag-0.5 Zr)

Fig. 1

Program Objectives

- Quantify tensile, creep and thermal conductivity at a level suitable for initial design work on hypersonic aircraft combustors and rocket combustion chamber liners

Fig. 2

Experimental Procedure

Production of Cu-Cr-Nb Alloys

- Conventionally atomized powders produced by Special Metals
- Extruded at 870°C (1575°F)
- 16:1 reduction in area
- Full consolidation achieved

Tensile Testing

- Subsized tensile specimens
- Vacuum testing
- Strain rate = 0.00011/sec

Fig. 3

Experimental Procedure (Cont.)

Creep Testing

- Vacuum testing
- Constant load
- Displacement recorded by computer DAQ unit

LCF Testing

- Only Cu-8 Cr-4 Nb alloy tested
- Strain controlled
- Fully reversed
- Triangular waveform
- Constant strain rate = 0.002/s

Fig. 4

Microstructure Of Cu-Cr-Nb Alloys

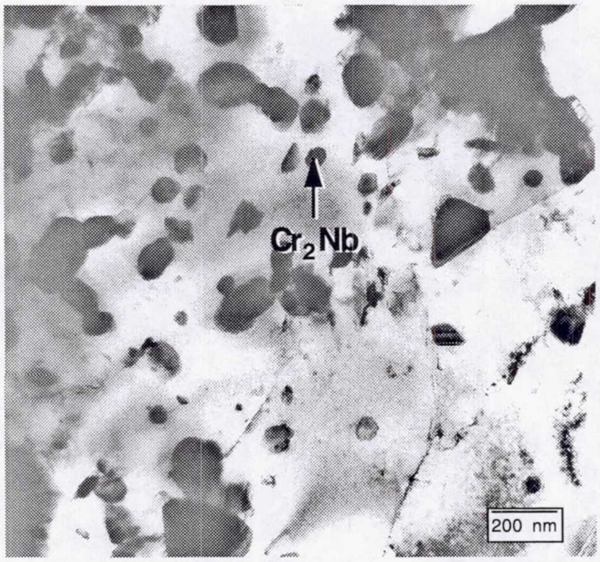

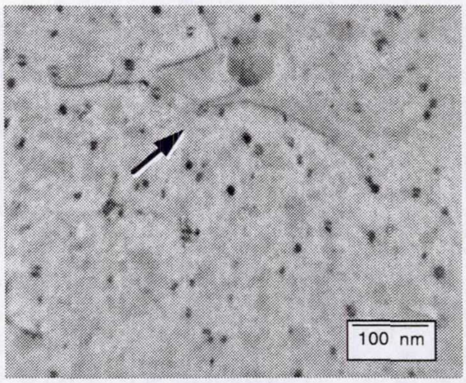

Arrow indicates two precipitates pinning dislocation

- Cr and Nb form a very high melting point intermetallic compound, Cr_2Nb
- Matrix is nearly pure Cu

Fig. 5

Alloy Chemistries

Alloy	Ag	Cr	Cu	Nb	O*	Zr	Cr:Nb
Cu-4 Cr-2 Nb - Powder†		3.27	Bal.	2.92	251		2.00
Cu-4 Cr-2 Nb		3.8	Bal.	3.6	N.A.		1.89
Cu-8 Cr-4 Nb - Powder†		6.45	Bal.	5.49	455		2.10
Cu-8 Cr-4 Nb		6.5	Bal.	5.5	640		2.11
NARloy-Z	3.0		Bal.		N.A.	0.5	

All chemistries in weight percent
*O is in ppm by weight
†Chemistry supplied by Special Metals
N.A. - Not available

- Alloy designations reflect amount of Cr and Nb in atomic percent
  - Cu-4 Cr-2 Nb = Cu-4 at.% Cr-2 at.% Nb

Fig. 6

Comparison Of Densities

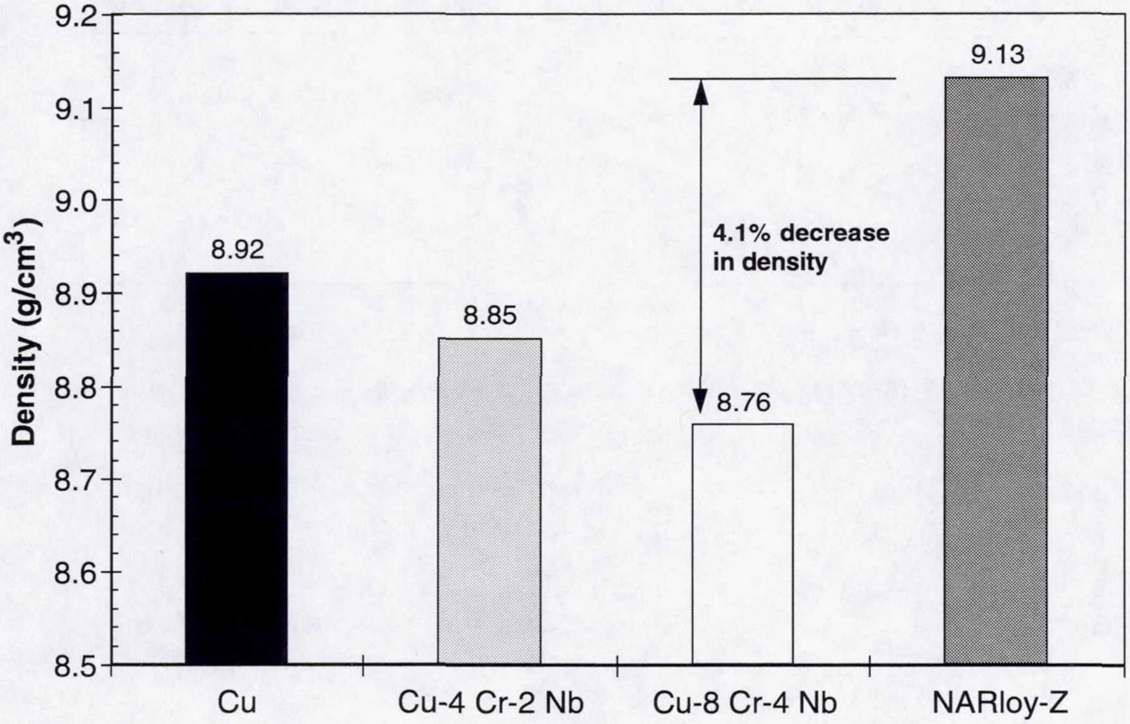

Fig. 7

Elevated Temperature Tensile Strength

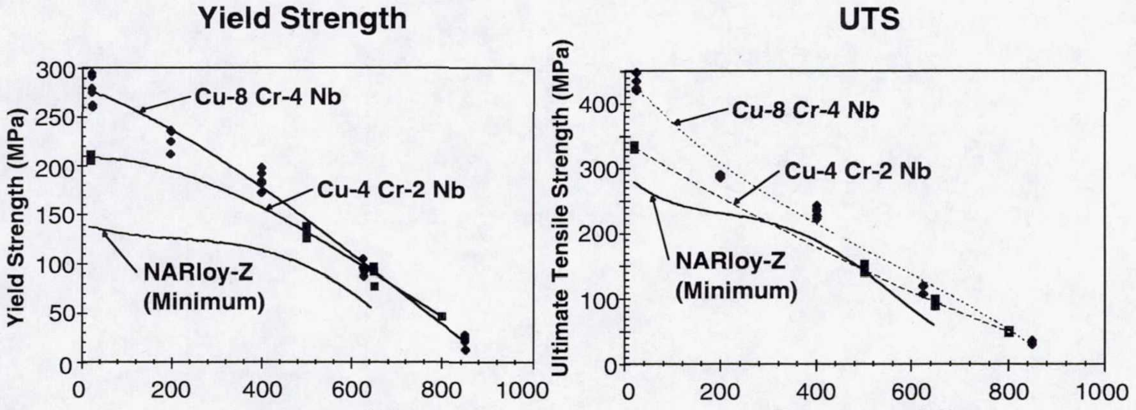

- Cu-Cr-Nb alloys have yield strengths approximately 1.5 - 2X higher than NARloy-Z
- Cu-8 Cr-4 Nb has a superior UTS compared to NARloy-Z
  - Cu-4 Cr-2 Nb has equal or better UTS than NARloy-Z

Fig. 8

Typical Creep Curves

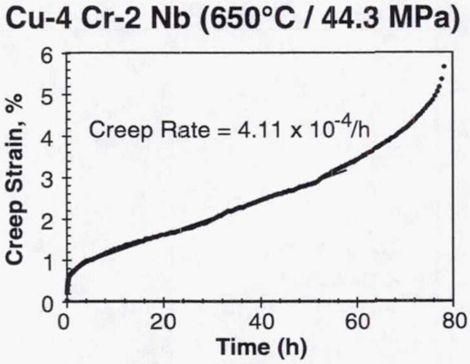

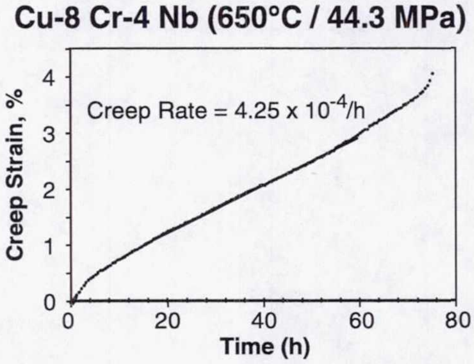

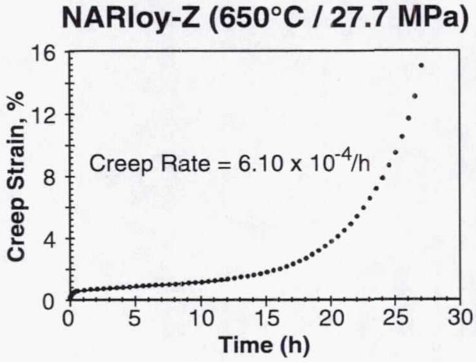

- Cu-Cr-Nb alloys spend the majority of their lives in Second Stage creep
- NARloy-Z can spend a significant portion of its life in Third Stage creep
- Cu-Cr-Nb creep elongations are generally lower than those of NARloy-Z

Fig. 9

Comparison Of Cu-Cr-Nb And NARloy-Z Creep Lives

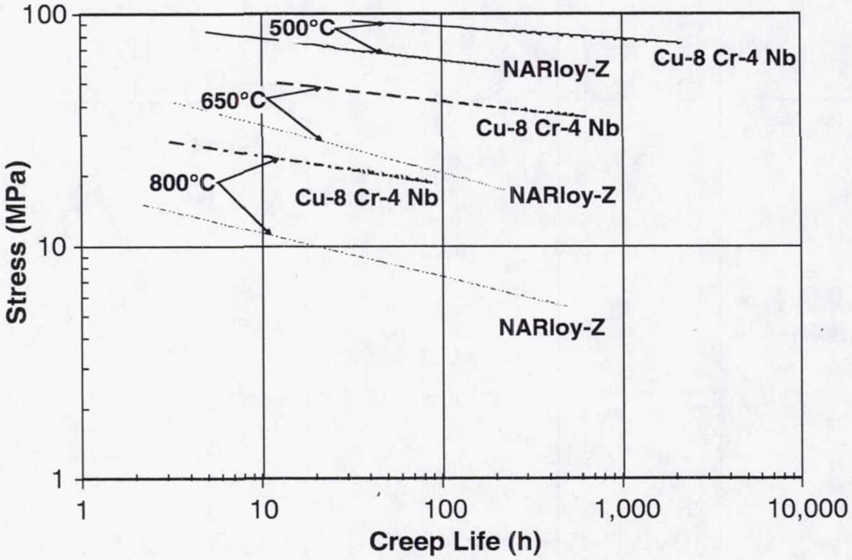

- Cu-4 Cr-2 Nb lives are approximately half that of Cu-8 Cr-4 Nb
- For a given life, Cu-8 Cr-4 Nb can support 20%+ higher stresses
- For a given stress, Cu-8 Cr-4 Nb alloy has lives 2 to 3 orders of magnitude longer than NARloy-Z

Fig. 10

Typical Cu-8 Cr-4 Nb LCF Loops

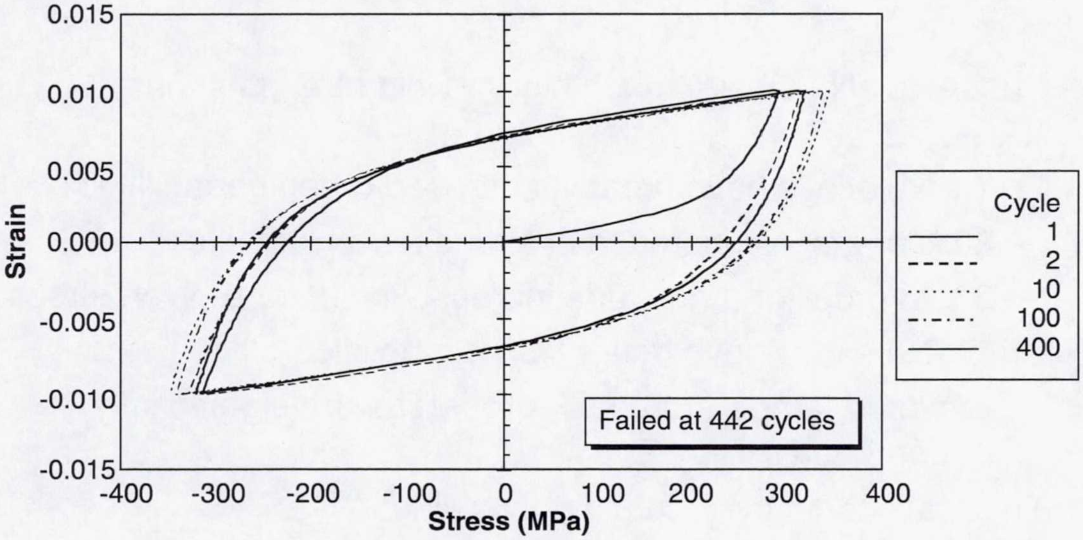

Room Temperature (Sample 1-1)

- Some strain hardening of Cu-8 Cr-4 Nb occurs
  - Not as much as Cu
- Consistent behavior up to failure

Fig. 11

Low Cycle Fatigue Lives

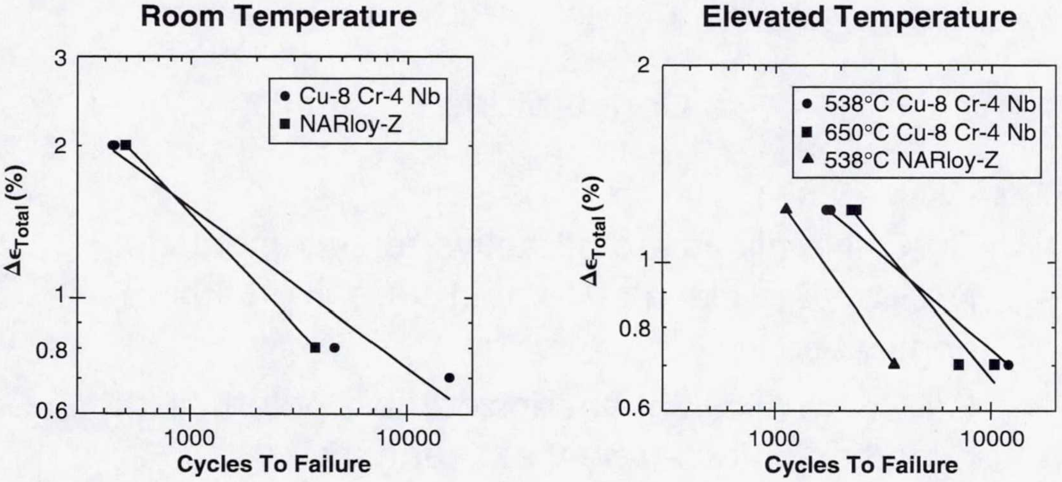

- Cu-8 Cr-4 Nb at least as good as NARloy-Z at room temperature
- Cu-8 Cr-4 Nb has 50% to 200% greater LCF life at 538°C (1000°F) than NARloy-Z
  - No significant difference between 538°C and 650°C (1202°F) Cu-8 Cr-4 Nb LCF lives

Fig. 12

Summary

- Cu-Cr-Nb alloys have much higher yield strengths than NARloy-Z
- Cu-Cr-Nb alloys have greatly increased creep capabilities
  - 20% or greater increase in stress for a given life
  - 2 to 3 order-of-magnitude increase in life for a given stress
- Cu-Cr-Nb alloys have better LCF capabilities
  - Elevated temperature LCF properties are significantly better than NARloy-Z
- Thermal conductivity data set available in NASA CR-198529

Fig. 13

Conclusions

- Cu-Cr-Nb alloys are attractive replacements for NARloy-Z in elevated temperature, high flux applications
- Cu-Cr-Nb alloys offer considerable potential for hypersonic aircraft heat exchangers

Fig. 14

Future Work

- Complete NARloy-Z tensile testing
- Perform microscopy on LCF samples
- Determine strengthening mechanism(s) by further TEM analysis
- Examine oxidation resistance of Cu-Cr-Nb alloys
  - Air
  - Water saturated air
  - Possible mixed $O_2/H_2/H_2O/CO/CO_2$ environment representative of hydrocarbon fueled engine
- Determine suitable rolling schedule and heat treatments to produce Cu-Cr-Nb sheet

Fig. 15

$MoSi_2$–BASE COMPOSITE FOR ENGINE APPLICATIONS

MOHAN G. HEBSUR
NYMA Inc.
Brookpark, Ohio

and

Michael V. Nathal
NASA Lewis Research Center
Cleveland, Ohio

Introduction

The intermetallic compound $MoSi_2$ has long been known as a high temperature material that has excellent oxidation resistance and electrical/thermal conductivity. Also its low cost, high melting point (2023 °C), relatively low density (6.2 g/cm^2 versus 8 g/cm^2 for current engine materials), and ease of machining make it an attractive structural material (ref. 1). However, the use of $MoSi_2$ has been hindered because of the brittle nature of the material at low temperatures, inadequate creep resistance at high temperatures, accelerated oxidation (also known as "pest" oxidation) at temperatures between approximately 400 and 500 °C, and a coefficient of thermal expansion (CTE) that is relatively high in comparison to potential reinforcing fibers such as SiC. This CTE mismatch between the fiber and the matrix resulted in severe matrix cracking during thermal cycling.

Maloney and Hecht (ref. 2) have done extensive work on the development of continuous-fiber-reinforced $MoSi_2$-base composites to achieve high temperature creep resistance and room temperature toughness. Candidate fibers consisted of ductile refractory metal fibers and high strength ceramic fibers. Refractory metal fiber reinforcement of $MoSi_2$ matrix composites was shown to increase both creep strength and fracture toughness. The addition of about 40 vol % of SiC in the form of whiskers and particulate was shown to lower the thermal expansion of $MoSi_2$-base matrix and prevent matrix cracking in a refractory fiber-reinforced composite. However, there was a severe reaction between refractory fibers and the matrix. Matrix cracking was observed during consolidation with an SCS-6-fiber-reinforced composite, even with the matrix containing up to 40 vol % SiC (40SiC) to modify thermal expansion. The SCS-6/$MoSi_2$-40SiC composite survived five thermal cycles at 1300 °C but was completely destroyed within 100 hours of exposure to air at 500 °C.

The pesting phenomenon was caused by the formation of voluminous Mo oxides in the microcracks. During the accelerated oxidation, MoO_3 and SiO_2 were simultaneously formed in amounts determined by their concentrations in the intermetallic. The accelerated oxidation is a necessary, but not sufficient, condition for pesting. Recent improvements in the fabrication of $MoSi_2$ have led to materials with less porosity that are correspondingly less susceptible to pest attack. However, because of increased surface areas and fabrication complexities from incorporating reinforcement phases in $MoSi_2$-based composites, pesting of composite materials is still a major concern.

Earlier work (ref. 3) to develop a $MoSi_2$ matrix suitable for SiC fiber reinforcement was carried out at NASA Lewis under the High Speed Civil Transport Enabling Propulsion Materials (HSCT/EPM) program. In that work, the addition of about 30 to 50 vol % of thermodynamically stable Si_3N_4 particulate was found to improve the low temperature accelerated oxidation resistance of $MoSi_2$ by forming a Si_2ON_2 protective scale, which eliminated the catastrophic pest failure. The Si_3N_4 addition doubled the low temperature toughness and increased the high temperature creep resistance of $MoSi_2$ by 5 orders of magnitude. More important, adding Si_3N_4 significantly lowered the CTE of the $MoSi_2$ and eliminated matrix cracking in SCS-6 reinforced composites, even after thermal cycling. These encouraging preliminary results led to a joint program for further development between Pratt & Whitney, the Office of Naval Research, and NASA Lewis. The overall aim of this long-range program is to develop these composites for advanced aircraft engine applications so that they can compete with the current superalloys and other advanced materials, primarily ceramic matrix composites (CMC's, see Fig. 1). A turbine blade outer air seal (BOAS) for the Pratt & Whitney ATEGG/JTD engine demonstrator was chosen as the first component upon which to focus. This paper briefly describes the progress made so far in developing $MoSi_2$-base hybrid composites.

Microstructure and Properties of SCS-6/$MoSi_2$-Base Composites

Figure 2 shows the transverse microstructure of the as-fabricated SCS-6 composite. Although in this case fiber distribution was not uniform, Fig. 2 clearly indicates an absence of matrix cracking. The CTE measurements made on the matrix-only plate and those made on the composites are plotted as a function of temperature in Fig. 3. The CTE's of monolithic $MoSi_2$, Si_3N_4, and SiC (ref. 2) are also included in this figure. It is clear from Fig. 3 that adding Si_3N_4 to $MoSi_2$ effectively lowered the CTE of the matrix, thereby reducing the CTE mismatch with the fibers; hence, no matrix cracks were found in the composite (Fig. 2). Figure 4 shows the SCS-6/$MoSi_2$ and SCS-6/$MoSi_2$-$30Si_3N_4$ composites exposed at 500^0 C. The SCS-6/$MoSi_2$ specimen, which had matrix cracks, was completely destroyed; it turned into powder within 24 cycles, whereas the SCS-6/$MoSi_2$-30 Si_3N_4 specimen was intact even after 200 cycles and did not show any pest oxide.

Figure 5 plots the load verses time for the SCS-6/$MoSi_2$-$30Si_3N_4$ monolithic, chevron-notched, 4-point- bend specimens tested at room temperature (RT). Even after testing for 2 hours, the composite specimen did not break. The critical stress intensity factor K_q, calculated from the maximum load data, was greater than 35 $MPa \bullet m^{0.5}$. This indicates that the composite specimen was seven times tougher than the monolithic material. The toughness of the hybrid composite also increased with temperature, reaching as high as 65 $MPa \bullet m^{0.5}$, at 1400 °C in an argon atmosphere. Charpy impact tests were conducted on ASTM standard specimens of the $MoSi_2$-$50Si_3N_4$ matrix and the SCS-6/$MoSi_2$-$50Si_3N_4$ hybrid composite between 23 (RT) and 1400 °C in air. The force-verses-time curves obtained from the Charpy impact tests indicate that much more energy is required for crack initiation in the composite specimens and that substantial energy is absorbed during crack propagation. The impact test results also showed that the impact resistance increased with an increase in temperature, and fiber reinforcement improved resistance by nearly five times, from 2.5 to 12 J (almost equal to cast Ni-base super alloys). The impact resistance of both the monolithic and the hybrid composite was superior to any material in the literature data on high temperature intermetallic or ceramic-based materials (Fig. 6).

In Fig. 7 the RT tensile stress-strain curve for SCS-6/$MoSi_2$-Si_3N_4 indicates composite-like behavior and three distinct regions: an initial linear region, followed by a nonlinear region, and a second linear region. The nonlinear region is due to matrix-cracking normal to the loading direction. The second linear region is controlled by fiber bundle strength. The carbon layer on SCS-6 fibers appears to have a significant influence on mechanical properties, particularly the tensile strain to fracture, which is a measure of composite toughness. The RT tensile stress-strain curves shown in Fig. 7 clearly demonstrate not only improved strength and toughness but also a graceful failure due to fiber pull-out. Tensile tests showed the temperature dependence of the ultimate tensile strength (see Fig. 8). For comparison, the data from SCS-6/RBSN (ref. 4) are also included. The $MoSi_2$ composite exhibits higher strength than SCS-6/RBSN at temperatures up to 900 °C; beyond that, it starts losing strength. Unlike CMC's, which have about 20 percent porosity, the $MoSi_2$-base composite is fully dense in the as-fabricated condition and, hence. exhibits a higher modulus than CMC's do. Preliminary results of stress rupture tests carried out on SCS-6 [0°]/$MoSi_2$-$50Si_3N_4$ composite specimens between 1000 and 1200 °C in vacuum indicated that this material is superior to Ni-base superalloys but inferior to monolithic ceramics such as AS 800 (AlliedSignal). A specimen tested at these temperatures exhibited the classical creep curve with a minimum creep rate of $2x10^{-9}$ sec $^{-1}$.

Advanced Processing and Fibers for Low Cost and Complex Shaped $MoSi_2$-Base Composites

Most of the outstanding strength and toughness values reported thus far were achieved with composites reinforced with SCS-6 fibers. This fiber does not have adequate creep strength at the high temperatures envisioned for $MoSi_2$, and it is too large to be bent around the sharp radii needed to make complex shapes. Finer diameter fibers would offer better cost, shape-making, creep resistance, and toughness properties. Hi-Nicalon (Nippon Carbon) is currently the best available fiber, although NASA's EPM program is developing improved SiC fibers that would be appropriate for a $MoSi_2$-Si_3N_4 matrix. In earlier studies, we used the powder cloth technique to produce composites. However, because this process is highly labor intensive and does not produce uniform fiber distribution, we recently switched to tape casting as the powder/metallurgy method for composite fabrication. Melt infiltration and chemical vapor infiltration are popular methods for processing of CMC's because of the potential for shape making and the lower cost, but they cannot produce thickness larger than 0.25 in. Problems with segregation and porosity are also aggravated in thick specimens made by these techniques. However, composites with small diameter fibers, such as SCS-9-reinforced (75-um diam.) and coated Hi-Nicalon-reinforced (18- to 20-um diam.) $MoSi_2$-Si_3N_4 composites were successfully fabricated in thickness greater than 0.4 in. Figure 9(a) clearly illustrates the range in fiber diameter in this study. Note how switching from powder cloth to tape casting improved the fiber spacing control. Figure 9 (b) displays efficient spreading of the fiber tows and infiltration of $MoSi_2$-Si_3N_4 powder particles.

As part of a study to investigate the influence of fiber diameter and architecture on mechanical behavior, tensile and fracture toughness tests were conducted on specimens of SCS-6-, SCS-9-, and BN/SiC-coated Hi-Nicalon/$MoSi_2$-$50Si_3N_4$ hybrid composites at RT (Fig. 10 (a) and (b)). Testing in the [0°] direction produced the highest strength (700 to 1000 MPa) and total strain (1.2 percent) to failure. Testing in the [90°] direction produced the lowest ultimate tensile strength, only 72 MPa, and strain (0.04 percent) to failure fora SCS-6-reinforced composite. The Hi-Nicalon-reinforced composite exhibited high strength and strain to failure in the [0°/90°] direction (about 60 percent of unidirectional values). RT fracture toughness also followed the same trend (Fig. 10 (a)). The SEM micrograph of fracture surfaces shows more fiber pullout in the Hi-Nicalon-reinforced composite than in the SCS-6 reinforced composite (Fig. 10(b)). The Hi-Nicalon/$MoSi_2$-Si_3N_4 in the [0°/90°] direction has a higher fracture toughness value than Hi-Nicalon/SiC, the CMC's, and Hi-Nicalon/Si_3N_4 in the [0°] direction (see Fig. 10 (c)). Because the CMC's were processed at much higher temperatures, the fibers were degraded, thereby decreasing the toughness; Hi-Nicalon/$MoSi_2$-Si_3N_4 was processed at lower temperatures and, therefore, exhibited lower toughness.

Conclusions

A wide spectrum of mechanical and environmental properties have been measured in order to establish feasibility of an $MoSi_2$-base composite with Si_3N_4 particulate and SiC fibers.The high impact resistance of the composite is of particular note , as it was a key property of interest listed by Pratt & Whitney. Processing issues have also been addressed in order to lower cost and improve shape making capability. These results indicate that this composite system remains competitive with other ceramics as potential replacement for superalloys.

Acknowledgments

The authors would like to acknowledge the Office of Naval Research, Washington, DC, and Pratt & Whitney Aircraft, West Palm Beach, FL, for financial support. Help received from Drs. P. Bartolotta and M. Verrilli during mechanical testing is also gratefully acknowledged.

References

1. Vasudevan, A.K.; and Petrovic, J.J.: A Comparative Overview of Molybdenum Disilicide Composites: High Temperature Structural Silicides. Proceedings of the High Temperature Structural Silicides Workshop, Gaithersburg, MD, 1991, pp 1-17.

2. Maloney, M.J.; and Hecht, R.J.: Development of Continuous-Fiber-Reinforced $MoSi_2$ -Base Composites. Proceedings of the High Temperature Structural Silicides Workshop, Gaithersburg, MD, 1991, pp. 19-31.

3 Hebsur, M.G.: Pest Resistant and Low CTE $MoSi_2$ -Matrix for High Temperature Structural Applications. Mat. Res. Soc. Symp. Proc., vol. 350, 1994, pp. 177-182.

4. Bhatt, R.T.; and Phillips, R.E.: Laminate Behavior for SiC Fiber-Reinforced Reaction-Bonded Silicon Nitride Matrix Composites, NASA TM–101350, 1988.

5. Nakano, K. et al.: SiC- and Si_3N_4 -Matrix Composites According to the Hot-Pressing, High Temperature Ceramic-Matrix Composites II. Manufacturing and Materials Development, A.G. Evans and R. N. Nasalin, eds., American Ceramic Society, 1995, pp. 215-229.

$SiC/MoSi_2$ COMPOSITE
NASA/P&W/ONR PROGRAM

- **OVERALL OBJECTIVE:**
  To provide R & D support to complement Pratt and Whitney's larger effort of developing IMC Blade Outer Air Seals (BOAS) for ATEGG/JTD Engines.
- **SPECIFIC OBJECTIVE:**
  To investigate the technical feasibility of SiC continuous fiber reinforced $MoSi_2$-base hybrid composites (IMC). This material system offers the potential for improved properties over the current baseline SiC particulate reinforced $(MoW)Si_2$-system. The longer range goal is cost reduction through processing.

Fig. 1

SEM-BSI OF AS-FABRICATED SCS-6/$MoSi_2$-$30Si_3N_4$ COMPOSITE SHOWING NO MATRIX CRACKING

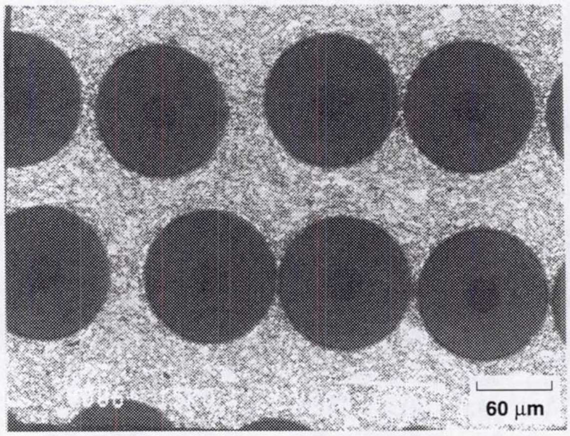

Fig. 2

CTE OF $MoSi_2$ REDUCED EFFECTIVELY BY THE ADDITION OF FINE Si_3N_4 PARTICULATE

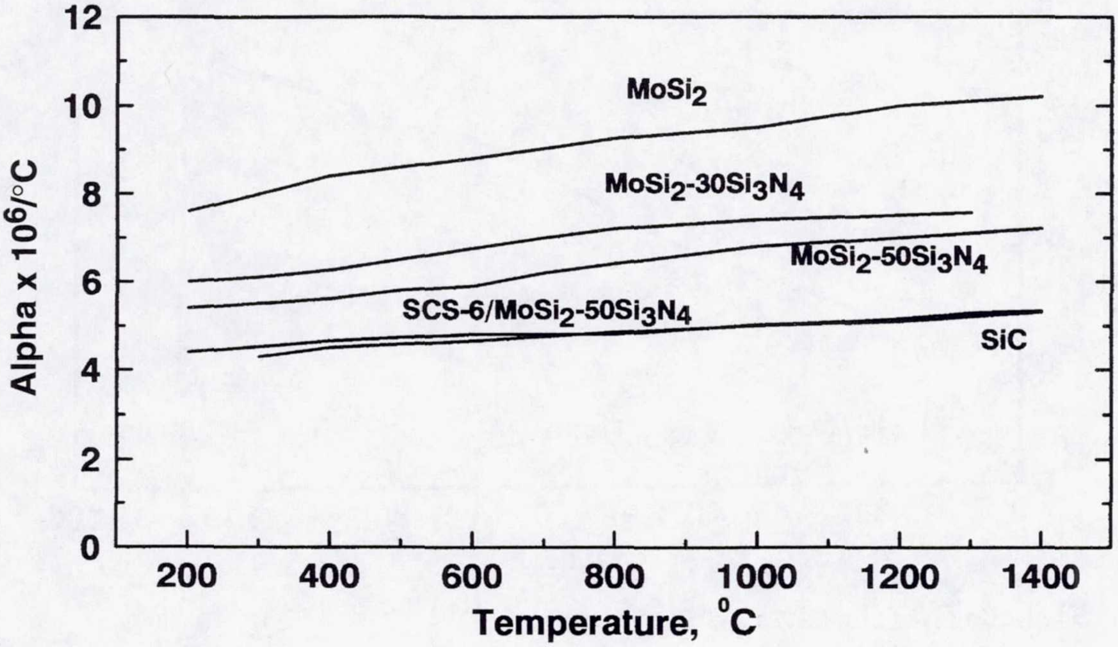

Fig. 3

SILICON NITRIDE ADDITION TOTALLY ELIMINATED PESTING IN MOLY DISILICIDE-BASE COMPOSITES

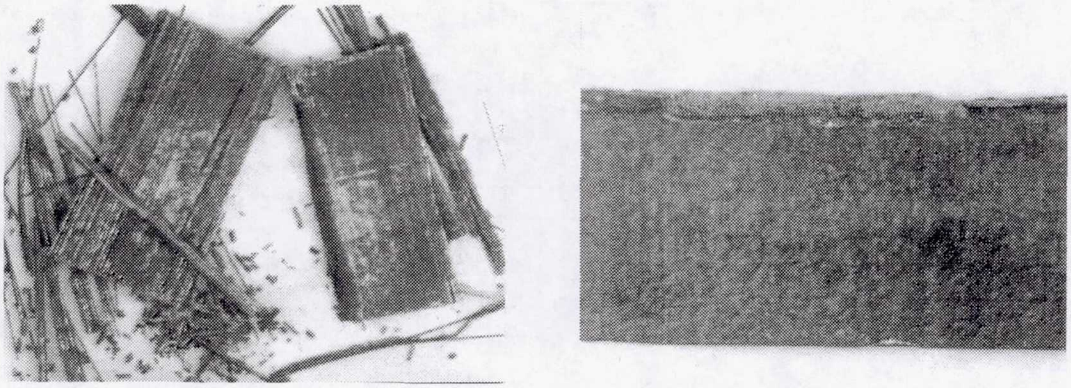

SCS-6/$MoSi_2$
500 °C/24 cycles
Pested

SCS-6/$MoSi_2$-Si_3N_4
500 °C/200 cycles
No pesting

Fig. 4

SCS-6/MoSi$_2$-Si$_3$N$_4$ COMPOSITE EXHIBITS SUPERIOR TOUGHNESS BEHAVIOR AT ROOM TEMPERATURE

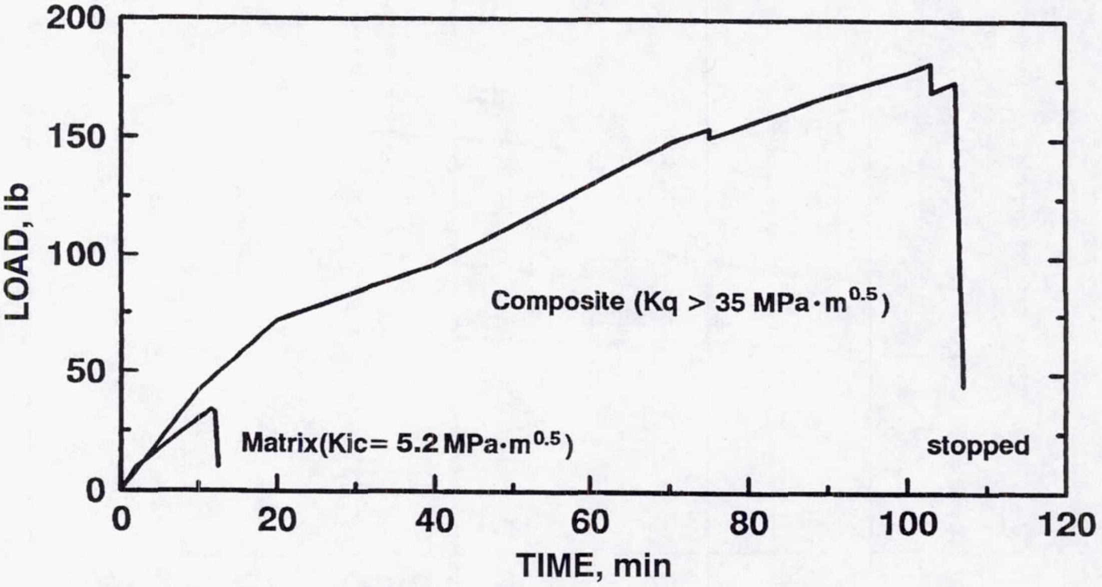

STRAIN RATE = 1.2×10^{-5} s^{-1}

Fig. 5

CVN ENERGY vs TEMPERATURE PLOT FOR MoSi$_2$-BASE COMPOSITES COMPARED WITH OTHER MATERIALS

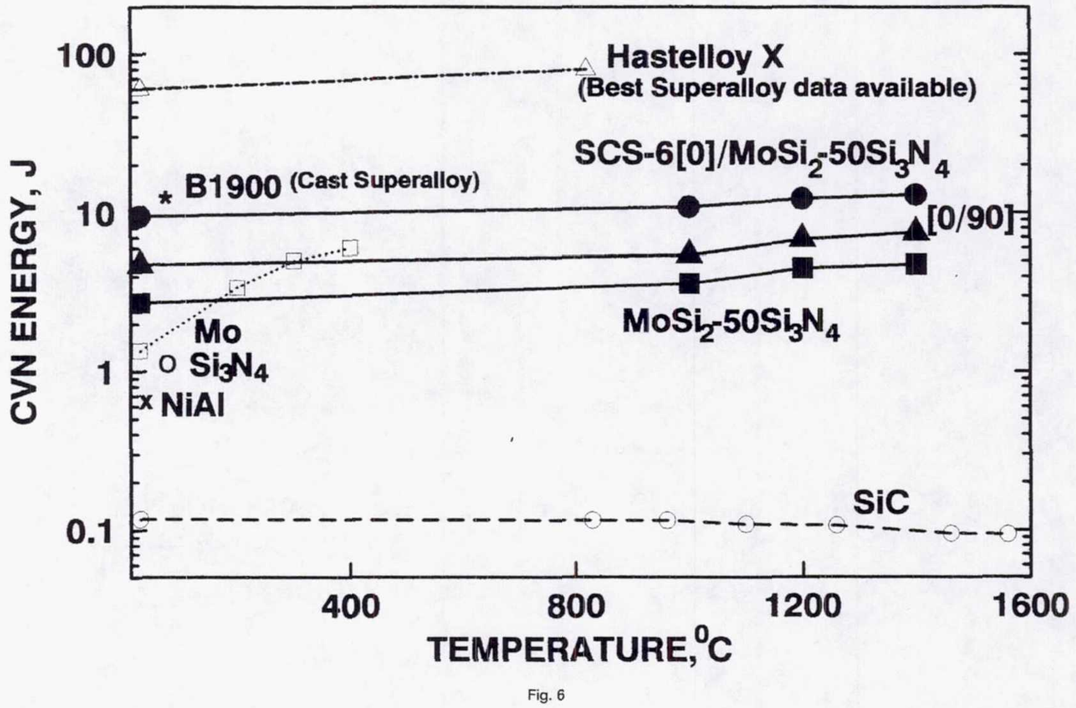

Fig. 6

ROOM TEMPERATURE STRESS-STRAIN CURVES FOR SCS-6/$MoSi_2$-$30Si_3N_4$ EXHIBIT A COMPOSITE LIKE BEHAVIOR

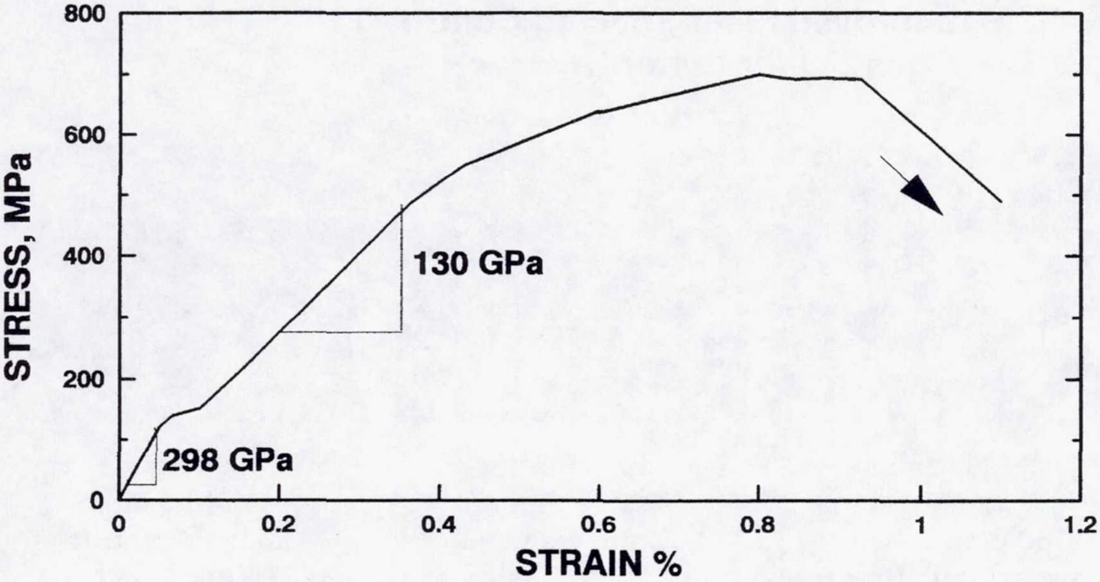

Fig. 7

TEMPERATURE DEPENDENCE OF ULTIMATE TENSILE STRENGTH OF SCS-6/$MoSi_2$-Si_3N_4 COMPOSITE

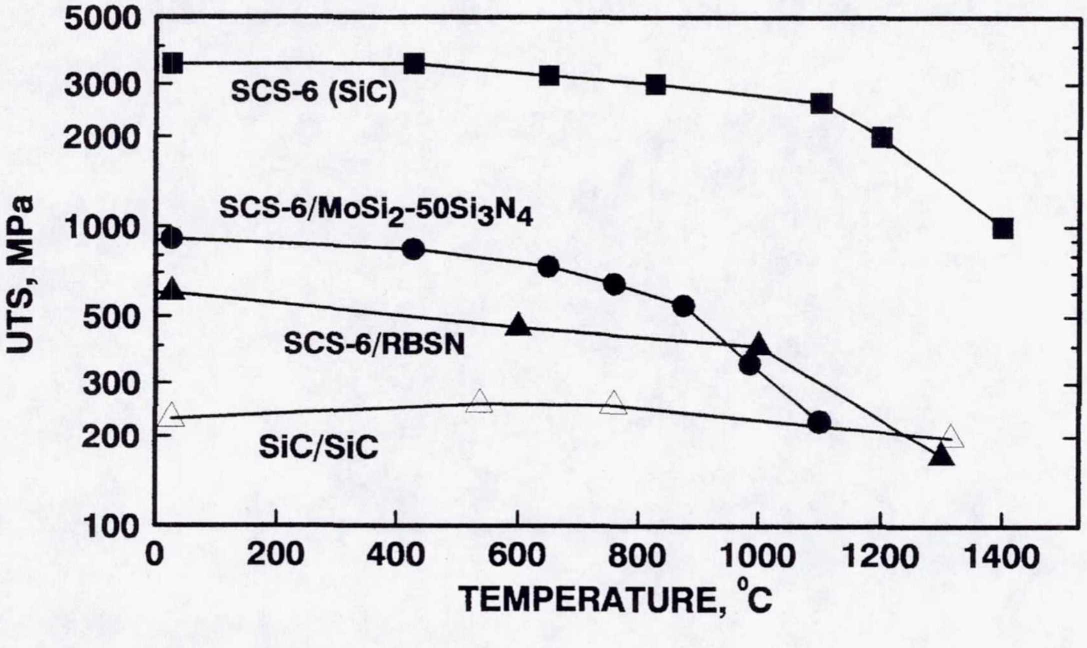

Fig. 8

PROCESS DEVELOPMENT FOR $MoSi_2$-Si_3N_4/SiC HYBRID COMPOSITES

- Finer Diameters for Near-Net Shape Capability
- Improved Fiber Spacing Control
- Potential for Lower Cost

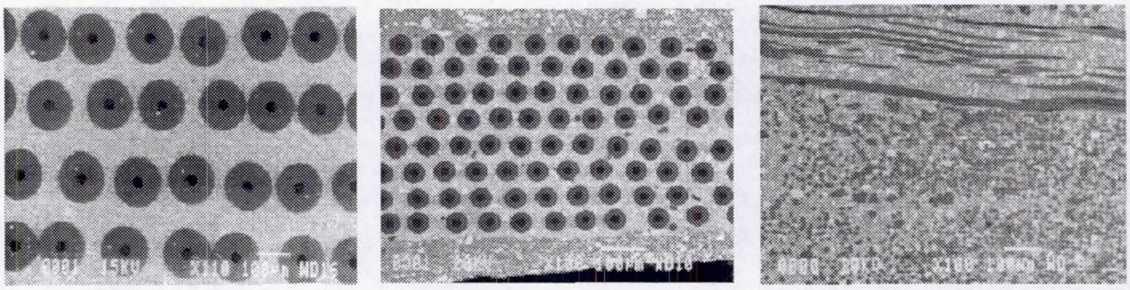

1993 Status	1995 Status	1995 Status
SCS-6 Fibers	SCS-9 Fibers	Hi-Nicalon
150 µm diameter	75 µm diameter	20 µm diameter
(Powder Cloth Process)	(Tape Cast)	(Tape Cast)

Fig. 9(a)

BN/SiC COATED Hi-NICALON/$MoSi_2$-$50Si_3N_4$ COMPOSITE SHOWING GOOD INFILTRATION

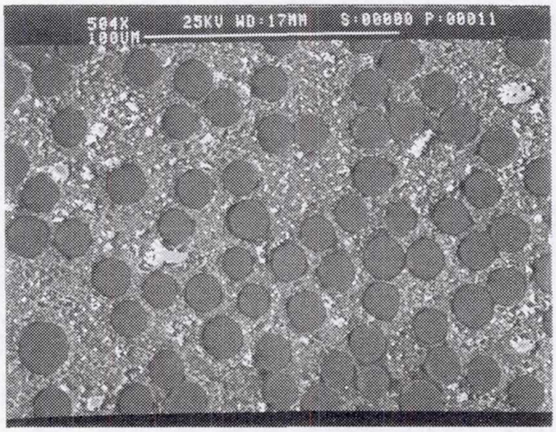

Fig. 9(b)

INFLUENCE OF FIBER DIAMETER AND ARCHITECTURE ON RT TENSILE STRENGTH OF $MoSi_2$-BASE COMPOSITES

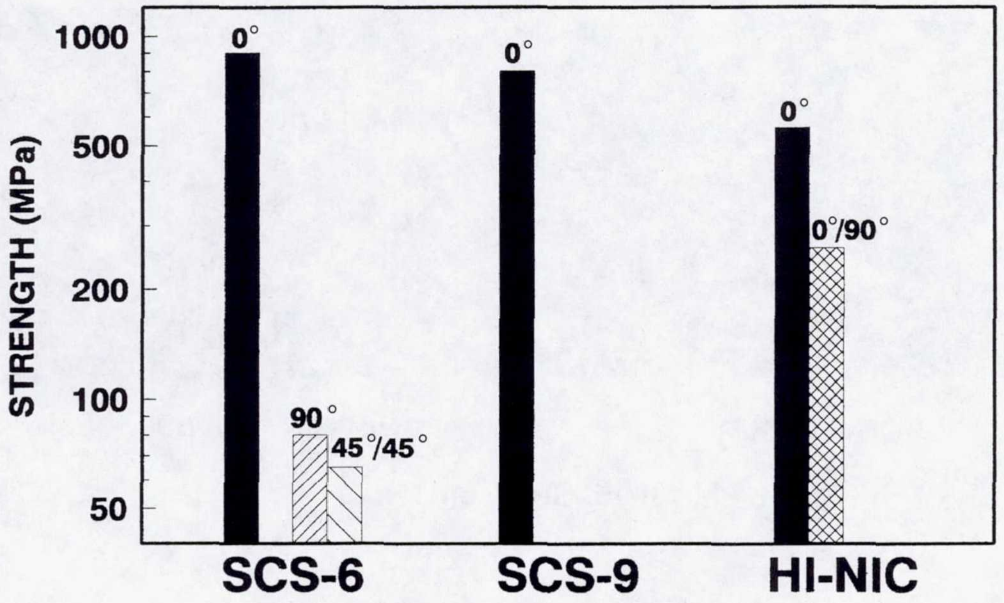

All single tests except triplicates of SCS-6[0]

Fig. 10(a)

INFLUENCE OF FIBER DIAMETER AND ARCHITECTURE ON RT FRACTURE TOUGHNESS OF $MoSi_2$-BASE COMPOSITES

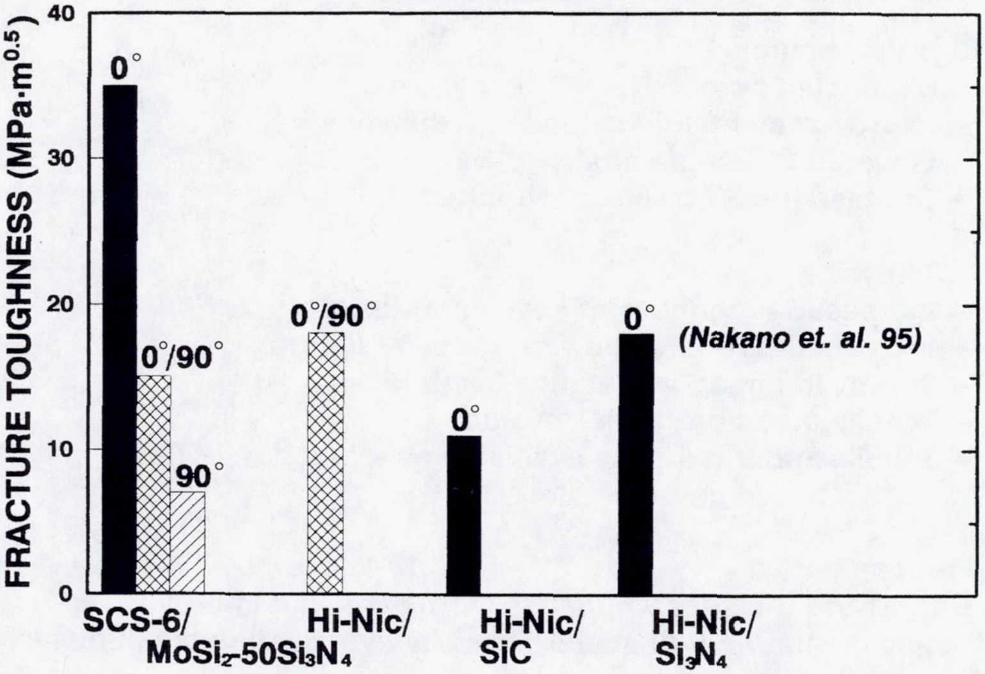

Fig. 10(b)

SEM-SE IMAGES OF RT FRACTURE TOUGHNESS TESTED SPECIMENS

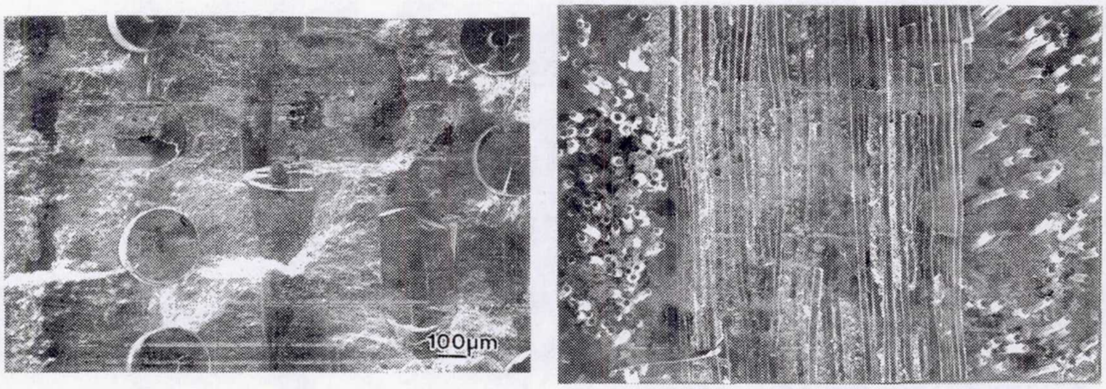

SCS-6 [0/90°] **BN/SiC/Hi-Nic [0/90°]**

$MoSi_2$-50Si_3N_4 MATRIX

Fig. 10(c)

SUMMARY

HYBRID COMPOSITE:
($MoSi_2$+Si_3N_4 particulate + continuous SiC fibers)

- **Si_3N_4 particulate**
  - **Eliminated pest**
  - **Improved creep and oxidation resistance**
  - **Lowered CTE and density**
  - **Doubled the RT fracture toughness**
- **SiC fibers**
  - **Increased toughness at all temperatures**
  - **Increased UTS and allowed "graceful failure"**
  - **Improved impact resistance five-fold**
  - **Tensile creep properties evaluated**
  - **Tensile and toughness evaluated as a function of fiber architecture and diameter**
- **Processing**

  Larger and thicker composites fabricated with improved fiber spacing and finer diameter fibers by tape casting technique

Fig. 11

CONCLUSION

- $MoSi_2$-base hybrid composites remain competitive with state-of-art ceramics as replacement for superalloys in jet engines

FUTURE PLANS

- *Continue exploring lower cost processing of hybrid composites*
- Continue $MoSi_2$-Si_3N_4 development
- Mechanical properties evaluation
- Optimizing fiber coatings

Fig. 12

MECHANICAL CHARACTERIZATION AND MICROMECHANICAL MODELING OF WOVEN CARBON/COPPER COMPOSITES[1]

BRETT A. BEDNARCYK[2] and Marek-Jerzy Pindera[3]
University of Virginia
Charlottesville, VA

David L. Ellis and Robert V. Miner
NASA Lewis Research Center
Cleveland, OH

Introduction

In recent years, interest in woven and braided composites has been on the rise. These materials consist of reinforcing fibers, or bundles of fibers called yarns, woven or braided into a desired preform prior to consolidation with traditional matrix materials. Woven and braided composites offer excellent out-of-plane impact and crack resistance while possessing far superior stability during manufacture compared to their traditional counterparts, Fig. 2.

The present investigation examines the in-plane mechanical behavior of a particular woven metal matrix composite (MMC); 8-harness (8H) satin carbon/copper (C/Cu). This is accomplished via mechanical testing as well as micromechanical modeling, Fig. 1. While the literature is replete with experimental and modeling efforts for woven and braided polymer matrix composites, little work has been done on woven and braided MMCs (ref. 1). Thus, the development and understanding of woven MMCs is at an early stage. 8H satin C/Cu owes its existence to the high thermal conductivity of copper and low density and thermal expansion of carbon fibers. It is a candidate material for high heat flux applications, such as space power radiator panels.

The experimental portion of this investigation consists of monotonic and cyclic tension, compression, and Iosipescu shear tests, as well as combined tension-compression tests. Tests were performed on composite specimens with three copper matrix alloy types: pure Cu, Cu-0.5 weight percent Ti (Cu-Ti), and Cu-0.7 weight percent Cr (Cu-Cr). The small alloying additions are present to promote fiber/matrix interfacial bonding (ref. 2, 3). The analytical modeling effort utilizes an approach in which a local micromechanical model is embedded in a global micromechanical model. This approach differs from previously developed analytical models for woven composites in that a true repeating unit cell is analyzed. However, unlike finite element modeling of woven composites, the geometry is sufficiently idealized to allow efficient geometric discretization and efficient execution.

Material System

Six plates with each matrix type were produced via pressure infiltration casting. The reinforcement phase was provided by Amoco, and it consisted of three layers of VCX-11 carbon fiber yarns woven in the 8H pattern (Fig. 3). The Cr and Ti matrix alloying additions have been shown to locate preferentially at fiber/matrix interfaces in C/Cu composites, allowing reaction and a superior bond (ref. 3). Fig. 4a

---

[1] Work funded under NASA Grant NAG3-1319.

[2] Ph.D. Candidate.

[3] Associate Professor.

shows an optical micrograph of a typical plate cross-section. Note the presence of porosity within the infiltrated fiber yarns (Fig. 4b).

Experimental Results

Fig. 5 shows the results of a typical monotonic tension test and a typical monotonic compression test on 8H satin C/Cu. The tensile response of the copper matrix and the carbon fiber (longitudinal and transverse) are included for comparison. In tension, the composite typically exhibited little elastic behavior and stiffened noticeably at higher strains. Failure in tension occurred by fracture of the matrix, leaving fiber yarns intact across the failure surface. In compression, the composite did not stiffen and failed at a lower stress and strain compared to tension. Failure occurred via microbuckling of the layers of the woven reinforcement. The apparent stiffer initial response in the compressive test compared to the tensile test (Fig. 5) is believed to be an artifact of the different specimens and test fixtures used in the different tests.

The effect of matrix alloy type on the monotonic tensile and compressive response of 8H satin C/Cu is shown in Fig. 6. Recall that the matrix alloying elements were added to improve fiber/matrix interfacial bonding, with the C/Cu-Cr composite possessing the best interfacial bond, followed by C/Cu-Ti, and finally by C/Cu. In tension, the observed trend in the three stress-strain curves is opposite that expected. That is, C/Cu-Cr, with its superior fiber-matrix bonding, would be expected to have the stiffest overall response, followed by C/Cu-Ti, and finally by C/Cu, which is not the case. In compression, on the other hand, the observed trend in the stress-strain curves follows the expected trend. Future work will attempt to explain these trends via detailed micromechanical modeling. Note in Fig. 6 that a greater amount of stiffening occurred in the alloyed-matrix composites compared to the C/Cu composite.

Fig. 7 shows the results of typical cyclic tension tests for composites with each matrix alloy type. Large amounts of hysteresis were present upon unloading for both the C/Cu-Cr and C/Cu composites. Examining the loading and unloading elastic modulus for each cycle revealed that the hysteresis is not caused by damage within the composite (ref. 1). It is believed that the hysteresis is caused by kinematic hardening of the matrix and frictional effects associated with sliding along the poorly-bonded fiber/matrix interface. The results of typical shear tests on 8H satin C/Cu composites with each alloy type are shown in Fig. 8. As was the case in compression, the shear stress-strain curves exhibited the trend expected based on the interfacial bond strength.

Model Results and Correlation

The model developed for this investigation consists of the original method of cells micromechanics model (ref. 4) embedded in the three-dimensional generalized method of cells (GMC-3D) micromechanics model (ref. 5) (Fig. 9). This embedded approach allows the global three-dimensional geometry of the woven composite to be represented by GMC-3D, while the local behavior of the infiltrated fiber yarns is modeled by the original method of cells. Matrix plasticity is included on the local level.

The simplest geometric representation of the repeating unit cell for an 8H satin woven composite is shown in Fig. 10a. Fig. 10b shows the next level of refinement in which the yarn cross-over regions are more accurately represented. The results presented herein are preliminary, generated using the simple geometry. Fig. 11 compares the predictions of the model with actual data from tension tests. Predictions are presented for the fully infiltrated case as well as the case in which the infiltrated fiber yarns contain 14% (by volume) porosity. Although experimental results for all three matrix alloy types are included, the model results should be compared with the C/Cu-Cr results since the present model treats the fiber and matrix as well-bonded. Hence, even when porosity is included the model overpredicts the tensile response of 8H satin C/Cu. Fig. 12 compares model predictions with the compressive response of the composite. In this case the model underpredicts the composite response, and inclusion of porosity degrades the correlation. Fig. 13 shows that in shear, the model significantly overpredicts the response of the composite. It is likely that the absence of fiber/matrix debonding in the model, which is probably present even in the C/Cu-Cr composite, accounts for a good deal of the discrepancy between the model and experiment. Other sources of the discrepancy include the coarse unit cell geometry used in the micromechanical model, and the absence of residual stresses from fabrication cool down.

Conclusions

The mechanical response of 8H satin C/Cu has been characterized via mechanical testing and micromechanical modeling. Tensile testing of the composite revealed a small elastic range, noticeable stiffening at higher strains, and large hysteresis loops upon unloading. The stiffening behavior has been attributed to straightening of the fiber yarns, while the hysteresis has been attributed to kinematic hardening of the matrix and frictional effects associated with the fiber/matrix interface. In tension, failure occurred by fracture of the matrix with the fiber yarns remaining intact. In compression, failure occurred via microbuckling, resulting in a lower ultimate strength and strain to failure than in tension, Fig. 14.

Comparing results for the three copper matrix alloy types with different degrees of fiber/matrix bonding showed that in tension, the observed trend in stress-strain curves is opposite to that expected. In compression and shear, however, the expected trend was observed. The unexpected behavior in tension may be due to a complex interaction of the microstructural architecture of the cross-over regions, fiber/matrix debonding, and residual stresses. These will be addressed in the future (Fig. 15, 16). Modeling the response of the composite was performed using a local/global embedding approach which allows an accurate yet efficient representation of the composite geometry. The model-experiment correlation was reasonably good for tension and compression, but poor for shear. Future work will involve improving this correlation via inclusion of fiber/matrix debonding, as well as other effects, in the model (Fig. 16), and utilizing a more refined unit cell geometry (Fig. 10b).

References

1. Bednarcyk, B.A.; Pauly, C.C.; and Pindera, M.-J.: Experimental Characterization and Micromechanical Modeling of Woven Carbon/Copper Composites. NASA CR-202318, 1997.

2. Ellis, D.L.: Properties of Graphite Fiber Reinforced Copper Matrix Composites for Space Power Applications. NASA CR-191026, 1992.

3. DeVincent, S.M.: Interfacial Effects on the Thermal and Mechanical Properties of Graphite/Copper Composites. NASA CR-198370, 1995.

4. Aboudi, J.: Micromechanical Analysis of Composites by the Method of Cells. App. Mech. Reviews, vol. 42, 1989, pp. 193-221.

5. Aboudi, J.: Micromechanical Analysis of Thermo-Inelastic Multiphase Short-Fiber Composites. NASA CR-195290, 1994.

Objectives

- Characterize the mechanical behavior of 8-harness (8H) satin C/Cu
  → Stress-strain response
  → Identification of factors affecting the behavior

  1. Mechanical testing
     - Tension tests (monotonic & cyclic)
     - Compression tests (monotonic & cyclic)
     - Combined tension-compression tests
     - Iosipescu shear tests (monotonic & cyclic)

  2. Micromechanical modeling: Embedded approach
     - Local model: Original Method of Cells
     - Global model: Three-Dimensional Generalized Method of Cells

Fig. 1

Woven Composites → Background

- Reinforcement → fabric woven from fiber or bundles of fibers (yarns)

- Simplifies handling during fabrication → fabric vs. individual fibers

- Near net-shaped woven or braided preforms

- Many different types of weaves:

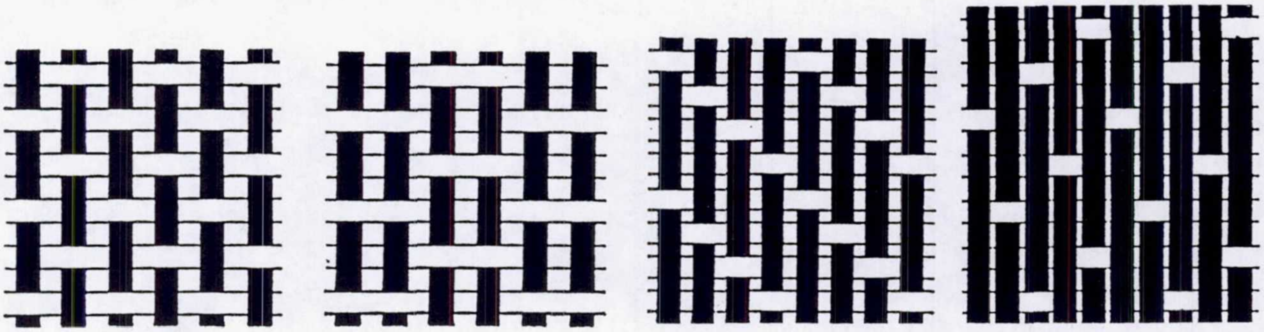

Plain Weave

2/2 Cord

3/1 Warp Twill

5-Harness Satin

Fig. 2

Material System → 8H Satin C/Cu

- Candidate for high heat flux aerospace applications: space power radiator panels
- 3 layers Amoco VCX-11 carbon fiber yarns of reinforcement woven in 8H satin pattern:

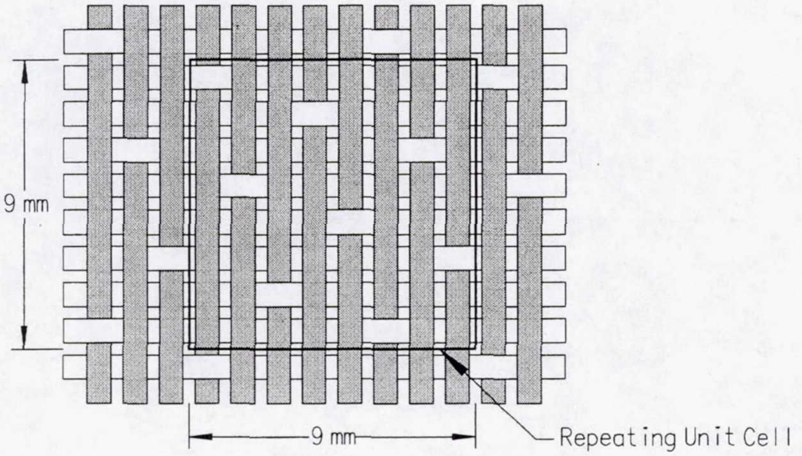

Fig. 3

Material System → 8H satin C/Cu

- Three Cu matrix alloy type: pure Cu, Cu-0.5 wt. % Ti, Cu-0.7 wt. % Cr
- Alloying additions present to improve fiber/matrix bonding, not to affect matrix mechanical properties
- Porosity present within infiltrated fiber yarns:

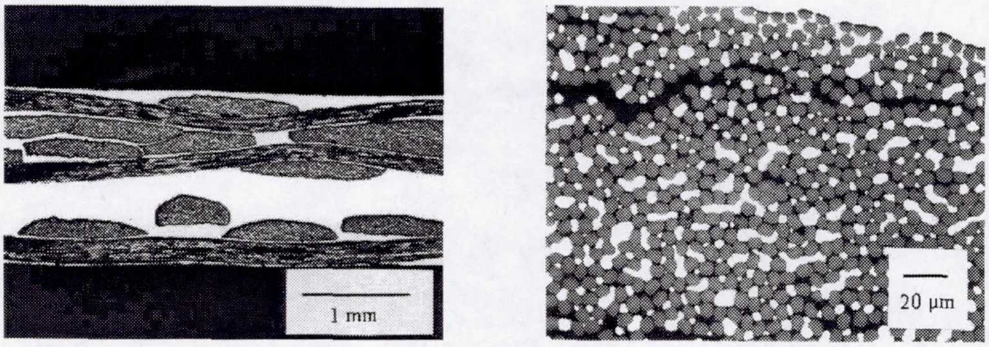

(a) (b)

Fig. 4

Experimental Results → Monotonic Tension & Compression

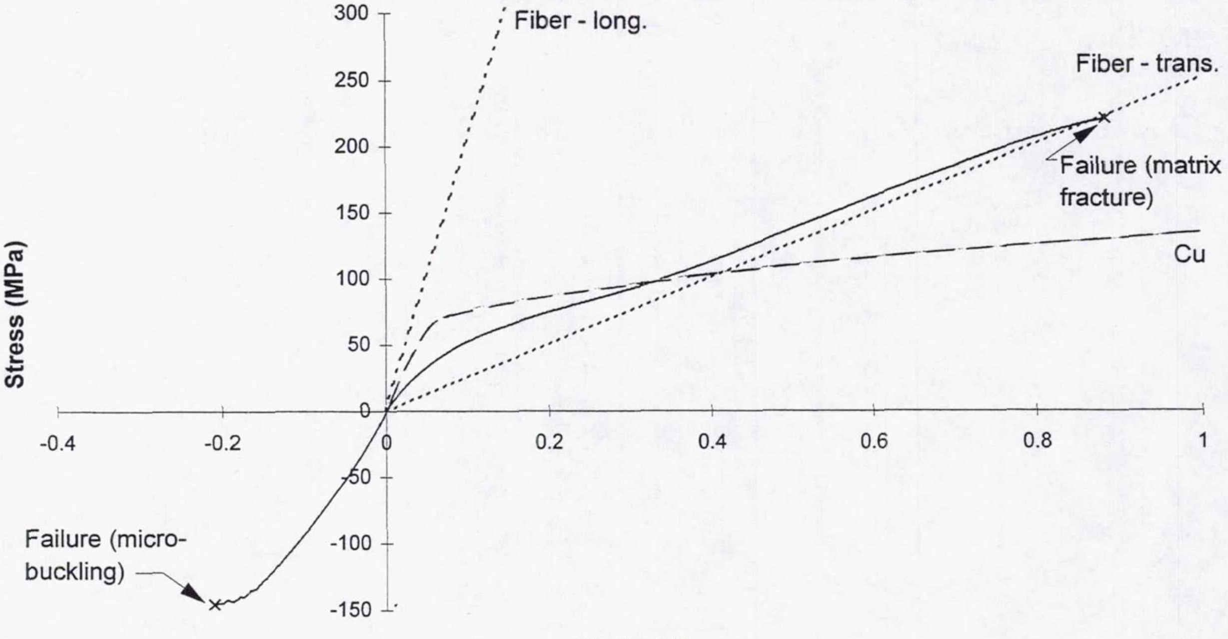

Fig. 5

Experimental Results → Monotonic Tension (Matrix Alloy)

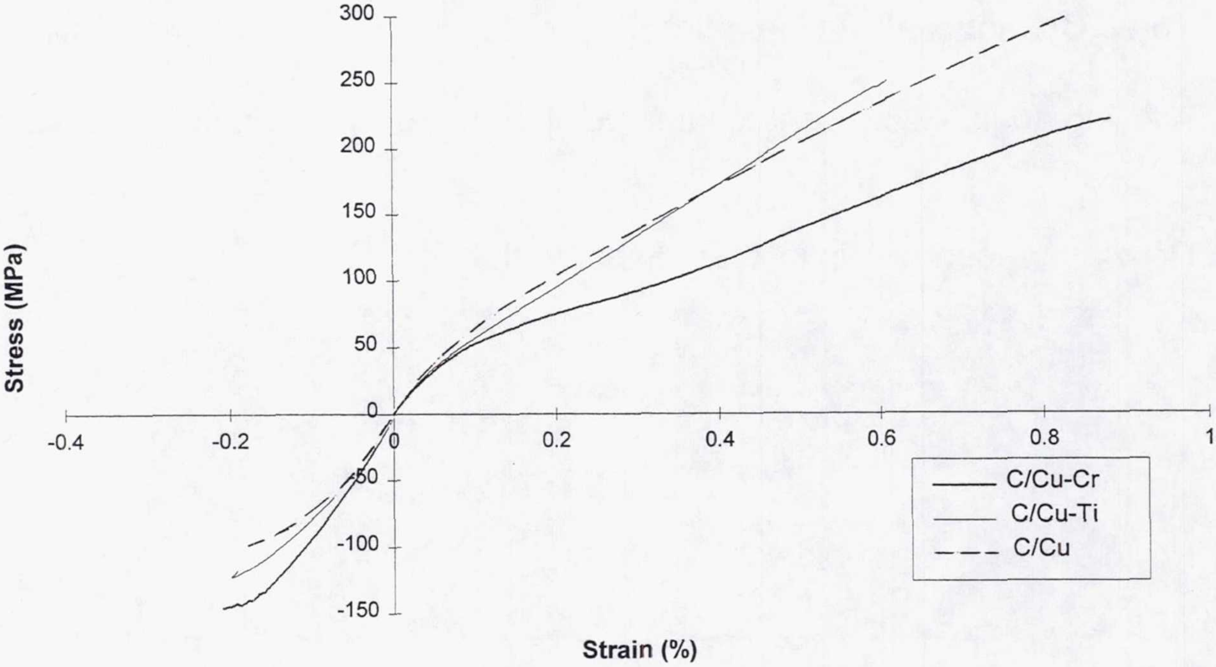

Fig. 6

Experimental Results → Cyclic Tension (Matrix Alloy)

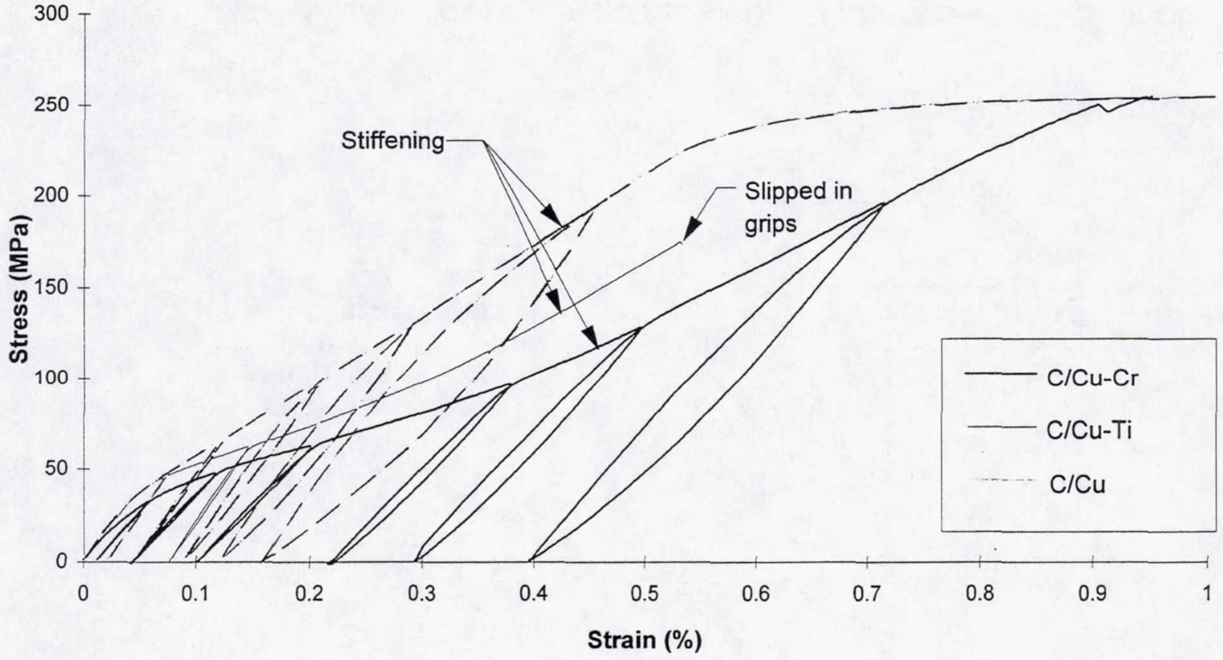

Fig. 7

Experimental Results → Monotonic Shear (Matrix Alloy)

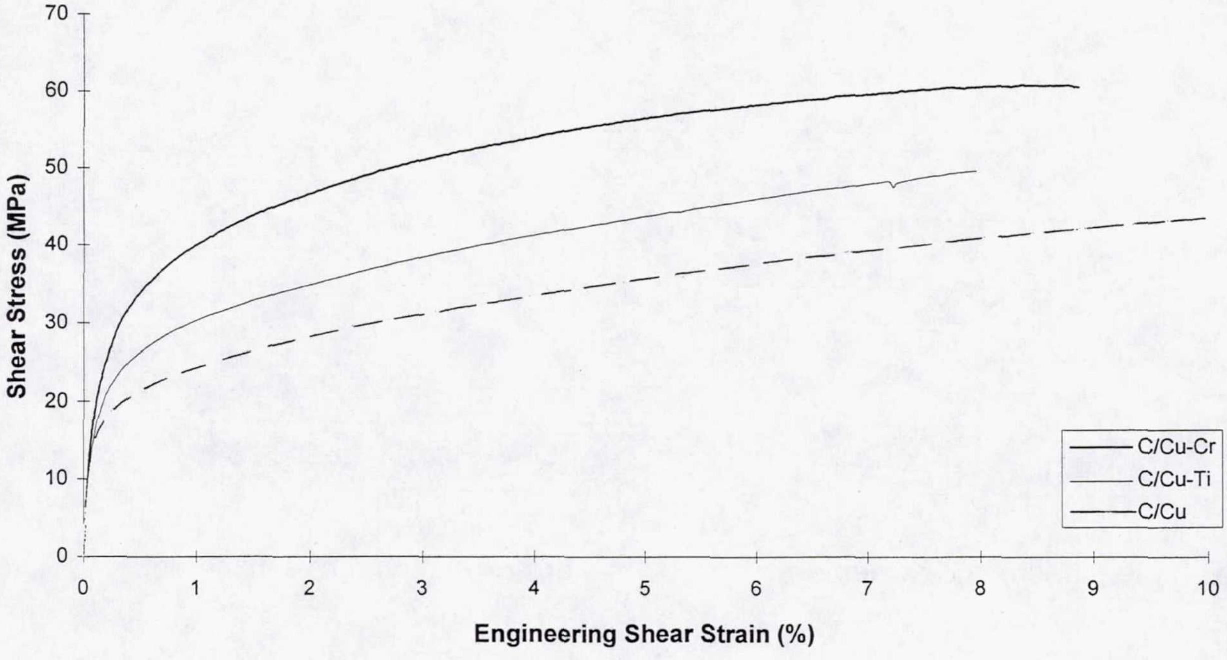

Fig. 8

Micromechanical Model → Approach

- Local model → original method of cells ➢ *embedded* ➣
- Global Model → GMC-3D

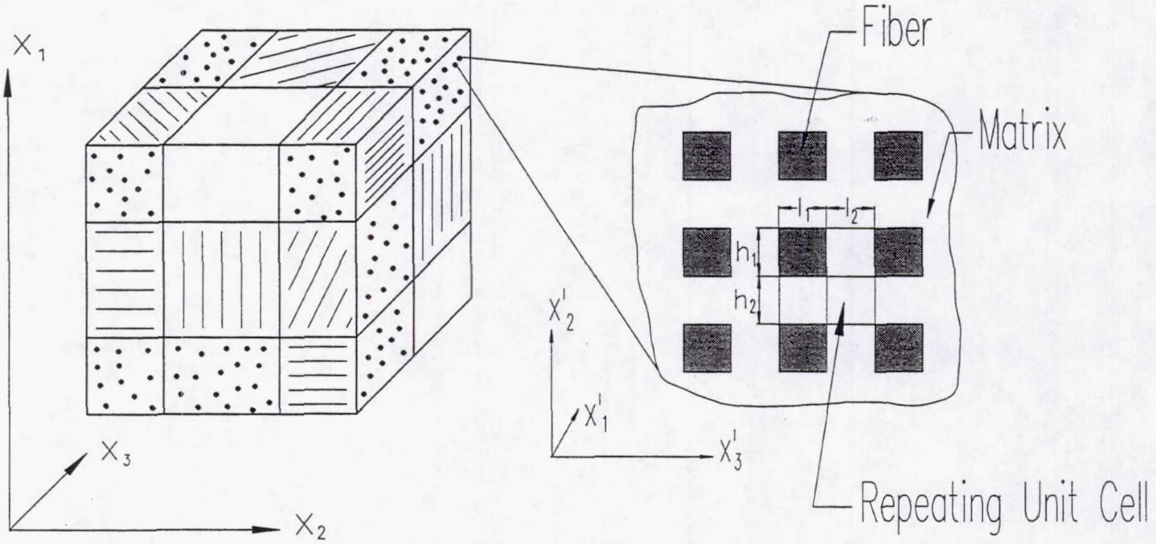

Fig. 9

Micromechanical Model → Repeating Unit Cells

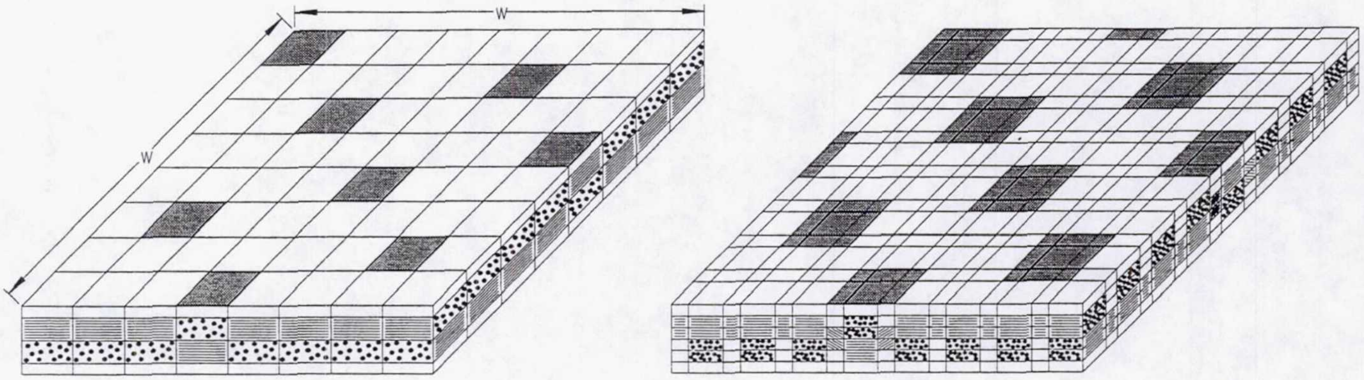

(a) Coarse geometric refinement

(b) Fine geometric refinement

Fig. 10

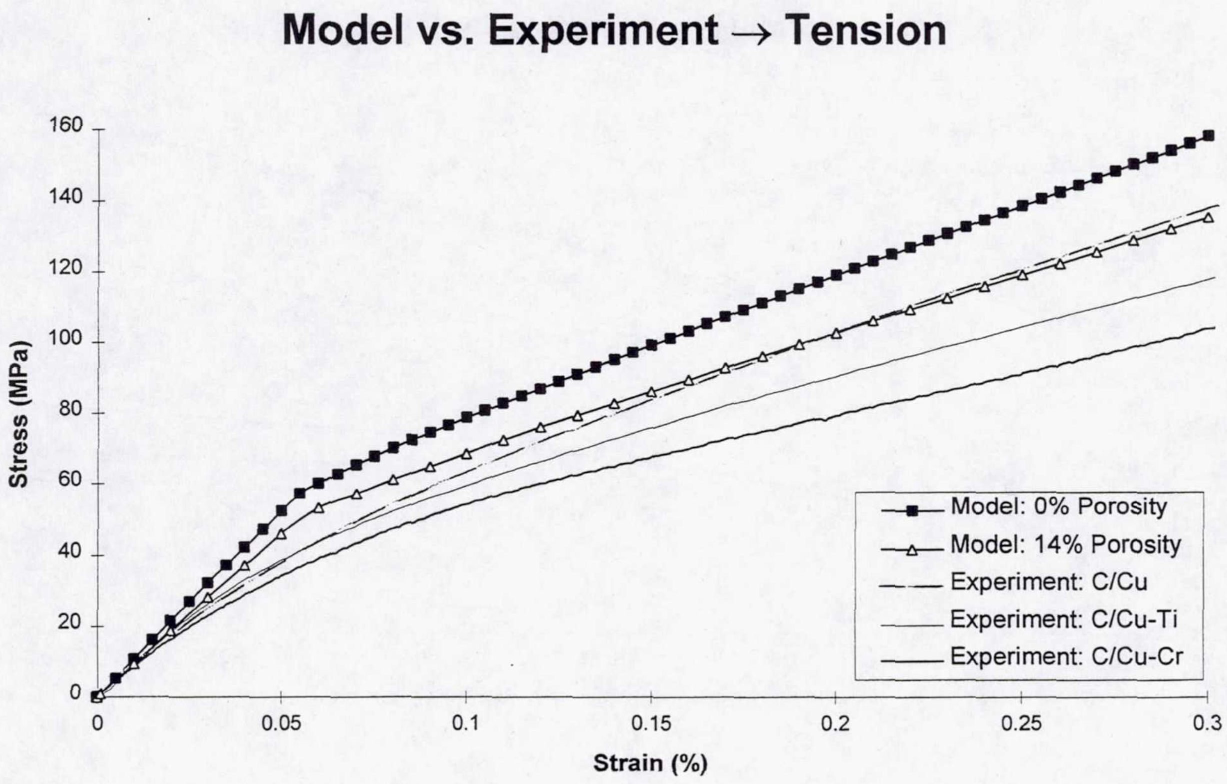
Model vs. Experiment → Tension
160
140
120
100
80
60
40
20
0
Stress (MPa)
0
0.05
0.1
0.15
0.2
0.25
0.3
Strain (%)
Model: 0% Porosity
Model: 14% Porosity
Experiment: C/Cu
Experiment: C/Cu-Ti
Experiment: C/Cu-Cr

Fig. 11

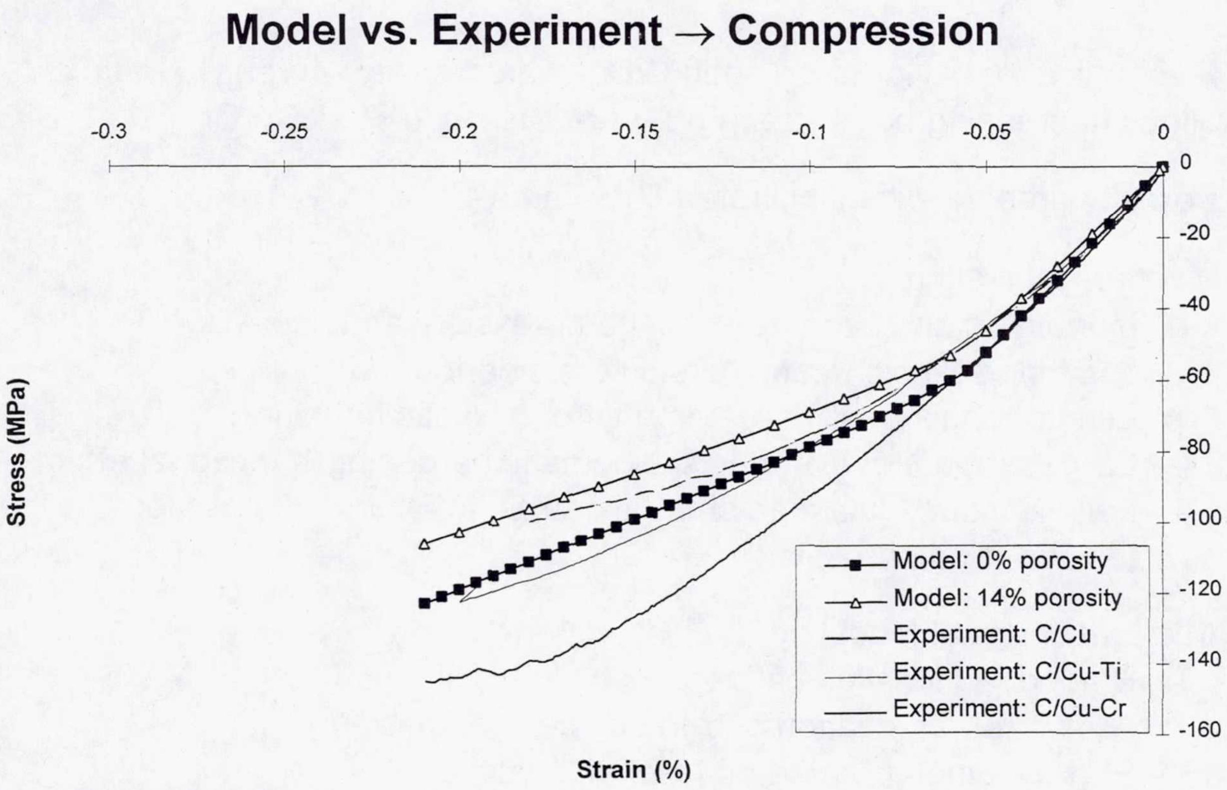
Model vs. Experiment → Compression
-0.3
-0.25
-0.2
-0.15
-0.1
-0.05
0
0
-20
-40
-60
-80
-100
-120
-140
-160
Stress (MPa)
Strain (%)
Model: 0% porosity
Model: 14% porosity
Experiment: C/Cu
Experiment: C/Cu-Ti
Experiment: C/Cu-Cr

Fig. 12

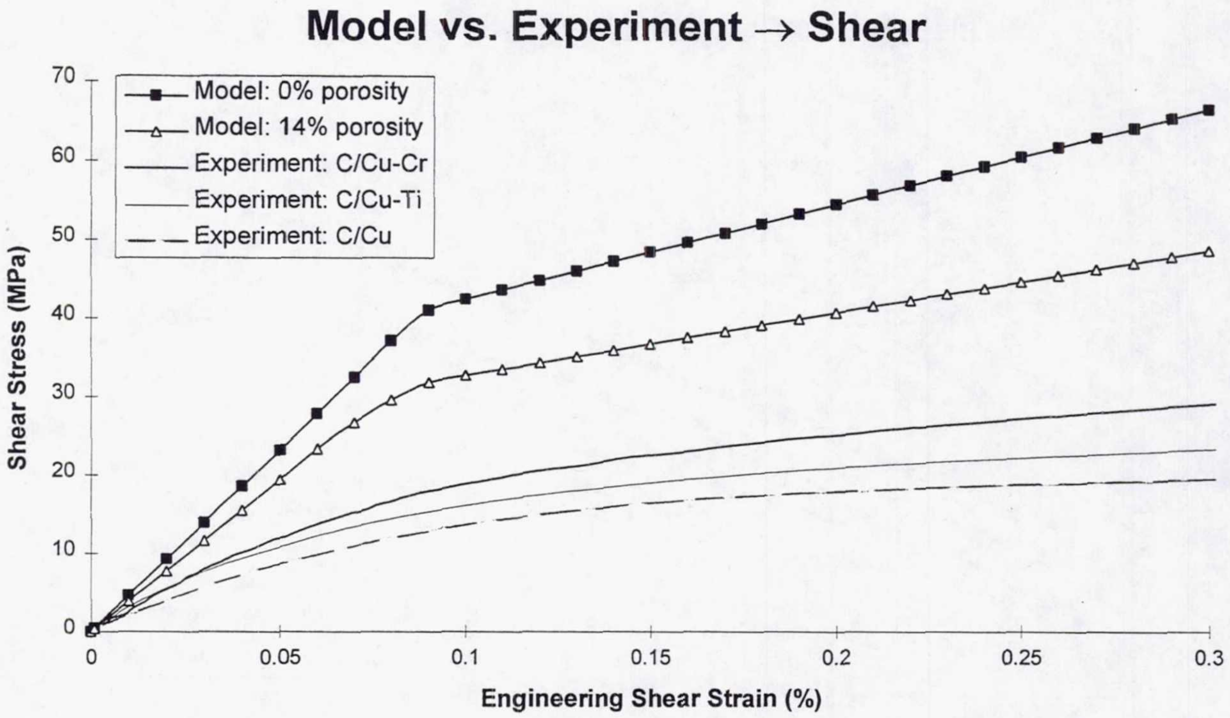

Fig. 13

Summary

- Mechanical behavior of 8H satin C/Cu characterized: three Cu matrix alloys (increasing bond strength): pure Cu → Cu-Ti → Cu-Cr
- Porosity present within infiltrated fiber yarns
- Mechanical testing:
  - → Monotonic and cyclic tension, compression, and shear and combined tension-compression tests performed
  - → Elastic range small, large amount of inelastic behavior
  - → Large amount of hysteresis: kinematic hardening & frictional effects
  - → Failure modes, ultimate strength, strain to failure different for tension & compression
- Micromechanical Modeling:
  - → Embedded local/global approach
  - → Allows representation of true unit cell geometry
  - → Plasticity incorporated on level of local model

Fig. 14

Conclusion

- Trend expected based on the fiber/matrix bond strength observed in compression and shear
- Trend opposite to that expected observed in tension

- Model predictions correlate reasonably well in tension and compression
- Model predictions are poor in shear

- To explain unexpected trend based on the fiber/matrix bond strength, and improve the model-experiment correlation, the following factors should be considered:

    → Fiber/matrix debonding
    → Porosity
    → Repeating unit cell geometric refinement
    → Residual stresses
    → Grip constraint effects (compression and combined tests only)

Fig. 15

Future Work

- Include fiber/matrix debonding in model

- Utilize more refined geometry in model

- Model residual stresses

- Model grip constraint effect for compression & combined tests

- Continued analysis of experimental results

Fig. 16

COMPUTATIONAL MODELING METHOD FOR SUPERALLOYS

GUILLERMO BOZZOLO
Ohio Aerospace Institute
and
Ronald D. Noebe and John Gayda
N.A.S.A. Lewis Research Center

Introduction

Computer modeling based on theoretical quantum techniques has been largely inefficient due to limitations on the methods or the computer needs associated with such calculations, thus perpetuating the notion that little help can be expected from computer simulations for the atomistic design of new materials. In a major effort to overcome these limitations and to provide a tool for efficiently assisting in the development of new alloys, we developed the BFS method for alloys (ref. 1), which together with the experimental results from previous and current research that validate its use for large-scale simulations, provide the ideal grounds for developing a computationally economical and physically sound procedure for supplementing the experimental work at great cost and time savings.

Background

The BFS method for alloys succeeds over other competing techniques in that it is not limited to any specific number of elements and it is not restricted to any particular crystallographic structure. These are major obstacles for other techniques, usually limited to the treatment of a few elements and just binary alloys. Moreover, other techniques only provide reliable results for bulk calculations offering little confidence in applications to extended defects (surfaces, interfaces). The BFS method is based on quantum perturbation theory and the solution of trascendental equations for each atom in the sample, in order to compute their contribution to the total energy. Thus, the computational requirements are trivial, favoring the use of BFS for large-scale simulations. The method relies on first-principles determined parameters with general transferrability to any situation, as opposed to competing techniques that have the additional disadvantage that their parameters or potentials should be determined and optimized for each specific application.

Based on the idea of determining the energy of formation of arbitrary atomic configurations (ΔH), the method determines the energy contribution of each atom (ε_i), partitioning this contribution into a strain (ε_i^{strain}) and a chemical component (ε_i^{chem}), providing separate information on the structural and compositional features of the sample (ref. 1). The two contributions are linked by a coupling function g_i so that $\Delta H = \sum_i \varepsilon_i = \sum_i (\varepsilon_i^{strain} + g_i \varepsilon_i^{chem})$. The three terms ($\varepsilon^{strain}$, ε^{chem}, g) are evaluated by solving perturbation theory-based equations which require input parameters determined for each element and each binary combination of elements via first-principles calculations. This amounts to solving three trascendental equations for each atom in the sample.

The BFS method has been recently applied to assist in HITEMP projects investigating the role of alloying additions to NiAl. Due to its simplicity and physically sound foundation, the method provides detailed atomistic information regarding fundamental properties (i.e. solubility limit of such additions, their site preference, metastable structures, formation of precipitates, interfacial segregation, physical properties, etc). The method is meant to provide a useful tool in the process of alloy design, by giving much needed insight in the basic mechanisms at the atomic level that guide the formation of the alloy and its ensuing properties. Due to its minimal hardware, time and cost requirements, it gives an alternative source of information that can only enhance the knowledge gained through experimental work.

Figs. 5-10 summarize the work done for NiAl-based alloys. In essence, the same procedure is now being applied to the study of partitioning ratios in superalloys, by individually examining the role of each alloying component and the interaction between them. In this study, we built a large set of sufficiently large atomic configurations, considering almost every possible atomic distribution in a given lattice. With the advance knowledge that all the alloys studied experimentally are bcc-based, we restricted the calculation to such crystallographic structure. First, we examined the defect structure of non-stoichiometric NiAl alloys (ref. 2), succesfully reproducing every known experimental fact: substitutional defects, triple defects, vacancies and their location, dependence of the lattice parameter with concentration, etc. (Fig. 6). We later added, separately, Ti, Cr, and Cu atoms, examining in each case the site preference of each element as a function of concentration and in the presence of other alloying additions, as well as the solubility limit and the formation of precipitates.

For Ti, it was found that it forms Heusler Ni_2AlTi precipitates above $x_{Ti} \sim 5\%$, in agreement with experiment. This was found by analyzing a large number of possible atomic configurations and defining the ground state structures for each concentration as the minimum energy states, finding that below 5 at. % Ti, disordered configurations are energetically favorable, but with a clear departure of ordered states (Heusler) beyond that value (Fig. 7). For Cr, a similar analysis determined that the solubility limit is approximately 1 at. % Cr, with the formation of α-Cr precipitates beyond that value. This is in excellent agreement with experiment (Fig. 8) and the known features of the ternary phase diagram, We later studied 4- and 5-element systems, concentrating on the interaction between the different alloying additions and how that affects the phase structure of the alloy. The 5-element (Ni-22.56Al-9.47Ti-33.5Cr-1.95Cu) alloy shown in Fig. 10 is a good example of the type of information that is easily available with this technique: the numerical simulation using BFS for calculating the energy shows that Ti and Cr retain their individual behavior (Heusler and α-Cr precipitate formation, respectively) with the addition of Cu segregation to the NiAl/Cr interface, as well as the formation of a new Ni-Al-Ti ordered phase in the NiAl/Cr interface. Other issues are apparent from the simulation, including the clustering of Ti atoms in the presence of antistructure Ni atoms in the NiAl matrix.

Progress in the BFS application to superalloys

We are currently in the initial stages of using a similar approach to the study of fcc-based superalloys. The main ingredient of the method - the parameterization of the BFS equations - is being implemented for up to 9 elements (Ni,Co,Cr,Al,Ti,Mo,Ta,W and Nb). Once the parameterization is completed, we plan to individually test the ternary, quaternary and then higher order additions to the base alloy and perform a similar analysis to that previously described for NiAl-based alloys. By comparing the BFS predictions for the ternary cases with available - although scarce - experimental data, we expect to develop the necessary confidence on the first-principles determined BFS parameters which will be the basis for the high-order calculations. Moreover, also in a similar fashion to the NiAl project, we will supplement our analytical BFS calculations with large-scale Monte Carlo/BFS computer simulations, concentrating on the temperature effects and simulated annealing, and its influence on the resulting microstructure.

In addition, previous work using BFS for the analysis of fcc Ni-based superalloys has been extensive and it provides a solid foundation to the upcoming research. Following the methodology described above (i.e. building a set of possible atomic configurations and calculating the energetics and properties with BFS), we completed the process of determining a specific set of physical properties (compressibility, density and energy of formation) to the experimental validation of the theoretical predictions. A Ni-25Al-12.5Cu-25Au alloy was specified from a set of 200+ alloys, and later processed and analyzed in the laboratory (Figs. 11-12).

The first step for our current program consists in the determination of the BFS parameters. These quantities (two for each pair of elements) as well as the necessary parameters for each individual atomic species (another four parameters) are determined using first-principles calculations. These parameters, unlike competing techniques, are determined once only and they are used, unchanged, in any other application involving these elements. The transferrability of the BFS parameters is a powerful advantage of BFS, as it allows for immediate application to other systems as soon as the initial work in determining them is completed. We are in the process of determining the necessary parameters for the 9 elements of interest (Ni,Al, Co,Cr,Ti,Mo,Ta,W and Nb) and the BFS parameters for every combination of them (Ni-Al, Ni-Co,...). Once this phase of the program is completed, we will proceed to analyze the behavior of each one of the alloying additions (Co, Ti, ...) in the Ni-Al-Cr base alloy, their solubility limit, the site preference scheme, etc. , and later examine higher-order combinations. In doing so, we expect to gain understanding on the observed and expected behavior of the final alloys, based on our knowledge on the individual effects and how each new element added modifies the behavior of the previous ones.

Conclusions

The BFS technique is capable of:

1) Determine the energetics, lattice parameter and other properties of complex alloys. 2) Provide the calculational basis for large-scale computer simulations of the alloy formation process therefore introducing substantial time and cost savings by assisting in the alloy design process. 3) Model complex systems: previous work dealt with up to 5-component, 3-phase systems which exhibit interfacial segregation. 4)With additional computational modules, it can be extended to calculate mechanical properties as well as improved modeling of the heat treatment and its relation to the microstructure of the alloy.

References

1. Bozzolo, G., Ferrante, J. and Kobistek, R., J. Computer-Aided Mater. Design **1** (1993) 305; Bozzolo, G. and Ferrante, J., J. Computer-Aided Mater. Design **2** (1995) 113.

2. Bozzolo, G., Noebe, R.D., Ferrante, J. and Amador, C., Scripta Metall. Mater. **33** (1995)1907.

OBJECTIVE

- To apply a recently developed computational modeling technique (the BFS method for alloys) to assist in the determination of superalloy properties.
- To introduce a new methodology in alloy design focusing on time, cost and hardware savings.

Fig. 1

THE BFS METHOD FOR ALLOYS

GENERAL CONCEPT

- Calculates the energy of formation of a predetermined atomic configuration for a given bulk composition.
- By comparing the energy of different configurations, it is then possible to determine the ground state structure by finding the minimum energy configuration.
- The calculation provides the energy of formation, lattice parameter and bulk modulus for each configuration. By adding other modules, other physical and mechanical properties could also be predicted.

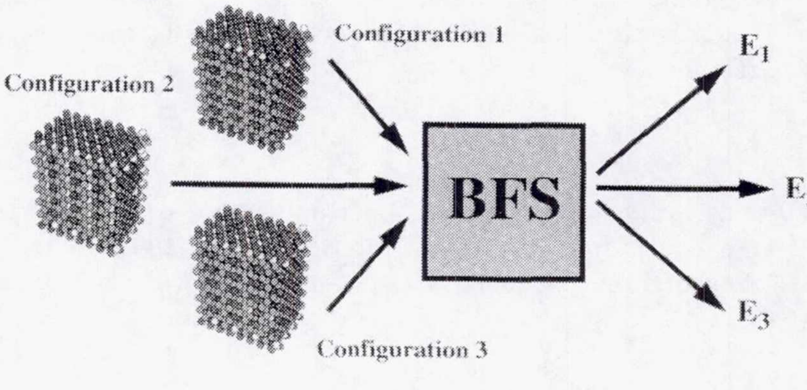

Fig. 2

THE BFS METHOD

- The energy of formation of an arbitrary alloy structure is the sum of individual atomic contributions in the alloy

$$\Delta H = \sum_i \varepsilon_i$$

- The energy of each atom consists of a strain energy (structural effects) and a chemical energy (compositional effects) contribution, linked by a coupling factor *g*

$$\varepsilon_i = \varepsilon_i^{strain} + g_i \varepsilon_i^{chem}$$

- The three quantities are determined by using methodology derived from Equivalent Crystal Theory, which is based on quantum perturbation theory.
- This involves solving transcendental equations for each term, for each atom, where the parameters used are determined only once, via first-principles calculations.
  - — The parameterization is universal and does not change with each specific application.
  - — The parameterization does not rely on experimental input.

Fig. 3

THE BFS METHOD : PROCEDURE

ANALYTICAL CALCULATIONS

1. Construct an arbitrary distribution of N atoms of different species in arbitrary sites.
2. Compute the energy of formation of such a structure:
   - For each atom, compute the contribution to the energy of formation by solving the BFS equations.
   - Add the contributions.
   - Compare the result with that of other distributions to determine the configuration with minimum energy.

THE QUALITY OF THE RESULTS DEPENDS ON THE NUMBER AND TYPE OF CONFIGURATIONS CONSIDERED

Output: Information on the ground state structure as well as metastable states.
Trends and behavior of properties (i.e. , lattice parameter dependence on composition).

NUMERICAL CALCULATIONS

Monte Carlo algorithms for simulating the heat processing of the sample.

Output: Details on the microstructure; influence of temperature.

Fig. 4

DETERMINATION OF THE DEFECT STRUCTURE OF BINARY NiAl ALLOYS

B2 structure

72-atom cell typically used for calculations

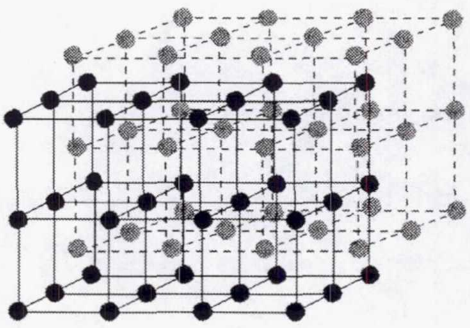

Different configurations are created by locating atoms and vacancies in different sites.

A large set of configurations can be created with possible distributions of atoms and vacancies.

The energy is then computed with BFS for each configuration in the set.

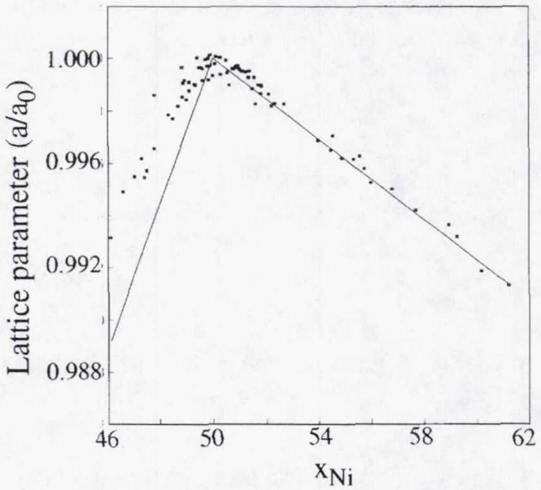

BFS Experiment ■

BFS results: obtained from the minimum energy structure at each concentration, from a 200+ set of possible distributions.

Fig. 5

ENERGY OF FORMATION OF 150 $Ni_{50}(Al,Ti)_{50}$ CONFIGURATIONS

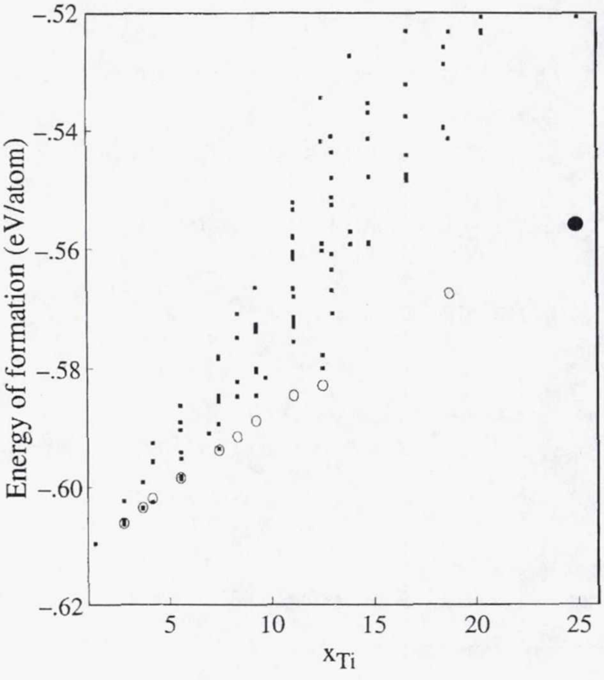

- ● Below 5 at. % Ti, the energy for disordered solid solutions is less than that for Heusler ordering.
- ● Above 5 at. % Ti, the energy for Ti in Heusler ordered arrangements is less than that for random solid solution configurations.
- ● From this analysis the solubility for Ti can be estimated at 5 at. % Ti.
- ● Lattice paramter of the constituent phase can also be determined.

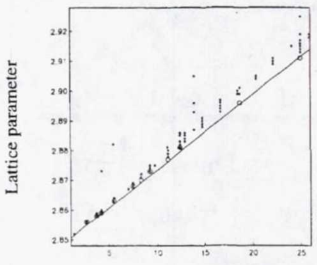

○ Heusler ordering ● Ni_2AlTi -Heusler phase ■ Disordered structures

Fig. 6

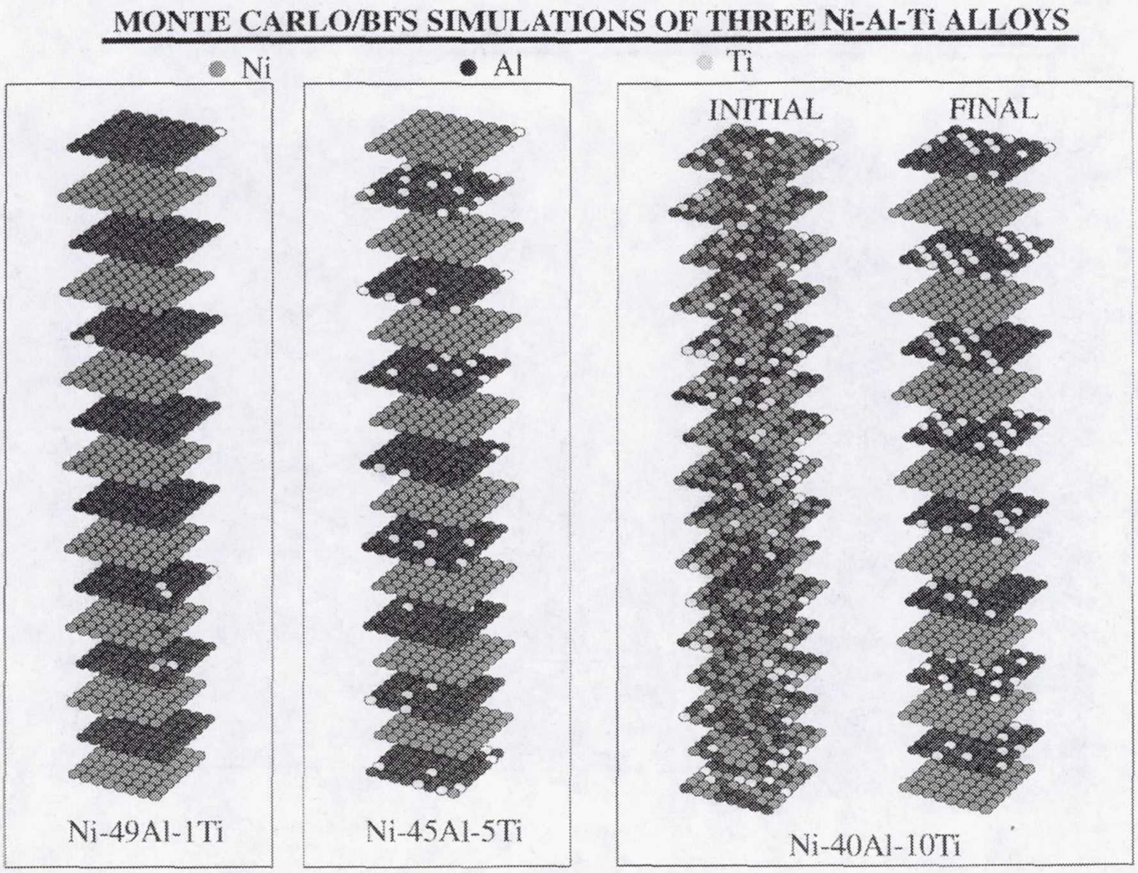
MONTE CARLO/BFS SIMULATIONS OF THREE Ni-Al-Ti ALLOYS
● Ni
● Al
● Ti
INITIAL
FINAL
Ni-49Al-1Ti
Ni-45Al-5Ti
Ni-40Al-10Ti

Fig. 7

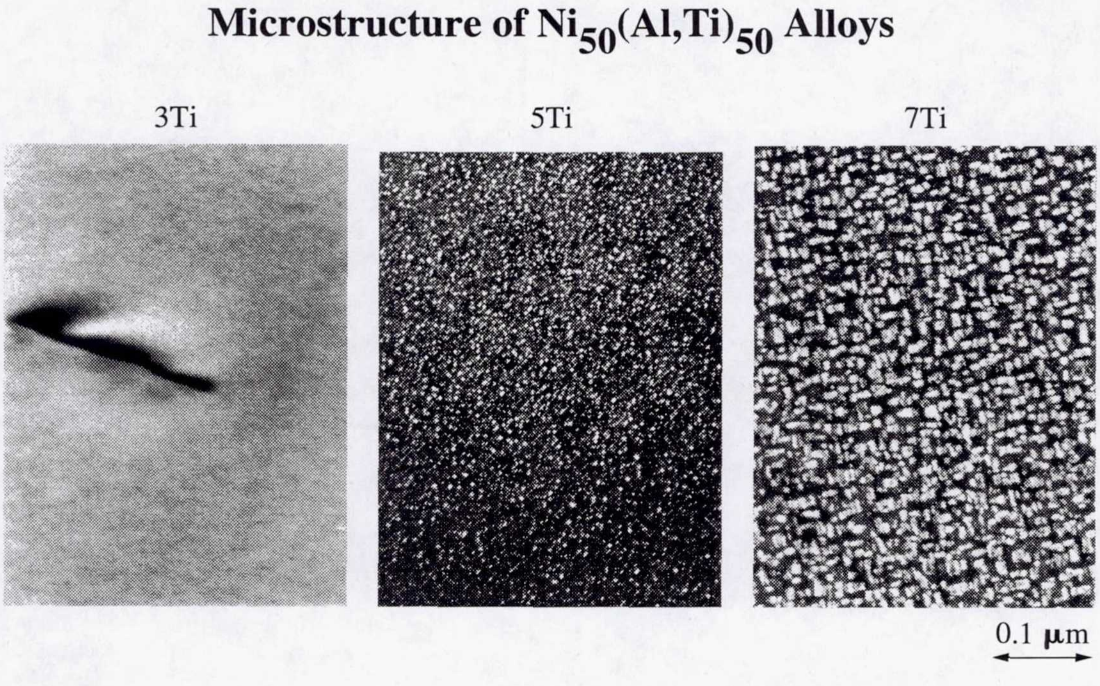
Microstructure of Ni50(Al,Ti)50 Alloys
3Ti
5Ti
7Ti
0.1 μm

Fig. 8

Monte Carlo/BFS simulations for two Ni-Al-Cr alloys

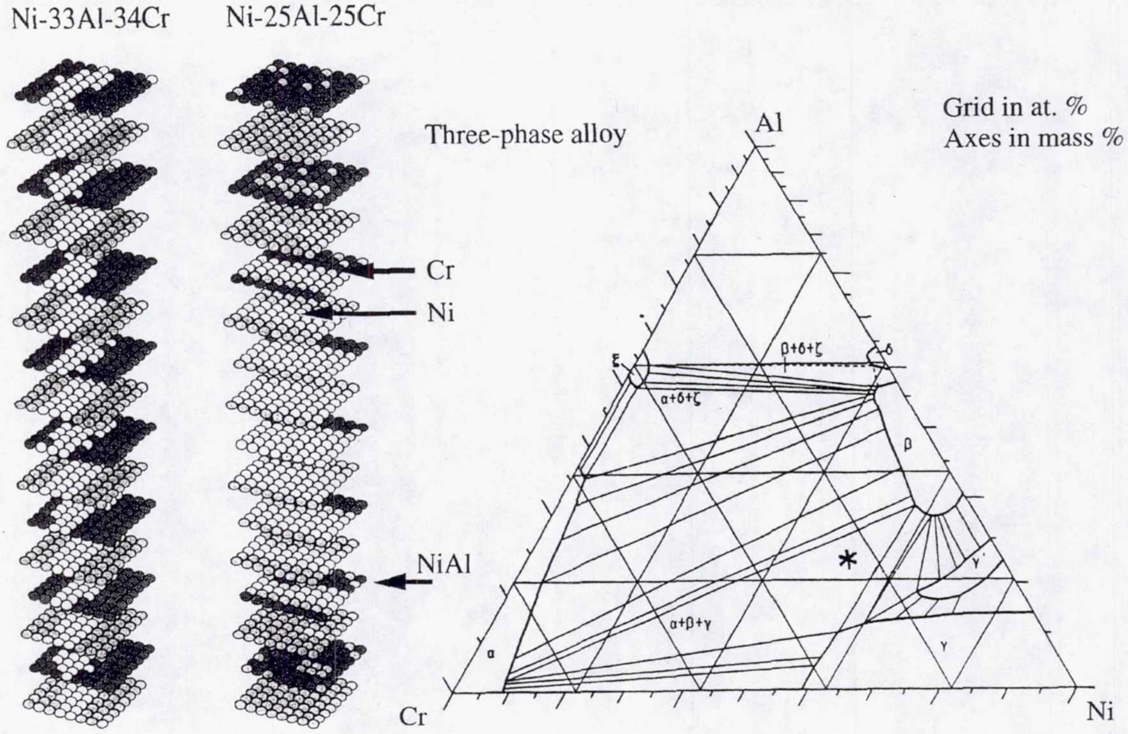

Fig. 9

PENTALLOY

Ni-22.56Al-9.47Ti-33.5Cr-1.95Cu

Ni-Al-Ti-Cr-Cu

● ● ○ ● ●

- Ground state configuration of a 1024 atom cell of a 5-element alloy, obtained with BFS
- Initial state: totally random distribution
- Final state: after slow cooling (simulated) of the sample via a Monte Carlo numerical calculation in which the BFS method was used to compute the energy at every step.

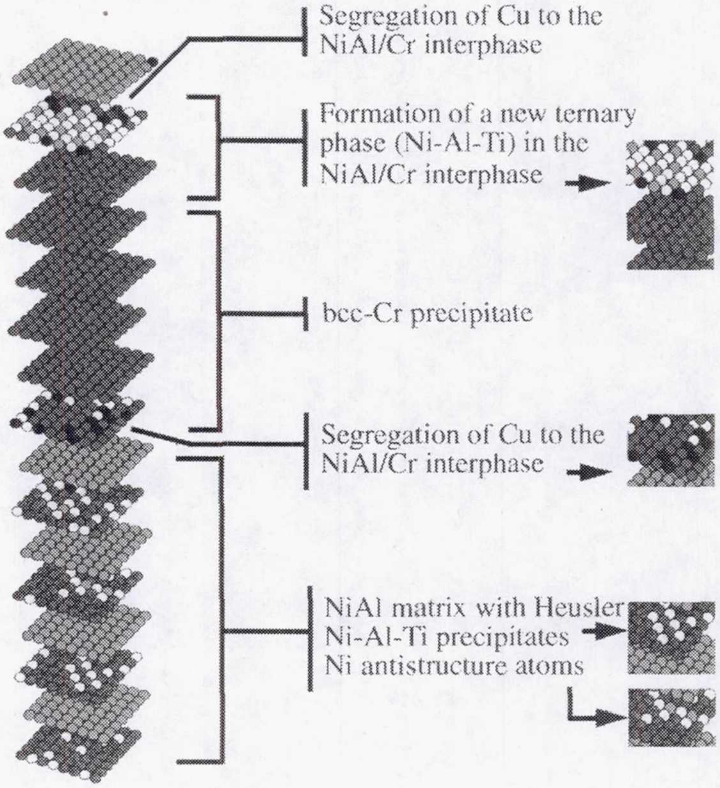

Segregation of Cu to the NiAl/Cr interphase

Formation of a new ternary phase (Ni-Al-Ti) in the NiAl/Cr interphase

bcc-Cr precipitate

Segregation of Cu to the NiAl/Cr interphase

NiAl matrix with Heusler Ni-Al-Ti precipitates Ni antistructure atoms

Fig. 10

FCC ALLOYS

BFS WAS PREVIOUSLY APPLIED TO THE DETERMINATION OF PHYSICAL PROPERTIES OF FCC-BASED QUATERNARY ALLOYS:

- A set of 350+ (Ni-Al-Cu-Au) alloys was defined and studied.
- Classified according to their density, compressibility and energy of formation.
- These alloys were later made and analyzed to confirm theoretical predictions.
- Methodology will be applied to the study of up to 9 component superalloys.

Fig. 11

MONTE CARLO/BFS SIMULATION OF A Ni-25Al-12.5Cu-25Au ALLOY

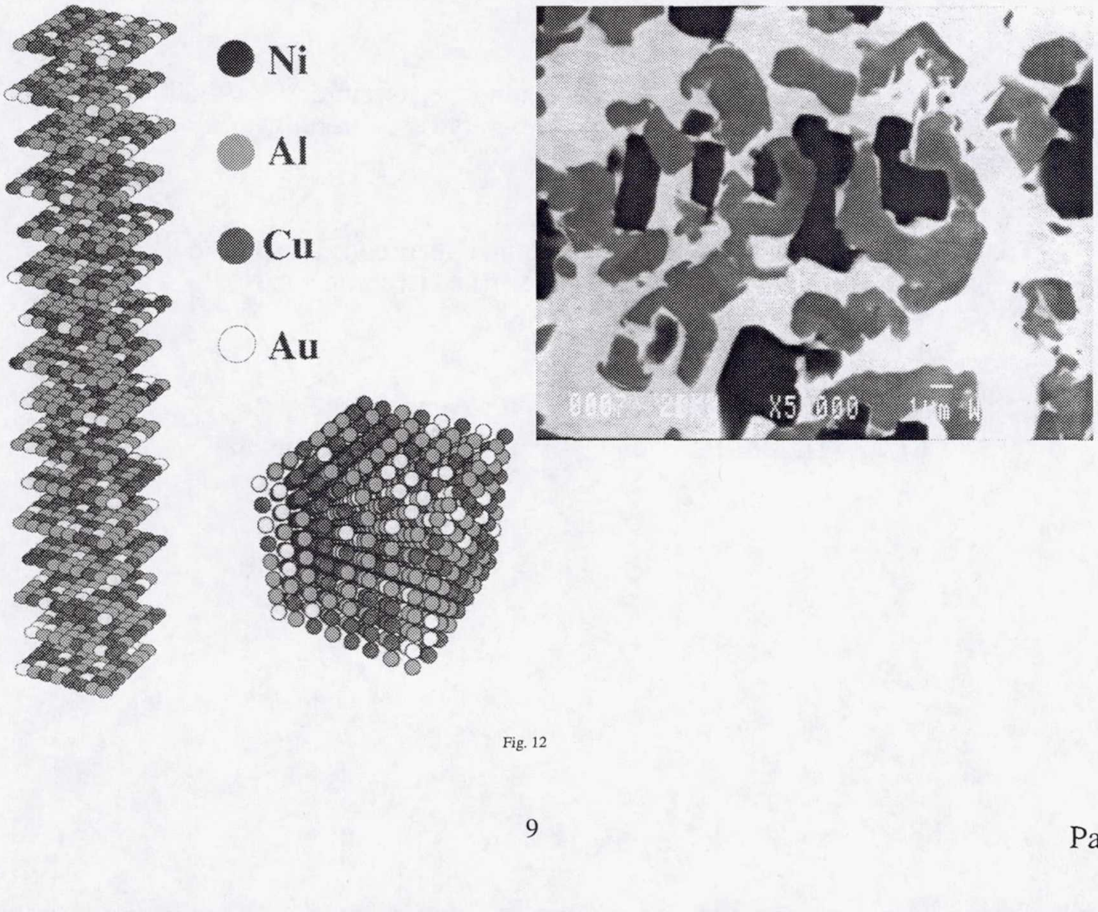

Fig. 12

APPLICATION OF BFS TO SUPERALLOYS

FOLLOWING A SIMILAR PROCEDURE TO THAT USED FOR NiAl ALLOYS, THE BFS METHOD WILL BE USED TO:

- INVESTIGATE THE BASIC PROPERTIES OF Ni-Al-Cr FCC-BASED ALLOYS
- INVESTIGATE THE BEHAVIOR OF ALLOYING ADDITIONS TO THE BASE ALLOY
  - INDIVIDUALLY, STUDYING ALL POSSIBLE QUATERNARY SYSTEMS.
  - SIMULTANEOUSLY INCREASING THE NUMBER OF ADDITIONS, STUDYING THE INTERACTION BETWEEN THEM AND THE RESULTING BEHAVIOR.
  - STUDYING THE FUNDAMENTAL PROPERTIES OF THE RESULTING ALLOYS.

Fig. 13

SUMMARY

- The BFS method has been used to determine the structure of NiAl alloys of increasing complexity, ranging from the binary B2 NiAl alloy to a 5-element alloy.
- The methodology was used to first determine, theoretically, specific properties of a 4-element fcc alloy, then verified experimentally.
- BFS parameters were determined for 9 alloy components (Ni, Al, Cr, Co, Ti, Mo, Ta, W and Nb) for application in superalloys.

Fig. 14

CONCLUSIONS

- Computer modeling using BFS provides the same description of NiAl, NiAl+Ti and NiAl+Cr properties that experiment does but also provides much needed additional information on atomistic effects.

- BFS efficiently assists in alloy design, providing detailed information concerning, for example

- alloy energetics
- site occupancy
- lattice parameter
- precipitate structure
- solubility limits
- lattice misfit
- temperature effects

- The flexibility of BFS can be extended to any arbitrary system, with any number of components and crystallographic structures. The methodlogy will be applied to the study of 9-component superalloys.

- At minimal cost, time, and personnel requirements, provides valuable support for alloy development programs.

Fig. 15

FUTURE WORK

•BFS INPUT:

Determine BFS parameters for Ni, Al, Cr, Co, Ti, Mo,Ta,W, and Nb.

Determine BFS parameters for all the binary combinations.

•ANALYTICAL BFS CALCULATIONS

Determine properties of ternary, quaternary, etc. alloys

•MONTE CARLO/BFS SIMULATIONS

Determine partitioning ratios γ/γ'.

Fig. 16

Characterization of Damage Accumulation in a C/SiC Composite at Elevated Temperatures

Jack Telesman, and Mike Verrilli
NASA Lewis Research Center
Cleveland, Ohio

Louis Ghosn
Case Western Reserve University
Cleveland, Ohio

Pete Kantzos
Ohio Aerospace Institute
Cleveland, Ohio

Introduction and Motivation

This research is part of a program aimed to evaluate and demonstrate the ability of candidate CMC materials for a variety of applications in reusable launch vehicles. The life and durability of these materials in rocket and engine applications are of major concern and there is a need to develop and validate life prediction methodology. In this study, material characterization and mechanical testing was performed in order to identify the failure modes, degradation mechanisms, and progression of damage in a C/SiC composite at elevated temperatures. The motivation for this work is to provide the relevant damage information that will form the basis for the development of a physically based life prediction methodology.

Material

The material used in this study is a DuPont Lanxide C/SiC manufactured using a proprietary infiltration procedure. The fiber architecture was a simple 0/90 two dimensional weave laminate. The composite was fabricated in 8" x 8"x 0.125" panels. Test specimens, having a typical dog bone geometry, were machined using diamond tooling and re-infiltrated following machining in order to protect the newly exposed surfaces.

The typical surface condition an microstructure of the composite is shown in Figure 3. It is obvious that in the as-received condition the material exhibits a variety of inherent cracking within the matrix, fiber tows, and surface. The majority of the internal cracks seem to be contained within the [90] plies, and the majority of the surface cracks seem to be within the coating itself.

Testing

The material was characterized by performing a variety of tensile, creep, and fatigue testing. The bulk of the mechanical testing was performed at 650^{o}C (1200^{o}F). Limited testing was also performed at 550 ^{o}C (1022^{o}F) and 450 ^{o}C (842^{o}F) in order to determine the temperature regime where the environmental effect is dominant.

In order to determine the progression and accumulation of damage, a significant number of tests were interrupted prior to failure and subjected to NDE and metallographic inspection. A NDE method was used to determine the resonant frequency as a function of life of a stress rupture specimen that was tested at 650 °C and 70 MPa and periodically interrupted. Similarly, stress rupture specimens tested at 650 °C and 70 MPa were interrupted after 30min, 75min, and 150min (corresponding to 10%, 25%, and 50% of life) and sectioned for metallography. Also where applicable, particularly in the fatigue tested specimens, the stiffness was monitored as a function of life.

Results

Stress Rupture Behavior

The stress-rupture behavior at various elevated temperatures is shown in Figures 4 and 5. The strength of the composite degrades very rapidly for temperatures above 550 °C. At 650 °C and 70 MPa the life is approximately 5hrs. At 450 °C and 200 MPa on the other hand the life is significantly greater than 50 hours and furthermore there is little degradation in the residual strength. The effect of damage accumulation was evident in the stress strain behavior of an interrupted specimen. As shown in Figure 6, a decrease in stiffness occurred very early in life and the degradation continued throughout the test. Similar degradation was observed in the resonant frequency response, Figure 7. At 650 °C the applied load has very little effect on the life, this observation in conjunction with the fact that damage occurs very early in life not only suggests that the environment governs the damage process but also that the presence of inherent cracking hastens the process.

Fatigue Behavior

Low cycle fatigue testing was performed in order to determine if any synergistic process occurs in the presence of fatigue. The results are shown in Figure 8 in comparison to the stress rupture data. In general, the strain accumulation is slower, and overall longer lives are attained during fatigue. The effect of cyclic induced damage was further investigated by performing a fatigue test at much higher frequency (100 Hz). The results indicate that even though the cycles to failure increased by several orders of magnitude, the time to failure was in the same order as the lower frequency fatigue tests and stress rupture tests, Figure 9. This observation reinforces the notion that overall at 650 °C the damage accumulation is governed by environmental exposure. Fatigue damage doesn't appear be have any additional effects. Similar to the observations of stress rupture damage, the damage accumulation that was observed in the low cycle fatigue tests manifests itself in the reduction of stiffness as shown in Figure 10. The reduction of stiffness with respect to the life fraction is not only consistent for the various fatigue testing conditions but it coincides well with the creep rupture behavior. This behavior further implies that damage accumulation is environmentally driven. Most importantly, however, this behavior, if indicative of the actual damage, can serve as the basis for life prediction methodology.

Metallography

Extensive metallography and fractographic examination was performed on the failed and interrupted specimens with the primary purpose of determining the mechanisms of damage. The surface of the specimens did not reveal any additional damage aside from the already existing cracks, Figure 11. This suggests that the coated surface (i.e. the matrix) is not an overwhelming contributor to the damage process and that the damage responsible for the failure is occurring internally.

This became evident upon inspection of the metallographic sections obtained from the interrupted specimens. As seen in Figure 12, fibers near the surface are being destroyed by the oxidizing environment which enters the specimen by the myriad of inherent cracks, Figure 13. This phenomenon is also apparent on the fracture surface of the stress rupture specimens, Figure 14, where for the most part the C fibers are missing and seem to have been consumed. The carbon fibers on the tensile specimens, on the other hand, are intact. Also evident from the interrupted tests is a progression of damage. The specimen interrupted at 50% of the life show the most extensive damage while the specimen interrupted at 10% of life exhibits the least amount of damage. The fact that damage appears at a very early stage in life, and manifests itself in the form of fiber damage, gives support to the observations that stiffness degradation reflects the presence and progression of damage.

Discussion and Summary

Based on the observations of the various mechanisms present and the material behavior, the damage process of C/SiC at elevated temperatures can summarized as follows:

1. early in life the existing cracks propagate into the composite and are bridged by the fibers
2. these cracks act as pipelines for the environment, which attacks the C fibers
3. failures in the oxidized fibers results into further crack propagation and linking up of cracks
4. as more fibers are oxidized the bridging effect diminishes until the net section in one of the locally oxidized regions is insufficient to carry and transfer load

In general, the damage seems to accumulate as crack propagation, linking up of cracks, and environmental degradation of the load bearing fibers. The toughening mechanisms, although very complex and interrelated, can be categorized as bridging, multiple cracking, and crack tortuousity. These mechanisms are also manifested at various scales. For example, crack bridging can occur within a fiber tow as shown in Figures 12 and 13 where individual fibers are bridging the crack. Also bridging can occur on a larger scale, as shown in Figure 15, where the whole fiber tows are bridging cracks. Understanding the interrelationships of these mechanisms as well as their degradation due to the environment is vital to developing vital and reliable life prediction methodology.

Conclusions

1. The strength of the C/SiC CMC degrades significantly during stress rupture testing for temperatures above 550 °C, whereas below 450 °C degradation is minimal.
2. Degradation of the modulus seems to occur very early in life and continue throughout the test. Low cycle fatigue testing at the same testing conditions exhibited longer time to failure than the stress rupture testing.
3. Examination of failed and interrupted specimens indicates that the C fibers are oxidizing very rapidly at these temperatures.
4. The accumulation of damage, the failure process, and degradation of strength above 550 °C is dominated by environmental degradation of the carbon fibers.

Future Work

The damage data obtained so far has been mainly qualitative, in the future emphasis will be placed on quantifying the observed damage and correlating it with observed mechanical behavior such as resonant frequency or stiffness degradation. This will serve as the basis for developing and evaluating a life prediction model based on actual material behavior. Also, the material fatigue properties will be further evaluated at lower temperature regimes where the environment does not dominate the failure process and damage accumulation occurs by other mechanisms. This will ensure that the major environmental and fatigue damage processes are incorporated in the lifing model.

MOTIVATION

LONG TERM GOAL:

- DEVELOP, CODIFY, AND VALIDATE LIFE PREDICTION METHODOLOGY FOR CERAMIC MATRIX COMPOSITE ENGINE COMPONENTS FOR REUSABLE LAUNCH VEHICLES.

SHORT TERM GOAL:

- IDENTIFY DEGRADATION MECHANISMS, DAMAGE PROGRESSION, AND FAILURE MODES TO SUPPORT THE DEVELOPMENT OF LIFING MODELS.

APPROACH

- CHARACTERIZE MECHANICAL BEHAVIOR OF 2-D WEAVE DuPONT LANXIDE C\SiC CMC (TENSILE, CREEP, AND FATIGUE PROPERTIES).
- IDENTIFY DEGRADATION MECHANISMS, DAMAGE PROGRESSION, AND FAILURE MODES IN THE CMC.
- DEVELOP LIFE MODELS BASED UPON CAPTURING AND MODELING THE PHYSICS OF THE DAMAGE ACCUMULATION PROCESSES.

Fig. 1

EXPERIMENTAL PROCEDURE

- ELEVATED TEMPERATURE TENSILE, CREEP, AND FATIGUE TESTS
- TEST TEMPERATURE: 650 °C (1200 °F), 550 °C (1022 °F), AND 450 °C (842 °F)
- STIFFNESS DATA MONITORED AND STORED THROUGHOUT THE TEST
- NDE INSPECTION PERFORMED ON SELECTED SPECIMENS (SPECIMENS WERE SUBJECTED TO INTERRUPTED TESTING AND REPEATED INSPECTION)
- FRACTOGRAPHIC AND METALLOGRAPHIC CHARACTERIZATION OF FAILED AND INTERRUPTED SPECIMENS

Fig. 2

MATERIAL

DUPONT LANXIDE
C/SiC CMC
2-D WEAVE LAMINATE

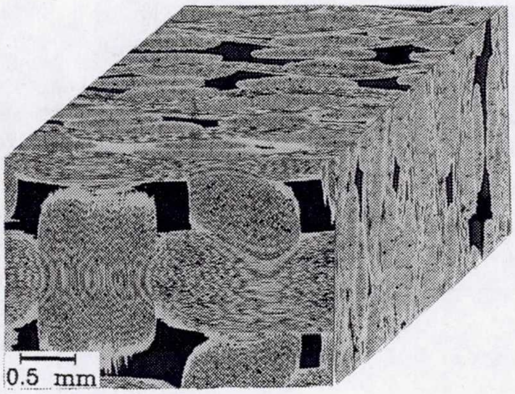

CMC HAS INHERENT CRACKING DUE TO FABRICATION

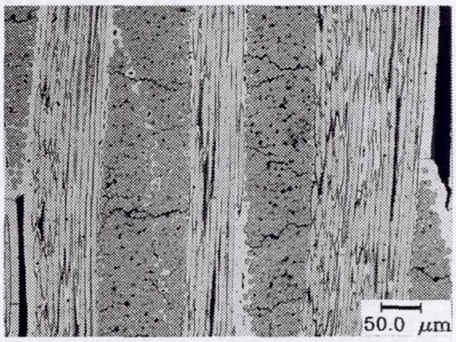

INTERNAL CRACKING CONTAINED WITHIN [90°] PLIES

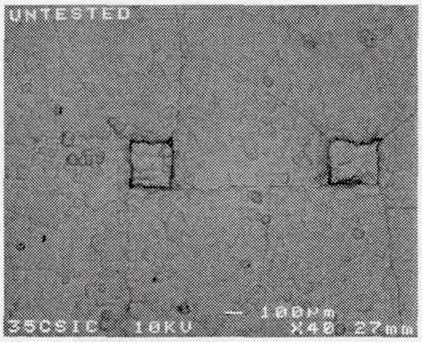

SURFACE CRACKING CONTAINED WITHIN SURFACE MATRIX COATING

Fig. 3

Stress-Rupture Data for DuPont C/SiC

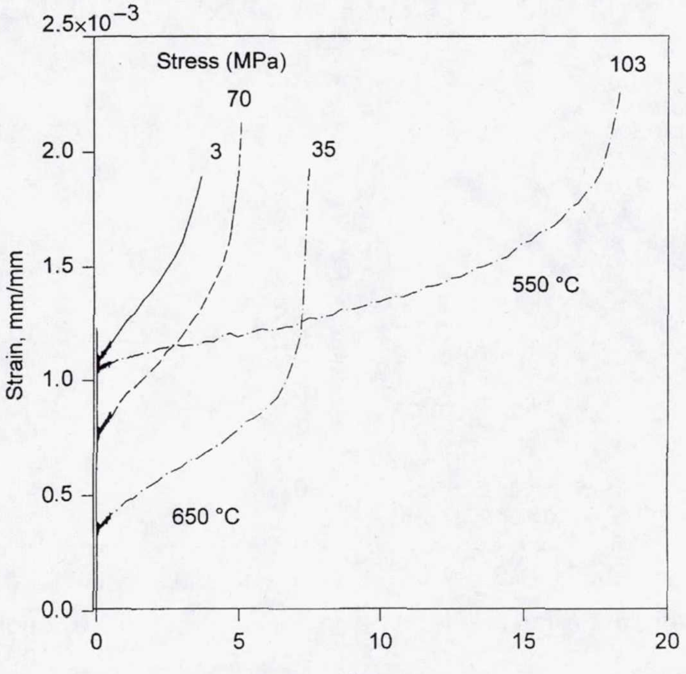

Fig. 4

STRESS-RUPTURE OF C/SiC CMC AT VARIOUS TEMPERATURES

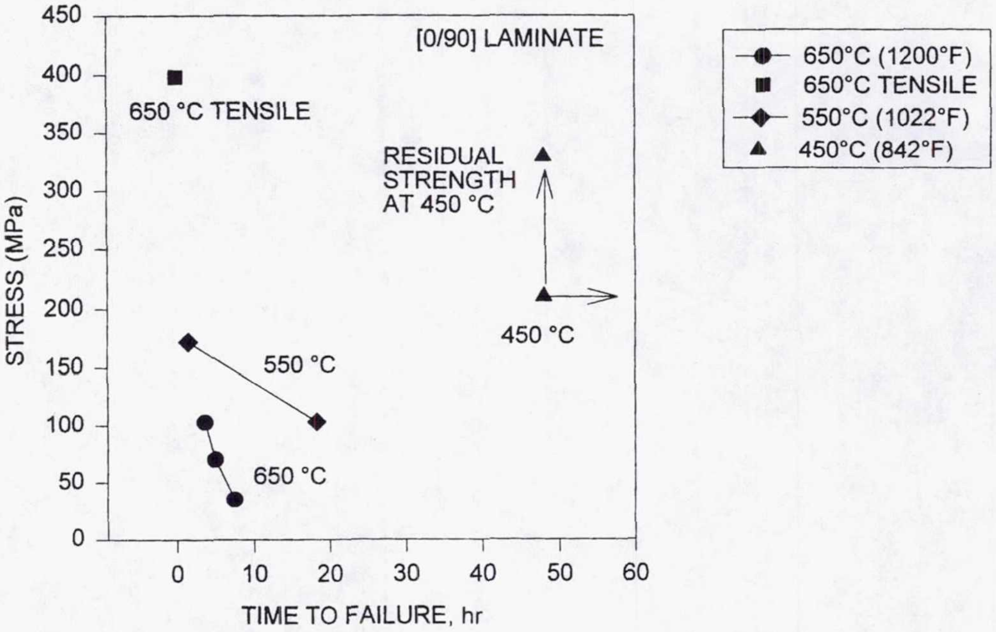

- STRENGTH OF CMC DEGRADES RAPIDLY ABOVE 550°C
- AT 450°C DEGRADATION IS MINIMAL

Fig. 5

STIFFNESS DEGRADATION AS A FUNCTION OF LIFE FRACTION DURING STRESS RUPTURE

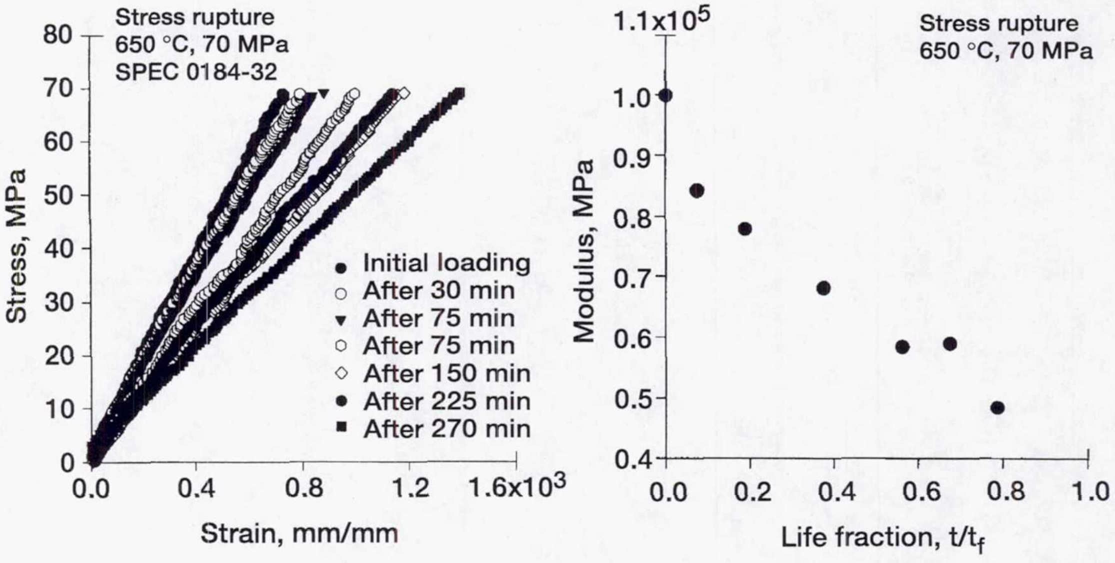

Fig. 6

RESONANT FREQUENCY RESULTS FOR INTERRUPTED 650 °C STRESS-RUPTURE TEST

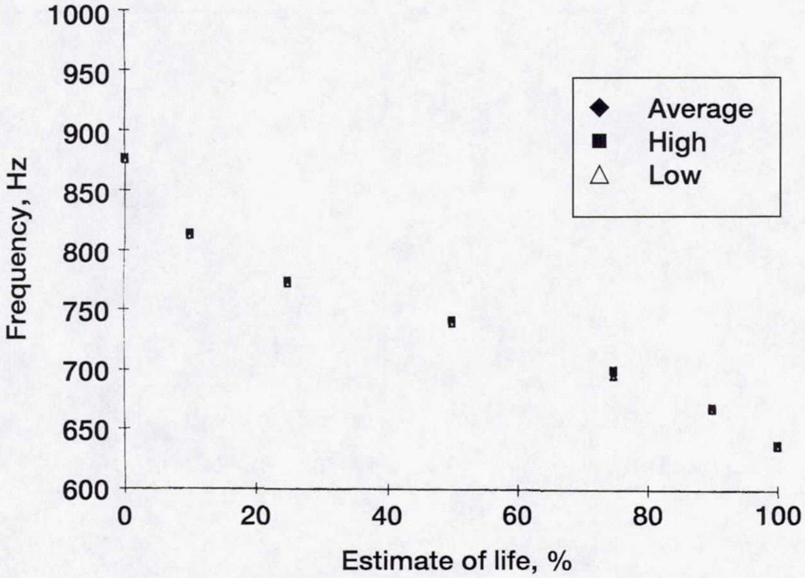

- VERY SENSITIVE AND HIGHLY REPEATABLE NDE TECHNIQUE
- CAPTURES CHANGE IN RESPONSE IN THE VERY EARLY STAGES

Fig. 7

STRESS-RUPTURE AND FATIGUE COMPARISONS AT 650 °C

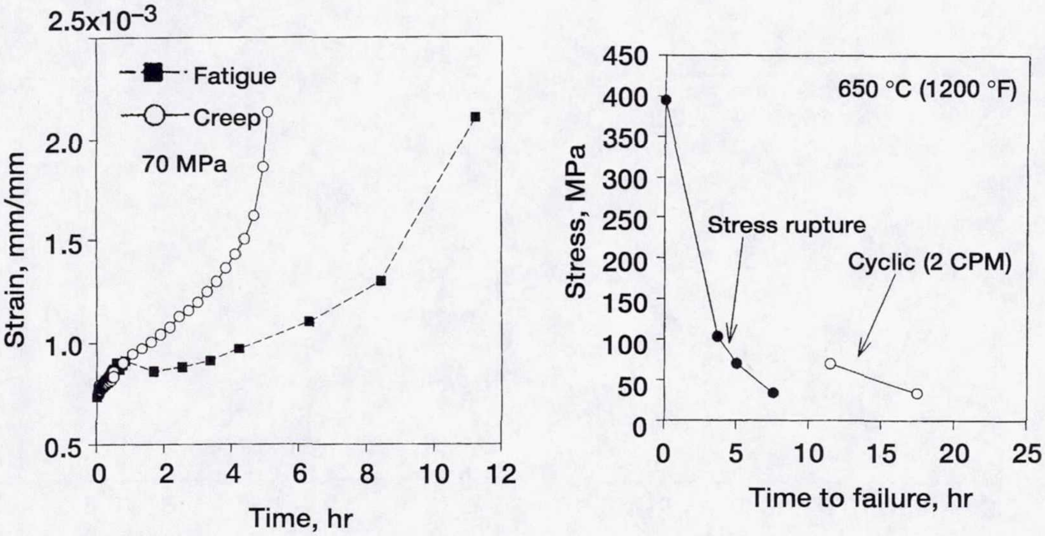

- STRAIN ACCUMULATES SLOWER DURING FATIGUE
- FATIGUE TESTS RESULT IN LONGER LIVES

Fig. 8

EFFECT OF CYCLIC FREQUENCY ON LCF RESULTS

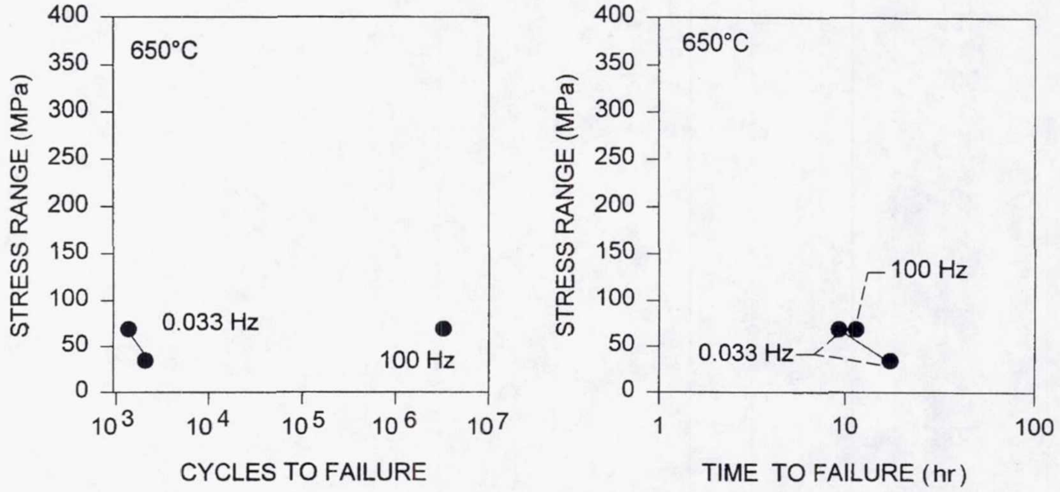

- CYCLIC FAILURE IS GOVERNED BY TIME AT TEMPERATURE

- ENVIRONMENTAL DEGRADATION CONTROLS FAILURE AT 650°C

Fig. 9

STIFFNESS DEGRADATION AS A FUNCTION OF LIFE FRACTION DURING LOW CYCLE FATIGUE

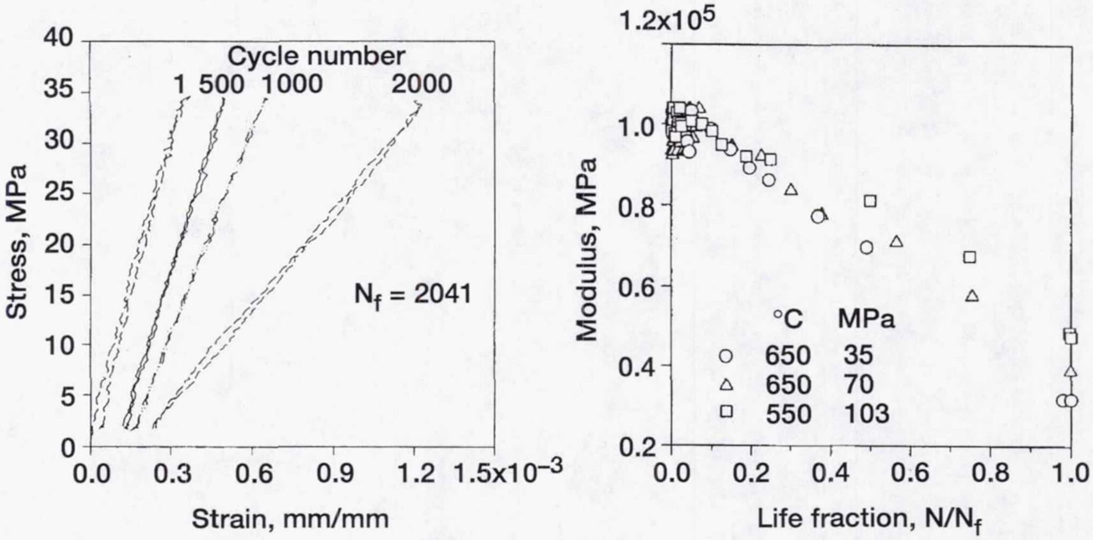

PHENOMENA COULD BE BASIS FOR LIFE PREDICTION MODEL

Fig. 10

SPECIMEN SURFACE BEFORE AND AFTER TESTING

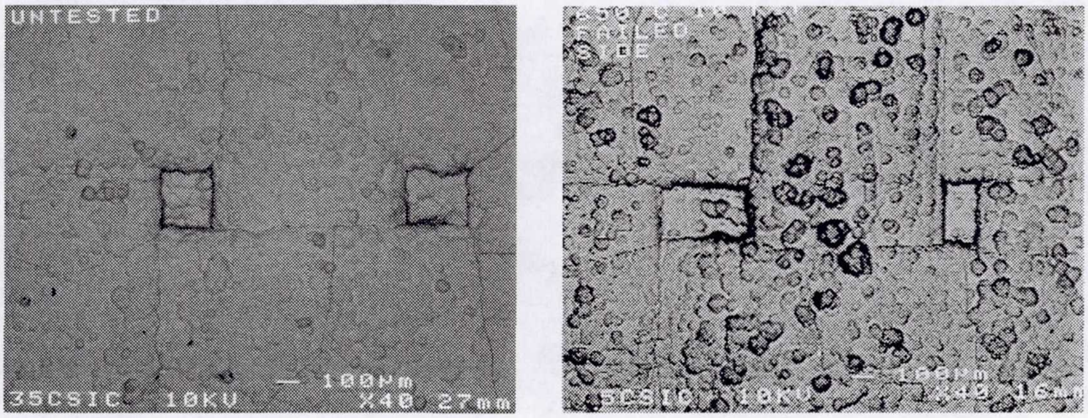

AS–FABRICATED CONDITION

TESTED AT 650 ^{0}C, 70 MPa

NETWORK OF FINE CRACKS PRESENT IN THE AS FABRICATED CONDITION

DENSITY AND APPEARANCE OF PRE–EXISTING CRACKS DO NOT CHANGE DURING TESTING

DAMAGE MUST BE INTERNAL

Fig. 11

DAMAGE ACCUMULATION AT 650 ^{0}C AND 70 MPa

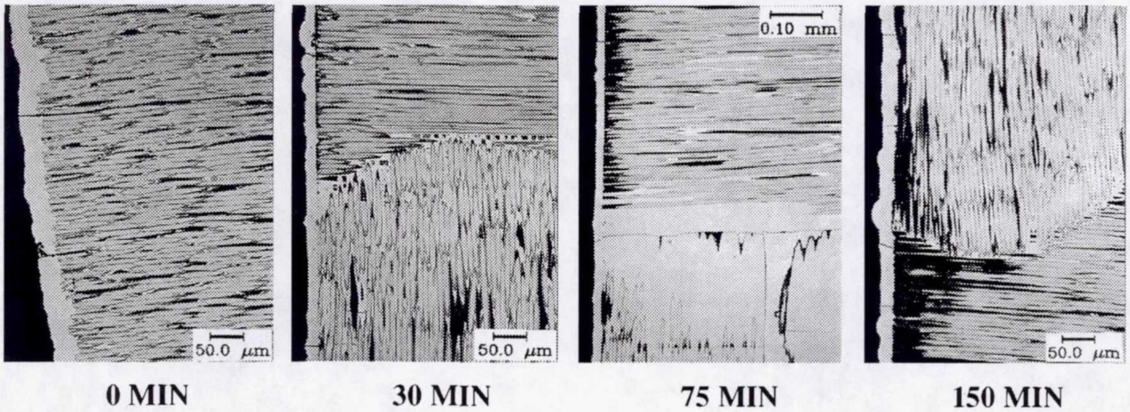

AS FABRICATED — **0 MIN**

10% OF LIFE — **30 MIN**

25% OF LIFE — **75 MIN**

50% OF LIFE — **150 MIN**

PRE–EXISTING CRACKS ACT AS PIPELINES FOR THE ENVIRONMENT

Fig. 12

ENVIRONMENTAL DAMAGE AT 650 ^{o}C

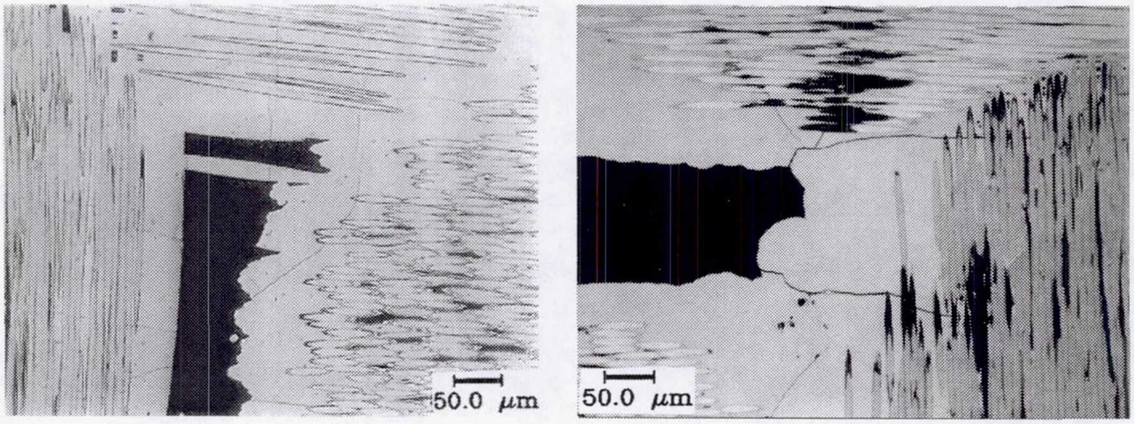

AS–FABRICATED CONDITION

TESTED AT 650 ^{o}C, 70 MPa

CRACKS INITIALLY ARE BRIDGED BY THE FIBERS

EXPOSURE AT 650 ^{o}C RESULTS IN FIBER OXIDATION AND LOSS OF BRIDGING

Fig. 13

FRACTOGRAPHY

* CARBON FIBERS SEVERELY OXIDIZED DURING STRESS RUPTURE TEST
* MOSTLY CRACKED SiC MATRIX LEFT NEAR SPECIMEN SURFACE

650 °C, 70 MPa STRESS RUPTURE

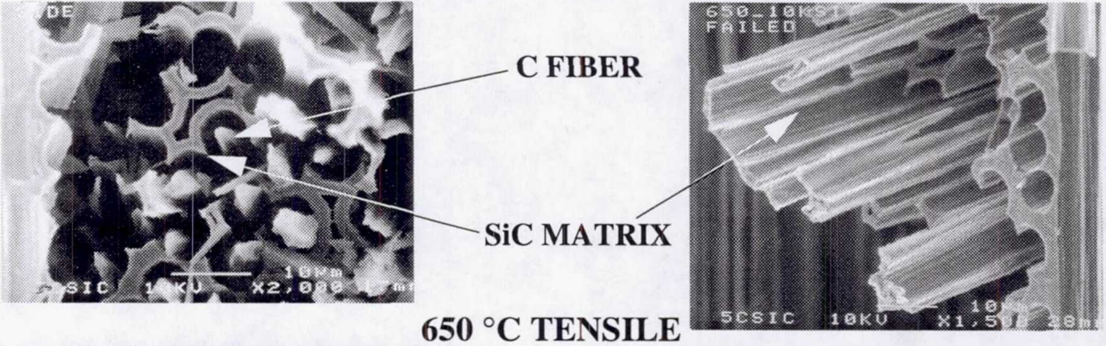

650 °C TENSILE

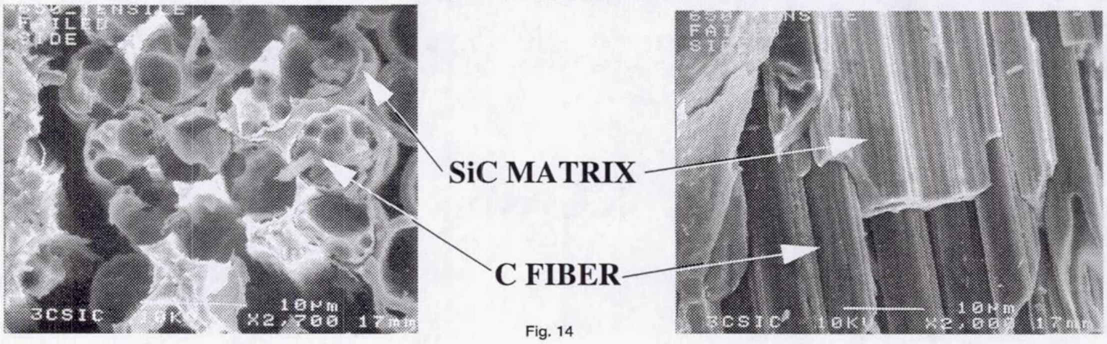

Fig. 14

DAMAGE PROGRESSION IN C/SiC AT 650 ^{o}C

1) REGULAR ARRAYS OF OXIDIZED CRACKS FORM VERY EARLY IN LIFE
2) CRACKS ARE BRIDGED BY VARIOUS METHODS
3) OXIDATION OF THE FIBERS DESTROYS THE BRIDGING, RESULTING IN FAILURE

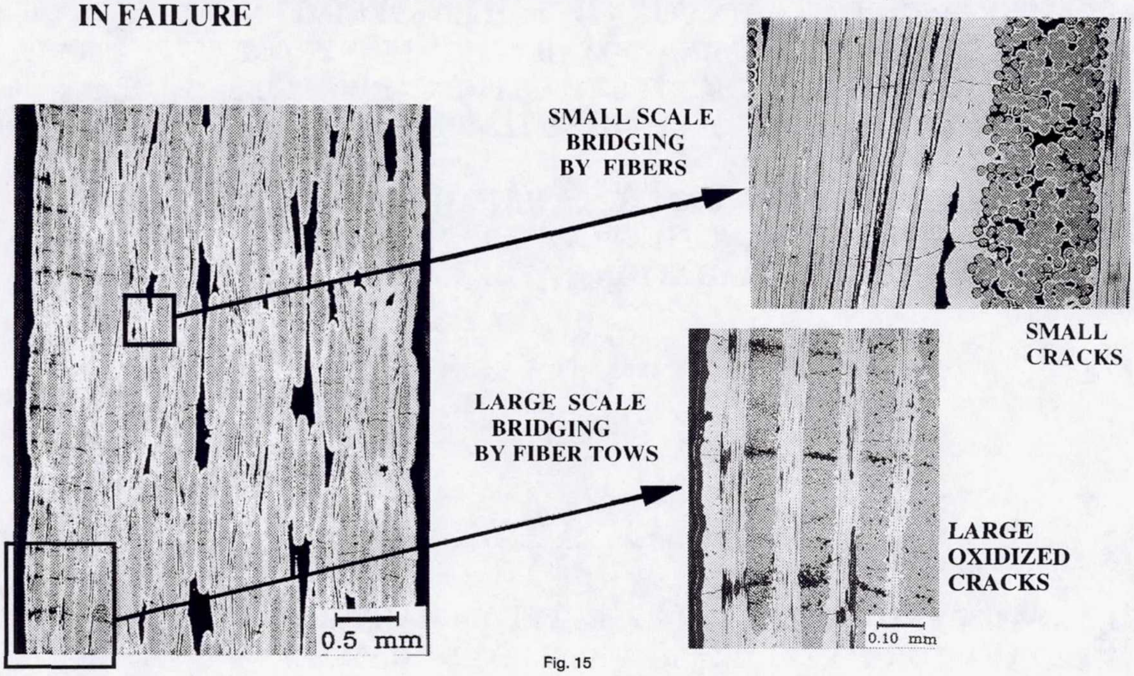

Fig. 15

SUMMARY AND CONCLUSIONS

1. THE STRENGTH OF THE C/SiC CMC DEGRADES SIGNIFICANTLY DURING STRESS RUPTURE TESTING FOR TEMPERATURES ABOVE 550 °C, WHEREAS BELOW 450 °C DEGRADATION IS MINIMAL.
2. LOW CYCLE FATIGUE TESTING AT THE SAME TESTING CONDITIONS PRODUCED LONGER TIME TO FAILURE THAN THE STRESS RUPTURE TESTING.
3. DEGRADATION OF THE MODULUS SEEMS TO OCCUR VERY EARLY IN LIFE AND CONTINUE THROUGHOUT THE TEST FOR BOTH STRESS RUPTURE AND FATIGUE LOADING.
4. FRACTOGRAPHIC EXAMINATION OF FAILED SPECIMENS AND METALLOGRAPHIC EXAMINATION OF SPECIMENS FROM INTERRUPTED TESTS INDICATES THAT THE CARBON FIBERS ARE OXIDIZING VERY RAPIDLY AT THESE TEMPERATURES.
5. THE ACCUMULATION OF DAMAGE, THE FAILURE PROCESS, AND DEGRADATION OF STRENGTH ABOVE 550 °C IS DOMINATED BY ENVIRONMENTAL DEGRADATION OF THE CARBON FIBERS.

Fig. 16

FUTURE WORK

- QUANTIFY AND CORRELATE OBSERVED DAMAGE AND STIFFNESS DEGRADATION TO ESTABLISH A BASIS FOR A DAMAGE ACCUMULATION MODEL
- INVESTIGATE FATIGUE MECHANISMS AND DAMAGE ACCUMULATION AT LOWER TEMPERATURE REGIMES WHERE ENVIRONMENTAL EFFECTS ARE NOT PRESENT
- INCORPORATE BOTH ENVIRONMENTAL AND FATIGUE DAMAGE MECHANISMS INTO A PHYSICALLY BASED LIFE PREDICTION MODEL

Fig. 17

ACCELERATED TESTING METHODOLOGY FOR THE DETERMINATION OF SLOW CRACK GROWTH OF ADVANCED CERAMICS

Sung R. Choi[*]
Cleveland State University
Cleveland, Ohio

Jonathan A. Salem and John P. Gyekenyesi
NASA Lewis Research Center
Cleveland, Ohio

Introduction

Constant stress-rate ("dynamic fatigue") testing has been used for several decades to characterize slow crack growth behavior of glass and ceramics at both ambient and elevated temperatures (refs. 1,2). The advantage of constant stress-rate testing over other methods lies in its simplicity: Strengths are measured in a routine manner at four or more stress rates by applying a constant crosshead speed or constant loading rate (Figs. 1 and 2). The slow crack growth parameters (n and A) required for design can be estimated from a relationship between strength and stress rate (refs. 1,2).

With the proper use of preloading in constant stress-rate testing, an appreciable saving of test time can be achieved (Fig. 2). If a preload corresponding to 50 % of the strength is applied to the specimen prior to testing, 50 % of the test time can be saved as long as the strength remains unchanged regardless of the applied preload. In fact, it has been a common, empirical practice in strength testing of ceramics or optical fibers to apply some preloading (<40%). The purpose of this work is to study the effect of preloading on the strength to lay a theoretical foundation on such an empirical practice. For this purpose, analytical and numerical solutions of strength as a function of preloading were developed. To verify the solution, constant stress-rate testing using glass and alumina at room temperature and alumina, silicon nitride, and silicon carbide at elevated temperatures was conducted in a range of preloadings from 0 to 90 %.

Solution

The analytical and numerical solutions of strength as a function of preloading has been obtained previously (refs. 3,4). For the natural flaw system with no residual stress field, the normalized (or 'reduced') strength as a function of preloading can be expressed as follows:

$$\bar{\sigma}_f = (1+\alpha_p^{n+1})^{1/(n+1)} \qquad (1)$$

where $\bar{\sigma}_f$ is the normalized strength, in which the strength with preloading is normalized with respect to the strength with zero preloading, α_p is the preloading factor $(1 \le \alpha_p < 1)$, where the preloading stress is normalized with respect to the strength with zero preloading, and n is the slow

---

[*] NASA Senior Resident Research Associate, Lewis Research Center, Cleveland, OH.

crack growth (SCG) parameter. In this analysis, slow crack growth was described by the following well-known power-law equation

$$v = da / dt = A[K_I / K_{IC}]^n \tag{2}$$

where v is the crack growth rate, a the crack size, t time, A the SCG parameter, K_I the mode I SIF, and K_{IC} fracture toughness of a material. The resulting plot of Eq .(1) for various values of n is shown in Fig. 4(a). For the indentation crack system where an additional term appears in the net SIF, due to the residual contact stress produced by elastic/plastic indentation deformation, analytical solution was not feasible. The solution was thus made via numerical methods (ref. 4). The result of the numerical solution of strength as a function of preloading is presented in Fig. 4(b).

Experimental

The materials used were soda-lime glass, 96 wt % alumina (ALSIMAG 614, G.E. Ceramics), NC132 silicon nitride (Norton Co.), and NC203 silicon carbide (Norton Co.). Constant stress-rate testing was conducted in four-point flexure using soda-lime glass plates and as-machined MOR alumina bars at room- temperature distilled water, and using as-machined alumina bars at 1000°C air, as-machined NC132 silicon nitride bars at 1100°C and as-machined NC203 silicon carbide bars at 1300°C. Indentation-induced surface flaws both with and without residual contact stress field were used for glass specimens. A typical range of applied stress rates was 0.03 to 333 MPa/s. After the regular constant stress-rate testing (i.e., without preloading), additional testing was performed to determine the influence of preloading on strength and to verify the solutions. Typically, five preloads ranging from 50 to 90 % were used at each chosen stress rate.

Results and Discussion

1) Constant Stress-Rate Testing

The results of the constant stress-rate testing for each material are shown in Fig. 6. The SCG parameter n was found to be: $n = 17.1 \pm 0.5$ for indented-and-annealed glass, $n' = 17.4 \pm 0.4$ for as-indented glass, $n = 41.7 \pm 2.3$ for as-machined alumina at RT, $n' = 40.2 \pm 4.9$ for as-indented alumina at RT, $n = 7.6 \pm 0.3$ for alumina at 1000°C, $n = 18.6 \pm 1.7$ for NC132 at 1100°C, and $n = 29.7 \pm 1.5$ for NC203 at 1300°C.

2) Strength as a Function of Preloading

The results of the preloading experiments for each material are shown in Fig. 7, where strength was plotted as a function of preloading from 0 to 90 %. The line in the figures represents the strength obtained with zero preloading at each test rate. It is evident from these figures that the strength is almost insensitive to preloading for most of the materials tested either at room temperature or at elevated temperatures.

3) Comparison with Theoretical Solutions

A comparison of the solutions with the experimental data can be made if the strength with preloading are normalized with respect to the strength without preloading at each stress rate, obtaining $\bar{\sigma}_f$ in accordance with Eq. (1) and the numerical solution. The resulting plots are shown in Fig. 8. The theoretical line by Eq. (1) or by the numerical solution calculated with the estimated SCG parameter *n* for each case was also included. Except for NC203, the theory is in good agreement with the experimental data, thereby indicating that the solutions are valid not only at room temperature but at elevated temperatures. Note that the variation in strength (about 5%) is attributed to the inherent scatter of strength exhibited by the materials. NC203 SiC exhibited the highest variation because of its low Weibull modulus ($m \approx 8$). The effect of strength scatter (Weibull modulus) on preloading is illustrated in Fig. 9. Excellent agreement is found in the indented glass specimens and the alumina specimens, since the specimens exhibited a high Weibull modulus of greater than 20.

4) Crack Growth Behavior

The reason why the preloading technique is workable is due to the fact that most of the crack growth occurs close to and/or at failure time at which fracture strength is defined. The nature of this long "incubation" time of an initial crack is a key aspect that makes the preloading technique feasible in constant stress-rate testing (see Fig. 10).

5) Implications

The most direct and powerful effect of preloading technique is the saving of test time, which gives a great impact on testing efficiency (Fig. 11). For example, if it takes about 9 h to test one ceramic specimen in constant stress rate testing and if a minimum of 20 specimens are required to obtain reliable statistical data, then total testing time at that stress-rate would be 180 h. But if a preloading of 80% is applied, the total testing time would be reduced to 36 h so that 80 % of the total test time can be saved. And 70 % saving for a preload of 70 %, and so on. This great advantage of the preloading technique has been adopted to a recently established ASTM standard on slow crack growth testing for advanced ceramics. Also, the preloading technique can be used as a tool identifying a mechanism associated with failure at elevated temperatures (ref. 3), as shown in Fig. 12.

References

1. Evans, A. G., Slow Crack Growth in Brittle Materials under Dynamic Loading Conditions, Int. J. Fract., vol. , no. 2, 1974, pp. 252-259.
2. Ritter, J. E., Engineering Design and Fatigue Failure of Brittle Materials," pp. 661-686 in Fracture Mechanics of Ceramics, vol. 4, edited by R. C. Bradt, D. P. H. Hasselman, and F. F. Lange, Plenum, New York, 1978.
3. Choi, S. R., and Salem, J. A., Effect of Preloading on Fatigue Strength in Dynamic Fatigue Testing of Ceramic Materials at Elevated Temperatures, Ceram. Eng. Sci. Proc., vol. 16, no. 4, 1995, pp. 87-94.
4. (a) Choi, S. R., Salem, J. A., and Gyekenyesi, J. P., Fatigue Strength as a Function of Preloading in Dynamic Fatigue Testing of Glass and Ceramics, ASME Paper # 96-GT-342, accept for publication in J. Eng. for Gas Turbines and Power, Trans. of ASME; (b) Choi, S. R., and Salem, J. A., Preloading Technique in Dynamic Fatigue Testing of Glass and Ceamics with an Indentation Flaw System, J. Am. Ceram. Soc., vol. 79, no. 3, 1996, pp. 1228-1232; (c) Choi, S. R., and Salem, J. A., Preloading Technique in Dynamic Fatigue Testing of Ceramics: Effect of Preloading on Strength Variation, J. Mater. Sci. Lett., vol. 15, 1996, pp. 1963-1965.

DETERMINATION OF SLOW CRACK GROWTH OF ADVANCED CERAMICS

$$\boxed{v = A\,[K_I/K_{IC}]^n}$$

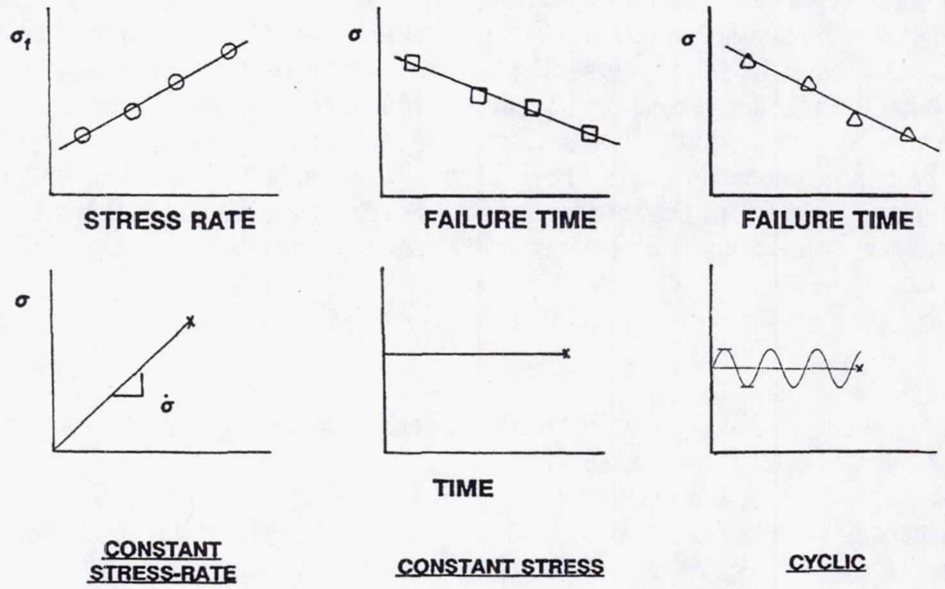

Fig. 1

CONSTANT STRESS-RATE ("DYNAMIC FATIGUE") TESTING

- QUICK AND SIMPLE
- STILL TIME CONSUMING
- EMPIRICAL USE OF PRELOADING

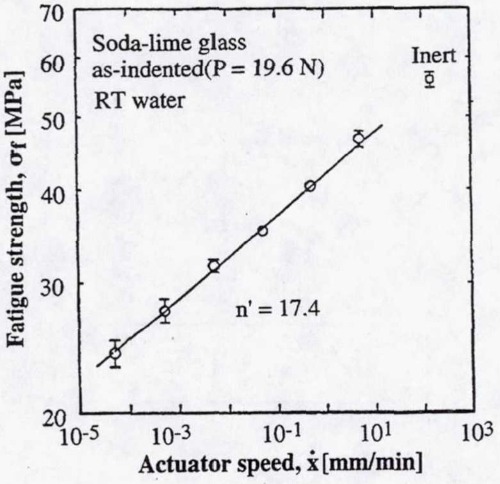

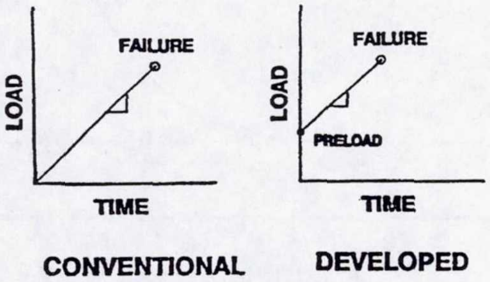

Fig. 2

PURPOSE OF STUDY

- TO DETERMINE EFFECT OF PRELOADING ON STRENGTH
- TO LAY A THEORETICAL FOUNDATION
- TO VERIFY WITH EXPERIMENT
- TO ESTABLISH AS A TESTING METHODLOGY

Fig. 3

ANALYTICAL AND NUMERICAL SOLUTIONS

1. NATURAL FLAWS

$$v = A[\frac{K_I}{K_{IC}}]^n$$

$$K_I = Y \sigma_a \sqrt{a}$$

$$\sigma_a = \sigma_o + \dot{\sigma} t$$

$$\boxed{\bar{\sigma}_f = [1 + \alpha_p^{n+1}]^{\frac{1}{n+1}}}$$

where

$$\bar{\sigma}_f = \frac{\sigma_{fp}}{\sigma_{fn}} = \frac{\text{Fatigue Strength w/ Preload}}{\text{Fatigue Strength w/o Preload}}$$

$$\alpha_p = \frac{\sigma_o}{\sigma_{fn}} = \frac{\text{Preload Stress}}{\text{Fatigue Strength w/o Preload}}$$

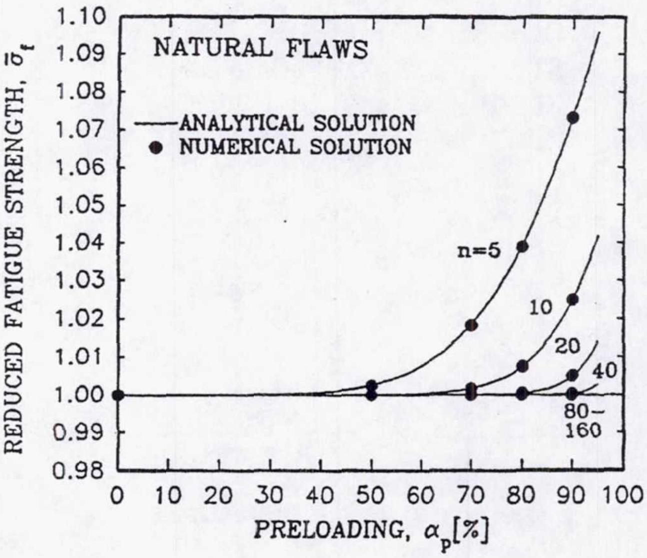

Fig. 4(a)

2. INDENTATION-INDUCED FLAWS (NUMERICAL SOLUTION)

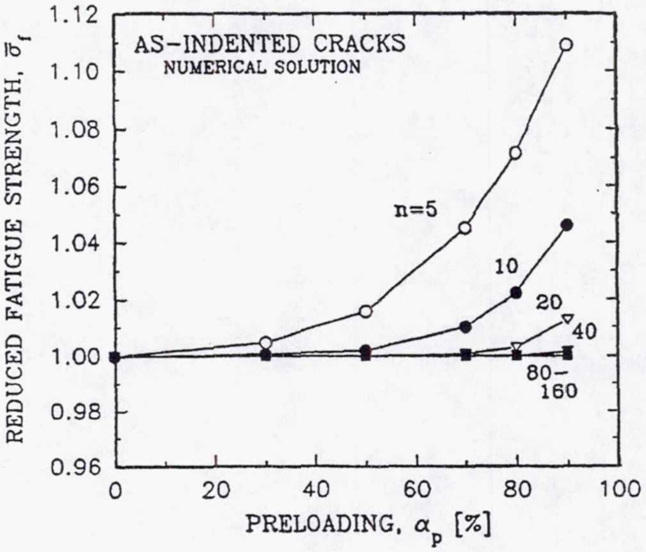

Fig. 4(b)

EXPERIMENTAL

- ¤ MATERIALS:
  - ROOM TEMPERATURE:
    - GLASS (AS-INDENTED & ANNEALED) (2)
    - ALUMINA (AS-INDENTED & AS-MACHINED) (2)
  - ELEVATED TEMPERATURES:
    - ALUMINA (1000°C)
    - NC132 SILICON NITRIDE (1100°C)
    - NC203 SILICON CARBIDE (1300°C)
- ¤ CONSTANT STRESS-RATE TESTING:
  - FOUR-POINT FLEXURE
  - 0.03 TO 333 MPa/s (A RANGE OF STRESS RATES)
- ¤ PRELOADING EXPERIMENT:
  - PRELOAD RANGING FROM 50 TO 90 %

Fig. 5

RESULTS OF CONSTANT STRESS-RATE TESTING

(ROOM TEMPERATURE)

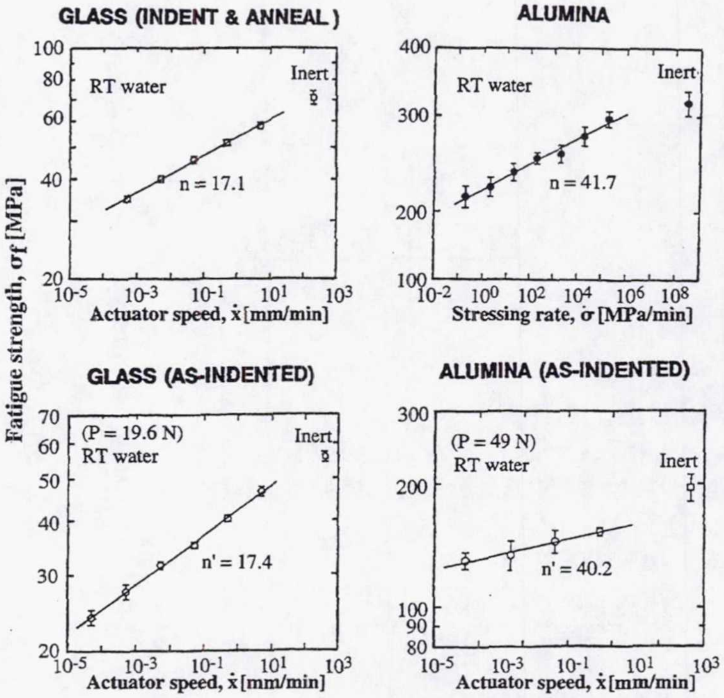

(HIGH TEMPERATURES)

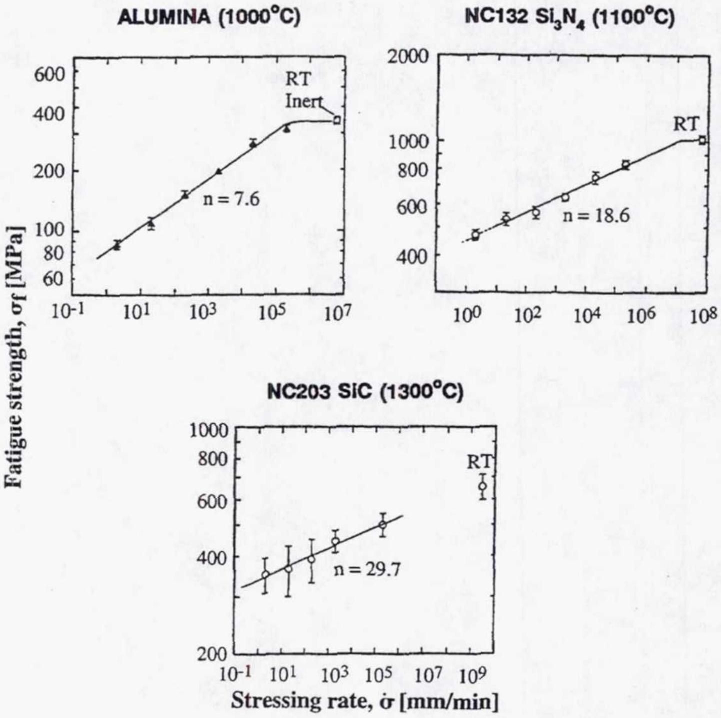

Fig. 6

RESULTS OF PRELOADING EXPERIMENTS

(ROOM TEMPERATURE)

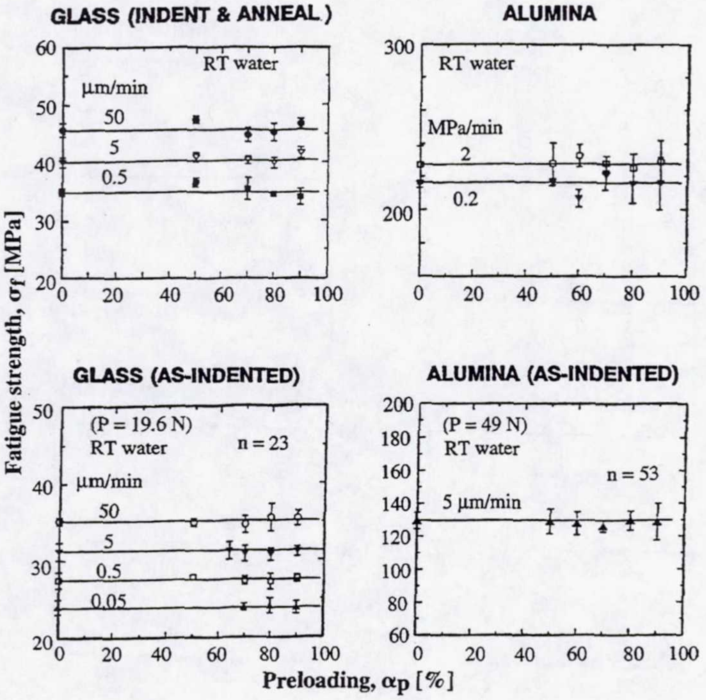

(HIGH TEMPERATURES)

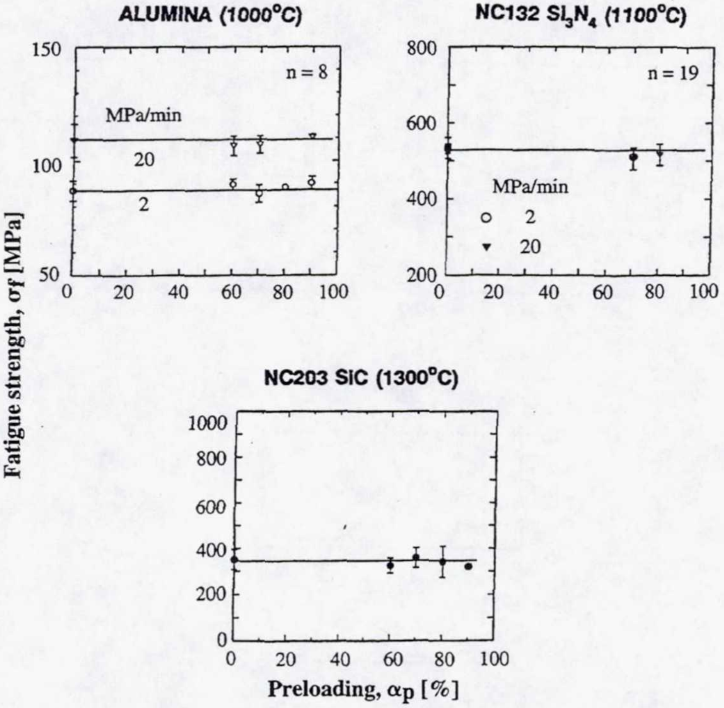

Fig. 7

COMPARISON WITH THEORY

(ROOM TEMPERATURE)

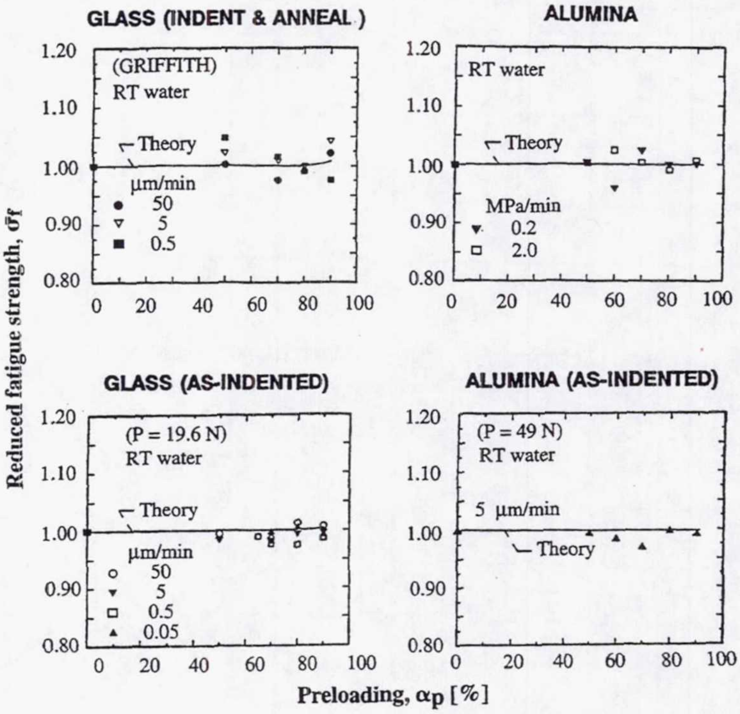

(HIGH TEMPERATURES)

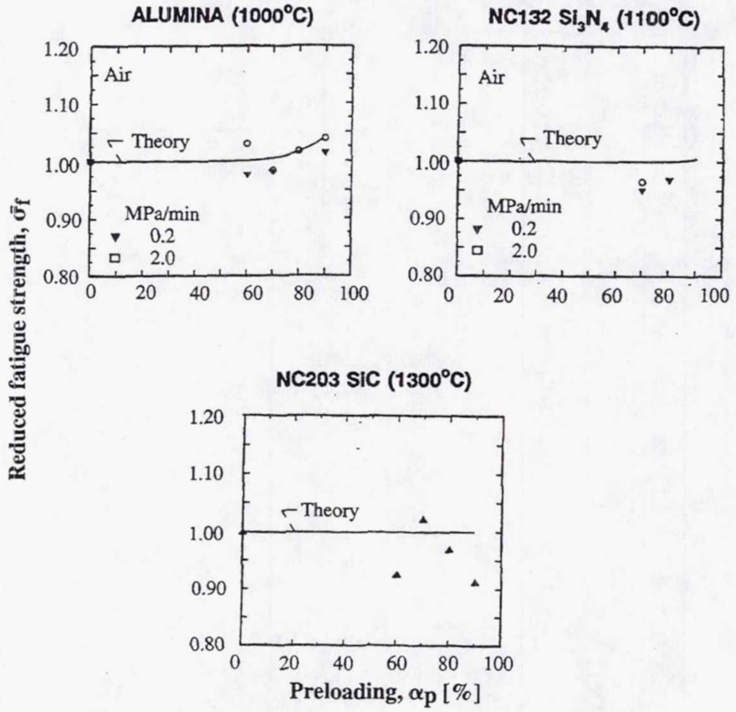

Fig. 8

EFFECT OF STRENGTH SCATTER ON PRELOADING

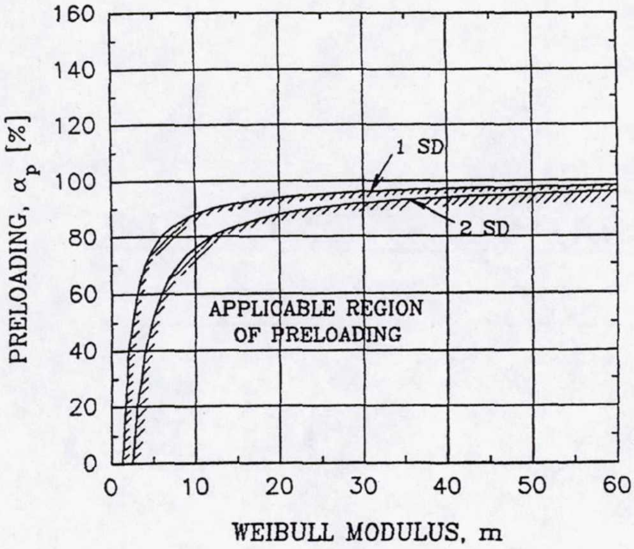

Fig. 9

REASON FOR WORKABILITY OF PRELOADING

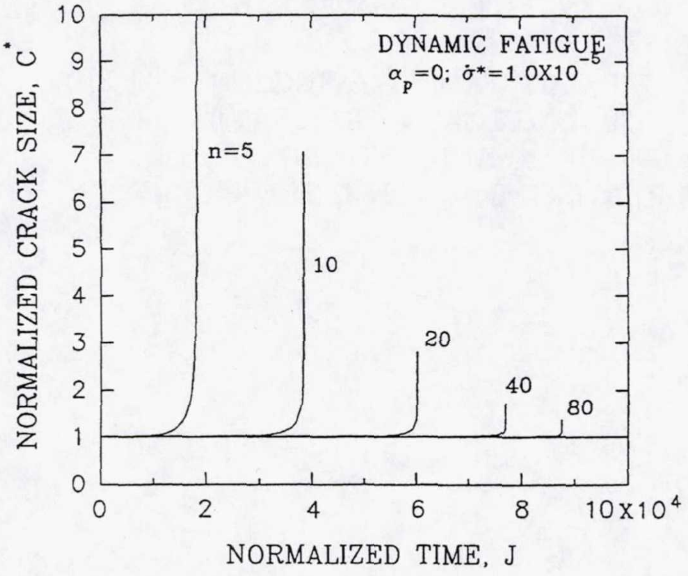

A CRACK STARTS TO GROW AFTER A LONG "INCUBATION" TIME !

Fig. 10

DRAMATIC TEST-TIME SAVING

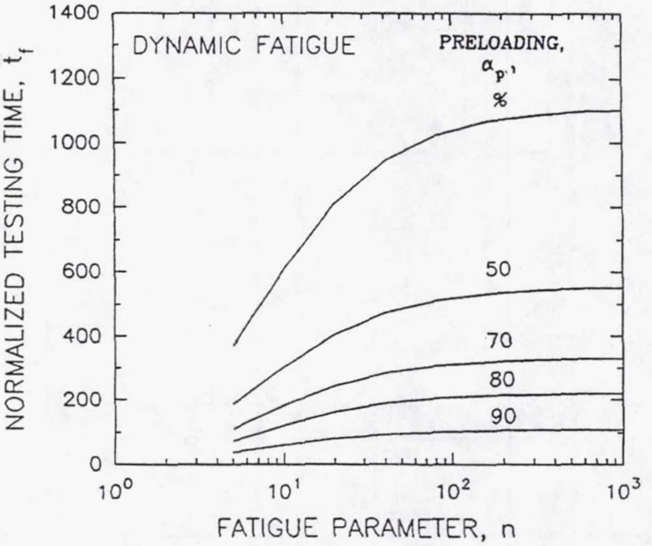

90 % PRELOAD ---- 90 % SAVING IN TEST TIME
80 % PRELOAD ---- 80 % SAVING
AND SO ON !
A GREATER IMPACT ON TEST EFFICIENCY!

Fig. 11

A TOOL IDENTIFYING A FAILURE MECHANISM

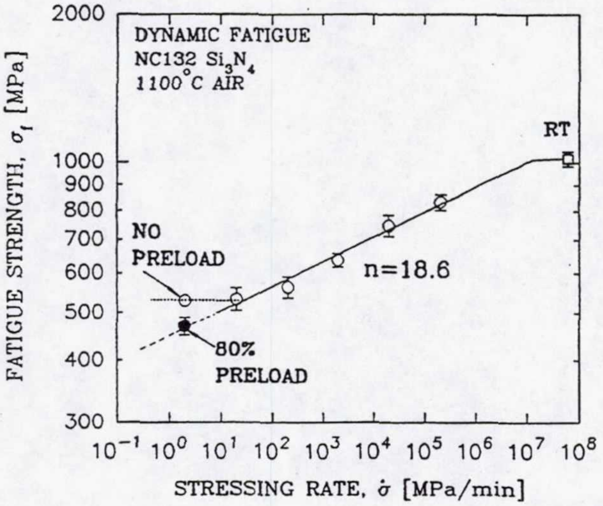

- **PROLONGED TIME --- CREEP DEFORMATION**
  CRACK BLUNTING
  STRENGTH INCREASE

- **80% PRELOADING --- DECREASED EXPOSURE TIME**
  CREEP MINIMIZED/OR VANISHED
  MAXIMIZES SLOW CRACK GROWTH

Fig. 12

CONCLUSIONS

¤ THE SOLUTION VERIFIED BY EXPERIMENTS

¤ PRELOAD UP TO 80 % POSSIBLE FOR MOST CERAMICS (n>20)

¤ THE TECHNIQUE --- DRAMATIC TEST-TIME SAVING
A GREAT IMPACT ON TEST EFFICIENCY

¤ THE TECHNIQUE --- ADOPTED IN AN 'ASTM' STANDARD ON
SLOW CRACK GROWTH TESTING OF CERAMICS

Fig. 13

ROBUST INTEGRATION SCHEMES FOR GENERALIZED VISCOPLASTICITY WITH INTERNAL-STATE VARIABLES *

Atef F. Saleeb

W. Li

THOMAS E. WILT

Department of Civil Engineering
The University of Akron
Akron, Ohio

Introduction

The scope of the work in this presentation focuses on the development of algorithms for the integration of rate dependent constitutive equations. In view of their robustness; i.e., their superior stability and convergence properties for isotropic and anisotropic coupled viscoplastic-damage models, implicit integration schemes have been selected. This is the simplest in its class and is one of the most widely used implicit integrators at present.

Viscoplastic Models

Several viscoplastic models have been proposed and developed to treat the complex time dependent viscoplastic behavior of metals, alloys and composites at high temperature. The deformation behavior of materials at high temperature involves energy dissipation and material stiffness variations due to physical changes in the material's microstructure. Consequently, thermodynamic arguments have often been utilized as a foundation on which phenomenological constitutive laws may be formulated. The complete potential-based class of inelastic constitutive models exhibit a number of unique advantages from both a theoretical and a computational standpoint, for example, the symmetry of the resulting consistent tangent stiffness matrix, and possesses a form which is convenient for further development of new deformation and damage models. The Generalized Viscoplastic with Potential Structure (GVIPS) [1] model possesses both the thermodynamic potential (Gibb's function) and the dissipation function (Ω form).

Another class of constitutive models are the Non-Associative Viscoplastic (NAV) models. the NAV models refer to those that have a partially (e.g. Ω form only) or totally incomplete potential form. An example of a NAV model is that of Freed [2]. Recent work

---

* Work funded under NASA Grant NAG3-1493 (Technical Monitor: Steven Arnold)

has demonstrated that the above models may be modified to restore the complete potential structure.

For these two different classes of models, a general computational framework suitable for implementation of both is needed.

Integration Schemes

Computational algorithms for the integration of constitutive relations play a key role in the inelastic finite element analysis of engineering structures. Consequently, much research effort has been devoted over the years to the development and critical assessment of integration schemes for the rate equations in these material models.

In early applications the explicit integration schemes, (i.e., forward Euler method) were predominate because of their ease of implementation, and because they do not require evaluating and inverting a Jacobian matrix. However, explicit integrators may not be efficient. That is, too many iteration steps may be required and convergence (stability) cannot be guaranteed. As a result, several alternative approaches have been used, for example, Gear's multi-step method [3] and Walker's asymptotic method [4]. Note that every integration scheme has its own particular application domain and is problem dependent.

The majority of recent work has emphasized the use of implicit integration methods in view of their stability and convergence properties. Based on the fully implicit, backward Euler scheme, the corresponding algorithmic (consistent) tangent stiffness arrays are derived from the integration rule, which are important for finite element solutions using (global) Newton-Raphson iterative methods.

Line Search

Although the implicit scheme is unconditionally stable, its successful application may still require proper selection of the size of the steps utilized. In this regard two factors are important: (i) accuracy, and (ii) convergence of the local iterations. A simple time subincrementing strategy was found to be effective in obtaining accurate results especially when dealing with regions of discontinuity in the state space. However this was found to be insufficient to obtain a computationally efficient solution for a highly nonlinear problem such as viscoplasticity. When a large time-step size is chosen, too many subincrementing are needed, which leads to inefficiency. Thus a more sophisticated solution procedure, namely, a line search algorithm, is required to produce an effective robust solution algorithm.

It is well know that classical Newton-Raphson is fast and stable only when the trial solution is close to the converged value. Thus, the purpose of the line search algorithm is to guide the solution towards convergence by searching for a scalar multiplier that adjusts the amount of the increment vector to be updated within each iteration [5]. The concept of line search may be applied at either the global (structural) iteration level or at the local (constitutive) iteration level. At the global level, the concept of the line search algorithm pertains to minimizing the total potential energy, that is, the work done by the residual force due to the iterative displacement. It has been suggested that the line search be incorporated with a consistent tangent stiffness and that the use of the line search is essential for robust performance of Newton's method [6,7]. It also demonstrated that in elasto-plastic analysis convergence is not guaranteed unless the global line search is used [8]. On the local (constitutive) level, line search is used to adjust the suitable increment of stress and internal variables to guarantee the convergence of the local iterations.

References

1. Arnold, S. and Saleeb, A. F.: On the Thermodynamic Framework of Generalized, Coupled Thermoelastic-Viscoplastic-Damage Modeling, Int. J. Plasticity, Vol. 10, No. 3, pp 263-278, 1994.

2. Freed, A. D. and Walker, K. P.: Viscoplasticity with Creep and Plasticity Bounds, Int. J. Plasticity, Vol. 9, 213-242, 1993.

3. Gear, G. W.: Numerical Initial Value Problems in Ordinary Differential Equations, Prentice-Hall, Inc., New Jersey, 1971.

4. Walker, K. P. and Freed, A. D.: Asymptotic Integration Algorithms for Nonhomogeneous, Nonlinear, First Order, Ordinary Differential Equations, NASA TM-103793, 1991.

5. Crisfield, M. A.: Nonlinear Finite Element Methods in Structures and Solids, Wiley, England, 1991.

6. Simo, J. C. and Taylor, R. L.: A Return Mapping Algorithm for Plane Stress Elastoplasticity, Int. J. Num. Meth. Eng., Vol. 22, pp. 649-670, 1986.

7. Simo, J. C. and Taylor, R. L.: Consistent Tangent Operators for Rate-Independent Elastoplasticity, Int. J. Num. Meth. Eng., Vol. 48, pp. 101-118, 1985.

8. Caddemi, S., and Martin, J. B.: Convergence of the Newton-Raphson Algorithm in Elastic-Plastic Incremental Analysis, Int. J. Num. Meth. Eng., Vol. 31, pp.177-191, 1991.

MOTIVATION

Two major obstacles for fully utilizing recent time-dependent/hereditary constitutive models in practical engineering analysis

- **Lack of efficient and robust integration algorithms**
  - Coupled system of tensorial rate (differential) equations or general kernal convolution integration
  - Increased mathematical complexity and associated numerical stiffness
- Difficulties associated with characterizing large number of required material parameters

Fig. 1

OBJECTIVE

- Develop a robust and efficient integration algorithm for viscoplastic constitutive equations

Fig. 2

BACKGROUND

- Computational algorithms for integrating the constitutive models are a key component for an efficient inelastic finite element analysis
- Two classes of integration schemes are: iterative and non-iterative
- Iterative

  - Fully implicit scheme
  - Requires local iterations

- Non-iterative

  - Semi-implicit
  - Fully explicit
  - No local iterations
  - Usually less "overhead"

- History dependent integral representation

  - Full history data storage

Fig. 3

INTEGRATORS

- General differential form: $\varepsilon^{I}_{n+1} = \varepsilon^{I}_{n} + \Delta t\left[(1-\alpha)\dot{\varepsilon}^{I}_{n} + \alpha\dot{\varepsilon}^{I}_{n+1}\right]$
- Fully explicit: ($\alpha = 0$) Forward Euler
- Fully implicit: ($\alpha = 1$) Backward Euler, ($\alpha = 1/2$) Midpoint rule

  - $\dot{\varepsilon}^{I}$ must be evaluated at $n + \alpha$, which requires a local iterative procedure

- Semi-implicit: ($0 \le \alpha \le 1$)

  - to avoid iterations, some methods employ an approximation for $\dot{\varepsilon}^{I}_{n+1}$
  - these are referred to as foward gradient methods, i.e., $\dot{\varepsilon}^{I}_{n+1}$ is approximated in terms of known quantities at time n using a Taylor series expansion,

$$\dot{\varepsilon}^{I}_{n+1} = \varepsilon^{I}_{n} + \left(\frac{\partial\dot{\varepsilon}^{I}}{\partial\sigma}\right)_{n}\Delta\sigma_{n} + \left(\frac{\partial\dot{\varepsilon}^{I}}{\partial\bar{\varepsilon}^{I}}\right)_{n}\Delta\bar{\varepsilon}^{I}_{n}$$

Fig. 4

INTEGRATORS

General Integral Form:

$$A = \int_0^t K(t, \tau)\dot{\varepsilon}(\tau)d\tau$$

A = Typical state variable

$K(t, \tau)$ = Kernal function, e.g.,

- exponential
- power form
- functional derivative

Fig. 5

MODEL CLASSES INVESTIGATED

- Differential/Internal variable type
  - nonassociative/dynamic recovery (NAV)
  - fully associative/nonlinear kinematic hardening (GVIPS)

Fig. 6

NON-ASSOCIATIVE MODELS (NAV)

FREED/WALKER VISCOPLASTIC MODEL (1993)

(DYNAMIC RECOVERY)

Flow Law: $\underset{\sim}{\dot{\varepsilon}}^{I} = f(J, D)\underset{\sim}{\Gamma} \qquad \underset{\sim}{\Gamma} = \underset{\sim}{M}(\underset{\sim}{\sigma} - \underset{\sim}{\alpha}) \qquad \underset{\sim}{\alpha} = \underset{\sim}{\alpha}_{s} + \underset{\sim}{\alpha}_{l}$

$$f(J, D) = \theta A \frac{1}{2\sqrt{J}} \sinh\left(\frac{\sqrt{J}}{D}\right)^{n}$$

$\underset{\sim}{M}$ = isotropic/deviatoric tensor operator

Evolution Laws:

$$\underset{\sim}{\dot{\alpha}}_{s} = 2\underset{\sim}{Z}\left[H_{s}\underset{\sim}{\dot{\varepsilon}}^{I} - g_{s}\underset{\sim}{\pi}_{s}\right] \qquad \underset{\sim}{\dot{\alpha}}_{l} = 2\underset{\sim}{Z}\left[H_{l}\underset{\sim}{\dot{\varepsilon}}^{I} - g_{l}\underset{\sim}{\pi}_{l}\right]$$

$$\underset{\sim}{\pi}_{s} = \underset{\sim}{M}\underset{\sim}{\alpha}_{s} \qquad \underset{\sim}{\pi}_{l} = \underset{\sim}{M}\underset{\sim}{\alpha}_{l} \quad \dot{D} = q_{J} - q_{D}$$

$\underset{\sim}{\alpha}_{s}$ = “short-term” back stress; $\underset{\sim}{\alpha}_{l}$ = “long-term” back stress

Fig. 7

POTENTIAL BASED MODELS

GENERALIZED VISCOPLASTICITY WITH POTENTIAL STRUCTURE, GVIPS

(NONLINEAR KINEMATIC HARDENING)

Gibb's Potential: $\Psi(\underset{\sim}{\sigma}, \underset{\sim}{\alpha}) = \Psi^{e}(\underset{\sim}{\sigma}) + \Psi^{i}(\underset{\sim}{\alpha})$ Dissipation Potential: $\Omega = \Omega(\underset{\sim}{\sigma}, \underset{\sim}{\alpha})$

Flow Law: $\underset{\sim}{\dot{\varepsilon}}^{I} = \dfrac{\partial\Omega}{\partial\underset{\sim}{\sigma}} = f(F)\underset{\sim}{\Gamma} \qquad \underset{\sim}{\Gamma} = \underset{\sim}{M}(\underset{\sim}{\sigma} - \underset{\sim}{\alpha})$

$\underset{\sim}{M}$ = isotropic/anisotropic tensor operator

$$f(F) = \frac{F^{n}}{2\mu}$$

Evolution Law: $\underset{\sim}{\dot{\alpha}} = \underset{\sim}{L}^{-1}\dfrac{\partial\Omega}{\partial\underset{\sim}{\alpha}} = \dfrac{\partial^{2}\Psi}{\partial\underset{\sim}{\alpha}\partial\underset{\sim}{\alpha}}\dfrac{\partial\Omega}{\partial\underset{\sim}{\alpha}} = \underset{\sim}{L}^{-1}\left(\underset{\sim}{\dot{\varepsilon}}^{I} - \dfrac{\gamma}{h}\underset{\sim}{\pi}\right) \qquad \underset{\sim}{\pi} = \underset{\sim}{M}\underset{\sim}{\alpha}$

$\underset{\sim}{L}^{-1} = \left[\dfrac{\partial^{2}\Psi}{\partial\underset{\sim}{\alpha}\partial\underset{\sim}{\alpha}}\right]^{-1}$ = hardening stiffness operator

Fig. 8

IMPLICIT INTEGRATOR

$$\underset{\sim}{\Sigma}_{n+1} = \underset{\sim}{\Sigma}_n + \eta d\underset{\sim}{\Sigma}_{n+1}$$

- $\underset{\sim}{\Sigma}_{n+1}$ is the vector of state variables

For the NAV model: $\underset{\sim}{\Sigma}_n = \begin{pmatrix} \underset{\sim}{\sigma}_n \\ \underset{\sim}{\alpha}_{sn} \\ \underset{\sim}{\alpha}_{ln} \\ D \end{pmatrix}$ and for GVIPS: $\underset{\sim}{\Sigma}_n = \begin{pmatrix} \underset{\sim}{\sigma}_n \\ \underset{\sim}{\alpha}_n \end{pmatrix}$

$\underset{\sim}{\sigma}_n$	stress
$\underset{\sim}{\alpha}_n$	back stress (*s* and *l* denote short and long term)
D	drag stress

Fig. 9

IMPLICIT INTEGRATOR

- $d\underset{\sim}{\Sigma}_{n+1}$ is the increment in state variables and may be expressed as:

$$d\underset{\sim}{\Sigma}_{n+1} = (\underset{\sim}{K}_{\Sigma})^{-1}\underset{\sim}{R}_{n+1}$$

- where $\underset{\sim}{K}_{\Sigma}$ is the iterative Jacobian matrix of state variables
- $\underset{\sim}{R}_{n+1}$ is the residual function of state variables, e.g., $\underset{\sim}{R}_{n+1} = \begin{pmatrix} \underset{\sim}{R}_{\sigma} \\ \underset{\sim}{R}_{\alpha_s} \\ \underset{\sim}{R}_{\alpha_l} \\ R_D \end{pmatrix}$
- and the residual functions for NAV are

$$\underset{\sim}{R}_{\sigma} = \underset{\sim}{\sigma}_{n+1} - \underset{\sim}{\sigma}_n - \underset{\sim}{C}^e(\Delta\underset{\sim}{\varepsilon} + \Delta t f \underset{\sim}{\Gamma}_{n+1})$$

$$\underset{\sim}{R}_{\alpha_{s,l}} = \underset{\sim}{\alpha}_{s,l_{n+1}} - \underset{\sim}{\alpha}_{s,l_n} - 2\Delta t H_{s,l} f \underset{\sim}{Z} \underset{\sim}{\Gamma}_{n+1} + 2\Delta t g_{s,l} \underset{\sim}{Z} \underset{\sim}{\pi}_{s,l_{n+1}}$$

$$\underset{\sim}{R}_{\alpha} = \underset{\sim}{R}_{\alpha_s} + \underset{\sim}{R}_{\alpha_l} \qquad R_D = D_{n+1} - D_n - \Delta t(q_J - q_D)$$

Fig. 10

LINE SEARCH

- The factor η is a scalar $(0 \leq \eta \leq 1)$ that adjusts the step size to optimize the iterative solution
  - η is obtained by a line search algorithm
  - the objective is to minimize the dot product $s_i = \left|\underset{\sim}{R}^{k}_{n+1} \bullet d\underset{\sim}{\Sigma}^{k}_{n+1}\right|$

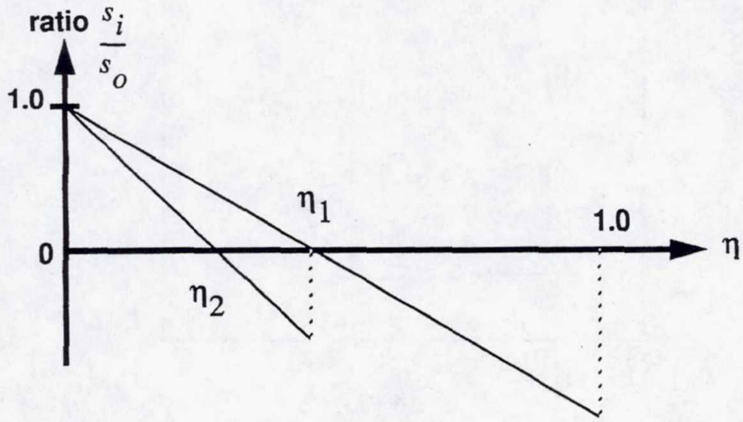

Fig. 11

VALIDATION TESTS

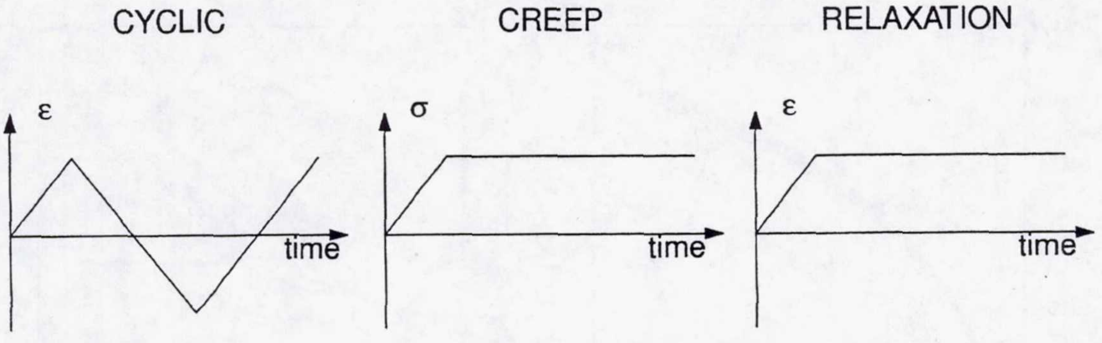
CYCLIC

CREEP

RELAXATION

$\dot{\varepsilon} = 2x10^{-3}$ s^{-1}

$\varepsilon_{max} = 0.0144$

$\dot{\sigma} = 1$ ksi/s

$\sigma_{max} = 10$ ksi

hold time = 1000 s

$\dot{\varepsilon} = 1x10^{-3}$ s^{-1}

$\varepsilon_{max} = 0.01$

hold time = 1000 s

Fig. 12

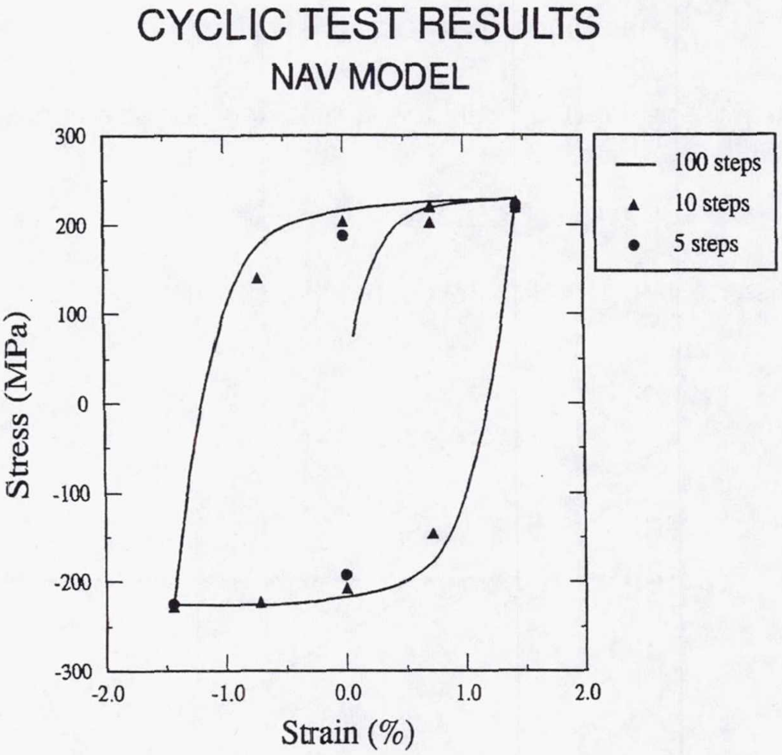
CYCLIC TEST RESULTS
NAV MODEL
Stress (MPa)
300
200
100
0
-100
-200
-300
-2.0
-1.0
0.0
1.0
2.0
Strain (%)
100 steps
10 steps
5 steps

Fig. 13

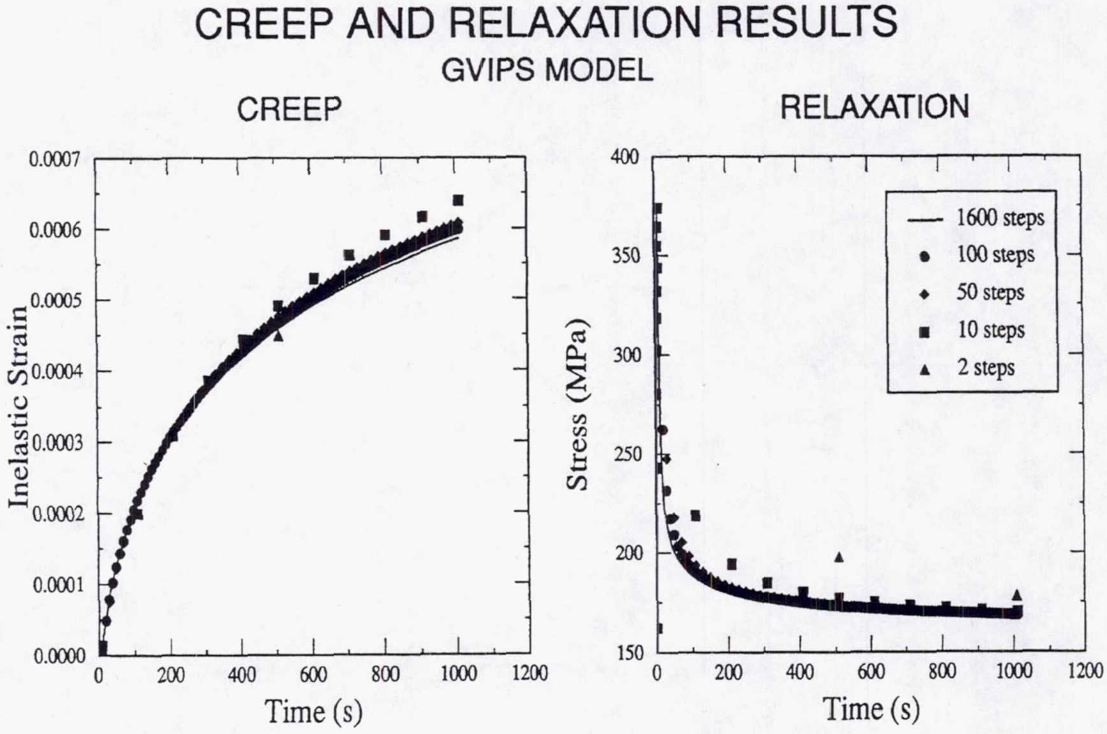
CREEP AND RELAXATION RESULTS
GVIPS MODEL
CREEP
RELAXATION
Inelastic Strain
0.0007
0.0006
0.0005
0.0004
0.0003
0.0002
0.0001
0.0000
0
200
400
600
800
1000
1200
Time (s)
Stress (MPa)
400
350
300
250
200
150
0
200
400
600
800
1000
1200
Time (s)
1600 steps
100 steps
50 steps
10 steps
2 steps

Fig. 14

CREEP AND RELAXATION RESULTS

NAV MODEL

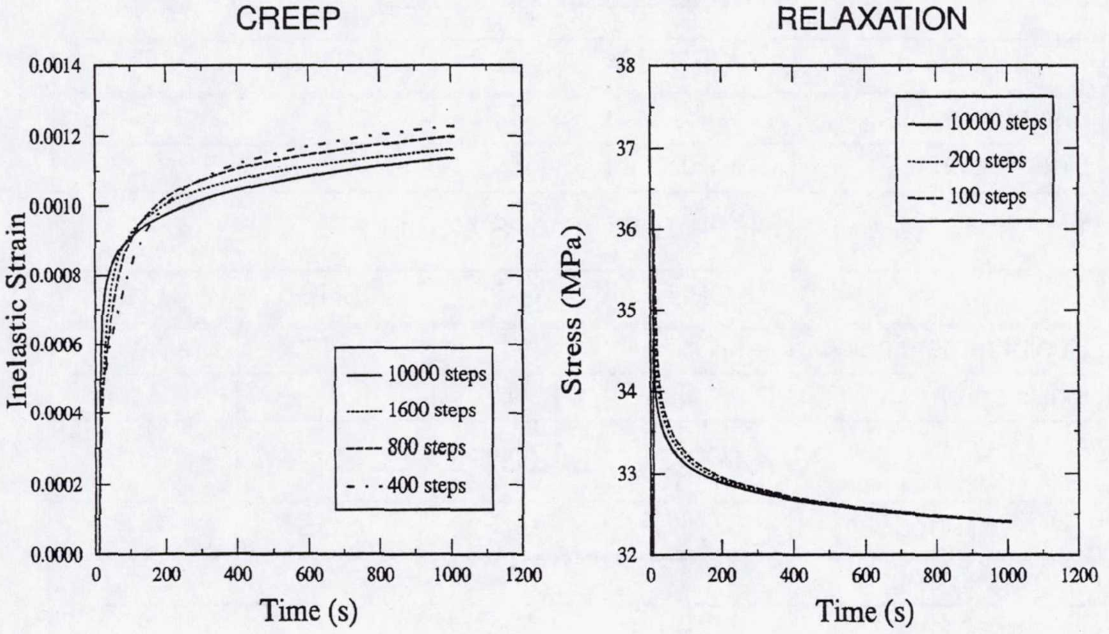

Fig. 15

NONPROPORTIONAL LOAD

NAV MODEL

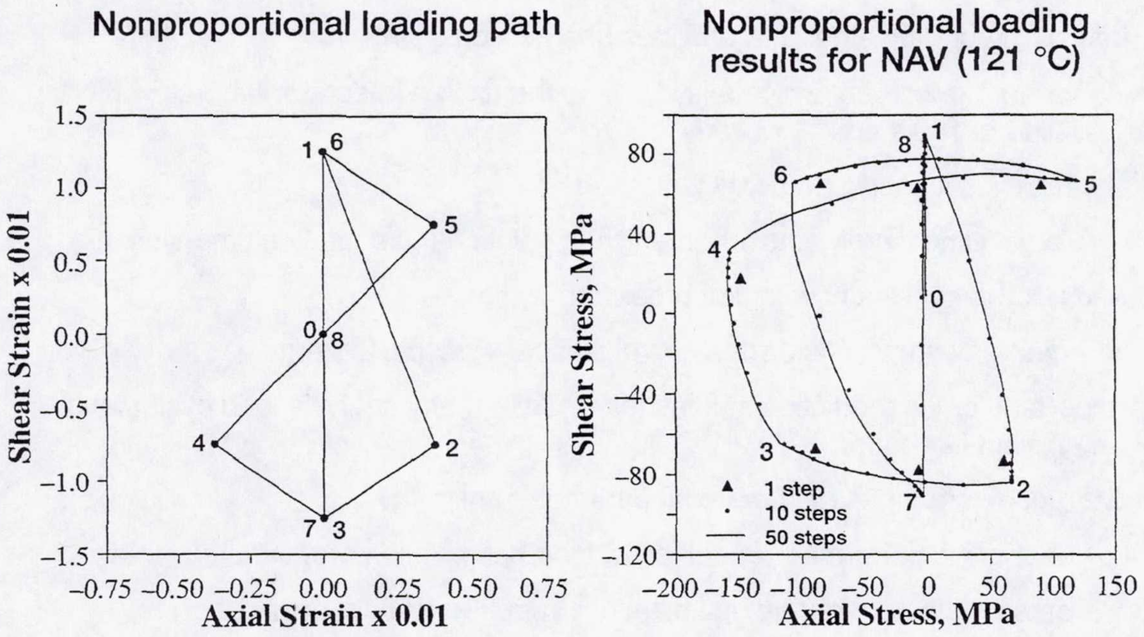

Fig. 16

LINE SEARCH COMPARISONS

CYCLIC TEST (NAV MODEL)

Method	CPU	GIT	SUB	LIT
Subincrementing	14.5	8	15	5
Line search	1.0	3	0	22

CREEP TEST (GVIPS MODEL)

Method	CPU	GIT	SUB	LIT
Subincrementing	1.5	4	4	2
Line search	1.0	4	0	2

RELAXATION TEST (GVIPS MODEL)

Method	CPU	GIT	SUB	LIT
Subincrementing	1.1	3	2	2
Line search	1.0	3	0	2

Fig. 17

SUMMARY/CONCLUSIONS

- Implicit integration algorithm provides unconditional stability
  - for both the creep and relaxation tests the explicit integrator (forward Euler) failed at 100 steps
  - implicit succeed using only 2 steps
  - "large" time increments for an efficient solution (computation time savings)
- Accuracy is consistent with first order formulation
  - creep: 2 steps, 8% error relaxation: 2 steps, 2% error
- Important for life prediction studies that require many analysis load cycles and an efficient integrator
- Current algorithm used in material parameter estimator
  - analysis is performed repeatedly during optimization: requires efficiency
  - parameters vary during optimization: requires robust integrator

Fig. 18

FUTURE RESEARCH

- Currently, implicit integration algorithm has been successfully implemented into the MARC user subroutine HYPELA
- Next: Implement algorithm into ABAQUS user subroutine UMAT
- Organize computer code to allow easier implementation of new constitutive models
- Develop for combined differential/integral hereditary representations

Fig. 19

PARAMETER ESTIMATION FOR VISCOPLASTIC MATERIAL MODELING*

ATEF F. SALEEB

Atef S. Gendy

Thomas E. Wilt

Department of Civil Engineering
The University of Akron
Akron, Ohio

Introduction

A key ingredient in the design of engineering components and structures under general thermomechanical loading is the use of mathematical constitutive models (e.g. in finite element analysis) capable of accurate representation of short and long term stress/deformation responses. In addition to the ever-increasing complexity of recent viscoplastic models of this type, they often also require a large number of material constants to describe a host of (anticipated) physical phenomena and complicated deformation mechanisms. In turn, the experimental characterization of these material parameters constitutes the major factor in the successful and effective utilization of any given constitutive model; i.e., the problem of constitutive parameter estimation from experimental measurements.

Traditionally, simple, basically trial-and-error procedures (graphical/mechanistic fitting) have been used for simple models, but these are certainly rather limited in more general situations Fig. 4 . This is particularly true in dealing with very large number of material constants that are often lacking in their direct physical interpretation, where complications due to the vastly different scaling and highly interactive nature of these parameters in a large test matrix under various controls (stress, strain, or mixed) under transient and steady-state conditions Fig. 2.

An urgent need and obvious need therefore exists for a systematic development of a general methodology for constitutive parameter estimation. This provides the main motivation for the present work.

Background and Approach

The problem belongs to the class of inverse problems [1] of mathematical programming and optimization theories. Its solution requires three major and interrelated parts Fig. 4 in its application to the present dynamic (time-variant) case; i.e., (a) primal analysis

---

* Work funded under NASA Grant NAG3-1746 (Technical Monitor: Steven Arnold)

(response functionals) for the differential form of the constitutive model, (b) sensitivity analysis, and (c) optimization of an error/cost function. The optimization algorithms for the last part (c) are presently very well developed [2]. This is not the case, however, regarding work on the other two, intimately related, parts (a) and (b). Mainly due to the greater mathematical complexity and associated intensive computational demands for the present dynamic and nonlinear case, compared to other more traditional optimization problems of linear structures. This renders unsuitable or even inapplicable several of the available solution methods and algorithms for primal and sensitivity analyses, Fig. 5.

For example, using an explicit integration method, with its known material-dependent conditional stability limits, becomes very ineffective for primal analysis, in which essentially thousands of "different materials" are being processed for response predictions (in a typical optimization cycle), thus making any adaptive time-stepping strategy very complicated, if at all possible. Similarly, in addition to several accuracy and numerical instability problems, the use of finite-differencing schemes for sensitivity analysis can easily become computationally prohibitive with the increase in material constants and time windows for fitting with long-duration tests.

The highlights of the mathematical formulations and main features of the present development (Figs. 6 and 7) are summarized as follows. Posed as a least-square, constrained, nonlinear mathematical optimization [2], we use an objective functional of the minimum-deviation-error type, i.e., differences in the predicted and measured responses at varying times. The material constants constitute the design variables, with several (side) constraints to ensure a physically-meaningful model. For the primal response analysis part, we utilize an implicit, unconditionally-stable, integration algorithm. Details and several applications of this scheme are described in a separate presentation in this proceeding; see also [3]. The sensitivity and analysis is of the direct type preformed on the basis of an explicit, recursive, form associated with the above integrator. Finally, the optimizer segment is of the gradient-based type, utilizing a sequential-quadratic programming scheme [4]. It is these three approaches combined that provide for the robustness and computational efficiency.

The overall strategy is summarized in the flow chart of Fig. 8. Its main driver (dubbed COMPARE for COnstitutive Model PARamter Estimator) controls the three solution modules (primal analysis, sensitivity, optimizer), together with the management of data files and results. From the practical standpoint (Fig. 9), the overall strategy is sufficiently general to handle comprehensive test-matrix data, under arbitrary load-control variables, multiaxial stress/strain tests, and transient as well as steady-state response measurements.

Results

All applications given utilize a viscoplastic model of the nonlinear kinematic-hardening type, GVIPS [5], having a total of eight material constants (Fig. 10). The first part of the studies [Figs. 11-15] are performed on a simulated ("exact") model material, for validation and to investigate the issues of parameter sensitivities, accuracy, comparisons, and

In the second part [Figs. 17-22], we use actual test-matrix results for TIMETAL21S material. This includes three tensile test under different strain rates, creep tests with three different imposed stresses, a relaxation test, as well as a three-step creep test. The "fitting" success in this latter, more realistic application, with vastly different conditions and very large number of data points, clearly points to the potential benefit and practicality of the general methodology.

References

1. Bui, H. D., and Tanaka, M. (editors): Inverse Problems in Engineering, Balkema, Rotterdam, 1994.

2. Luenberger, D. G.: Linear and Nonlinear Programming, second edition, Addison-Wesley, Reading, 1984.

3. Saleeb, A. F. and Li, W.: Robust Implicit Integration Schemes for Generalized Viscoplastic Models - Part I: Theoretical Developments and Applications; Part II: Algorithmic Developments and Implementation, NASA CR-195453, 1995.

4. Schittkowski, K.: The Nonlinear Programming Method of Wilson, Han, and Powell with an Augmented Lagrangian Type Line Search Function, Numerische Mathematik, Vol. 38, No. 1, pp.83-114, 1981.

5. Arnold, S. M., Saleeb, A. F., and Castelli, M. G.: A Fully Associative, Nonlinear Kinematic, Unified Viscoplastic Model for Titanium Based Matrices, Life Prediction Methodology for Titanium Matrix Composites, ASTM STP 1253, W. S. Johnson, J. M. Larsen, and B. N. Cox, Eds. 1996, or NASA TM-106609, 1994.

OUTLINE

- Motivation
- Objectives
- Background
- Mathematical formulation
- Computational algorithms
- Sensitivity analysis
- Applications

Fig. 1

MOTIVATION

Two major obstacles to fully utilizing recent time-dependent/hereditary constitutive models in practical engineering analysis:

- Lack of efficient and robust integration algorithms
- **Difficulties associated with characterizing large number of required material parameters**
  - Most material parameters lack obvious/direct physical interpretations
  - Even under load histories in simple laboratory tests, several parameters will highly interact to affect predicted responses
  - Further complications due to:
    - (i) Incompleteness of response measurment in both time and state
    - (ii) Vastly different scaling of constitutive parameters
  - Urgent need exists for specific guidelines in the systematic development of general methodology for constitutive- parameter-identification

Fig. 2

OBJECTIVES

General: Systematic development of general methodology for constitutive parameter estimation

Specific:

- Mathematical formulation of a basic optimal material parameter estimation scheme
- Computational algorithms for implementation
- Validation tests and performance studies
- Alternatives for further refinements in fitting;
  that is, variable/cost function scaling, weights, multicriteria optimization theories, etc.

Fig. 3

BACKGROUND

- "Traditional" approaches for constitutive parameter estimations:
  - Essentially trial-and-error in nature
  - Based on several assumptions about test conditions and material behavior that are rarely satisfied in actual tests
  - Difficult to control error propagation in sequential evaluations of parameters
  - Rather limited in applications
- Modern approaches for constiutive parameter estimations based on mathematical programming and optimization theories:
  - More general/systematically derived
  - Three major parts for modular implementations:
    - (a) Primal analysis for response functionals (integrated history)
    - (b) Sensitivity analysis
    - (c) Optimization of "cost" function

Fig. 4

BACKGROUND

- Methods and algorithmic details differ greatly for the sensitivity analysis:
  - Finite difference methods (prohibitively expensive; prone to errors)
  - Evolutionary sensitivities approach (expensive two-subproblem integrations; special coding for number of parameters dependent sizes of arrays; stiffness/singularity problems)
  - Adjoint sensitivity approach (regressive computations with large storage requirements; or increased computational cost for terminal adjoint problems)
  - Direct-differentiation sensitivity (most effective and accurate when consistently derived with the underlying implicit integration of the model)

Fig. 5

MATHEMATICAL FORMULATION

- Framework required characteristics:
  - Coupled nonlinear system (internal/external state variables)
  - Transient response with different possible steady-state conditions (time variance)
  - Arbitrary (optional) control variables; i.e., stress-, strain-, mixed-types of loading (general test matrix)
- Approach:
  - A least-square, constrained, nonlinear mathematical optimization problem
  - Material parameters constitute the design variables, with several associated side constraints to ensure physically meaningfull model
  - The technique is of the minimum-deviation-error type, for the integrated multiaxial response (functionals)

Fig. 6

MATHEMATICAL FORMULATION

- Noteworthy aspects:

  (i) Robustness and effectiveness:

  - Unconditionally stable implicit integration for primal analysis (model problem)
  - Direct-differentiation approach for accurate sensitivity analysis
  - State-of-the-art optimizer using sequential quadratic programming (with exact gradient and variable metric/Hessian) for least-squares minimization

  (ii) Computational efficiency:

  - Non-iterative "exact" sensitivities (once after primal analysis time-step convergence)
  - Effective scaling for both the design variables and the objective function in optimization
  - Enhanced iterations with line searches in implicit integration

Fig. 7

COMPUTATIONAL ALGORITHM

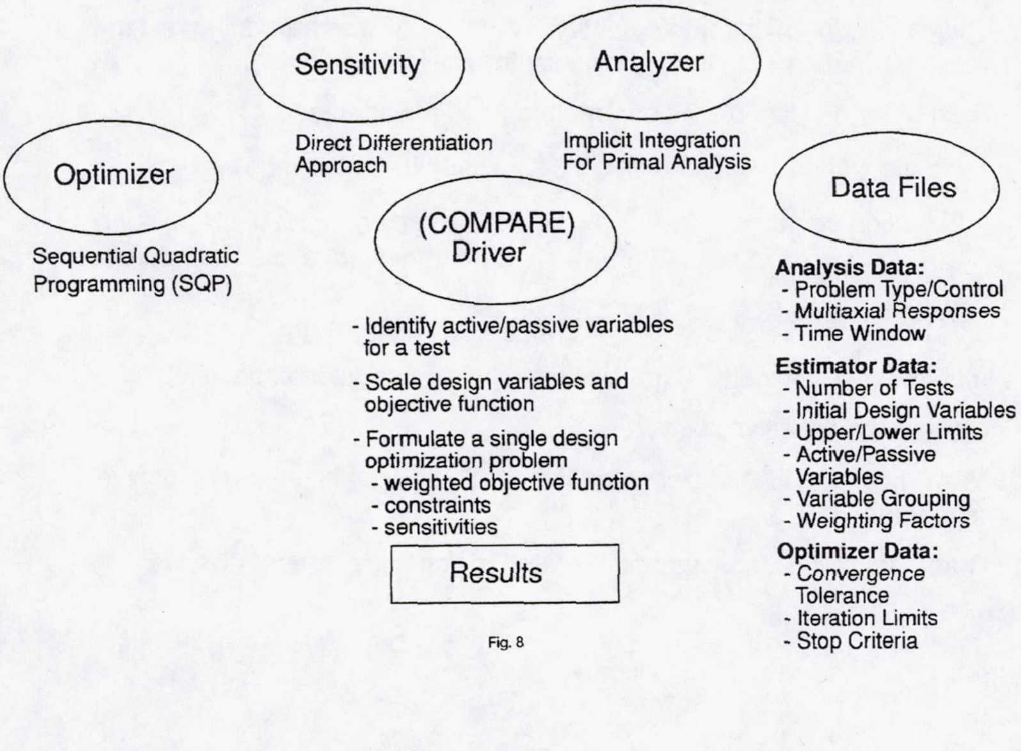

Sensitivity

Direct Differentiation Approach

Analyzer

Implicit Integration For Primal Analysis

Optimizer

Sequential Quadratic Programming (SQP)

(COMPARE) Driver

- Identify active/passive variables for a test
- Scale design variables and objective function
- Formulate a single design optimization problem
  - weighted objective function
  - constraints
  - sensitivities

Results

Data Files

Analysis Data:
- Problem Type/Control
- Multiaxial Responses
- Time Window

Estimator Data:
- Number of Tests
- Initial Design Variables
- Upper/Lower Limits
- Active/Passive Variables
- Variable Grouping
- Weighting Factors

Optimizer Data:
- Convergence Tolerance
- Iteration Limits
- Stop Criteria

Fig. 8

COMPUTATIONAL ALGORITHMS

- Features and capabilities:
  - General test matrix with arbitrary control (stress, strain, or mixed) with multiaxial measurements (two normal plus one shear component), e.g.,

Stress-control	Creep
Mixed-control	Relaxation
Stress-control	Tension/constant stress rate
Mixed-control	Tension/torsion test

  - Active/passive design parameter activation (e.g., parametric study)
  - Upper/lower side constraints
  - Arbitrary number of tests and time windows selected for fitting
  - Goodness-of-fit statistical measures

Fig. 9

SENSITIVITY ANALYSIS

- Model problem
  - Unified viscoplasticity with potential GVIPS (nonlinear hardening; static recovery mechanism; isotropic/nonisotropic yielding)
  - Total of seven viscoplastic parameters (design variables)

Flow equation = 2 (viscosity μ; exponent n)

Evolution equation = 4 2 (hardening; modulus H, exponent β)
+ 2 (recovery; modulus R, exponent m)

Yield threshold = 1 (κ_t)

- Simulated "actual" material (perfect model representation capability)
  - Normalized sensitivity plots
  - "Accuracy" and efficiency comparisons with traditional finite-differencing schemes
  - Creep, relaxation, constant-strain-rate tension as representative tests

Fig. 10

SENSITIVITY ANALYSIS (SIMULATED TESTS)

DESIGN PARAMETERS	T_1		T_{25}		T_{50}	
	IMPLICIT	F.D.	IMPLICIT	F.D.	IMPLICIT	F.D.
κ_T	1.7899 (10)-1	1.7864 (10)-1	4.5844	4.5816	4.5844	4.5817
n	-1.1361 (10)-1	-1.1384 (10)-1	2.1588 (10)-1	2.1525 (10)-1	2.1588 (10)-1	2.1525 (10)-1
μ	1.4583 (10)-6	1.4570 (10)-6	-1.7294 (10)-6	-1.7291 (10)-6	-1.7295 (10)-6	-1.7291 (10)-6
m	9.2111 (10)-19	0.000	-6.3965 (10)-6	-6.4033 (10)-6	-1.5127 (10)-5	-1.5144 (10)-5
β	4.2054 (10)-3	4.2041 (10)-3	-9.4439 (10)-1	-9.4236 (10)-1	-9.4395 (10)-1	-9.4325 (10)-1
R	-9.1043 (10)-9	0.000	-9293.57	-9293.71	-2.1978 (10)+5	-2.1976 (10)+5
H	1.4634 (10)-7	1.4628 (10)-7	3.6125 (10)-5	3.6085 (10)-5	3.6124 (10)-5	3.6084 (10)-5

Scaling

Time Evolution

Fig. 11

SENSITIVITY ANALYSIS (SIMULATED TESTS)

TIME EVOLUTION

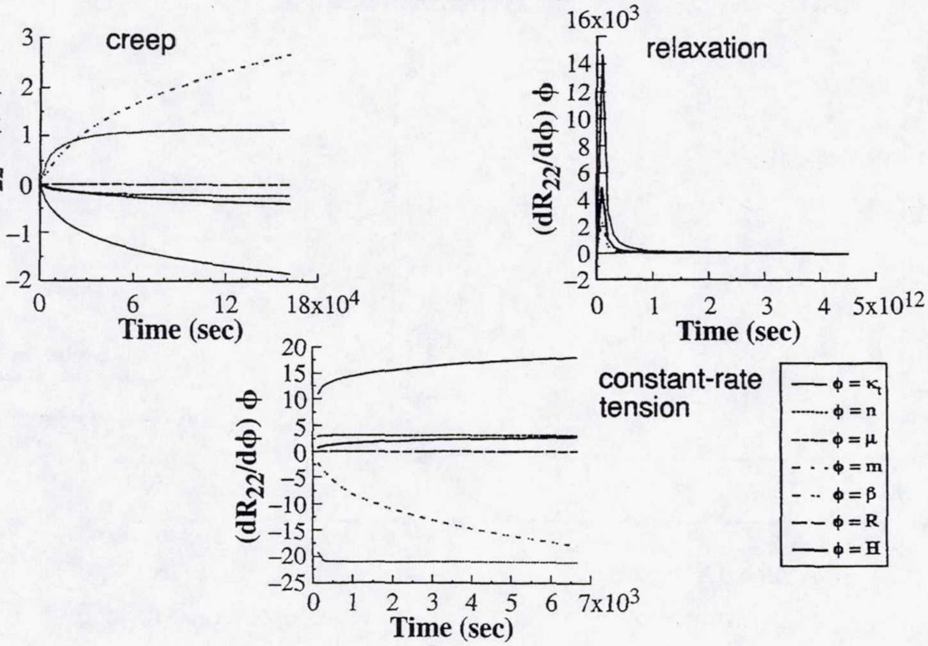

Fig. 12

EFFICIENCY OF IMPLICIT SENSITIVITY SCHEME

		TENSILE	CREEP	RELAXATION
RELATIVE CPU	IMPLICIT	1.0	1.0	1.0
	F.D.	8.004	8.235	7.931

General Estimate:

Relative CPU $\cong 8 \times N_i \times N_w \times N_t \times \eta$

N_i = Number of integration steps per each (equal) optimization interval

N_w = Number of (equal) sampling points (time windows) per test

N_t = Number of total tests

η = Trial-Differencing-Accuracy Factor $\eta = 2 \rightarrow 10 \rightarrow ?$

Fig. 13

TYPICAL CONVERGENCE AND FITTING ACCURACY
(SIMULATED MATERIAL FOR TENSILE/CREEP/RELAXATION TEST)

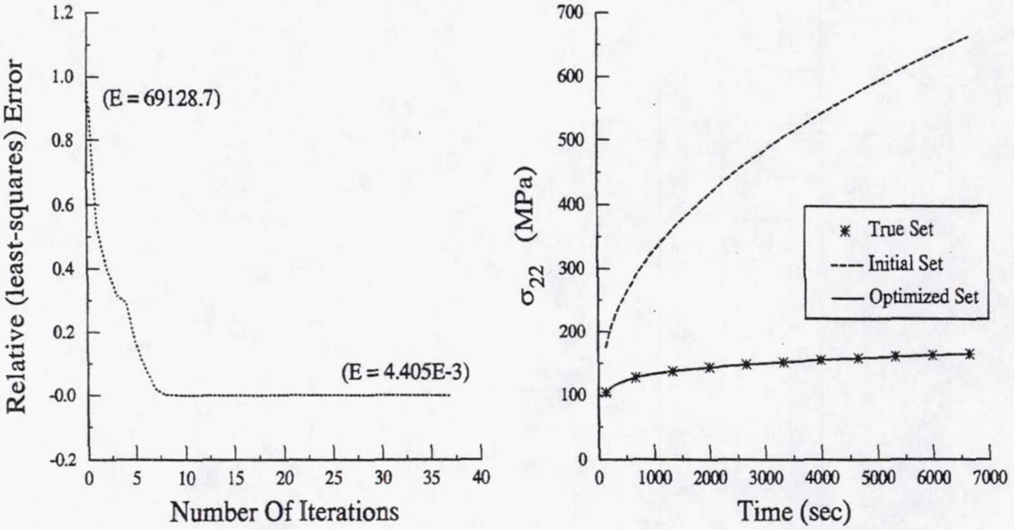

Convergence

Accuracy in Tensile Test

Fig. 14

TYPICAL CONVERGENCE AND FITTING ACCURACY

(SIMULATED MATERIAL FOR TENSILE/CREEP/RELAXATION TEST

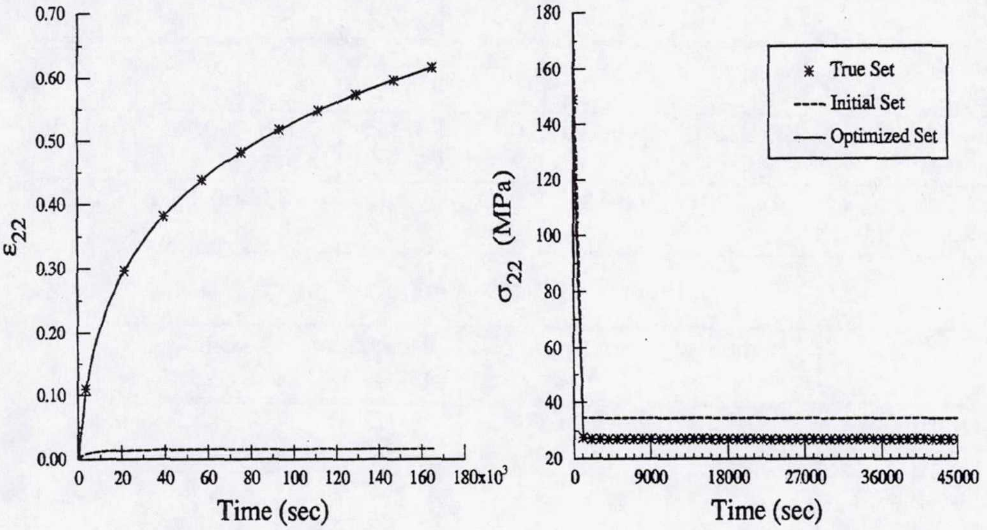

Accuracy in Creep Test

Accuracy in Relaxation Test

Fig. 15

APPLICATIONS

- Material: - *TIMETAL 21S*
  - Temperature = 650°C
- Experimental tests available
  - (a) 3 tensile tests
  - (b) 3 creep test
  - (c) 1 relaxation test
  - (d) single 3-step creep test
- Results/Studies
  - varied number of tests included in fitting
  - varied sampling-time intervals within each test
  - varied material-parameter bounds and optimization weights
  - comprehensive case: all tests (a)-(d) included in fitting

Fig. 16

SUMMARY OF COMPREHENSIVE FIT CASE

(*TIMETAL 21S*; 8 TESTS; T=Tensile, C=Creep, R=Relaxation, SC=3-Step Creep)

	T1	T2	T3	C1	C2	C3	R	SC
Number of Fitting Points	93	67	57	96	103	107	72	285
Weight Factors (equal weight)	0.125	0.125	0.125	0.125	0.125	0.125	0.125	0.125
Weight Factors (variable weight)	0.1193	0.1657	0.1947	0.116	0.1077	0.1037	0.1542	0.0389

a) Fitted Points and Weights

	Number of Iterations	Number of Function Calls	Number of Gradient Calls	Normalized CPU
Estimated (equal)	53	61	54	1.0
Estimated (variable)	49	54	50	0.882

b) Solution Efficiency

Fig. 17

SUMMARY OF COMPREHENSIVE FIT CASE

(*TIMETAL 21S*; 8 TESTS)

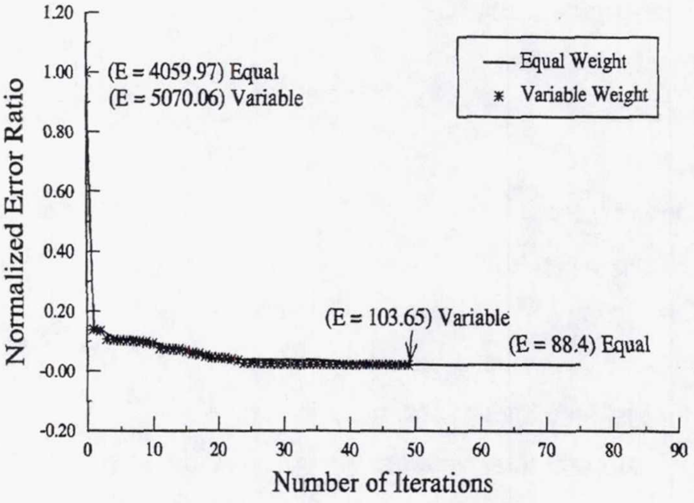

Fig. 18

TENSILE BEHAVIOR CORRELATION

(COMPREHENSIVE FIT)

Given:

- a "far" initial guess
- with/without bounds on parameters

→ *unique "optimal" response*

$\dot{\varepsilon}_0 = 8.333x10^{-6}$

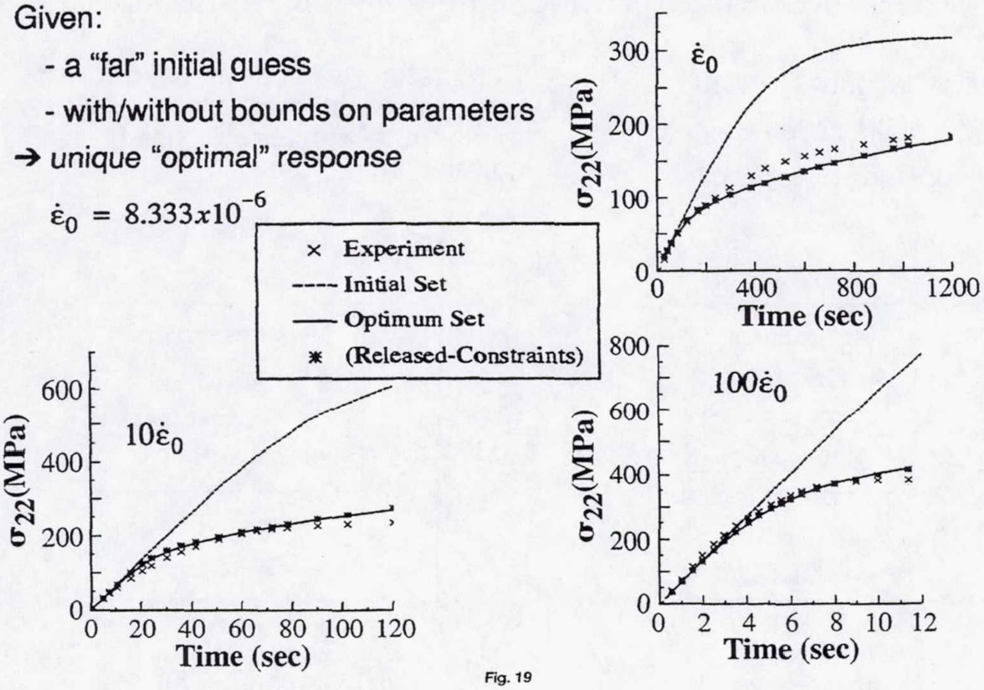

Fig. 19

CREEP BEHAVIOR CORRELATION

(COMPREHENSIVE FIT)

Given:

- a "far" initial guess
- varying sample-time intervals

→ unique "optimal" response

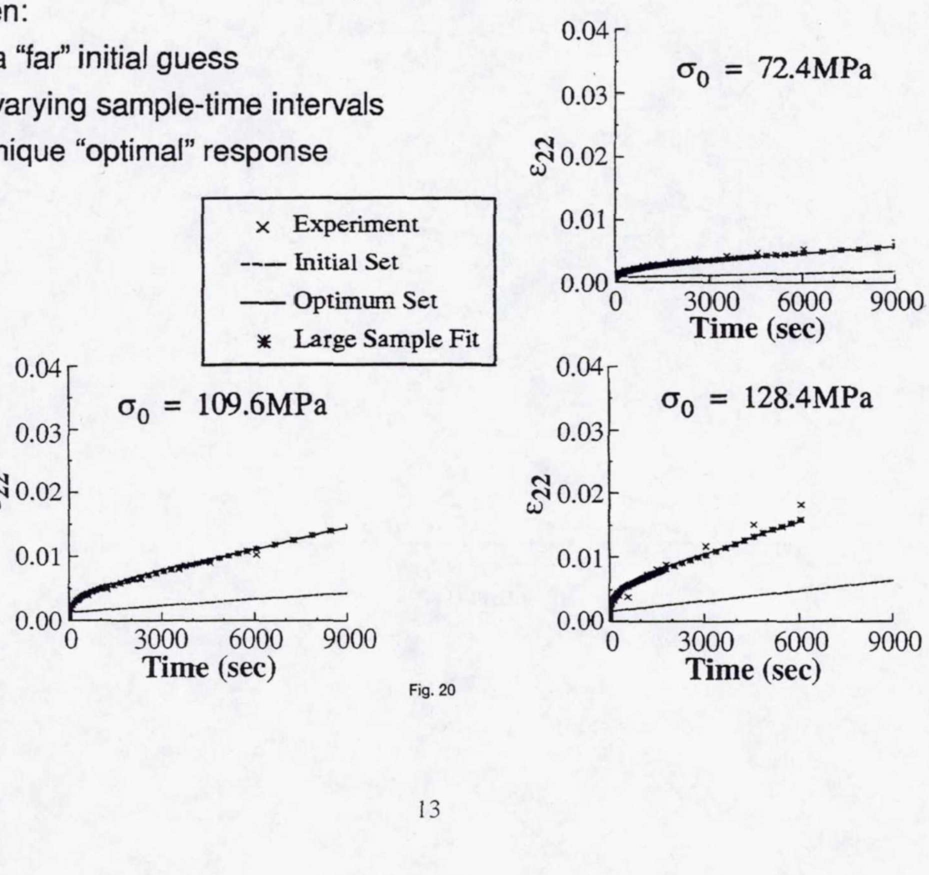

Fig. 20

RELAXATION BEHAVIOR CORRELATION

(COMPREHENSIVE vs. SINGLE-RELAXATION TEST FIT

Given:

- a "far" initial guess
- variable optimization weights

→ unique optimized response

Comprehensive fit gives better overall predictions with comparable accuracy to the "pure" single-response curve correlation

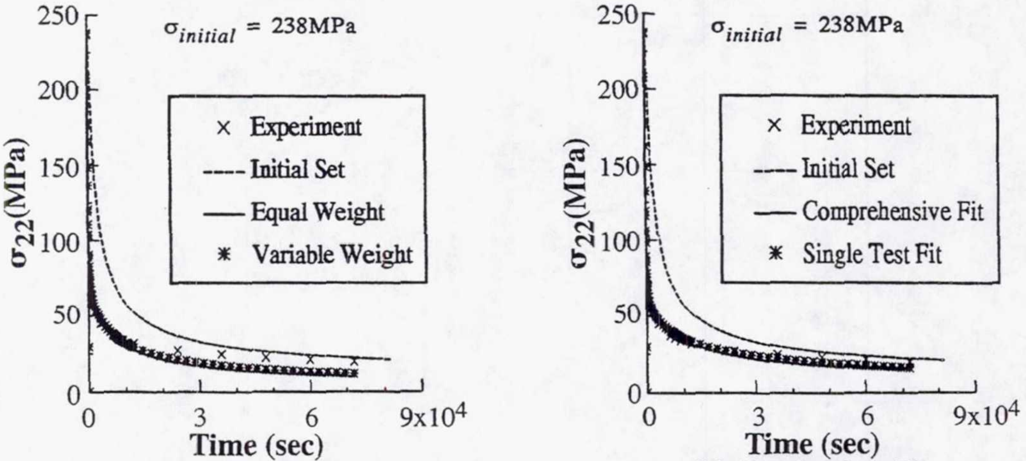

(a) Comprehensive Fit

(b) Single-Test Fit

Fig. 21

3-STEP CREEP CORRELATION

(COMPREHENSIVE FIT)

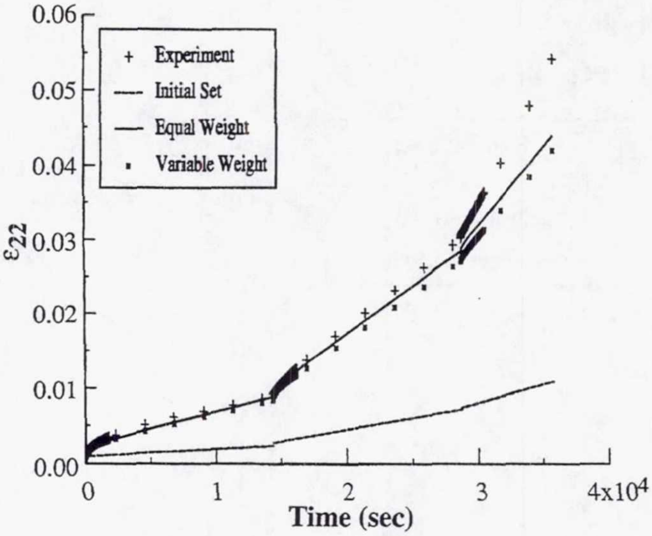

Fig. 22

SUMMARY/CONCLUSIONS

- Validation with exact (simulated) material
    - Given an accurate constitutive model, exact correlation is achievable by COMPARE
- Assessment with real materials (*TIMETAL 21S*)
    - Automated material parameter estimation enables the model to achieve its "best" correlation
    - Serves as a tool for identifying critical experiments to maximize pertinent "data content" (e.g., one test for tension, creep, cyclic and (initial) relaxation)
    - Requires minimum "user expertise"
    - Gives a measure for model suitability and directions for its further enhancement in realistic range of applications
    - Estimates for effects of model versus experimental (noisy data) deficiencies (COMPARE's knowledge of parameter sensitivities)

Fig. 23

SUMMARY/CONCLUSIONS

- Including more data points in fitting enhances the optimizer convergence speed

- New model implementation
    - Demands more than just a definition of elementary (differential) flow/evolution equations - integrated form Jacobian

Fig. 24

FUTURE WORK

- Inclusion of new material models in COMPARE library
- Experience in applications with multiaxial test fitting
- "User-friendly" enhancements

Fig. 25

A VISCOPLASTIC CONSTITUTIVE THEORY FOR MONOLITHIC CERAMIC MATERIALS--I

LESLEY A. JANOSIK
NASA Lewis Research Center
Cleveland, Ohio

and

Stephen F. Duffy, PhD, PE*
Cleveland State University
Cleveland, Ohio

Introduction

With increasing use of ceramic materials in high temperature structural applications such as advanced heat engine components, the need arises to accurately predict thermomechanical behavior (Fig. 1). This paper, which is the first of two in a series, will focus on inelastic deformation behavior associated with these service conditions by providing an overview of a viscoplastic constitutive model that accounts for time-dependent hereditary material deformation (e.g., creep, stress relaxation, etc.) in monolithic structural ceramics.

Early work in the field of metal plasticity indicated that inelastic deformations are essentially unaffected by hydrostatic stress. This is not the case, however, for ceramic-based material systems, unless the ceramic is fully dense. The theory presented here allows for fully dense material behavior as a limiting case. In addition, ceramic materials exhibit different time-dependent behavior in tension and compression. Thus, inelastic deformation models for ceramics must be constructed in a fashion that admits both sensitivity to hydrostatic stress and differing behavior in tension and compression. A number of constitutive theories for materials that exhibit sensitivity to the hydrostatic component of stress have been proposed that characterize deformation using time-independent classical plasticity as a foundation. However, none of these theories allow different behavior in tension and compression. In addition, these theories are somewhat lacking in that they are unable to capture creep, relaxation, and rate-sensitive phenomena exhibited by ceramic materials at high temperature.

When subjected to elevated service temperatures, ceramic materials exhibit complex thermomechanical behavior that is inherently time-dependent, and hereditary in the sense that current behavior depends not only on current conditions, but also on thermo-mechanical history. The objective of this work (Fig. 2) is to present the formulation of a macroscopic continuum theory that captures these time-dependent phenomena. Specifically, the overview contained in this paper focuses on the multiaxial derivation of the constitutive model, and examines the scalar threshold function and its attending geometrical implications. For complete details of the model, the reader is directed to the recent publication by Janosik and Duffy (ref. 1).

Flow Potential

Using continuum principles of engineering mechanics, the complete viscoplastic theory (Fig. 3) is derived from a scalar dissipative potential function, identified here as Ω (Fig. 4), first proposed by Robinson (ref. 2) for a J_2 model, and later extended to sintered powder metals by Duffy (ref. 3). The specific form adopted for the flow potential is an

---

* NASA Resident Research Associate at Lewis Research Center.

integral format proposed by Robinson (ref. 2) that has similar geometrical interpretations (e.g., convexity and normality) as the yield function encountered in classical plasticity. This isothermal formulation includes parameters for viscosity, hardening, recovery, and unitless stress exponents. Also included is the octahedral threshold shear stress, K, which is generally considered a scalar state variable that accounts for isotropic hardening (or softening). However, since isotropic hardening is often negligible at high homologous temperatures (≥ 0.5), to a first approximation K is taken to be a constant for metals. This assumption is adopted in the present work regarding ceramic materials. Specific details regarding the experimental test matrix needed to characterize these parameters will appear in a second article.

Threshold Function

The specific formulation used here for the threshold function, F (a component of the flow potential function), was originally proposed by Willam and Warnke (ref. 4) in order to formulate constitutive equations for time-independent classical plasticity behavior observed in cement and unreinforced concrete. Willam and Warnke (ref. 4) proposed a yield criterion for concrete that admits a dependence on the hydrostatic component of stress and explicitly allows different material responses in tension and compression (Fig. 5). Several formulations of their model exist, i.e., a three-parameter formulation and a five-parameter formulation. For simplicity, the work presented here builds on the three-parameter formulation shown in Fig. 6.

The Willam-Warnke criterion uses stress invariants to define the functional dependence on the Cauchy stress (σ_{ij}) and internal state variable (α_{ij}). The invariants $\tilde{I}_1$ and $\tilde{J}_3$ admit a sensitivity to hydrostatic stress, and account for different behavior in tension and compression (since this invariant changes sign when the direction of a stress component is reversed), respectively. Note that a threshold flow stress is similar in nature to a yield stress in classical plasticity. The specific details involved in deriving the final form of the function F can be found in Willam and Warnke (ref. 4). A similar functional form is adopted for the scalar state function G. This formulation assumes a threshold does not exist for the scalar function G, and follows the framework of previously proposed constitutive models based on Robinson's (ref. 2) viscoplastic law.

For the Willam-Warnke three-parameter formulation, the model parameters include σ_t, the tensile uniaxial threshold stress, σ_c, the compressive uniaxial threshold stress, and σ_{bc}, the equal biaxial compressive threshold stress (Fig. 7). The Willam-Warnke model yields a flow surface in the shape of a pyramid with a triangular base in the Haigh-Westergaard stress space, as depicted in Fig. 5. As a reference, typical J_2 plasticity models have yield surfaces that are right circular cylinders in the Haigh-Westergaard stress space.

Flow Surfaces - Interpretation

As in Robinson's original theory, the current model is closely tied to the concepts of a potential function and normality. It is this potential-normality structure that provides a consistent framework. According to the stability postulate of Drucker (ref. 5), the concepts of normality and convexity are important requirements which must be imposed on the development of a flow or yield surface. Constitutive relationships developed on the basis of these requirements assure that the inelastic boundary-value problem is well posed, and solutions obtained are unique. Experimental work by Robinson and Ellis (ref. 6) has demonstrated the validity of the potential-normality structure relative to an isotropic J_2 alloy (i.e., type 316 stainless steel). With this structure, the direction of the inelastic strain rate vector for each stress point on a given surface is directed normal to the flow surface $F=constant$, as illustrated in Fig. 8. Without experimental evidence to the contrary, it is postulated that this structure is similarly valid for isotropic monolithic ceramic materials. The convexity of the proposed flow surface assures stable material behavior, i.e., positive dissipation of inelastic work, which is based on thermodynamic principles. The convexity requirement (Fig. 8) also implies that level surfaces of a function are closed surfaces, since an open region of the flow surface allows the existence of a load path along which failure will never occur. Finally, the Willam-Warnke flow criterion (and the constitutive theory presented herein) degenerates to simpler models (e.g., the two-parameter Drucker-Prager and the one-parameter Von Mises) under special limiting conditions (Fig. 9).

Constitutive Model

Constitutive equations formulated for the flow law (strain rate) and evolutionary law are given in Fig. 10. These relationships employ stress invariants to define the functional dependence on the Cauchy stress and a tensorial state variable. The potential nature of Ω is exhibited by the manner in which the flow and evolutionary laws are derived. The flow law, $\dot{\varepsilon}_{ij}$, is derived from Ω by taking the partial derivative with respect to the applied stress. The adoption of a flow potential and the concept of normality, as expressed in the flow law, were introduced by Rice (ref. 7). In his work this relationship was established using thermodynamic arguments. The authors wish to point out that this concept holds for each individual inelastic state. The evolutionary law, $\dot{\alpha}_{ij}$, is similarly derived from the flow potential. The rate of change of the internal stress is expressed by taking the partial derivative of Ω with respect to the internal stress, and multiplying by a scalar hardening function dependent on the inelastic state variable (i.e., the internal stress) only. Using arguments similar to Rice's, Ponter and Leckie (ref. 8) have demonstrated the appropriateness of this type of evolutionary law.

Example

A preliminary example was performed to illustrate some of the capabilities of the multiaxial constitutive model developed herein, and to compare the results with those obtained utilizing a J_2 model. In addition, the effects of varying the Willam-Warnke parameters were demonstrated. Figs. 11-13 depict the applied loading condition, approach, and observed results.

A second article will examine specific time-dependent stress-strain behavior that can be modeled with the constitutive relationship presented in this article. No attempt is made here to assess the accuracy of the model in comparison to experiment. A quantitative assessment is reserved for a later date, after the material constants have been suitably characterized for a specific ceramic material.

Summary/Conclusion

The overview presented in this paper is intended to provide a qualitative assessment of the capabilities of this viscoplastic model in capturing the complex thermomechanical behavior exhibited by ceramic materials at elevated service temperatures. Constitutive equations for the flow law (strain rate) and evolutionary law have been formulated based on a threshold function which exhibits a sensitivity to hydrostatic stress and allows different behavior in tension and compression. Further, inelastic deformation is treated as inherently time-dependent. A rate of inelastic strain is associated with every state of stress. As a result, creep, stress relaxation, and rate sensitivity are phenomena resulting from applied boundary conditions and are not treated separately in an ad hoc fashion. Incorporating this model into a non-linear finite element code would provide industry the means to numerically simulate the inherently time-dependent and hereditary phenomena exhibited by these materials in service.

References

1. Janosik, L.A.; Duffy, Stephen F.: "A Viscoplastic Constitutive Theory for Monolithic Ceramics - I," Transactions of the ASME Journal of Engineering for Gas Turbines and Power, Paper No. 96-GT-368. Presented at the ASME International Gas Turbine Congress, Exposition, and Users' Symposium, Birmingham, UK, June 10-13, 1996.
2. Robinson, D.N.: "A Unified Creep-Plasticity Model for Structural Metals at High Temperature," ORNL/TM 5969, 1978.
3. Duffy, S.F.: "A Unified Inelastic Constitutive Theory for Sintered Powder Metals," *Mechanics of Materials*, Vol. 7, 1988, pp. 245-254.
4. Willam, K.J.; and Warnke, E.P.: "Constitutive Model for the Triaxial Behaviour of Concrete, *Int. Assoc. Bridge Struct. Eng. Proc.*, Vol. 19, 1975, pp. 1-30.
5. Drucker, D.C.: "A Definition of Stable Inelastic Material", *Journal of Applied Mechanics*, Vol. 26; *ASME Transactions*, Vol. 81, 1959, pp. 101-106.
6. Robinson, D.N.; and Ellis, J.R.: "Experimental Determination of Flow Potential Surfaces supporting a Multiaxial Formulation of Viscoplasticity," *Proceedings, 5th International Seminar on Inelastic Analysis and Life Prediction in High Temperature Environments*, Paris, France, 1985.
7. Rice, J.R.: "On the Structure of Stress-Strain Relations for Time-Dependent Plastic Deformation in Metals," *Journal of Applied Mechanics*, 37, 728, 1970.
8. Ponter, A.R.S.; and Leckie, F.A.: "Constitutive Relationships for Time-Dependent Deformation of Metals," *ASME Journal of Engineering Materials and Technology*, Vol. 98, 1976.

CERAMIC LIFE PREDICTION ANALYSIS

POTENTIAL FAILURE MODES IN HEAT ENGINE APPLICATIONS:

- Time-Independent Failure Modes:
  - Fast fracture (tension, compression, shear)
  - Buckling
- Time-Dependent Failure Modes:
  - Static, dynamic, and cyclic fatigue
  - Creep crack growth
  - Creep deformation response
  - Stress corrosion and oxidation
  - Impact and contact loading response

Current Capabilities:

✔Fast-fracture
✔Subcritical Crack Growth

➨ High loading
➨ Low to intermediate temperatures (~2000 °F)

Needed Capabilities:

- Creep deformation
- Creep rupture

➨ Extended duration loading
➨ Elevated temperatures (~2400 °F)

Fig. 1

OBJECTIVE

To present a multiaxial continuum theory which accounts for time-dependent hereditary material deformation behavior of isotropic structural ceramics.

OUTLINE:

- Introduction to Viscoplasticity
- Flow Potential
- Threshold Function
- Flow Surfaces-Interpretation
- Constitutive Model
- Example
- Conclusions/Enhancements

Fig. 2

VISCOPLASTICITY

Phenomenological Approach:

Scalar Potential Function → → *Continuum principles* → **Viscoplastic Constitutive Model**

(Considers effects at the macrostructural level)

Plasticity:

$F<0$	Elastic Behavior
$F=0$	Yield Surface
$F>0$	Not Allowed

Viscoplasticity:

$F<0$	Elastic Behavior
$F=0$	Threshold Flow Surface
$F\geq 0$	Viscoplastic Flow

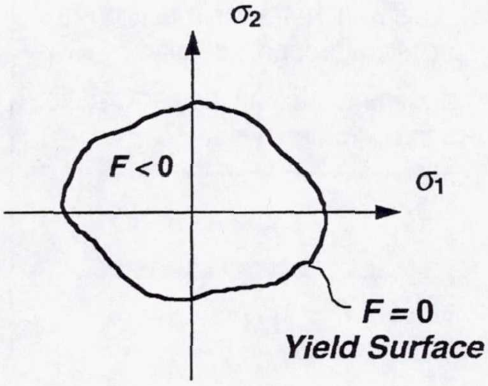

Fig. 3

FLOW POTENTIAL FUNCTION

General form:

$$\Omega = \Omega\left(\sigma_{ij},\alpha_{ij},T\right) \xrightarrow[\text{Assume isothermal conditions}]{} \Omega = \Omega\left(\underset{\text{applied stress}}{\sigma_{ij}},\underset{\text{internal state variable}}{\alpha_{ij}}\right)$$

Specific form:

$$\boxed{\Omega = K^2\left[\left(\frac{1}{2\mu}\right)\int F^n dF + \left(\frac{R}{H}\right)\int G^m dG\right]}$$

(Robinson, 1978)

where μ, R, H, n, m, and K are material constants characterizing viscoplasticity

$$\boxed{F = F\left(\Sigma_{ij},\eta_{ij}\right)} \qquad \boxed{G = G\left(a_{ij},\alpha_{ij}\right)}$$

where:

$$\Sigma_{ij} = S_{ij} - a_{ij} \qquad S_{ij} = \sigma_{ij} - (1/3)\,\sigma_{kk}\,\delta_{ij}$$
$$\eta_{ij} = \sigma_{ij} - \alpha_{ij} \qquad a_{ij} = \alpha_{ij} - (1/3)\,\alpha_{kk}\,\delta_{ij}$$

Fig. 4

THRESHOLD FUNCTION

- Originally proposed to formulate constitutive equations for time-independent classical plasticity behavior in cement and unreinforced concrete
- Three-parameter model
- Assumes material is isotropic
- Allows different behavior in tension & compression through the invariant J_3
- Admits dependence on the hydrostatic stress through the invariant I_1

$$\boxed{F = F(I_1, J_2, J_3)}$$

where $I_1 = (1/3)\ \sigma_{ii}$
$J_2 = (1/2)\ S_{ij}\ S_{ji}$
$J_3 = (1/3)\ S_{ij}S_{jk}S_{ki}$

Willam-Warnke Model

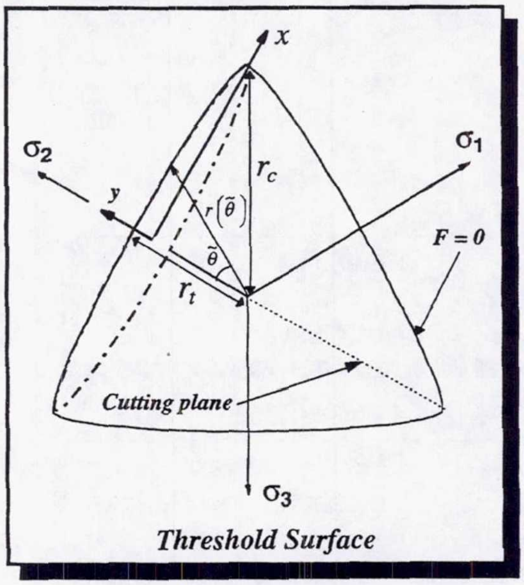

Threshold Surface

Fig. 5

THRESHOLD FUNCTION

Inelastic deformation occurs for stress states where

$$\boxed{F\left(\Sigma_{ij}, \eta_{ij}\right) > 0}$$

Define:

$$\tilde{I}_1 = \eta_{ii}$$

$$\tilde{J}_2 = \left(\frac{1}{2}\right) \Sigma_{ij}\, \Sigma_{ij}$$

$$\tilde{J}_3 = \left(\frac{1}{3}\right) \Sigma_{ij}\, \Sigma_{jk}\, \Sigma_{ki}$$

Willam-Warnke
3-Parameter Formulation:

$$\boxed{F\left(\tilde{I}_1, \tilde{J}_2, \tilde{J}_3\right) = \frac{1}{\sigma_c}\left[\frac{1}{r(\tilde{\theta})}\right]\left[\frac{2\tilde{J}_2}{5}\right]^{1/2} + \frac{\tilde{I}_1}{3\rho\sigma_c} - 1}$$

(Willam and Warnke, 1975)

The dependence on $\tilde{J}_3$ is introduced through the angle of similitude $\tilde{\theta}$

$$Cos\left(3\tilde{\theta}\right) = \frac{\left(3\sqrt{3}\right)\tilde{J}_3}{2\left(\tilde{J}_2\right)^{3/2}}$$

Note that similar relationships exist for scalar function *G*.

Fig. 6

THRESHOLD PARAMETERS

σ_t = Uniaxial tensile stress
σ_c = Uniaxial compressive stress
σ_{bc} = Equal biaxial compressive stress

$$Y_t = \frac{\sigma_t}{\sigma_c} \qquad Y_{bc} = \frac{\sigma_{bc}}{\sigma_c}$$

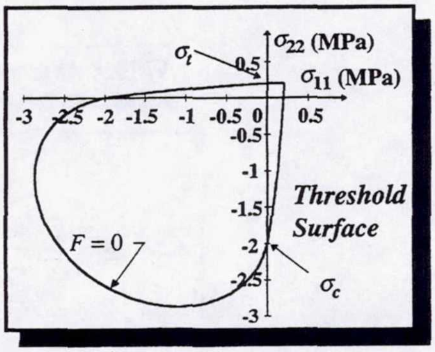

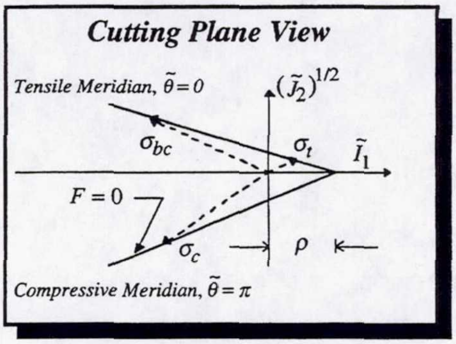

$$\rho = \frac{Y_{bc}\, Y_t}{Y_{bc} - Y_t}$$

$$r_t = \left(\frac{6}{5}\right)^{1/2} \frac{Y_{bc} Y_t}{2Y_{bc} + Y_t}$$

$$r_c = \left(\frac{6}{5}\right)^{1/2} \left[\frac{Y_{bc} Y_t}{3\, Y_{bc} Y_t + Y_{bc} - Y_t}\right]$$

Fig. 7

FLOW SURFACES

Normality Condition:

The direction of the inelastic strain rate vector for each stress point on a given surface is directed normal to the flow surface *F=constant.*

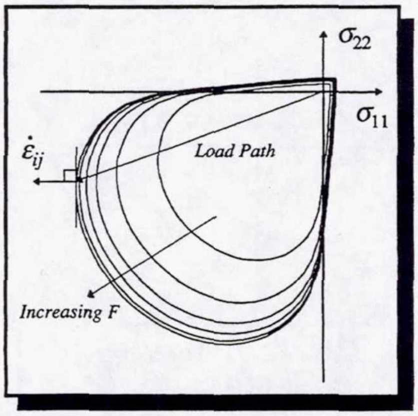

- Flow surfaces eventually cluster forming a limiting surface.
- Implies large changes in elastic strain rate for only small stress changes.

Fig. 8a

FLOW SURFACES

Convexity Condition:

Willam-Warnke: $0.5r_c < r_t \le r_c$

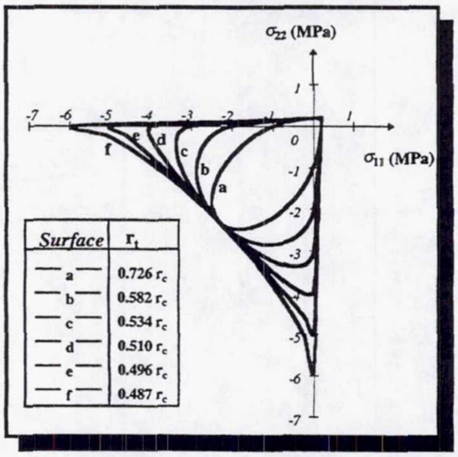

- Assures stable material behavior (i.e., positive dissipation of inelastic work).
- Implies that level surfaces of a function are closed surfaces.

Fig. 8b

FLOW SURFACES
(Degeneration to "simpler" models)

Limiting Conditions:

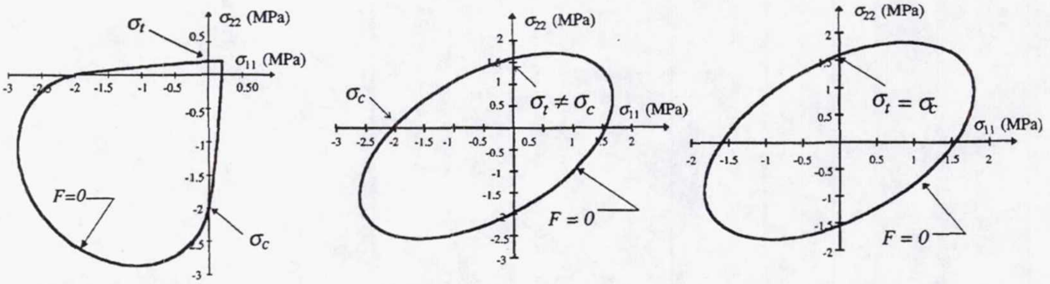

Willam-Warnke
("Triangle" in π-plane)
3 Parameters
r_t, r_c, ρ

Drucker-Prager
(Circle in π-plane)
2 Parameters
r_o, ρ

Von Mises
(Circle in π-plane)
1 Parameter
r_o

$r_c = r_t = r_o$

$r_c = r_t = r_o$
$\rho \to \infty$

Fig. 9

CONSTITUTIVE MODEL

The potential nature of Ω is exhibited in the extended normality structure

Flow Law:

$$\boxed{\dot{\varepsilon}_{ij} = \frac{\partial \Omega}{\partial \sigma_{ij}}} \Rightarrow \boxed{\dot{\varepsilon}_{ij} = C_0\left[C_1\delta_{ij} + C_2\Sigma_{ij} + C_3\left(\Sigma_{jq}\Sigma_{qi} - \frac{2\tilde{J}_2\delta_{ij}}{3}\right)\right]}$$

[Rice (1967), (1971)]

Limiting Conditions:
$r_c = r_t = r_o$ ***and*** $\rho \rightarrow \infty$ ➡➡ ***J_2 Model*** $\dot{\varepsilon}_{ij} = C_0\left[C_2\Sigma_{ij}\right]$

Evolutionary Law:

$$\boxed{\dot{\alpha}_{ij} = -\,h\frac{\partial \Omega}{\partial \alpha_{ij}}} \Rightarrow \boxed{\dot{\alpha}_{ij} = h\left\{\dot{\varepsilon}_{ij} - C_4\left[C_1\delta_{ij} + C_5a_{ij} + C_6\left(a_{jq}a_{qi} - \frac{2\mathcal{J}_2\delta_{ij}}{3}\right)\right]\right\}}$$

[Ponter & Leckie (1976), Ponter (1976)]

where h is a hardening function dependent on the internal stress

Limiting Conditions:
$r_c = r_t = r_o$ ***and*** $\rho \rightarrow \infty$ ➡➡ ***J_2 Model*** $\dot{\alpha}_{ij} = h\left\{\dot{\varepsilon}_{ij} - C_4\left[C_5a_{ij}\right]\right\}$

Fig. 10

Example: Willam-Warnke Model vs. J_2 Model

$$\sigma_{ij} = \begin{bmatrix} 10 & 0 & 0 \\ 0 & 0 & 0 \\ 0 & 0 & 0 \end{bmatrix} \text{ ksi}$$

Willam-Warnke Model:

Subcase $\boxed{A}$	Subcase $\boxed{B}$	Subcase $\boxed{C}$
$\sigma_t = 0.2$ $\sigma_c = 2.0$ $\sigma_{bc} = 2.32$	$\sigma_t = 0.2$ $\sigma_c = 2.0$ $\sigma_{bc} = 0.2$	$\sigma_t = 0.5$ $\sigma_c = 1.0$ $\sigma_{bc} = 1.5$

J_2 Model:

$\sigma_t = 1.732$
$\sigma_c = 1.732$
$\sigma_{bc} = 1.732$

APPROACH

Viscoplasticity parameters
μ, R, H, n, m, b

Willam-Warnke parameters
(σ_t, σ_c, σ_{bc}) or (ρ, r_t, r_c)

↓

Computer Algorithm
(Constitutive Model)

↓

- **Creep Curve (Strain vs. Time)**
- **State Variable vs. Time**
- **Flow Surface**

Fig. 11

Willam-Warnke Model vs. J_2 Model

CUTTING PLANE VIEW

J_2 Model

- ***Threshold Parameters***

$$\sigma_t = \sigma_c = \sigma_{bc}$$

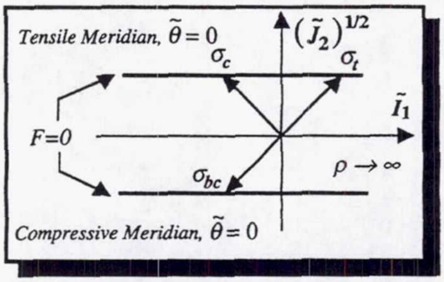

$$\rho \to \infty$$

- Meridians are linear
- Meridians are parallel

Willam-Warnke Model

- **Threshold Parameters**

$$\sigma_t \neq \sigma_c \neq \sigma_{bc}$$

(For typical ceramics, $\sigma_t < \sigma_c < \sigma_{bc}$)

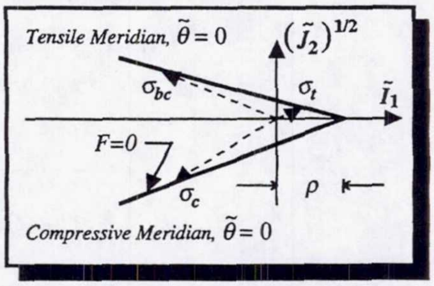

$$\rho = \frac{\sigma_t \, \sigma_{bc}}{\sigma_c \, (\sigma_{bc} - \sigma_t)}$$

- Meridians are linear
- Meridians intersect hydrostatic axis

Fig. 12

Willam-Warnke Model vs. J_2 Model

J_2 Model

- *Poisson effect ($\nu \approx 0.5$)*
- $\varepsilon_{11} = -2\varepsilon_{22} = -2\varepsilon_{33}$

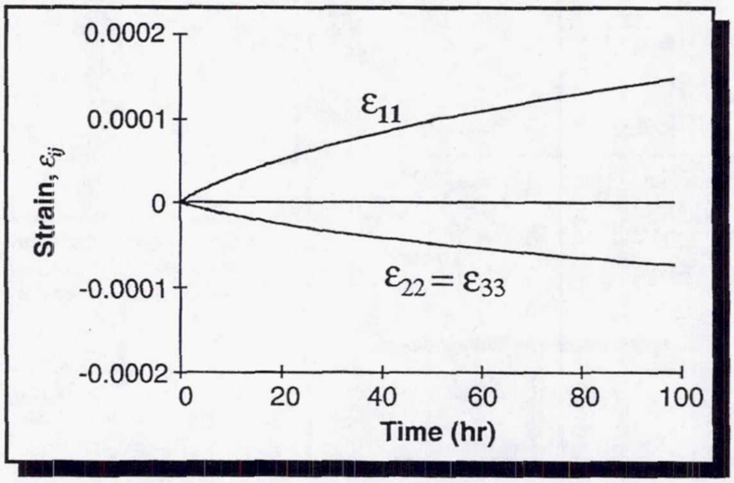

Fig. 13a

Willam-Warnke Model vs. J_2 Model

Willam-Warnke Model

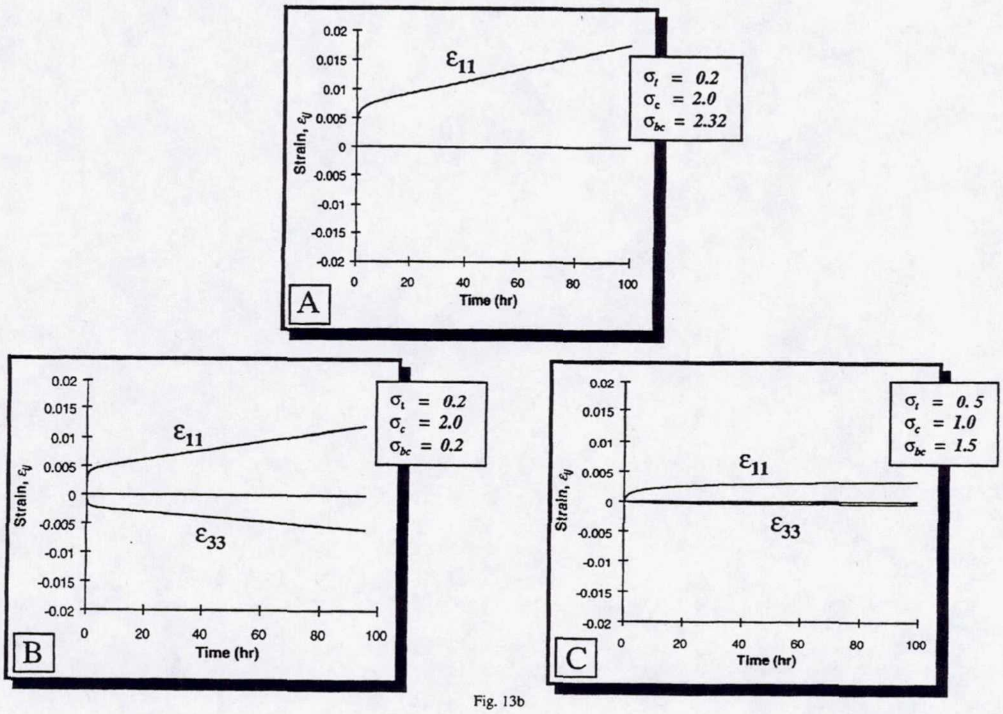

Fig. 13b

SUMMARY

- ***Fundamental concepts of viscoplasticity***
- ***Specific form for the potential function***
- ***Multiaxial derivation of viscoplastic constitutive model***
- ***Preliminary applications of constitutive model***

FUTURE ENDEAVORS

- ***Incorporate model into computer algorithm***
- ***Develop experimental test matrix***
- ***Identify parameters applicable to ceramics***
- ***Model phenomena such as creep, stress relaxation, strain-rate sensitivity, etc.***
- ***Develop user-defined subroutines for commercial FEA software packages***

Fig. 14

CREEP LIFE PREDICTION OF CERAMIC COMPONENTS USING THE FINITE ELEMENT BASED INTEGRATED DESIGN PROGRAM (CARES/*CREEP*) *

OSAMA M. JADAAN
University of Wisconsin-Platteville
Platteville, Wisconsin

Lynn M. Powers**
Case Western Reserve University
Cleveland, Ohio

and

John P. Gyekenyesi
NASA Lewis Research Center
Cleveland, Ohio

Introduction and Theory

The desirable properties of ceramics at high temperatures have generated interest in their use for structural applications such as in advanced turbine systems. Design lives for such systems can exceed 10,000 hours. Such long life requirements necessitate subjecting the components to relatively low stresses. The combination of high temperatures and low stresses typically places failure for monolithic ceramics in the creep regime (ref 1).

The objective of this work is to present a design methodology for predicting the lifetimes of structural components subjected to multiaxial creep loading. This methodology utilizes commercially available finite element packages and takes into account the time varying creep stress distributions (stress relaxation). In this methodology, the creep life of a component is divided into short time steps, during which, the stress and strain distributions are assumed constant. The damage, D, is calculated for each time step based on a modified Monkman-Grant creep rupture criterion (ref 2). For components subjected to predominantly tensile loading, failure is assumed to occur when the normalized accumulated damage at any point in the component is greater than or equal to unity.

Some ceramic components, such as vanes and rotors, are subjected to concurrent tensile and compressive stress fields. For such components, failure generally starts at or near the most highly stressed point and subsequently propagates across the section. The creep rupture life for members subjected to concurrent tensile and compressive loading is divided into two stages. The first is called the stage of latent failure (damage initiation). During this stage, the damage accumulates

---

* Work funded under NASA Grant NAG3-1968 and NASA Cooperative Agreement NCC3-518.

** NASA Resident Research Associate at Lewis Research Center.

until it reaches unity at some point within the component, and failure begins. Hence, this portion of life for members subjected to concurrent tensile and compressive loading represents the entire predicted life for predominantly tensile components. Damage due to compressive stresses is assumed to be negligible, although in this methodology, it can be accounted for very easily if it is determined to be of any significance. Subsequently, the second stage, named the damage propagation takes place. During this stage a damage front defined by the condition D=1 will travel through the body or surface of the component. Component failure occurs at the end of this stage when its total load carrying capacity is expended. In CARES/*Creep* (**C**eramics **A**nalysis and **R**eliability **E**valuation of **S**tructures/***Creep***), this means that failure is assumed to occur when D=1 at the periphery of the expanded critical damage zone. The corresponding time will be the creep rupture life for that component. This size of the critical damage zone corresponding to creep rupture failure varies depending on the load conditions and component configuration. One estimation for the duration of the propagation stage is to assume it equal to the time it takes the damage zone to penetrate the initial tensile stressed portion of the structure.

Two examples were chosen to demonstrate the viability of the creep life prediction methodology presented above. The integrated design code CARES/*Creep* (Fig. 7) which utilizes this damage accumulation model was used for this purpose. The first example, silicon nitride NCX-5100 notched tensile specimen, represents the application of this approach to predicting the creep rupture life for components subjected to multiaxial predominantly tensile creep loading. The second example, siliconized silicon carbide KX01 bend specimen, represents the application of this approach to components subjected to uniaxial tensile-compressive creep loading. It was found that the methodology described in this paper yielded good creep rupture life predictions for both examples, given the amount of scatter usually found in the creep rupture life data.

Examples

1) Notched Tensile Specimen:

The creep experiments were conducted on two types of silicon nitride NCX-5100 specimens. First, smooth tensile tests were investigated in order to characterize the creep response of the silicon nitride. Second, experiments on notched tensile bars (Fig. 8) provided a multiaxial stress state, especially near the notch root, where the creep life may be predicted from data obtained from the smooth tensile specimens. Creep data used in this example were obtained from ref 3.

Using CARES/*Creep*, the secondary creep rate parameters, C_7, C_8, and C_{10}, were determined to be $7.858\times10^{-26}/\text{Pa}^{6.75}$ hour, 6.75, and 127560°K, respectively. Figure 9 shows the experimental secondary creep strain rate vs. the analytical secondary creep strain rate. This figure shows that the data scatters relatively close to the 45° line, indicating that the Norton secondary creep rate model (Fig. 9) was successful in describing the secondary creep behavior of the NCX-5100 material.

Four notched bars were tested (ref 3). The reduced section average stresses were 105, 120, 135, and 150 MPa. The maximum principal stress distribution for the 120 MPa reduced average section stress specimen as a function of time is shown in Fig. 10. A multiaxial stress state exists in the vicinity of the notch root, while the stress state away from the notch is constant and uniaxial. When the load is initially applied, time=0, the maximum principal stress is located at the root of the notch. As time progresses, the stress relaxes and, the local maximum moves into the interior of the notched bar. This stress relaxation, which occurs due to nonlinear creep deformation, will influence the damage calculations. This is because it was found that the location of the maximum cumulative damage also moves away from the surface as time elapses, indicating that failure could originate at the interior of the specimen.

The Monkman-Grant criterion in association with the damage model was used to predict the creep life for the notched specimens. Since this component is entirely subjected to tensile stress state, failure was assumed to occur when D first reached unity at any point. The Table shown in Fig. 11 gives a summary of the failure predictions for the notched bars as a function of their reduced section stress. The predicted lives using the methodology described in this paper and computed via CARES/*Creep* for these specimens compare well to the experimental failure times. Figure 11 also shows a cumulative damage map for the 120 MPa specimen after 80 hours. The cumulative damage is equal to one and is located near to but not directly the root of the notch.

2) Bend bar

This example is presented to demonstrate the methodology discussed in this paper for predicting the creep life of ceramic components subjected to simultaneous tensile/compressive stresses. Wiederhorn et al. (ref 4) conducted creep testing on the KX01 siliconized silicon carbide material at 1300°C using flexure, tensile and compressive specimens. They found that this material spent most of its life in the secondary creep region. Further, they found that the KX01 material displays significant asymmetric creep behavior, and that in both tension and compression, the creep rate displayed a bilinear power (Norton) law behavior with a transition point at a threshold stress (Fig. 13). In this example, CARES/*Creep* was used to predict the creep lives of four point bend specimens using the tensile and compressive creep and creep rupture properties of the material. These predicted lives were then compared to the experimental ones.

Figure 14 displays the evolution of stress as function of time (stress relaxation) for the bar tested at 250 MPa. The stress distribution in the bend bar converged to its stationary value ten hours after the load was applied. This figure also shows how the neutral axis shifts towards the compressive region as the specimen creeps.

Figure 15 show the evolution of damage in the flexure bar tested at 250 MPa initially, at t=14.5 hours corresponding to the time when the damage first reached unity (latent stage of failure), and at t=80 hours corresponding to the time when the final predicted failure occurred (end of damage propagation stage). In this analysis, it was assumed that failure would occur when the initial portion of the bend bar stressed in tension is damage (half the depth). The table shown in Fig. 16 indicates that excellent agreement between experimental and predicted creep lives exists for the bend bars.

Several advantages are apparent to this creep rupture life methodology. First, this methodology yields a cumulative damage map for the component showing the critical locations where failure would originate. This capability is very helpful in the redesign of such components. In creep type loading applications, it is not a trivial task to predict the location of failure since the multiaxial stress components redistribute as time elapses. Thus, failure will not necessarily occur at the location where stresses are highest at the beginning of loading or at the time of failure, but can take place elsewhere, as shown by the notched tensile specimen. Second, this design methodology is capable of incorporating the primary creep strain effect into the analysis (influences the stress state) which could predict shorter lives (conservative predictions) compared to when only the secondary creep stain effect is used. Third, any equivalent stress criterion can be used to predict the component's life. As multiaxial creep data emerge in the future and we understand better how ceramics fail under such applications, the CARES/*Creep* code can be modified accordingly. Fourth, any creep rupture criterion (Continuum damage mechanics, Larson-Miller, minimum commitment method, etc.) can be utilized to compute the damage and predict life.

References

1. Wiederhorn, S.; Quinn, G.; and Krause, R.: "Fracture Mechanism Maps: Their Applicability to Silicon Nitride," *Life Prediction Methodologies and Data for Ceramic Materials*, ASTM STP-1201, Brinkman, C. R., and Duffy, S. F., eds., American Society for Testing and Materials, Philadelphia, pp. 36-61, 1993.

2. Powers, L. M.; Jadaan, O. M.; Gyekenyesi, J. P.: "Creep Life of Ceramic Components Using a Finite Element Based Integrated Design Program (CARES/*Creep*)," ASME paper 96-GT-369, 1996.

3. White, C.; Vartabedian, A; Wade, J; and Tracey, D: "Notched Tensile Creep Testing of Ceramics," *Materials Science and Engineering*, A203, 217-221, 1995.

4. Wiederhorn, S. M.; Roberts, D. E.; Chuang, T.-J.; and Chuck, L.: "Damage Enhanced Creep in a Siliconized Silicon Carbide: Phenomenology," *Journal of American Ceramic Society*, Vol. 71, pp. 602-608, 1988.

Objective

To develop an integrated design program for predicting the lifetime of structural ceramic components subjected to multiaxial creep loads. This methodology utilizes commercially available finite element packages and takes into account the time varying creep stress distribution (stress relaxation).

Fig. 1

Constitutive Creep Laws

Total Creep Strain

$$\varepsilon_{cr} = \varepsilon_{Primary} + \varepsilon_{Secondary}$$

Primary Creep Strain Increment — Bailey–Norton Law

$$\Delta\varepsilon_p = C_1\, \sigma^{C_2}\, t^{C_3} \exp\left[-\frac{C_4}{T}\right] \Delta t$$

Secondary Creep Strain Increment — Norton Law

$$\Delta\varepsilon_s = C_7\, \sigma^{C_8} \exp\left[-\frac{C_{10}}{T}\right] \Delta t$$

where σ is the stress
t is the time
T is the absolute temperature
C_i are experimentally determined constants

Fig. 2

Multiaxial Creep Model

Flow Rule

$$\dot{\varepsilon}_{ij}^{cr} = \lambda S_{ij}$$

Proportionality Constant

$$\lambda = \frac{3}{2\sigma_e} \frac{d\bar{\varepsilon}^{cr}}{dt}$$

Secondary Creep Strain Rate

$$\dot{\varepsilon}_{ij}^{cr} = \frac{3}{2} S_{ij} C_7 \sigma_e^{C_8 - 1} \exp\left[-\frac{C_{10}}{T}\right]$$

where S_{ij} is the deviatoric stress

Fig. 3

Effective Stress

$$\sigma_e = \frac{1}{\sqrt{2}}\{(\sigma_1 - \sigma_2)^2 + (\sigma_2 - \sigma_3)^2 + (\sigma_3 - \sigma_1)^2\}^{1/2}$$

Effective Secondary Creep Strain

$$\bar{\varepsilon}^{cr} = C_7 \sigma_e^{C_8} t \exp\left[-\frac{C_{10}}{T}\right]$$

where σ_1, σ_2, and σ_3 are the principal stresses

Fig. 4

Creep Rupture

Monkman–Grant

$$t_f = b_1 \, \dot{\varepsilon}_s^{\,-b_2}$$

Modified Monkman–Grant
Temperature Stratification

$$\ln t_f = d_1 - d_2 \ln \dot{\varepsilon}_s + \frac{d_3}{T}$$

where b_i and d_i are constants

Fig. 5

Damage Assessment

Damage

$$0 \leq D \leq 1$$

where $D = 0$ for an undamaged component
$D = 1$ for a failed component

$$D = \sum_{i=1}^{N} \frac{\Delta \mathbf{t_i}}{\exp\left[\, d_1 - d_2 \ln \dot{\varepsilon}_{s_i} + d_3/T_i \,\right]}$$

where Δt_i is the duration of the i^{th} time step
N is the number of time steps

Fig. 6

Integrated Design Program

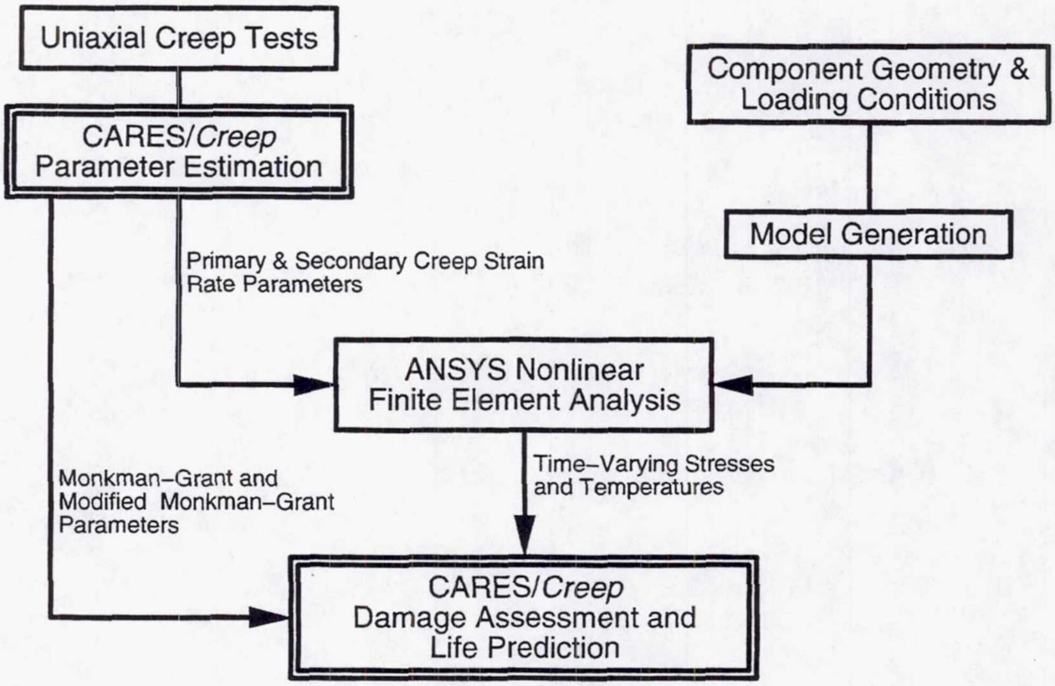

Uniaxial Creep Tests

CARES/*Creep* Parameter Estimation

Component Geometry & Loading Conditions

Model Generation

Primary & Secondary Creep Strain Rate Parameters

ANSYS Nonlinear Finite Element Analysis

Monkman–Grant and Modified Monkman–Grant Parameters

Time–Varying Stresses and Temperatures

CARES/*Creep* Damage Assessment and Life Prediction

Fig. 7

CARES/*Creep* Multiaxial Tensile Creep Benchmark

Notched Tensile Specimen – Norton Company

NCX–5100 Silicon Nitride

Axisymmetric Model

Temperature = 1370°C

Constant Applied Load

Axisymmetric Model
1047 PLANE82 elements

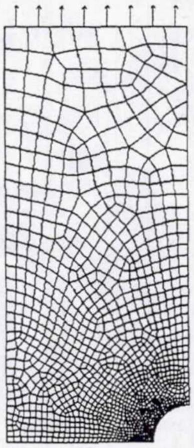

Height = 8.9 cm
Model Height = 0.72 cm
Diameter = 0.32 cm
Notch Radius = 0.032 cm

Fig. 8

Parameter Estimation

Silicon Nitride - N CX-5100

37 Tensile Specimens

Temperatures = 1275-1425 °C

Applied Load = 120-250 MPa

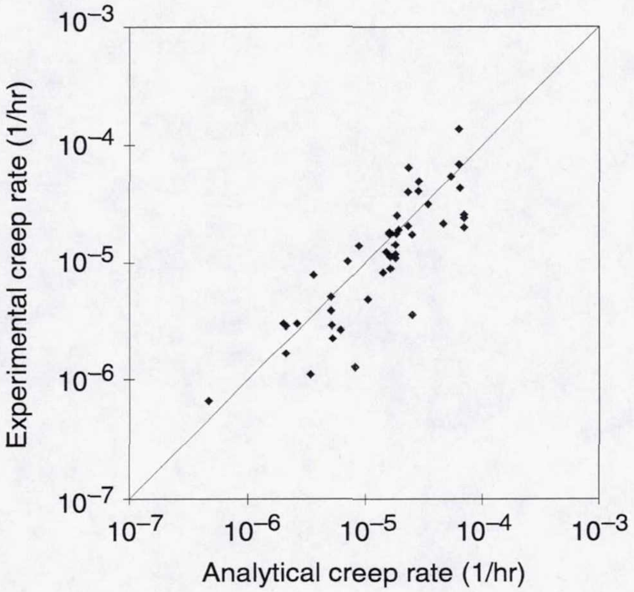

Fig. 9

Stress Relaxation Near the Notch Root

Nominal Reduced Section Stress=120 MPa

Equivalent Stress

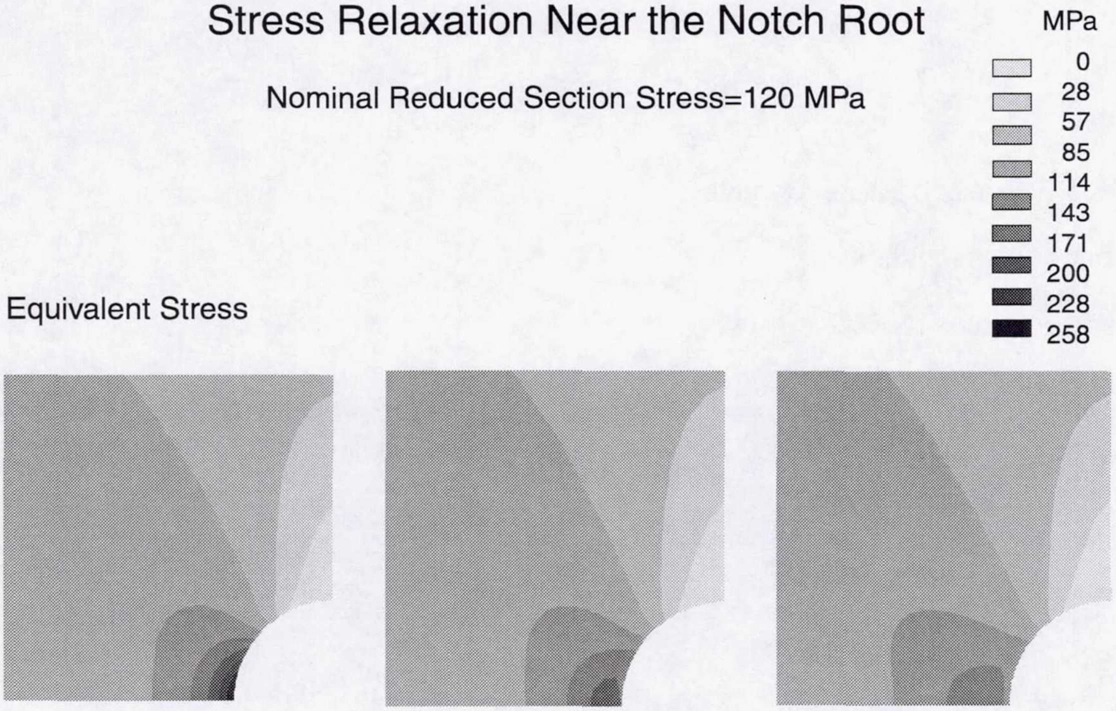

Time = 0 hours

10 hours

100 hours

Fig. 10

Notched Tensile Specimen

Damage Map

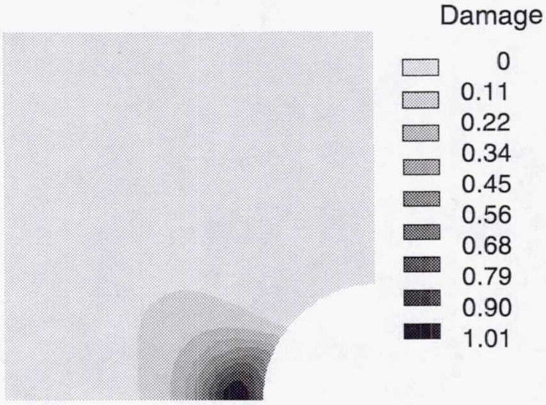

Results

Nominal Reduced Section Stress (MPa)	Experimental Failure Time (hours)	Predicted Lifetime (hours)
105	314	179
120	44	80
135	39	42
150	3.5	17

Secondary Creep
Monkman-Grant Criterion

Fig. 11

CARES/*Creep* Uniaxial Tensile – Compressive Creep Benchmark

Flexural Specimen – NIST

KX01 Siliconized Silicon Carbide

Plane Stress Model

Temperature = 1300°C

Constant Applied Load

Half Symmetry Model
1200 PLANE82 elements

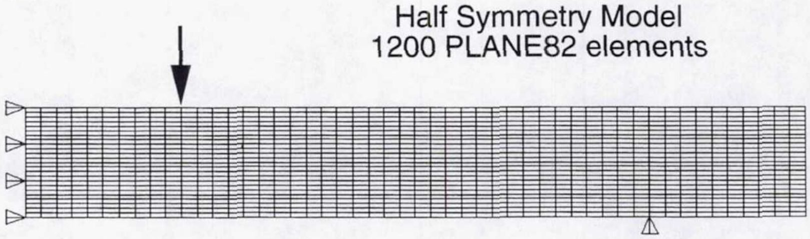

Height = 4.0 mm
Length = 50 mm
Depth = 3 mm

Fig. 12

Parameter Estimation

Siliconized Silicon Carbide - KX01

Uniaxial Tension and Compression Tests at 1300°C

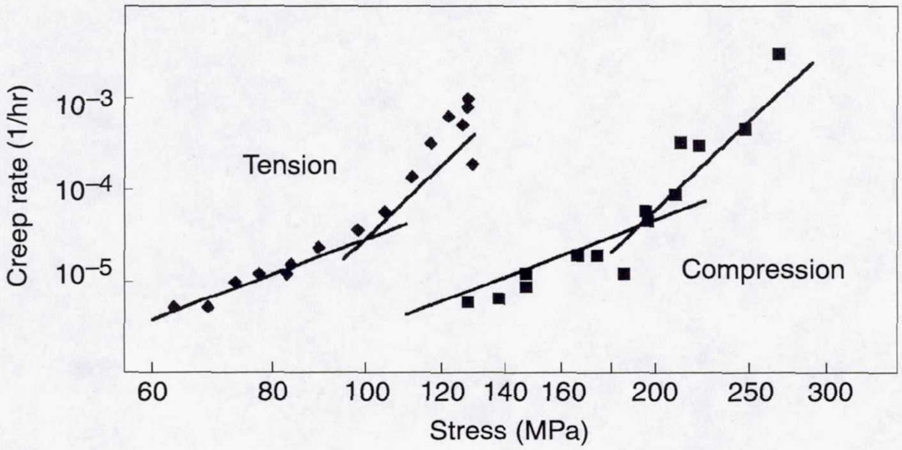

Material displays asymmetric bilinear creep behavior in tension and compression

Fig. 13

Stress Relaxation

Maximum Elastic Stress=250 MPa

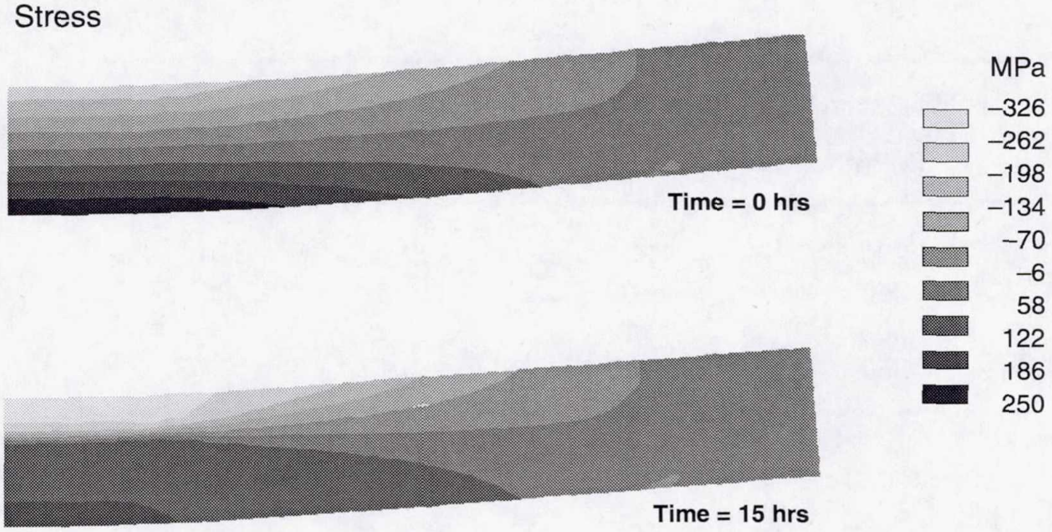

Fig. 14

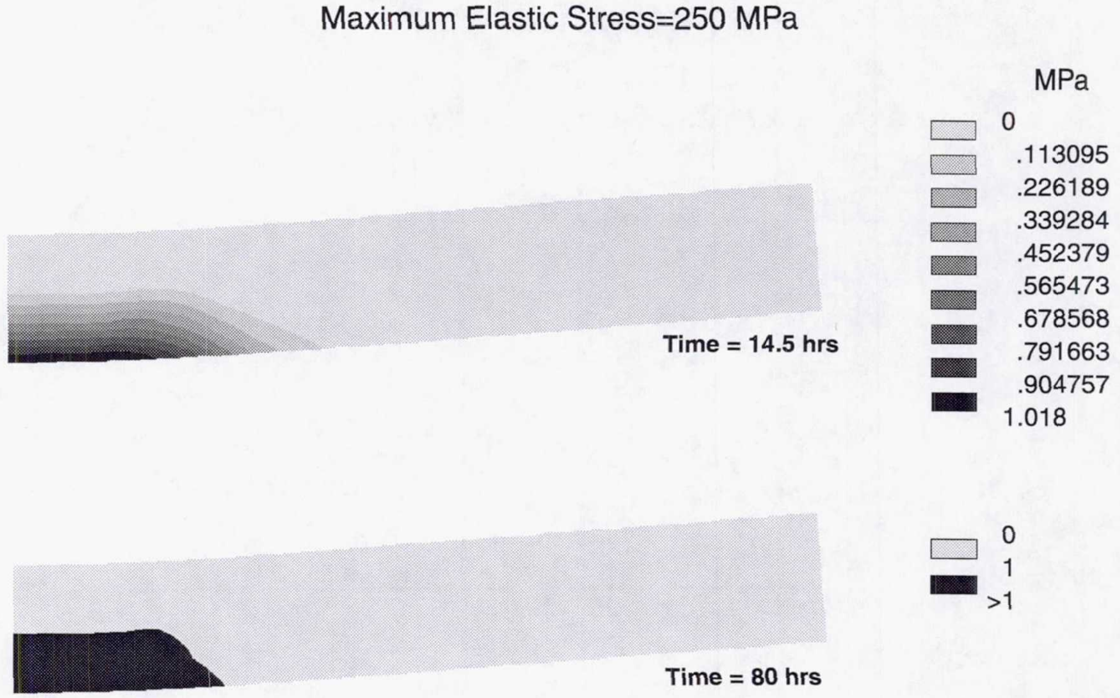

Fig. 15

Flexure Specimen

Results

Initial Maximum Elastic Stress (MPa)	Experimental Failure Time (hours)	Damage Initiation (hours)	Predicted Lifetime (hours)
200	830	200	830
250	55	14.5	80
300	12	1.2	8.6
350	1.3	0.12	1.3

Secondary Creep
Monkman–Grant Criterion

Fig. 16

Summary and Conclusions

A general purpose creep life prediction code, CARES/*Creep*, has been developed. It is integrated with ANSYS finite element software, and can be used to design monolithic ceramic components.

Creep life was predicted based on accumulated damage and the Monkman–Grant and the Modified Monkman–Grant failure criteria.

The creep life was well predicted for components subjected to multiaxial tensile and uniaxial tensile–compressive stress states.

Life prediction for a component with simultaneous tensile–compressive stress states is a two step process involving damage initiation and propagation.

This creep life prediction methodology results in damage maps showing critical regions and, hence, can be used in the components design.

Fig. 17

Focus of Future Research

- Creep Response
  - Multiaxial Tensile–Compressive Modeling
  - Continuum Damage Mechanics
- Creep Rupture
  - Probabilistic Methods
  - Creep–Fatigue Interaction
  - Integration with CARES/*Life*

Fig. 18

CARES/*LIFE* SOFTWARE FOR DESIGNING MORE RELIABLE CERAMIC PARTS

NOEL N. NEMETH
NASA Lewis Research Center
Cleveland, Ohio

Lynn M. Powers*
Case Western Reserve University
Cleveland, Ohio

and

Eric H. Baker*
Cleveland State University
Cleveland, Ohio

Introduction

Products made from advanced ceramics show great promise for revolutionizing aerospace and terrestrial propulsion, and power generation. However, ceramic components are difficult to design because brittle materials in general have widely varying strength values. The CARES/*Life* software (refs. 1 to 5) eases this task by providing a tool to optimize the design and manufacture of brittle material components using probabilistic reliability analysis techniques.

Probabilistic component design involves predicting the probability of failure for a thermomechanically loaded component from specimen rupture data. Typically, these experiments are performed using many simple geometry flexural or tensile test specimens. A static, dynamic, or cyclic load is applied to each specimen until fracture. Statistical strength and SCG (fatigue) parameters are then determined from these data. Using these parameters and the results obtained from a finite element analysis, the time-dependent reliability for a complex component geometry and loading is then predicted. Appropriate design changes are made until an acceptable probability of failure has been reached.

CARES/*Life* is an integrated package that predicts the probability of a monolithic ceramic component's failure as a function of time in service. It couples commercial finite element programs -- which resolve a component's temperature and stress distribution -- to reliability evaluation and fracture mechanics routines for modeling strength-limiting defects. These routines are based on calculations of the probabilistic nature of the brittle material's strength. CARES/*Life* accounts for the phenomenon of subcritical crack growth (SCG) by utilizing the

---

*NASA Resident Research Associate at Lewis Research Center.

power law, Paris law, or Walker equation. The two-parameter Weibull cumulative distribution function is used to characterize the variation in component strength. The effects of multiaxial stresses are modeled using either the principal of independent action (PIA), the Weibull normal stress averaging method (NSA), or the Batdorf theory. Inert strength and fatigue parameters are estimated from rupture strength data of naturally flawed specimens loaded on static, dynamic, or cyclic fatigue.

The capability, flexibility, and uniqueness of CARES/*Life* has attracted much interest. Initially, the program was developed with an emphasis on technical features and less regard was given to ease-of-use. However, over time the program became more intricate -- requiring a higher level of expertise needed to achieve a desired result. Based on feedback from users, who typically used the program on an intermittent basis, it was found that the program's capabilities were underutilized because of it's complexity. First and foremost users wanted an easier to use program. To begin to address this criticism, CARES/*Life* has been upgraded with the following:

- Data files to create graphic templates for common business presentation software such as Lotus Freelance Graphics. This feature, known as CARES/*Graphics*, produces Weibull and fatigue plots of specimen rupture data and estimated parameters.

- An interactive input preparation program has been prepared which guides the user through various program control options and data input formats. This program, known as CARES/*Input*, is written in FORTRAN 77 and operates on PC's as well as Unix machines.

- A new interface program between the ANSYS finite element analysis program and CARES/*Life*. This program, known as ANSCARES, has a finite element model geometry surface recognition feature allowing surface flaw reliability to be performed without the previous requirement of shell elements being attached to the model's surface nodes. This program also has an expanded element library, including axisymmetric elements.

- A grinding damage model (ref. 6) has been added to account for flaws introduced from finishing (grinding) operations on components. This model is based on Batdorf methodology modified to account for non-random (anisotropic) orientation of flaws.

- Capability to use a finite element model of a specimen geometry and loading to obtain volume and area normalized Weibull and fatigue parameters.

CARES/*Life* has been in high demand world-wide, although present technology transfer efforts are primarily focused on U.S.-based organizations. Success stories can be cited in several industrial sectors including aerospace, automotive, biomedical, electronic, glass, nuclear, and conventional power generation industries. In 1997 Lewis Research Center (LeRC) in partnership with Philips Display Components Company (PDCC) and Corning Incorporated, won the American Ceramic Society Corporate Technical Achievement Award for the design and manufacture of an improved television picture tube (by PDCC) for the U.S. consumer market. Also an R&D 100 Award from R&D Magazine was recieved in 1995, the NASA Software of the Year Award, and a Federal Laboratory Consortium Technology Transfer Award were received in 1994.

References

1. Nemeth, N. N., Powers, L. M., Janosik, L. A., and Gyekenyesi, J. P.: "Time-Dependent Reliability Analysis of Monolithic Ceramic Components Using the CARES/*Life* Integrated Design Program," Life Prediction Methodologies and Data for Ceramic Materials, ASTM STP 1201, C. R. Brinkman, and S. F. Duffy, Eds., American Society for Testing and Materials, Philadelphia, 1993, pp. 390-408.

2. Powers, L. M., Janosik, L. A., Nemeth, N. N., and Gyekenyesi, J. P.: "Lifetime Reliability Evaluation of Monolithic Ceramic Components Using the CARES/*Life* Integrated Design Program," Proceedings of the American Ceramic Society Meeting and Exposition, Cincinnati, Ohio, April 19-22, 1993.

3. Nemeth, N. N., Powers, L. M., Janosik, L. A., and Gyekenyesi, J. P.: "Designing Ceramic Components for Durability," American Ceramic Society Bulletin, Vol 72, no. 12, December, 1993, pp. 59-66.

4. Nemeth, N. N., Powers, L. M., Janosik, L. A., and Gyekenyesi, J. P.: "Durability Evaluation of Ceramic Components Using CARES/*Life*," ASME Transactions; Journal of Engineering For Gas Turbines and Power, Vol. 118, No. 1, January 1996, pp. 150-158.

5. Janosik, L. A., Gyekenyesi, J. P., Nemeth, N. N., and Powers, L. M.: "NASA CARES Dual-Use Ceramic Technology Spinoff Applications." Proceedings of the Thirty-Second Space Congress, Cocoa Beach, FL, April 25-28, 1995.

6. Salem, J. A., Nemeth, N.N., Choi, S. R., and Powers, L. M.: "Reliability Analysis of Uniaxially Ground Brittle Materials", ASME Transactions; Journal of Engineering For Gas Turbines and Power, Vol. 118, No. 4, October 1996, pp. 863-871.

Outline

- Probabilistic ceramic component design
- CARES/*Life* computer program
- Ease-of-use enhancements
- Technology transfer
- Conclusion

Fig. 1

Objective

Develop probabilistic based integrated design programs for the life analysis of brittle material structural components

Fig. 2

Typical Defect Populations Found in Engineering Ceramics Manufactured From Powders

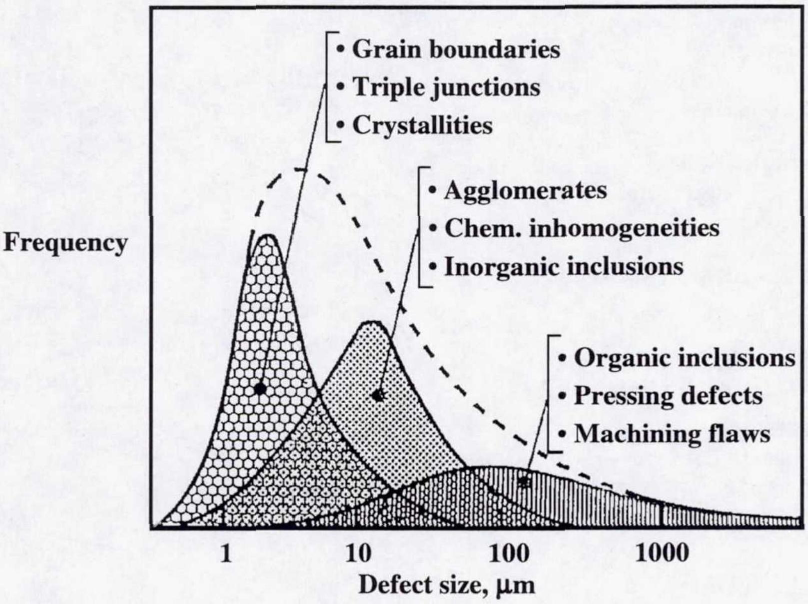

Fig. 3

Fracture Map of Hot Pressed Si_3N_4

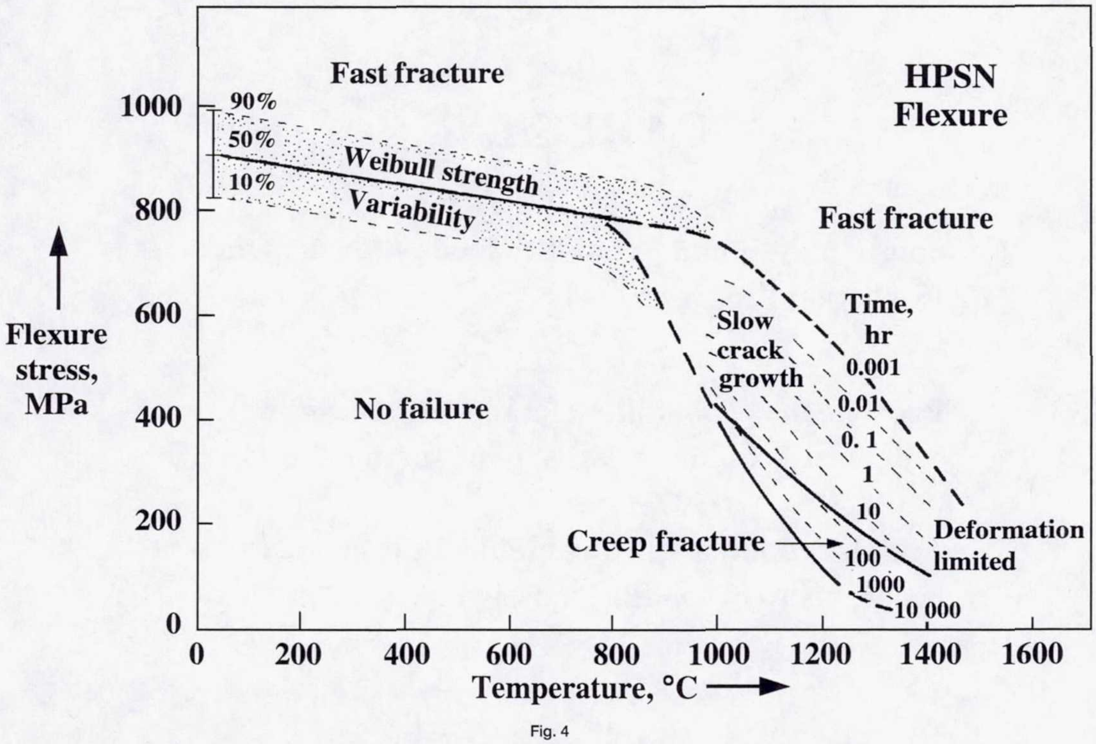

Fig. 4

Probabilistic Component Design Procedure

- **Material failure characterization**
  - Rupture tests of many simple specimens
  - Fast–fracture experiments: Estimate Weibull parameters
  - Static, dynamic, or cyclic fatigue experiments: Estimate fatigue parameters
- **Fractographic examination of ruptured specimens to determine the mode of failure**
- **Component finite-element analysis**
  - Thermal analysis
  - Stress analysis
- **Component reliability evaluation**
  - Specify probabilistic failure theory, crack type, fracture criterion, crack growth law, Weibull parameters, and fatigue parameters
- **Design optimization**
  - Risk-of-rupture intensity plot
  - Generate design diagrams: Failure probability versus time, strength–probability–time (SPT) diagrams, etc.

4–Point Flexure

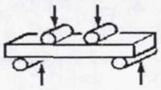

Uniaxial Tension

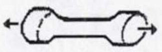

Weibull Plot

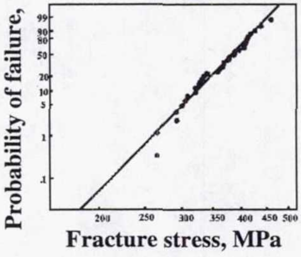

Dynamic Fatigue

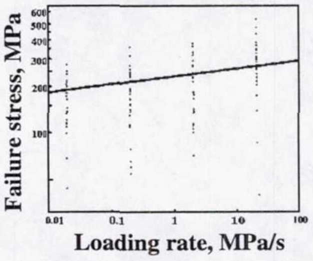

FEA Model

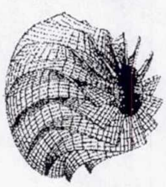

Design Diagram

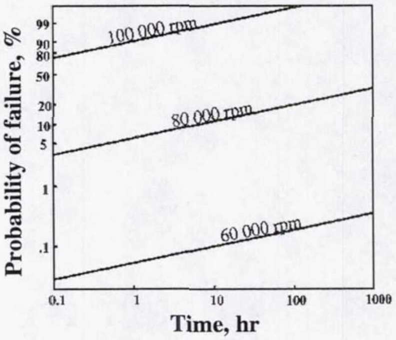

Fig. 5

CARES/*Life*

Ceramics Analysis and Reliability Evaluation of Structures
***Life* Prediction Program**

- **Predicts the probability of a monolithic ceramic components failure relative to its service life**
- **Couples commercially available finite element programs to probabilistic design**

Fig. 6

NASA/CARES - Modular Format

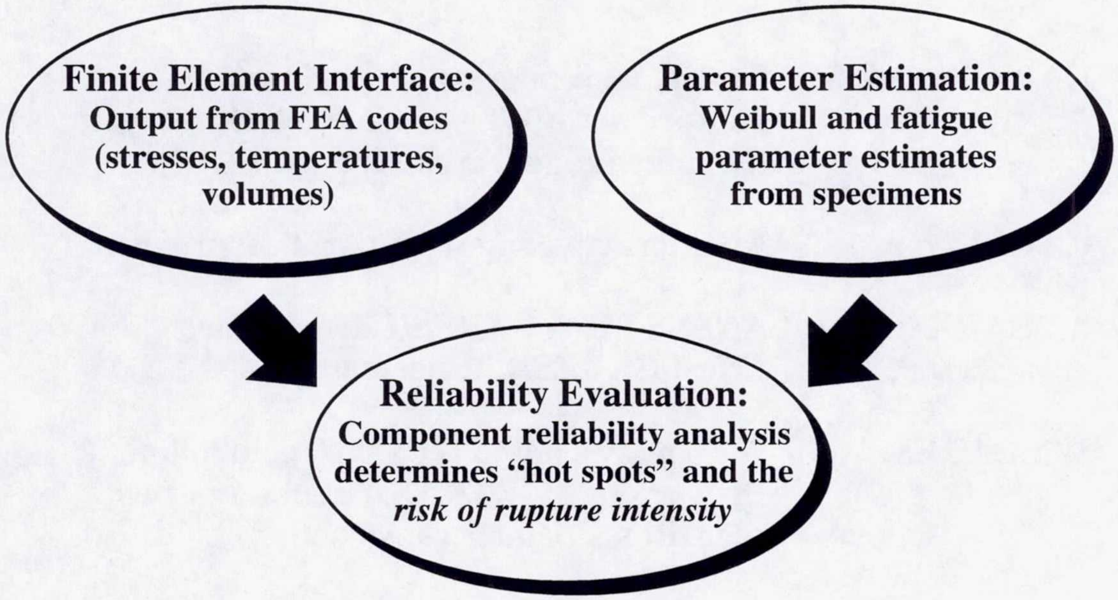

Finite Element Interface:
Output from FEA codes (stresses, temperatures, volumes)

Parameter Estimation:
Weibull and fatigue parameter estimates from specimens

Reliability Evaluation:
Component reliability analysis determines "hot spots" and the *risk of rupture intensity*

Fig. 7

CARES/*Life* Capabilities

- **Component reliability evaluation**
  - **Fast-fracture**
  - **Time- or cycle-dependent**
  - **Multiaxial stress states**
  - **Proof test loads**
  - **Random or *non-random* flaw orientation *(new capability)***

- **Material characterization**
  - **Any specimen geometry *(new capability)***
  - **Instantaneous load**
  - **Static load**
  - **Constant stress rate load**
  - **Cyclic load**

Fig. 8

Version 5 - New Features and Changes

Enhance Functionality and Ease-of-Use

CARES/Graphics: Graphical rendering of specimen rupture data; Weibull plots, static fatigue, dynamic fatigue, cyclic fatigue

CARES/Input: An interactive input preparation program

ANCARES: ANSYS FEA–CARES/Life interface (Most CARES/Life users have ANSYS)

WinCARES: A Windows based GUI shell controlling the various FORTRAN-based numerical algorithms (Under construction)

Fig. 9

CARES/*Graphics*

User friendly graphics templates for common business presentation software

Two Parameter Weibull Plot of Fast Fracture Data

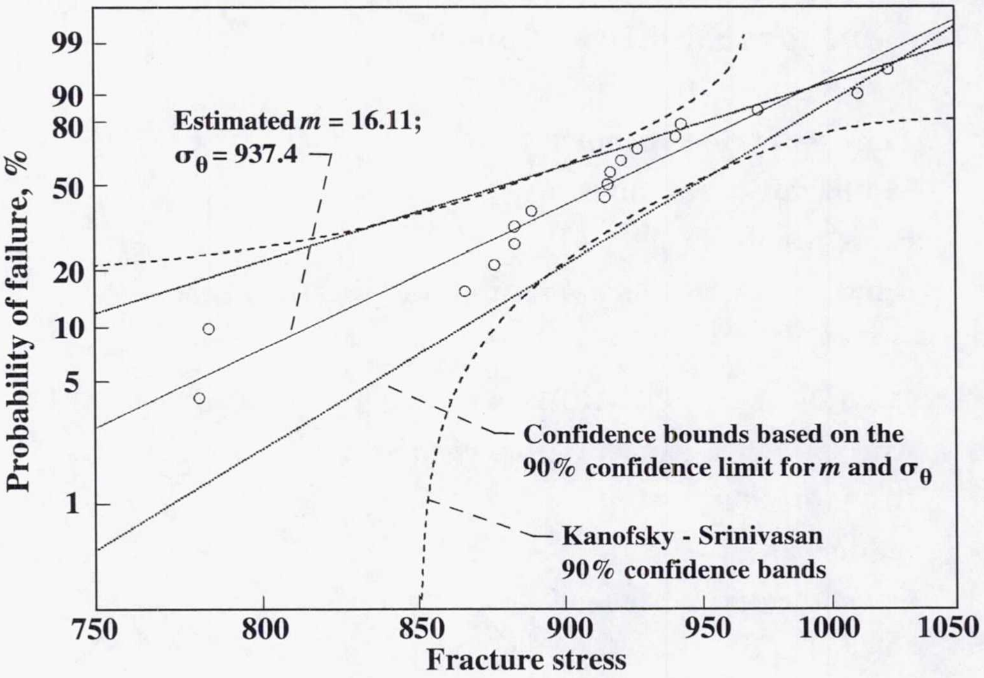

Fig. 10

CARES/*Input*

Interactive Input File Preparation for CARES/*Life*

- **Simplifies the *"bewildering array of input files and keywords"* confronting the user**
- **Step-by-step walk through of input file creation**
- **Error checking diagnostics**

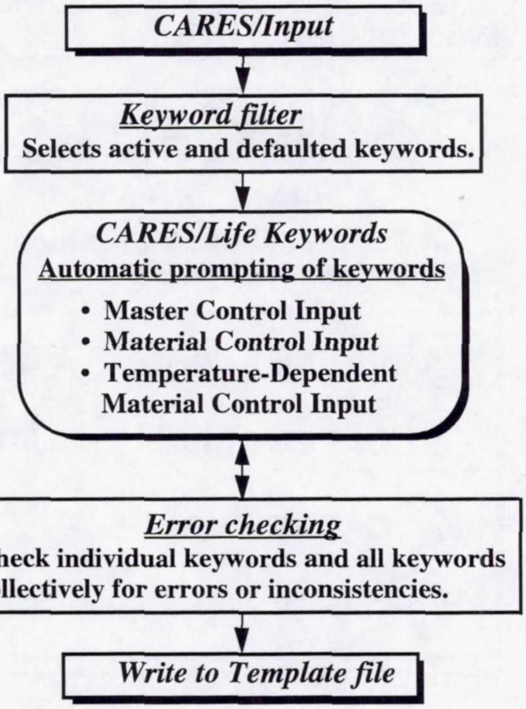

CARES/Input

Keyword filter
Selects active and defaulted keywords.

CARES/Life Keywords
Automatic prompting of keywords
- **Master Control Input**
- **Material Control Input**
- **Temperature-Dependent Material Control Input**

Error checking
Check individual keywords and all keywords collectively for errors or inconsistencies.

Write to Template file

Fig. 11

ANSYS–CARES Interface

- **Automatic detection and modeling of component surfaces**
- **Component risk of rupture rendering**
- **Robust element library (solid, shell, axisymemetric)**

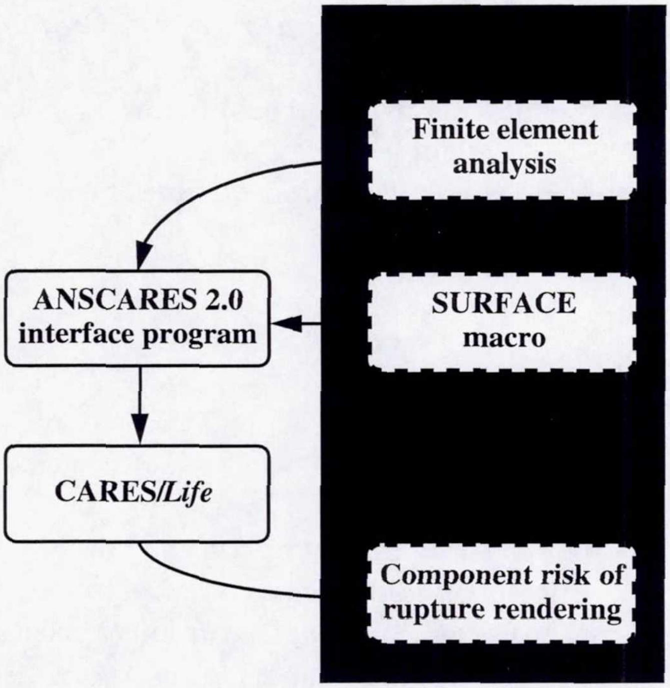

Finite element analysis

ANSCARES 2.0 interface program

SURFACE macro

CARES/*Life*

Component risk of rupture rendering

Fig. 12

WINCARES: A GUI for the CARES/*Life* algorithm

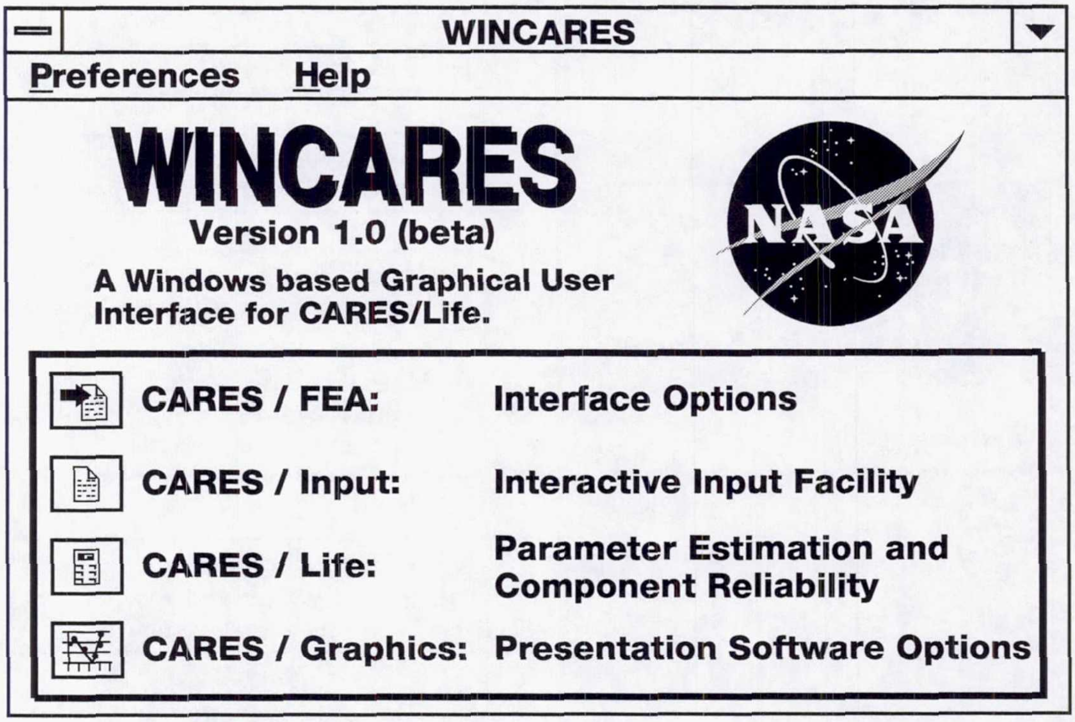

WINCARES

Version 1.0 (beta)

A Windows based Graphical User Interface for CARES/Life.

CARES / FEA:	Interface Options
CARES / Input:	Interactive Input Facility
CARES / Life:	Parameter Estimation and Component Reliability
CARES / Graphics:	Presentation Software Options

Fig. 13

Diverse Range of *CARES/Life* Applications

Aerospace/Terrestrial Power & Propulsion Applications

- Turbocharger rotors
- Rocker arm and cam followers
- Radient heater tubes
- Prototype ceramic turbines
- Poppet valves
- Combustors
- Heat exchangers

Bioengineering Applications

- Dental crowns
- Hip implants

Other Dual-Use Applications

- Infrared transmission windows
- Ceramic packaging for microprocessors
- Cathode ray tubes

Fig. 14

Successful Technology Transfer

- **Customer Focus**
- **Cooperative Efforts**
- **Dual–Use Technology**

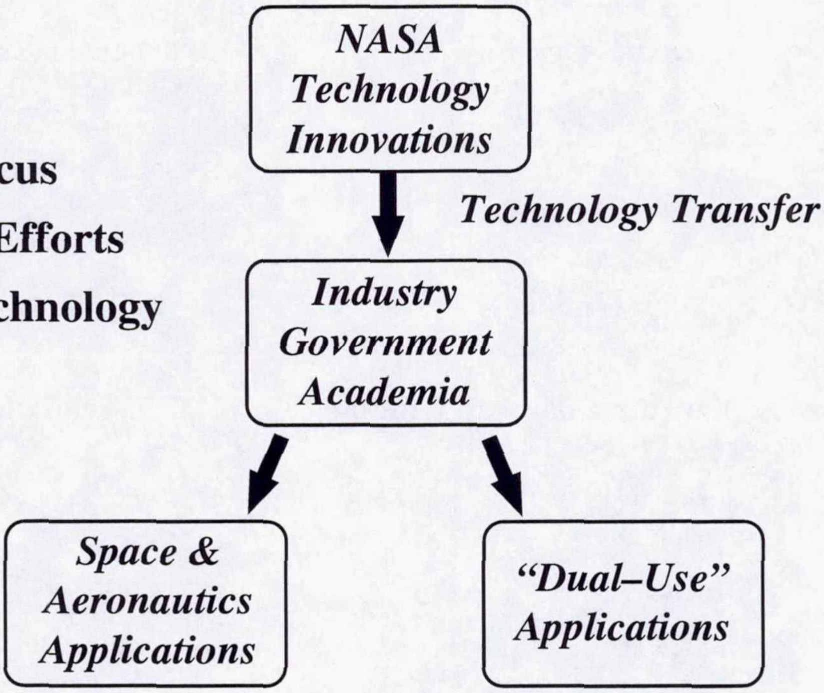

NASA Technology Innovations

Technology Transfer

Industry Government Academia

Space & Aeronautics Applications

"Dual–Use" Applications

Fig. 15

Requests for CARES/*Life* in Past Year (U.S.)

AlliedSignal	*APU Turbine Rotors*
Army	*Chip Packages and Electronic Hardware*
Battelle	*Composites Consortium*
Caterpillar	*Various Engine Parts*
Ceramatec	*Fuel Cells, Oxygen Generators, Sensors*
Cummins	*Fuel Injectors*
Los Alamos Nat. Lab.	*Alumina Windows for Particle Accelerators*
MIT/ARPA	*Micro Gas Turbines*
3M	*Various Ceramic Parts*
NASA Ames	*Reusable Spacecraft Thermal Protection*
NGK	*Various Ceramic Parts*
Novellus	*Semiconductor Wafer Manufacturing Equipment*
Snaprogetti	*Heat Exchangers, Chemical Reactors*
Teledyne TCAE	*Auto. Gas Turbines*
Thomson	*Television Picture Tubes*
U. Of Mass.	*Research, and Teaching*
U. Of Penn.	*Research*
Westinghouse	*Submarine Reactor Thrust Bearing*

Fig. 16

NASA/CARES Dual-Use Ceramics Design Examples

Dental Crown

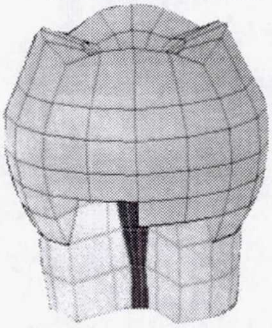

Turbocharger Wheel

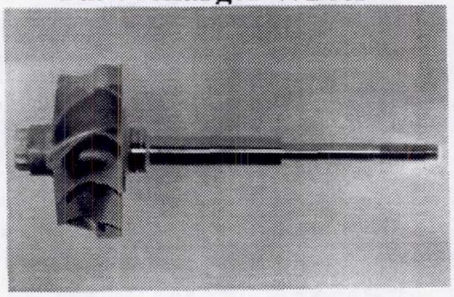

ZnSe Vacuum Chamber Window

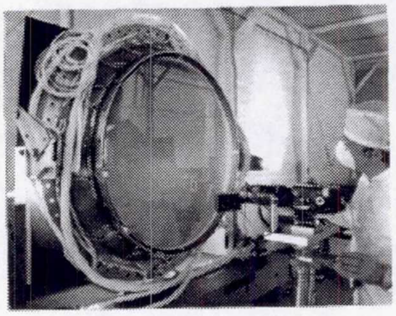

Television Picture Tube

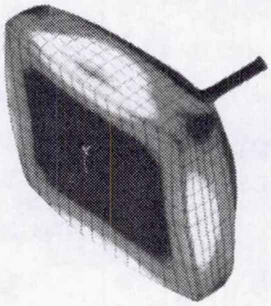

Evacuated tube stresses

Fig. 17

NASA LeRC's innovative CARES/*Life* software design tool allowed Philips to develop superior glass television picture tubes

- **Manufactured over 1 million components**
- **Realized cost savings in excess of $1 million/year**
- **Optimized structural design for safety, reliability, performance, and efficiency**
- **Optimized component fabrication process through use of design-for-manufacturability (DFM) techniques**
- **Reduced glass consumption, tube weight, hazardous waste, and x-ray emissions**

Fig. 18

CARES Award–Winning Software

- ★ **1996 American Ceramic Society Corporate Technical Achievement Award**
- ★ **1995 R&D 100 Award**
- ★ **1994 NASA Software-of-the-Year Award**
- ★ **1994 Federal Laboratory Consortium Technology Transfer Award**

Fig. 19

Conclusions

- **Lighter weight and more durable ceramic components can be designed using *CARES/Life***
- **Program ease of use is enhanced with new graphics, input preparation, and finite element interface modules**
- **Diligent technology transfer efforts have led to successful employment of *CARES/Life* across a diverse range of industrial sectors**

Fig. 20

FIBER CONTRACTION APPROACHES
FOR IMPROVING CMC PROPORTIONAL LIMIT

JAMES A. DiCARLO
NASA Lewis Research Center
and
Hee Mann Yun*
Cleveland State University
Cleveland, Ohio

Introduction

The fact that the service life of ceramic matrix composites (CMC) decreases dramatically for stresses above the CMC proportional limit has triggered a variety of research activities to develop microstructural approaches that can significantly improve this limit. As discussed in a previous report (ref. 1), both local and global approaches exist for hindering the propagation of cracks through the CMC matrix, the physical source for the proportional limit. Local approaches include: (1) minimizing fiber diameter and matrix modulus; (2) maximizing fiber volume fraction, fiber modulus, and matrix toughness; and (3) optimizing fiber-matrix interfacial shear strength; all of which should reduce the stress concentration at the tip of cracks pre-existing or created in the matrix during CMC service. Global approaches, as with pre-stressed concrete, center on seeking mechanisms for utilizing the reinforcing fiber to subject the matrix to in-situ compressive stresses which will remain stable during CMC service. Demonstrated CMC examples for the viability of this residual stress approach are based on strain mismatches between the fiber and matrix in their free states, such as, thermal expansion mismatch and creep mismatch (cf. refs. 1 and 2). However, these particular mismatch approaches are application limited in that the residual stresses from expansion mismatch are optimum only at low CMC service temperatures and the residual stresses from creep mismatch are typically unidirectional and difficult to implement in complex-shaped CMC.

The general objective of the present research is to determine the technical feasibility for improving the CMC proportional limit by a strain-mismatch approach which is based on the high-temperature in-situ axial contraction of the reinforcing fibers. The theory and technical details of this concept are explained in Fig.1. The prime motivation for examining such an approach was the observation, during fiber research studies at NASA Lewis, that some polycrystalline ceramic fibers currently being utilized as CMC reinforcement will display large axial contractions under certain high temperature conditions (refs. 3 and 4). These contractions occur even under the application of high tensile stress, suggesting that they should also occur within CMC, even under the back-stresses provided by the matrix during compression. As an initial step toward understanding the feasibility of the fiber contraction approach, the objective of this study (Fig. 2) was to measure and model the effects of time, temperature, and tensile stress on the free-state axial contraction of SiC fibers by two mechanisms: (I) decomposition and densification and (II) anelastic creep recovery.

Contraction Mechanism I: Decomposition/Densification

The underlying theory for Mechanism I (Fig. 3) is the fact that due to their processing approach, some polymer-derived fibers contain unstable oxide impurity phases which are not eliminated at the maximum production temperatures for the fibers (typically near 1200°C). Thermally treating these fibers above this

---

* NASA Resident Research Associate at Lewis Research Center

temperature will result in decomposition of these phases, mass loss by volatilization of carbon and silicon monoxide, densification of the resulting microstructure, and axial and radial contraction of the fiber. Using the experimental approach described in Fig. 4, the time- and temperature-dependent contraction strain results shown in Fig. 5 were obtained for multifilament tows of polymer-derived Hi-Nicalon and Nicalon fibers. For these data, the tows were held at effectively zero stress in an argon environment. Applying thermal activation theory (ref. 5), the contraction data for the lower oxygen-containing and thus more technically-viable Hi-Nicalon fiber were found to be closely modeled by the master contraction curve shown in Fig. 6. The fact that all the data do not fit this curve can possibly be explained by measurement difficulties during the initial, very rapid, decomposition stages at the higher temperatures.

Two primary concerns for applying Mechanism I to CMC are (1) concurrent creep of the fiber during contraction so that the matrix back-stresses could possibly negate the benefits of contraction, and (2) loss of significant fiber tensile strength due to the decomposition process. Fig. 7 for Hi-Nicalon fibers in single and tow form show that as long as tensile back-stresses do not exceed ~100 MPa, the fibers can indeed achieve a net contraction of ~0.1%, a minimum desirable level since CMC proportional limits are currently less than this value. But, as Fig. 8 shows, Hi-Nicalon tows treated in argon can lose approximately 50% of their initial room-temperature strength and that, for treatments in vacuum, the strength loss can be even worse under certain conditions. Thus, as discussed in Fig. 9, for optimum application of contraction Mechanism I using Hi-Nicalon fibers, the CMC should preferably contain a large volume fraction of fibers and a low modulus matrix in order to minimize effects due to matrix back-stresses and fiber strength degradation. Additional unknown concerns could be chemical alteration of the fiber-matrix interface by the fiber decomposition products, and alteration of the decomposition kinetics by the fiber interfacial coating or by the matrix.

Contraction Mechanism II: Anelastic Creep Recovery

The underlying theory for contraction Mechanism II (Fig. 10) is based on the transient creep behavior observed for all SiC fibers tested to date (ref. 6). This transient behavior indicates that during creep at a constant level of applied stress, internal stresses (associated with grain boundary sliding) build up in the fiber microstructure which may eventually fully oppose the applied stress, resulting in saturation of creep strain. When the creep stress is completely removed, it has been observed that these internal stresses drive the creep strain back towards zero at a rate dependent on time and temperature (anelastic behavior; cf. ref. 4). It has also been observed that under zero back stress, the amount of recovered strain is some fraction of the total creep strain and that this fraction decreases with increasing creep strain (ref. 7). Thus, as discussed in Fig. 11, if thermally-stable SiC fibers were pre-crept, for example, by tensioning devices during or after fiber production, these fibers with their internal stresses could then be inserted into CMC by use of matrix fabrication time-temperature conditions less than those used during the pre-creeping stage. The CMC could then be thermally treated above the matrix fabrication temperature to allow in-situ fiber contraction in which the fiber internal stresses act to overcome the matrix back-stresses. Thus high applied creep stresses are needed to more easily overcome matrix back-stresses; but they can also be beneficial for achieving a given creep strain in a cost-effective short time.

For those studies aimed at measuring and modeling Mechanism II, SCS-6 monofilaments were used to generate data for tensile creep and recovery. This large-diameter SiC fiber was chosen because bend data exist for its creep/recovery behavior and because this behavior should be typical of thermally-stable small-diameter SiC fibers which are more technically viable for complex-shaped CMC. The experimental approach (Fig. 12) focused on determining (1) whether time- and temperature-dependent creep-recovery models developed previously from bend tests on SCS-6 fibers also applied for tensile tests on SCS-6 and (2) whether Mechanism II could provide tensile contraction strains (i.e. recovered strains) greater than

0.1% after the application of a high applied creep stress (750 MPa). The recovered strain versus creep strain results shown in Fig. 13 pertain to both questions. First, the solid curves calculated from SCS-6 bend recovery data and an anelastic creep model (ref. 7) show that although the recovered strain (for zero back-stress) increases with increasing creep strain, its fraction of the creep strain decreases. However, at a given total creep strain, the recovered strain can be increased by increasing the stress applied during the creep stage. These curves should apply in a qualitative manner to all SiC fibers which display transient creep. The close agreement between the 800 MPa predicted curve and the two SCS-6 data points supports the use of this anelastic model to also predict the amount of tensile creep recovery after achieving a given creep strain level. To estimate the conditions needed to achieve this creep strain, one can use the empirical equation shown for the abscissa in Fig. 13. Using this equation, NASA studies have determined the empirical creep constants for all SiC fibers of current technical interest (ref. 6). For the second question, it can be observed in Fig. 13 that the recovered strains for the SCS-6 tensile data were ~ 0.3%, a value well above the level needed for possible CMC application of Mechanism II. Also since the fiber internal stresses associated with the 0.3% recovered strain were ~750 MPa, fiber contractions within CMC should be able to withstand high matrix back-stresses.

Concluding Remarks

The key results of this study are summarized in Fig. 14. Regarding general conclusions from the current study (Fig. 15), Mechanisms I and II appear to be feasible for increasing CMC proportional limits. To demonstrate this, models now exist for estimating the proper fiber and CMC treatment conditions for activating these mechanisms and also the maximum amount of free-state fiber contraction. Prime concerns for the applicability of Mechanism I with Hi-Nicalon fibers are low contraction under high matrix back-stress and tensile strength loss during contraction. On the other hand, Mechanism II with SCS-6 fibers does not appear to suffer from these issues. Nevertheless, there still remains concern that the required fiber pre-creeping stage may be difficult to implement at high applied stress, for example, because of a lack of adequate tensioning devices for continuous tows of small-diameter fibers or because of a high incidence of random fiber breaks in the tows. Finally, as detailed in Fig. 16, future research will attempt to demonstrate both mechanisms in mini-CMC using SiC matrices fabricated by chemical vapor deposition (CVI). This matrix type has many advantages: (1) fabrication temperatures below those of the contraction mechanisms, (2) capability for remaining elastic during fiber contraction, and (3) the existence of a large vendor base for CMC fabrication.

References

1. DiCarlo, J.A.: Microstructural Design of Structurally Reliable CMC. HiTEMP Review, 1993, NASA CP19117, 1993, pp. 62-1 to 62-11.
2. Widjaja, S.; Jakus, K.; Ritter, J.E.; Lara-Curzio, E.; Sun, E.; Watkins, T.R.; and Brennan, J.J.: High-Temperature Load Transfer in Nicalon/BMAS Glass-Ceramic Matrix Composites. Ceram. Eng. & Sci. Proc., 1997.
3. Yun, H.M. and DiCarlo, J.A.: High Temperature Contraction Behavior of Polymer-Derived SiC Fibers. Ceram. Eng. & Sci. Proc., 1997.
4. DiCarlo, J.A.: Creep of Chemically Vapour Deposited SiC Fibers. J. of Mat. Sci., vol. 21, 1986, pp. 217-224.
5. DiCarlo, J.A.; Yun, H.M.; and Morscher, G.N.: Models for the Thermostructural Properties of SiC Fibers. Proceedings for HTCMC-2, Ceramic Transactions, vol. 57, 1995, pp. 343-348.
6. DiCarlo, J.A. and Yun, H.M.: Creep and Stress Rupture Behavior of Advanced SiC Fibers. Proceedings of ICCM-10, Whistler, B.C., Canada, vol. VI, 1995, pp. 315-322.
7. DiCarlo, J.A.; Goldsby, J.C.; and Morscher, G.N.: Relationships Between Damping, Creep, and Stress-Relaxation of Ceramic Fibers. 1995, unpublished.

CONCEPT OF INCREASING CMC PROPORTIONAL LIMIT BY FIBER CONTRACTION

- High-Temperature Mechanisms Exist Which Cause Fibers To Contract Axially Even Under The Application of High Tensile Stress. If This Contraction Is Allowed To Occur Within Consolidated CMC, It Should Provide A Compression of The Matrix Along The Fiber Directions.

- Since Matrix Fracture Strains In CMC Are ~0.1%, Small Fiber Contraction Strains At or Above This Level Should Significantly Improve The CMC Proportional Limit And Service Life.

- For Optimum Compression, Matrix Fabrication Temperatures Should Be Below The Fiber Contraction Temperatures. Thus Post-Thermal Treatment Of The CMC Will Generally Be Required To Implement Concept.

- Likewise, Treated CMC Should Be Utilized Under Service Conditions Where Fiber And Matrix Remain Elastic, In Order To Retain A Time And Temperature-Independent Compression Of The Matrix.

Fig. 1

OBJECTIVES

GENERAL

Investigate The Feasibility For Compressing CMC Matrices And Improving CMC Proportional Limits By The In-Situ Axial Contraction Of The Reinforcing Fibers

THIS STUDY

As An Initial Step, Measure And Model The Effects Of Time, Temperature, And Stress On The Free-State Contraction Of SiC Fibers By Two Mechanisms:

I. Decomposition/Densification
II. Anelastic Creep Recovery

Fig. 2

Mechanism I: Fiber Contraction By Decomposition And Densification

Underlying Theory

- Polymer-Derived SiC Fibers, Like Nicalon And Hi-Nicalon, Are Typically Processed At Maximum Temperatures (~1200°C) Which Allow The Retention Of Unstable Oxide Phases And Porosity In The Microstructure Inherent In The Fiber Process

- Thermal Treatment Above The Maximum Processing Temperature Will Cause The Oxide Phases To Decompose And The Resulting Microstructure To Densify, Thereby Causing Fiber Axial And Radial Contraction

Fig. 3

Mechanism I: Fiber Contraction By Decomposition And Densification

Experimental Approach

- Measure And Model Kinetics For Contraction Of Hi-Nicalon Fibers Under Unstressed And Stressed Conditions

- Determine Residual Strength Of Contracted Fibers At Room Temperature

- Test Conditions:
    - Specimens: Hi-Nicalon Tows (N = 500, Nippon Carbon)
    - Fiber Creep Facilities: Grip-Grip Length ~ 250 mm
Hot Zone ~ 120 mm
    - Temperatures (Constant): 1200 to 1700°C
    - Environments: Argon, Vacuum
    - Stress (Constant): 0.6 to 140 MPa
    - Strength Test (Tow): Gauge Length ~ 25 mm

Fig. 4

TYPICAL CONTRACTION CURVES FOR Hi-NICALON AND NICALON TOWS IN ARGON

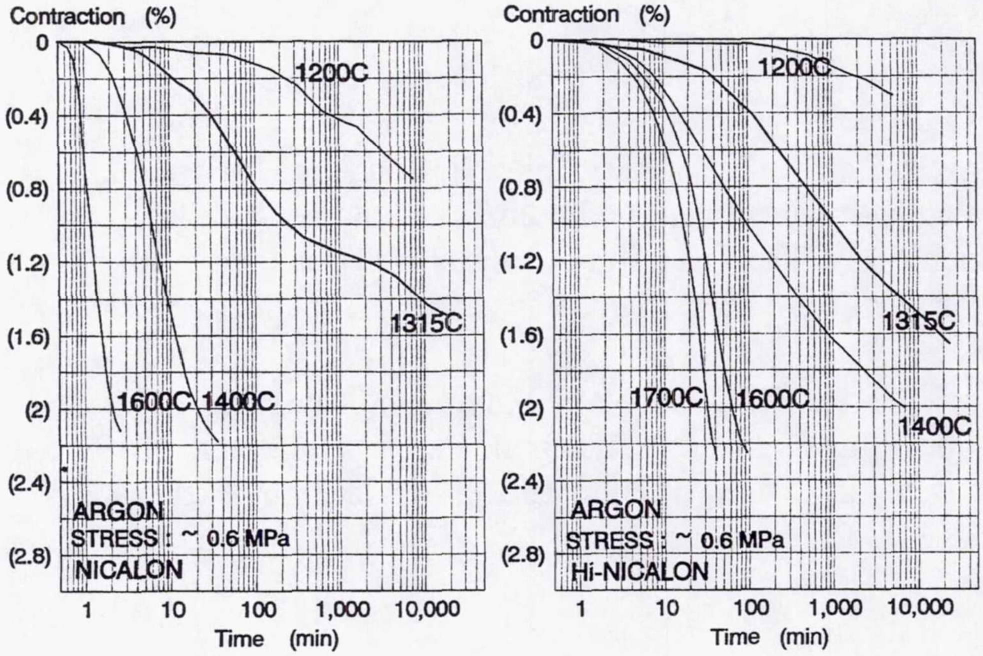

Fig. 5

MASTER CONTRACTION CURVE FOR Hi-NICALON TOWS IN ARGON USING ACTIVATION MODEL

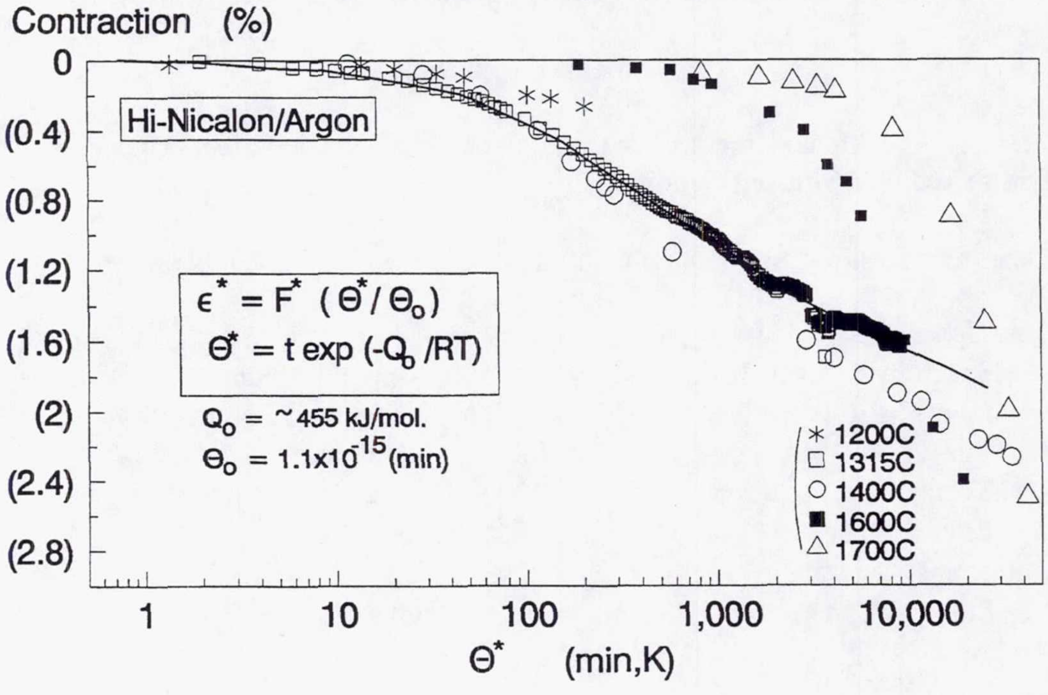

Fig. 6

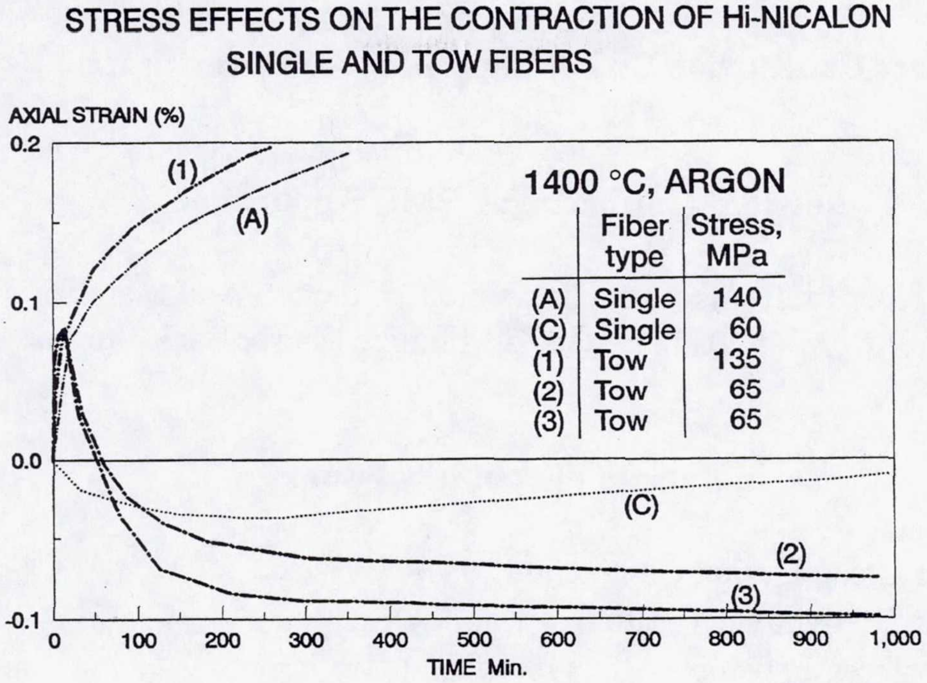
STRESS EFFECTS ON THE CONTRACTION OF Hi-NICALON SINGLE AND TOW FIBERS
AXIAL STRAIN (%)
0.2
0.1
0.0
-0.1
0
100
200
300
400
500
600
700
800
900
1,000
TIME Min.
1400 °C, ARGON
Fiber type
Stress, MPa
(A) Single 140
(C) Single 60
(1) Tow 135
(2) Tow 65
(3) Tow 65
(1)
(A)
(C)
(2)
(3)

Fig. 7

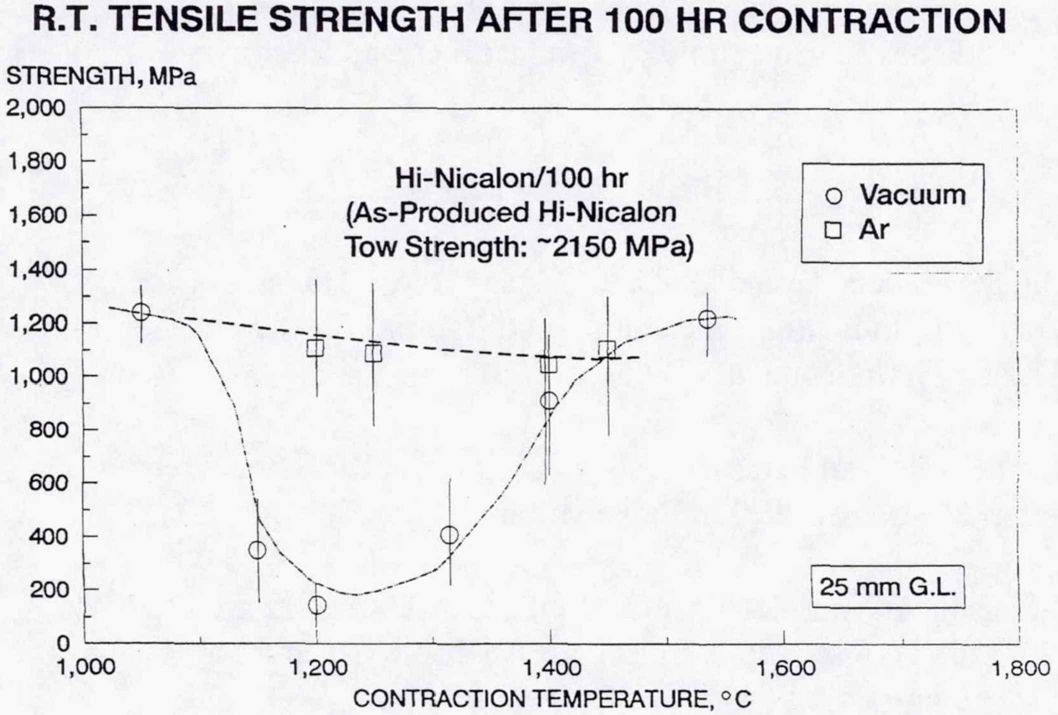
R.T. TENSILE STRENGTH AFTER 100 HR CONTRACTION
STRENGTH, MPa
2,000
1,800
1,600
1,400
1,200
1,000
800
600
400
200
0
1,000
1,200
1,400
1,600
1,800
CONTRACTION TEMPERATURE, °C
Hi-Nicalon/100 hr
(As-Produced Hi-Nicalon
Tow Strength: ~2150 MPa)
○ Vacuum
□ Ar
25 mm G.L.

Fig. 8

Mechanism I:
Fiber Contraction By Decomposition And Densification

Possible Approach For CMC Application

- Use Fiber Preforms With High Volume Fraction And Matrices With Low Modulus In Order To Minmize Matrix Back-Stress

Potential Feasibility Issues

- Fiber Creep During Contraction
- Fiber Strength Degradation
- Fiber Decomposition Alters Interfacial Coating

Fig. 9

Mechanism II:
Fiber Contraction By Anelastic Creep Recovery

Underlying Theory

- All SiC Fibers Tested To-Date Display Large Transient Creep Behavior, Indicating The Buildup Of Internal Elastic Stresses During Grain Boundary Sliding

- Decreasing Temperature And Releasing Appled Stress Freezes Internal Stresses Within Fiber Microstructure

- Subsequent Thermal Treatment Of Fiber Allows Internal Elastic Stresses To Recover, Resulting In Anelastic Creep Recovery Or <u>Fiber Contraction</u> From The Crept Condition

Fig. 10

Mechanism II:
Fiber Contraction By Anelastic Creep Recovery

Potential Approach For CMC Application:

- Choose Stoichiometric SiC Fibers Which Are Thermally Stable And Creep At High Temperatures Above Typical Matrix Fabrication Temperatures
- Pre-Creep Fibers At High Stress Without Causing Rupture
  (At Fiber Vendor During Or After Fiber Production)
- Consolidate CMC And Post Treat To Allow In-Situ Recovery Of Fiber Creep Strain

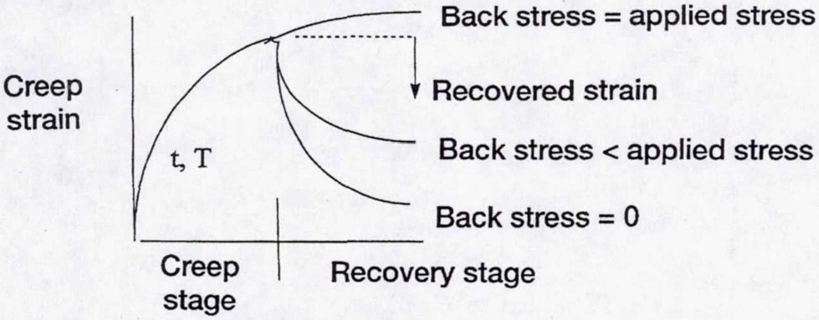

- High Applied Creep Stresses Are Needed To Provide
  ---Resistance To Matrix Back-Stress During Fiber Contraction
  ---Short Creep Times For Cost-Effectiveness

Fig. 11

Mechanism II
Fiber Contraction By Anelastic Creep Recovery

Experimental Approach

- Determine And Model The Relationships Between Tensile Creep Recovery And Tensile Creep Using SCS-6 Monofilament Fibers

- Determine The Tensile Creep Conditions For Achieving Fiber Contraction Strains Greater Than 0.1%

- Test Conditions:
  - Fiber Creep/Recovery Facilities: Hot Zone ~ 120 mm
  - Environment: Argon
  - Creep Temperatures/Time: 1300 and 1400 °C / 1 Hour
  - Creep Stress: 750 MPa
  - Recovery Temperature/Time: 1500 °C / 10 Hours
  - Recovery Stress: < 1 MPa

Fig. 12

Mechanism II:
Fiber Contraction By Anelastic Creep Recovery

Results For Recovered Strain Vs Creep Strain

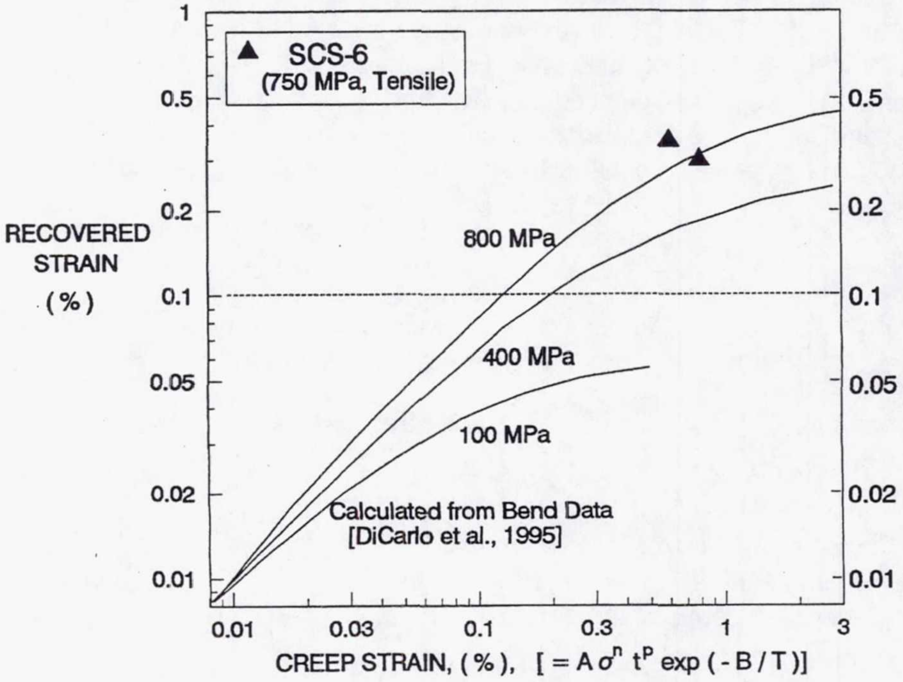

Fig. 13

SUMMARY OF RESULTS

- Measurements Have Been Made And Models Developed Which Describe The Effects of Time, Temperature, And Stress on The Axial Contraction Strain of SiC Fibers Which can Occur By Two Mechanisms:
  I: Fiber Decomposition And Densification
  II: Anelastic Strain Recovery After Fiber Creep

- For Mechanism I And Hi-Nicalon Fibers, Contraction Strains Well Above 1% Can Be Achieved, But At The Expense of Fiber Strength Degradation By ~50%. Maximum Back-Stresses For Hi-Nicalon Contraction Are ~ 100 MPa.

- For Mechanism II And SCS-6 Fibers, Contraction Strains Up To 0.3% Were Achieved At High Stress (~750 MPa) and Low Total Creep. Tensile Results Agree Closely With Anelastic Creep Recovery Model Developed From Fiber Bend Data.

Fig. 14

CONCLUSIONS

- Models Now Exist For Understanding And Predicting The Free-State Contraction Of Hi-Nicalon Fibers By Decomposition/Densification And of Thermally Stable SiC Fibers, Like SCS-6, By Anelastic Creep Recovery.

- Both Mechanisms Appear Feasible For Causing Sufficient Matrix Compression In CMC To Significantly Increase The Proportional Limit.

- Potential Issues For Using Hi-Nicalon Fibers And Mechanism I Are Fiber Strength Loss And Fiber Creep At The Decomposition/Densification Temperatures.

- Potential Issues For Using Mechanism II Appear To Be In The Pre-Creeping Stage, i.e., Stress Capability Of Fiber Tensioning Devices And Possible Random Fiber Fracture During Tensioning.

Fig. 15

FUTURE RESEARCH

- To Demonstrate the Feasibility of Fiber Contraction Mechanisms I and II, Mini-CMC Composites Will Be Fabricated Using CVI Matrices Reinforced By
    - Single Tows of As-Produced Hi-Nicalon Fibers
    - Single Fibers of Pre-Crept SCS-6 Monofilaments

- Initial Models Taking Into Account Matrix Back-Stress Effects Will Be Developed In Order To Estimate Best Conditions For Thermal Treatment of The Mini-CMC and For Creep of the SCS-6 Fibers.

- Changes In Matrix Cracking Behavior Will Be Monitored Using Tensile Stress-Strain Hysteresis And Acoustic Emission.

Fig. 16

THERMAL FATIGUE LIMITATIONS OF CONTINUOUS FIBER METAL MATRIX COMPOSITES

GARY R. HALFORD
Lewis Research Center
Cleveland, Ohio

and

Vinod K. Arya*
University of Akron
Akron, Ohio

Introduction

The potential structural benefits of unidirectional, continuous-fiber, metal matrix composites (MMCs) are legendary. When compared to their monolithic matrices, MMCs possess superior properties such as higher stiffness and tensile strength, and lower coefficient of thermal expansion in the direction of the reinforcing fibers. As an added bonus, the MMC density will be lower if the fibers are less dense than the matrix material they replace. The potential has been demonstrated unequivocally both analytically and experimentally, especially at ambient temperatures. Successes prompted heavily-funded National efforts within the United States (USAF and NASA) and elsewhere to extend the promise of MMCs into the temperature regime wherein creep, stress relaxation, oxidation, and thermal fatigue damage mechanisms lurk. This is the very regime for which alternative high-temperature materials are becoming mandatory, since further enhancement of state-of-the-art monolithic alloys is rapidly approaching a point of diminishing returns.

Unfortunately, MMCs offer but limited improvement in creep, relaxation, and oxidization resistance, since these resistances are governed largely by the matrix material *per se*, and the matrix is still very much in evidence in the MMC. More seriously, however, MMCs are at a distinct disadvantage over their monolithic matrix counterpart when it comes to resisting damage induced by repeated thermal cycling between ambient temperature and maximum service operating temperatures. As will be shown, thermal cycling is the Achilles' heal of MMCs owing to the large internal thermal stresses and strains that develop in the constituent matrix and fibers because of their significant mismatch in thermal expansion α. The mismatch is an inherent one provided a mismatch in matrix/fiber modulii of elasticity is one of the desired characteristics of an MMC. This is to be expected from the Grüneisen equation (see, for example, ref. 1) that inversely relates α to bulk modulus of elasticity K,

$$\alpha = (\gamma C_v/3KV) \tag{1}$$

---

* NASA Resident Research Associate at Lewis Research Center.

where γ is Grüneisen's constant that is related directly to the sum of the two powers in the equations for the attractive- and repulsive-energy versus atomic spacing equations, C_v is the specific heat, and V is the molar volume. Bulk and Young's moduli E are linearly related. Figure 1 depicts Eq. (1) for three major classes of materials; organic, metallic, and ceramic (ref. 2). The more disparate are the values of the modulus between fiber and matrix, the greater the thermal expansion mismatch and hence the greater will be the thermal stresses and strains for a given thermal excursion.

The current analytic research examines the thermal stresses and strains in unit cubes of MMCs induced by exposure of one face to a heat flux, Q, and the opposite face to a fixed temperature heat sink. Faces parallel to the x-direction heat flux were assumed insulated to make the analyses more tractable. A comprehensive range of fiber/matrix MMC architectures and relative orientations to the heat flux Q have been analyzed. The objective, Fig. 2, is to determine which architectures, if any, are the least susceptible to thermal stresses and strains, and hence which offer the greatest potential resistance to thermal fatigue cracking.

Material, Properties, Composite Cubes

A continuous fiber (silicon carbide, SCS6, 33% by vol.) reinforced titanium matrix (Ti-15-3) composite was analyzed. Pertinent time-independent, temperature-dependent material properties of the constituent materials are given in Fig. 3. Figure 4 lists discrete ply properties vs. temperature, computed from METCAN (ref. 3). The composite cubes consist of symmetric 12 ply lay ups with each ply having the dimensions 0.262 x 0.262 x 0.022 cm (0.665 x 0.665 x 0.0559 in). Several laminated architectures were selected to represent the extreme combinations of plies relative to the x-direction of heat flux, Fig. 5. One of the 12 cubes represents the stand-alone matrix material (Case 0). Four distinct laminate lay-ups (labelled I, II, III, and IV) are positioned in three orientations (A, B, and C) relative to a heat flux in the x-direction. Case IA is equivalent to Case IC, so Case IA is dropped and Case 0 is shown in its place. The Case indexing scheme follows a progression to a thinner center laminate and thicker laminate faces, Fig. 6

Thermal Loading, and Structural Finite Element Analyses

Elementary cubes were thermally loaded (Fig. 5) with temperature rising from 21°C (70°F) to a maximum on the heated face while the opposite face was maintained at 21°C (70°F). Side faces were insulated. Maximum temperatures for the stand-alone matrix and composite cubes were determined by assuming both to be subjected to the same heat flux. For the arbitrarily prescribed maximum temperature of 800°C (1471°F) for the stand-alone matrix, thermal conductivity calculations based on a constant heat flux resulted in a maximum temperature of 910°C (1670°F) for the composite cubes owing to their lower thermal conductivity. Both continuum (Unit Cube with 1728 elements, 2197 nodes) and micromechanical (Unit Cell with 3072 elements, 3689 nodes) elastic finite element structural analyses were performed using MARC (ref. 4) with 8-noded, solid hexagonal elements, Fig. 7. The micromechanical model is a sub-element of the continuum. Parallel faces in both models were forced to remain parallel during thermal loading. The elastic analyses enables generalization of results to other ranges of thermal cycling. Sensitivity studies (varying α and E by factors of 2) permit extrapolation of results to other MMC systems.

Results

Stand-alone matrix results (Case 0) are shown in Figs. 8 and 9. The maximum thermal stress range (428 Mpa (62 ksi)) and mechanical strain range (0.48 %) are in the transverse (y and z) directions. The effects of increasing or decreasing α and E by factors of two are as expected and are also displayed. Figure 10 displays the maximum continuum stress range (and corresponding orthogonal stress ranges) found in each of the 11 composite Cases. The location of the maximum stress ranges are shown by the big **X** in fig. 5. In every composite Case, there is a transverse stress that is greater than the maximum stress in Case 0. The maximum ranges are always at the cube face whose temperature cycled between the maximum and the minimum. The most benign case (I-B) has a stress 25% higher than that found in Case 0. Unfortunately, the direction perpendicular to a fiber is the weakest possible direction in any composite. Combining the highest thermal stresses with the weakest directions will invariably give rise to much poorer thermal fatigue resistance than the stand-alone matrix, thereby negating any potential structural benefit of the composite for thermally-loaded components. The extent of the poorer performance, while not experimentally evaluated herein, is indicated by the following observations of others. Tensile strengths of [90] composites are less than the tensile strength of stand-alone matrix material, and isothermal fatigue strengths of [90] composites can be as low as 10% of [0] fatigue strengths (ref. 5). Furthermore, thermal fatigue resistances of composites are expected to be even less than their isothermal fatigue resistance (ref. 6). To better understand why this can be so, it is necessary to examine the thermal stresses and strains inside the composite using a micromechanical structural analysis (Fig. 7). Figure 11 shows the mechanical component of the cyclic thermal strain range developed within the matrix material for each of the 11 composite Cases. Comparable maximum strain ranges are also shown for Case 0 for comparison. In every Case, every strain range in every direction is higher than the maximum strain range in the stand-alone matrix material by 35 to 110%. Furthermore, the maximum strain ranges are always in a direction transverse to the local fiber direction. A summary of results, conclusions, and future research efforts are presented in Figs. 12-14.

References

1. Richards, C. W.: *Engineering Mats. Science.*, Wadsworth, San Francisco, 1961, p. 518.
2. Halford, G. R.: Obstacles to High Temperature Cyclic Structural Durability of Continuous-Fiber Composites. *Computational Mechanics `95, Theory & Application*, S.N.Atluri, G.Yagawa, and T.A.Cruse, Eds., Springer-Verlag, 1995, pp. 1128-1133.
3. Lee, H.-J.; Gotsis, P. K.; Murthy, P. L. N. ; and Hopkins, D. A.: Metal Matrix Composite Analyzer (METCAN), *User's Manual - Version 4.0*, NASA TM-105244, 1991.
4. Anon., *MARC General Purpose Finite Element Program*. Vols. A-D, MARC Analysis Research Corp., Palo Alto, CA, 1992.
5. Hashin, Z. And Rotem, A.: A Fatigue Failure Criterion for Fiber Reinforced Materials. *Journal of. Composite. Materials.*, Vol. 7, 1973, pp 448-464.
6. Halford, G. R.; Lerch, B. A.; and Saltsman, J. F.: Proposed Framework for Thermomechanical Fatigue Life Modeling of Metal Matrix Composites. NASA TP-3320, July 1993.

INVERSE CORRELATION

Stiffness (E) versus Thermal Expansion (α)

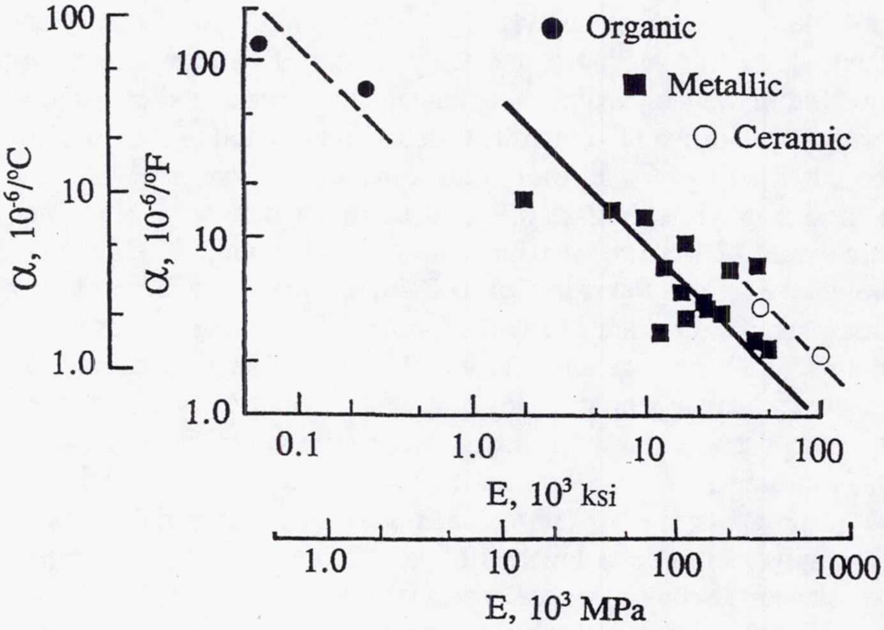

Fig. 1

OBJECTIVE

TO DETERMINE:

Which composite ply architectures suffer the lowest thermal stresses and strains and hence offer the greatest potential resistance to thermal fatigue cracking.

Fig. 2

MECHANICAL PROPERTIES OF CONSTITUENTS

Temp	°C	20.0	130.0	240.0	350.0	460.0	570.0	680.0	790.0	900.0
	°F	70.0	270.0	470.0	670.0	870.0	1070.0	1270.0	1470.0	1670.0
Fiber	E	8.98	8.88	8.79	8.68	8.58	8.47	8.36	8.23	8.11
	v	0.1898	0.1878	0.1857	0.1835	0.1813	0.1790	0.1766	0.1741	0.1715
	α	0.1512	0.1546	0.1579	0.1616	0.1655	0.1695	0.1739	0.1786	0.1836
Matrix	E	1.78	1.67	1.56	1.44	1.30	1.15	0.98	0.78	0.48
	v	0.3196	0.3005	0.2802	0.2582	0.2342	0.2075	0.1768	0.1395	0.0875
	α	0.2503	0.2609	0.2733	0.2811	0.3063	0.3298	0.3622	0.4160	0.5278
Units	E in 10^6xMPa (1MPa = 0.145 KSI); α in (10^{-5} °C^{-1} or 5.56 x 10^{-7} °F)									

E: Young's modulus
v: Poisson's ratio
α: Coefficient of thermal expansion

Fig. 3

EFFECTIVE ORTHOTROPIC PROPERTIES OF THE COMPOSITE

TEMP	C	20.0	130.0	240.0	350.0	460.0	570.0	680.0	790.0	900.0
	F	70.0	270.0	470.0	670.0	870.0	1070.0	1270.0	1470.0	1670.0
E_{11}		2.6600	2.5200	2.3600	2.2200	2.0200	1.8100	1.5700	1.2600	0.8200
E_{22}		4.1600	4.0600	3.9500	3.8300	3.7100	3.5700	3.4200	3.2400	3.0000
υ_{12}		0.1768	0.1634	0.1492	0.1342	0.1180	0.1004	0.0810	0.0588	0.0313
υ_{23}		0.2768	0.2633	0.2490	0.2336	0.2167	0.1981	0.1767	0.1509	0.1152
υ_{31}		0.3038	0.2874	0.2697	0.2504	0.2290	0.2049	0.1768	0.1417	0.0911
G_{12}		1.0210	0.9670	0.9080	0.8450	0.7440	0.6940	0.6000	0.4820	0.3110
G_{23}		1.0210	0.9670	0.9080	0.8450	0.7440	0.6940	0.6000	0.4820	0.3110
G_{31}		1.0180	0.9770	0.9310	0.8800	0.8200	0.7510	0.6600	0.5520	0.3740
α_{11}		0.2096	0.2170	0.2254	0.2352	0.2471	0.2620	0.2820	0.3128	0.3786
α_{22}		0.1797	0.1829	0.1864	0.1899	0.1936	0.1974	0.2009	0.2039	0.2034
Units	E and G in 10^6xMPa (1 MPa = 0.145 KSI) and α in (10^{-5} °C^{-1} or 5.56 x 10^{-7} °F)									

$E_{22} = E_{33}$
$\alpha_{22} = \alpha_{33}$
G: Shear Modulus

Fig. 4

COMPOSITE ARCHITECTURES

Heat Flux in x-direction

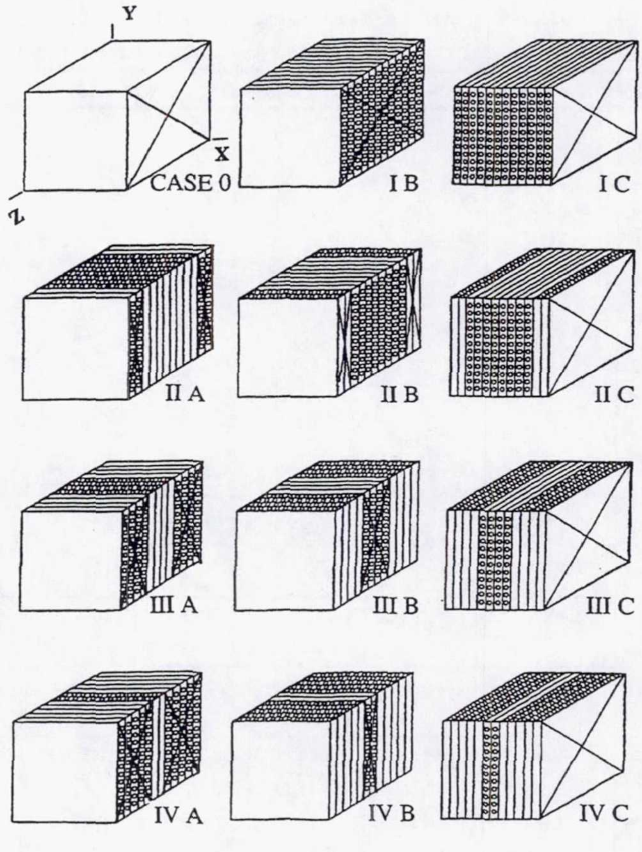

Fig. 5

INDEXING SCHEME FOR COMPOSITE CUBES

I	Center 12 ply laminate between faces of a 0 ply laminate at 90°
II	Center 8 ply laminate between faces of a 2 ply laminate at 90°
III	Center 4 ply laminate between faces of a 4 ply laminate at 90°
IV	Center 2 ply laminate between faces of a 5 ply laminate at 90°
Orientation A	Heat flux perpendicular to fibers in center laminate and parallel to fibers in face laminates
Orientation B	Heat flux perpendicular to fibers in face laminates and parallel to fibers in center laminate
Orientation C	Heat flux perpendicular to fibers in both center and face laminates

Fig. 6

FINITE ELEMENT MODELS

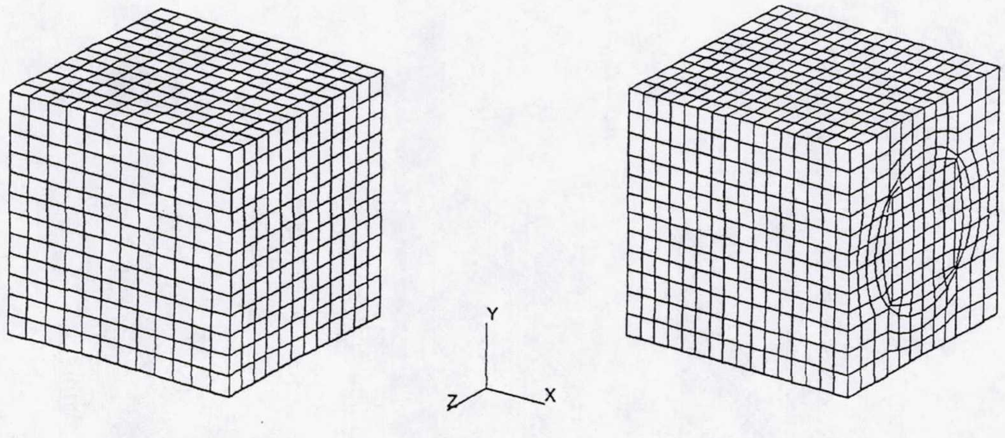

Continuum Model

Micromechanical Model

Fig. 7

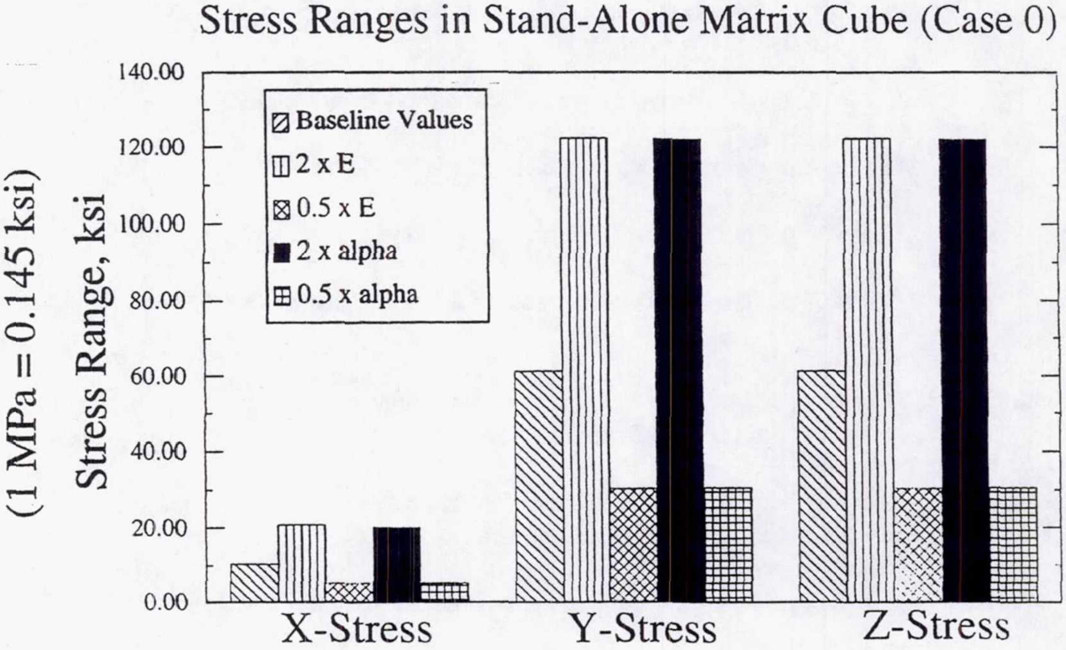
Stress Ranges in Stand-Alone Matrix Cube (Case 0)

Fig. 8

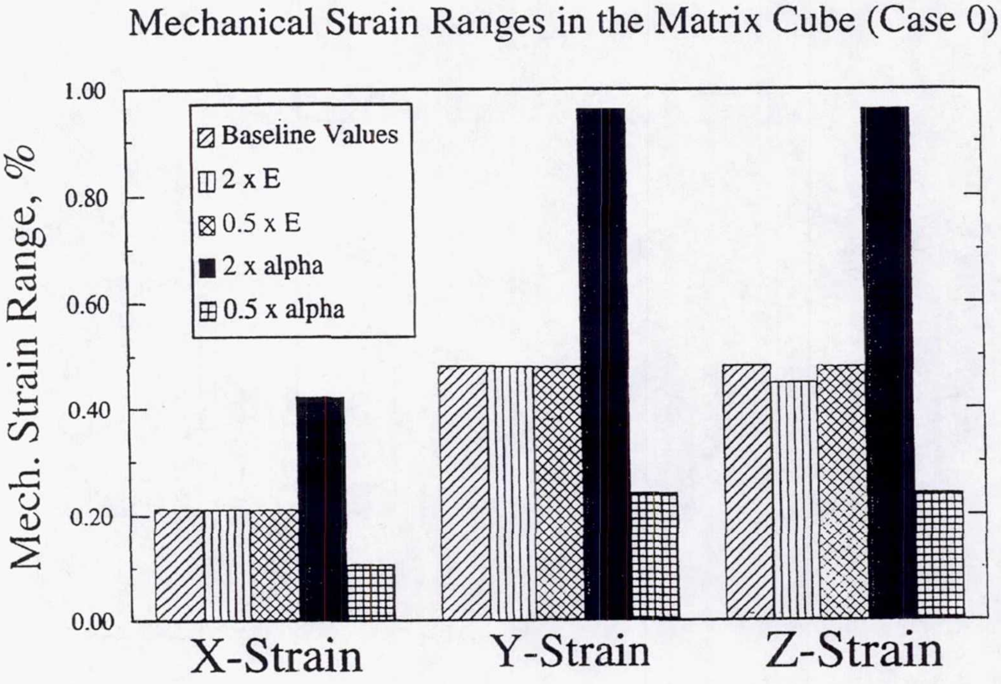
Mechanical Strain Ranges in the Matrix Cube (Case 0)

Fig. 9

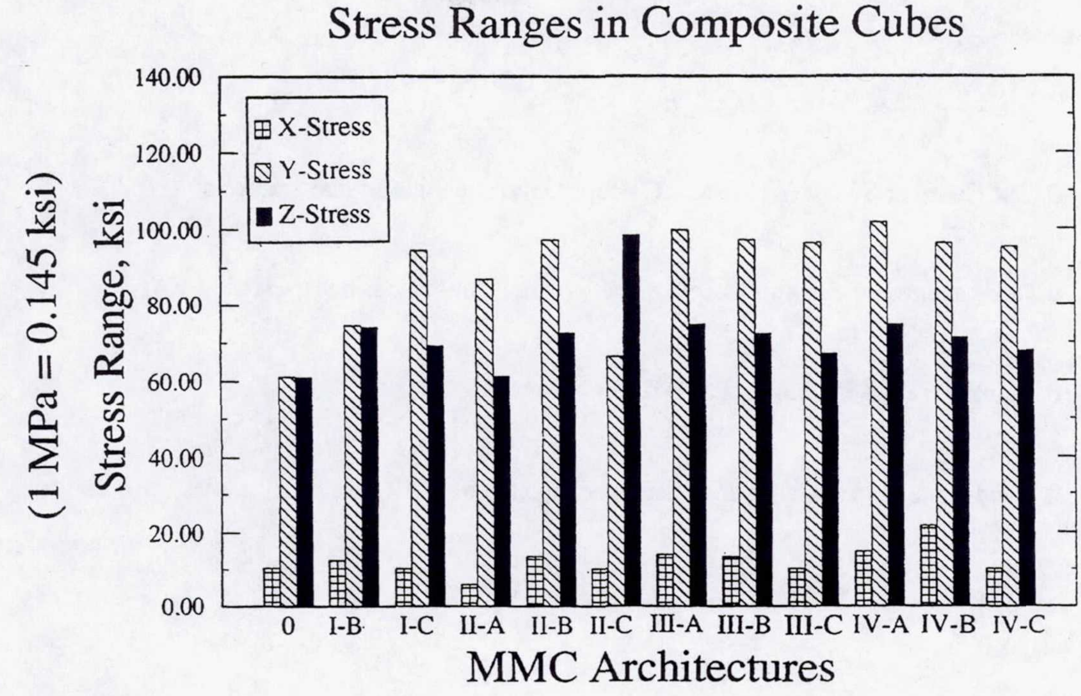
Stress Ranges in Composite Cubes
Stress Range, ksi
(1 MPa = 0.145 ksi)
140.00
120.00
100.00
80.00
60.00
40.00
20.00
0.00
⊞ X-Stress
▧ Y-Stress
■ Z-Stress
0
I-B
I-C
II-A
II-B
II-C
III-A
III-B
III-C
IV-A
IV-B
IV-C
MMC Architectures

Fig. 10

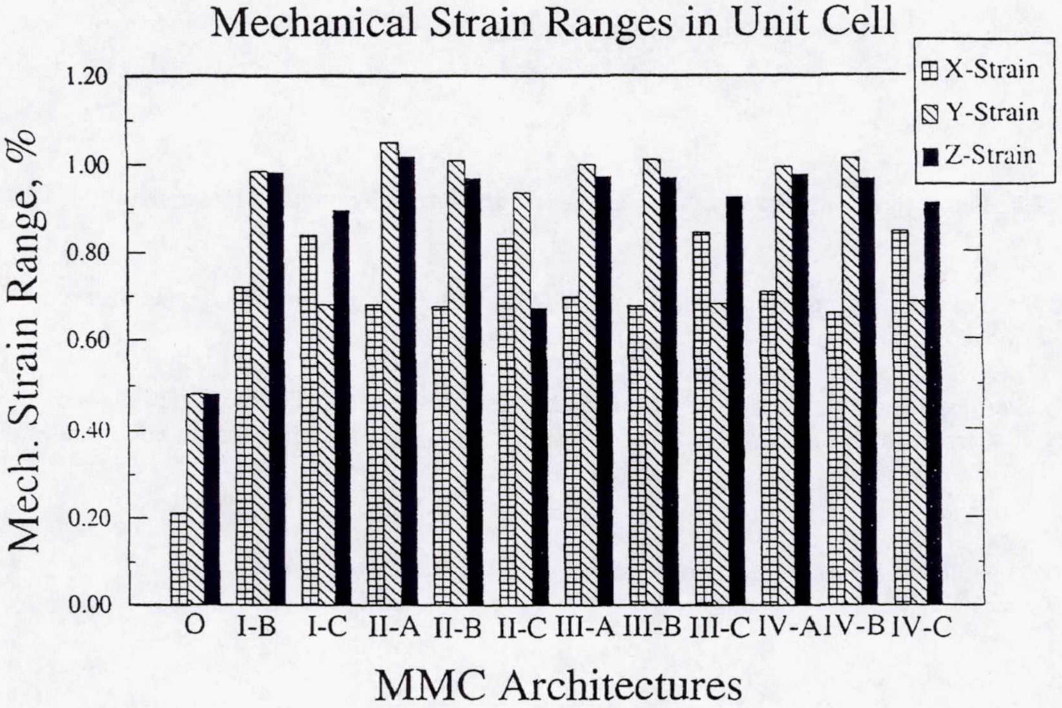
Mechanical Strain Ranges in Unit Cell
Mech. Strain Range, %
1.20
1.00
0.80
0.60
0.40
0.20
0.00
⊞ X-Strain
▧ Y-Strain
■ Z-Strain
O
I-B
I-C
II-A
II-B
II-C
III-A
III-B
III-C
IV-A
IV-B
IV-C
MMC Architectures

Fig. 11

SUMMARY OF RESULTS

0 Unit Cubes of SCS6/Ti-15-3 MMC subjected to analytic thermal gradients

0 Thermal stresses and strains calculated w/continuum-based, linear-elastic FEA

0 Inclusive range of symmetric MMC architectures analyzed

0 Stand-alone matrix Cubes analyzed for comparison + X2 sensitivity studies for E and α

Fig. 12a

SUMMARY OF RESULTS
(Concluded)

0 Continuum thermal stresses in MMCs compared to stand-alone matrix material

0 Max. continuum composite thermal stresses always greater than for stand-alone material

0 Micromechanics Unit Cell analyses at critical locations in MMC Cubes reveal ranges of thermal strain transverse to fiber much greater (35 to 118% higher) than max. ranges of strain in stand-alone matrix material

0 Generally recognized, direction transverse to fibers is weakest

Fig. 12b

CONCLUSIONS

0 Thermally induced ranges of stress and mechanical strain in MMC matrix significantly greater than in stand-alone matrix material

0 Most benign MMC architecture is Case I-C (all plies & fibers perpendicular to heat flux) Yet, max. mechanical range of strain is 88% higher than in stand-alone matrix

0 Case II-A least benign w/range of strain 118% higher than in stand-alone matrix material

0 High thermally-induced ranges of strain in the weakest possible direction

0 Thermal fatigue resistance of continuous-fiber reinforced MMCs severely compromised

Fig. 13

FOCUS OF FUTURE RESEARCH

There are no formal plans for future research on this subject matter.

Fig. 14

APPENDIX—CONTENTS OF VOLUME II

APPLIED LIFE MODELS

DESIGN

VIBRATION CONTROL

LUBRICATION

MECHANICAL COMPONENTS & TRIBOLOGY

REPORT DOCUMENTATION PAGE

Form Approved
OMB No. 0704-0188

1. AGENCY USE ONLY (*Leave blank*)	2. REPORT DATE	3. REPORT TYPE AND DATES COVERED
	April 1997	Conference Publication

4. TITLE AND SUBTITLE

Physics & Process Modeling (PPM) and Other Propulsion R&T
Volume I: Materials Processing, Characterization, and Modeling; Lifing Models

5. FUNDING NUMBERS

WU–523–22–13

6. AUTHOR(S)

7. PERFORMING ORGANIZATION NAME(S) AND ADDRESS(ES)

National Aeronautics and Space Administration
Lewis Research Center
Cleveland, Ohio 44135–3191

8. PERFORMING ORGANIZATION REPORT NUMBER

E–10644

9. SPONSORING/MONITORING AGENCY NAME(S) AND ADDRESS(ES)

National Aeronautics and Space Administration
Washington, D.C. 20546–0001

10. SPONSORING/MONITORING AGENCY REPORT NUMBER

NASA CP–10193

11. SUPPLEMENTARY NOTES

This is a compilation of 36 technical presentations from the PPM and Other Propulsion R&T in the format of extended abstracts followed by tables and figures. Volume I includes papers presented in the sessions on Materials Processing, Materials Characteristics, Materials Modeling, and Lifing Models. Volume II is a compilation of the papers presented at sessions on Applied Life Models, Design, Vibration Control; Mechanical Components, and Tribology. Responsible person, Doug Rohn, organization code 2200, (216) 433–3325.

12a. DISTRIBUTION/AVAILABILITY STATEMENT

Unclassified - Unlimited
Subject Categories 23, 39, and 37

This publication is available from the NASA Center for AeroSpace Information, (301) 621–0390.

12b. DISTRIBUTION CODE

13. ABSTRACT *(Maximum 200 words)*

This CP contains the extended abstracts and presentation figures of 36 papers presented at the PPM and Other Propulsion R&T Conference held in Cleveland, Ohio, on May 1, 1997. The focus of the research described in these presentations is on materials and structures technologies that are parts of the various projects within the NASA Aeronautics Propulsion Systems Research and Technology Base Program. These projects include Physics and Process Modeling; Smart, Green Engine; Fast, Quiet Engine; High Temperature Engine Materials Program; and Hybrid Hyperspeed Propulsion. Also presented were research results from the Rotorcraft Systems Program and work supported by the NASA Lewis Director's Discretionary Fund. Authors from NASA Lewis Research Center, industry, and universities conducted research in the following areas: material processing, material characterization, modeling, lifing, applied life models, design techniques, vibration control, mechanical components, and tribology. Key issues, research accomplishments, and future directions are summarized in this publication.

14. SUBJECT TERMS

Processing; Modeling; Alloys; Composites; Ceramic matrix; Gears; Bearings; Optimization; Tribology

15. NUMBER OF PAGES

234

16. PRICE CODE

A11

17. SECURITY CLASSIFICATION OF REPORT	18. SECURITY CLASSIFICATION OF THIS PAGE	19. SECURITY CLASSIFICATION OF ABSTRACT	20. LIMITATION OF ABSTRACT
Unclassified	Unclassified	Unclassified	

NSN 7540-01-280-5500

Standard Form 298 (Rev. 2-89)
Prescribed by ANSI Std. Z39-18
298-102